

University of St Andrews



Full metadata for this thesis is available in
St Andrews Research Repository
at:

<http://research-repository.st-andrews.ac.uk/>

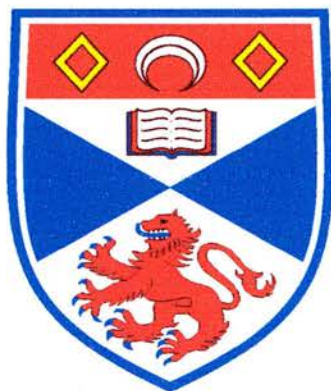
This thesis is protected by original copyright

Structural, Electrochemical and Magnetic Studies of some Lithium Titanates and Lithium Titanium Ferrites

A thesis presented for examination for the title of Ph.D

by

Julian Richard Tolchard



University of St. Andrews

Nov 2001



TL
E22

I, Julian Richard Tolchard, hereby certify that this thesis, which is approximately 37,000 words in length, has been written by me, that it is the record of work carried out by me and that it has not been submitted in any previous application for a higher degree.

Date 18/01/02 Signature of Candidate

I was admitted as a research student in September 1996 and as a candidate for the degree of Doctor of Philosophy in September 1997, the higher study for which this is a record was carried out in the University of St. Andrews between 1996 and 2001.

Date 18/01/02 Signature of Candidate

I hereby certify that the candidate has fulfilled the conditions of the Resolution and Regulations appropriate for the degree of Doctor of Philosophy in the University of St. Andrews and that the candidate is qualified to submit this thesis in application for that degree.

Date 18/01/02 Signature of Supervisor

In submitting this thesis to the University of St. Andrews I understand that I am giving permission for it to be made available for use in accordance with the regulations of the University Library for the time being in force, subject to any copyright vested in the work not being affected thereby. I also understand that the title and abstract will be published, and that a copy of the work may be made and supplied by any *bona fide* library or research worker.

Date 18/01/02 Signature of Candidate

Acknowledgements

As with any work of this kind, this thesis is not just the solitary work of the author, but the product of many peoples labour and advice. I would therefore like to thank some of these people for their time and efforts.

First and foremost I would like to thank my supervisor, Prof. J.T.S. Irvine, for his faith, patience and his confidence that I would someday produce this thesis. I would also like to thank all the past and present members of the JTSI research group, particularly Richard Gover and Brian Mitchell for their humour and healthy cynicism.

Thanks go also to Shannon Brown for his assistance with magnetism and NMR and to my long time friend and office-mate, Jez, for making my attendance and work ethic appear better than they were.

A big thanks goes to the technical staff, both at St. Andrews and at the central facilities at which much of my work was performed, and to Antonio Fernandez Fuentes and his group at Monterrey, where I spent an enjoyable 3 weeks and carried out some of my lithium battery work.

Abstract

In this work we present the results of our studies on a series of ramsdellite structured lithium titanates and a new system of reduced spinel lithium titanate ferrites lying in the nominal spinel stoichiometry “ Li_3O_4 ”-“ Ti_3O_4 ”- Fe_3O_4 ternary phase diagram.

High resolution neutron powder diffraction carried out on the ramsdellite materials showed very high temperature factors for the channel sited lithium. These were refined anisotropically, and some interesting behaviour seen regarding their mode of movement, with lithium showing a preference for movement within the a-b plane, rather than down the c-axis channels. For one sample, the plotted thermal ellipsoids were also seen to “rotate” within the channel with increasing temperature.

Low temperature XRD, NMR and magnetic susceptibility experiments on a sample of LiTi_2O_4 showed a previously unknown structural transition occurring between 200K and 280K and a magnetic transition below 200K.

Neutron and x-ray diffraction studies have been carried out on a sample of chemically delithiated LiTi_2O_4 and the material well characterised as a ramsdellite polymorph of TiO_2 . This material has also been shown to retain the ramsdellite structure on chemical relithiation.

Electrochemical evaluation of LiTi_2O_4 and $\text{TiO}_2(\text{R})$ has shown both to be promising Li battery anodes, particularly the latter, which shows excellent cyclability, a very flat charge/discharge plateau and capacity in excess of 300mAh/g.

Neutron and x-ray diffraction studies have been carried out on a new system of reduced spinel structured lithium titanium ferrites and a large region of 1:3 octahedral ordering found. It has been shown that this ordering, rather than being an “on-off” effect, can in fact be characterised in terms of cation distribution and the length scale of the ordering. Focussing on two solid solutions within this series, $\text{LiFe}_x\text{Ti}_{2-x}\text{O}_4$ and $\text{Li}_{4/3-4/3x}\text{Fe}_{2x}\text{Ti}_{5/3-2/3x}\text{O}_4$, we have also found an unusual tetrahedral coordination preference for Fe^{2+} .

Susceptibility data collected for the $\text{LiFe}_x\text{Ti}_{2-x}\text{O}_4$ series has shown very unusual magnetisation behaviour, with two compensation points being found in addition to the Curie temperature. Low temperature neutron diffraction on a sample of LiFeTiO_4 has shown that the material displays canted ferrimagnetic ordering.

Lithium battery testing of these spinels has also shown unusual behaviour, with very large initial capacities being observed at voltages reminiscent of amorphous insertion, though in-situ x-ray diffraction studies indicate that the spinel framework is retained on cycling. A very large apparent polarisation is also seen between the insertion and deinsertion steps.

Table of contents

Chapter 1 – Literature Review, Background and Theory.....	8
Chapter 2 – Experimental	48
Chapter 3 – Studies on Ramsdellite Lithium Titanates.....	81
Chapter 4 – Studies on some new Lithium Titanium Ferrites.....	149
Appendix 1.....	214

“If we knew what we were doing, it wouldn’t be called research, would it?”

- Albert Einstein (1879 – 1955)

**Chapter 1 - Literature Review, Background and
Theory.**

CHAPTER 1 - LITERATURE REVIEW, BACKGROUND AND THEORY.....	8
1.1 THE RAMSDELLITE STRUCTURE AND MATERIALS.....	10
1.2 THE SPINEL STRUCTURE AND MATERIALS.....	13
1.2.1 Cation distribution.....	14
1.2.2 Cation ordering.....	19
1.2.3 Literature review - The phase diagram: " Li_3O_4 " - " Ti_3O_4 " - Fe_3O_4	20
1.2.3.1 The Fe_3O_4 -" Ti_3O_4 " system.....	20
1.2.3.2 The LiTi_2O_4 - $\text{Li}_4\text{Ti}_5\text{O}_{12}$ system.....	22
1.2.3.3 The LiFe_5O_8 - $\text{Li}_4\text{Ti}_5\text{O}_{12}$ system.....	23
1.2.3.4 Other spinels - the lithium manganates.....	25
1.3 INTRODUCTION TO MAGNETISM.....	26
1.3.1 Magnetic moments and magnetisation.....	29
1.3.2 Comparison of theory with experiment.....	30
1.3.3 Magnetic order.....	32
1.3.3.1 Diamagnetism.....	32
1.3.3.2 Paramagnetism.....	32
1.3.3.3 Ferromagnetism and Antiferromagnetism.....	33
1.3.3.4 Ferrimagnetism.....	35
1.3.3.5 The Néel theory of collinear Ferrimagnetism.....	35
1.3.3.6 Behaviour below the Curie point.....	36
1.3.3.7 Behaviour above the Curie point.....	39
1.3.4 Exchange interactions.....	40

1.1 The ramsdellite structure and materials

The ramsdellite structure was first described by Bryström¹ for γ -MnO₂, in 1949. For this material the author described an orthorhombic, framework-type structure (space group Pbnm), constructed from distorted MnO₆ octahedra. These octahedra are connected in three ways; firstly, by sharing opposite edges, continuous chains of octahedra are formed in the c-direction. Two such chains are then linked together, by sharing edges, one chain being displaced by $\frac{1}{2}c$ relative to the other. In this way a continuous 2x1 column of octahedra is formed. These columns then corner-share with one another to form a framework containing empty 2x1 channels. Within these channels are several sites² in which smaller ions such as Li⁺ or H⁺ can reside. The structure and channel sites are shown in Figure 1-1 below.

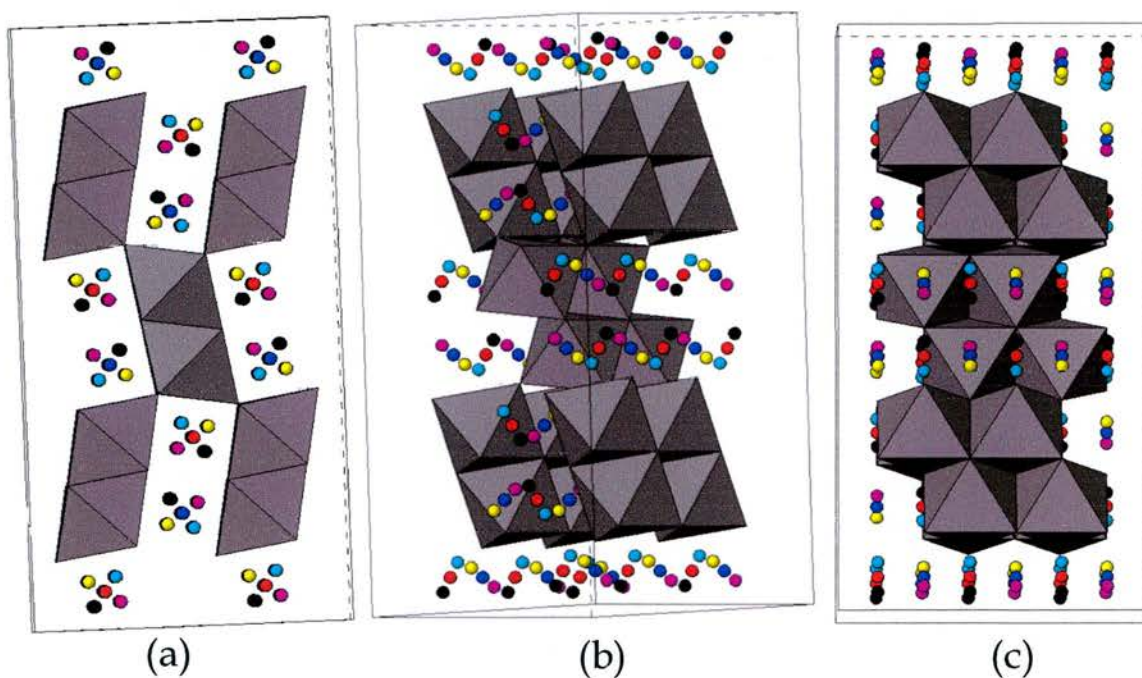


Figure 1-1: The ramsdellite structure as described by Brystrom¹, viewed down the (a) [001], (b) [110] and (c) [100] directions. Channel sites are as described by Grins and West².

Not surprisingly, most of the work on ramsdellite materials has concentrated on the manganates, initially because of their application in Leclanché cells, and later because they showed themselves to be most promising candidates for lithium

battery applications. Much of the earlier work was on determining the exact structure of the natural ramsdellite manganates, because many features of the XRD pattern could not be explained by the original structure proposed by Bryström¹, and because there were considerable electrochemical differences between different γ -MnO₂ samples. In 1959, De Wolff³ suggested that natural ramsdellites actually exist as a random intergrowth between ramsdellite and the rutile-type structured pyrolusite. The concentration of these defects he expressed quantitatively using P_r , defined as the probability that the "next" layer in the structure is rutile-type. Thus, for ramsdellite $P_r=0$, and for pyrolusite $P_r=1$. γ -MnO₂ he proposed, has intermediate values of P_r .

Although this model holds well for natural γ -MnO₂ materials, it does not account well for the diffraction patterns of chemically (CMD) and electrochemically (EMD) prepared samples. In order to explain the XRD patterns of these samples, a new structural model was proposed by Pannetier which describes the presence of two kinds of structural defects: (i) The ramsdellite-rutile intergrowth, as described by De Wolff, and (ii) micro-twinning of the ramsdellite lattice type on the (021) and/or (061) planes^{4,5}. With this model it is possible to explain not just the structural features of the manganese dioxides⁶ used in batteries, but also why their electrochemical performance is so dependent on their mode of synthesis^{7,8,9,10,11,12}.

Less thoroughly investigated, but nevertheless well characterised, are the isostructural compounds LiTi₂O₄, Li₂Ti₃O₇, LiFeSnO₄, and Li₂MgSn₃O₈. The best known of these, and the most thoroughly investigated, is Li₂Ti₃O₇. This composition was first reported by Jonker¹³ in 1956, but was not identified as ramsdellite until 1964¹⁴. Later work by Liebert and Huggins¹⁵ in 1978, and by Boyce and Mikkelsen^{16,17} in 1979 has showed the material to be a good ionic conductor, although conduction was found to be highly anisotropic. More recently there has been interest in the material as an insertion electrode, with several groups reporting reversible lithium insertion^{18,19}, and one group reporting insertion of 2.4Li per formula Li₂Ti₃O₇²⁰.

In 1976, Johnston²¹ reported that on heating LiTi_2O_4 a ramsdellite type phase, similar to $\text{Li}_2\text{Ti}_3\text{O}_7$, was formed, though unfortunately he was unable to confirm the stoichiometry of this phase. In 1994, though, Akimoto *et al*²² succeeded in preparing and characterising a single crystal of LiTi_2O_4 ramsdellite and were able to confirm both the structure and stoichiometry of the phase. High temperature neutron diffraction carried out by Gover *et al*²³ confirmed this stoichiometry, placed the spinel-ramsdellite transition as occurring between 875°C and 925°C, and showed that that no intermediate phase is involved in the transition. In follow up work, Akimoto²⁴ has shown that reaction of LiTi_2O_4 with dilute HCl completely removes the lithium, to leave a ramsdellite structured material of composition TiO_2 .

Interestingly, the cation distribution reported by both Akimoto *et al* and Gover *et al* for LiTi_2O_4 differs significantly from that reported for $\text{Li}_2\text{Ti}_3\text{O}_7$. Whereas studies of the latter^{25,26} have placed lithium on both octahedral framework, and tetrahedral channel sites, Akimoto *et al* placed lithium in LiTi_2O_4 on channel sites only. Furthermore, they report occupancy of only one tetrahedral channel site, as opposed to the two sites reported for $\text{Li}_2\text{Ti}_3\text{O}_7$. This result is extended in further work by Gover and Irvine²⁷, in which a solution linking LiTi_2O_4 and $\text{Li}_2\text{Ti}_3\text{O}_7$ is reported. They report that for all compositions, including $\text{Li}_2\text{Ti}_3\text{O}_7$, only one tetrahedral channel site was found to be occupied. Reports on other ramsdellites have also shown similar discrepancies regarding the position of channel sited lithium. For the $\text{Li}_{1+x}(\text{Li}_{2/3x}\text{Fe}_{1-x}\text{Sn}_{1+x/3})\text{O}_4$ system, Lacorre *et al*^{28,29} reported occupancy of both T1 and T2 tetrahedral sites for composition $x=0$ (LiFeSnO_4), whereas for $x=0.25$ they reported lithium on T1 only.

The explanation for these differing reports may lie in the cooling regime applied to the materials under study. Certainly in the earlier $\text{Li}_2\text{Ti}_3\text{O}_7$ work, the samples were quenched from their reaction temperature, whereas Akimoto *et al* and Gover *et al* both slow cooled their samples. In the $\text{Li}_{1+x}(\text{Li}_{2/3x}\text{Fe}_{1-x}\text{Sn}_{1+x/3})\text{O}_4$ work, though, this explanation cannot be applied and the authors explain the anomalous cation distribution by the deformation of one of the oxygen positions. Whatever the explanation, as most of the interest in ramsdellites is for lithium

battery applications, the position and mode of movement of the electrochemically mobile cations must be of considerable interest, and undoubtedly warrants further attention.

1.2 The spinel structure and materials

The determination of the spinel crystal structure by Bragg³⁰ (and separately by Nishikawa³¹) in 1915 was the one of the early triumphs of x-ray crystal analysis. Based on investigations of both $MgAl_2O_4$ (spinel) and Fe_3O_4 (magnetite) both authors were able to describe a structure that has now become possibly the best investigated, and most thoroughly characterised crystal structure known. It is also one of the most technologically important, with the spinel materials having many commercial applications including microwave technology, magnets, and most recently, lithium batteries.

Spinel can be described by the general formula AB_2X_4 , where A and B are cations and X is an anion such as a halide or chalcogenide. By far the most common anion, though, is oxygen. The structure itself is composed of a cubic close packed lattice of X anions (which fully occupy the 32e site of the Fd-3m space group), in which the A and B cations respectively occupy tetrahedral (8a) and octahedral (16d) interstices. The structure thus formed is FCC by virtue of the cation positions. It is important to note that whilst the tetrahedral and octahedral cation positions are crystallographically "special" sites (and are thus fixed), the anion 32e site is not, and it is normal for the anion to be slightly displaced from its ideal position. This distortion is described by the positional parameter **u**.

The spinel structure can be visually represented in several ways (Figure 1-2). While the conventional "ball and stick" depiction shows the cation face centring well, it is more common for the structure to be depicted in terms of the A and B site coordination. This is because when drawn in this way, the environment of the cations with respect to each other is much clearer. Using this representation,

it can be seen that each BX_6 octahedron shares an edge with 6 others to form an open, 3D "framework", and that each AX_4 tetrahedron shares all corners with BX_6 octahedra, but has no contact with any other tetrahedron. Thus, the A-A distance is considerably greater than either the A-B or B-B distances.

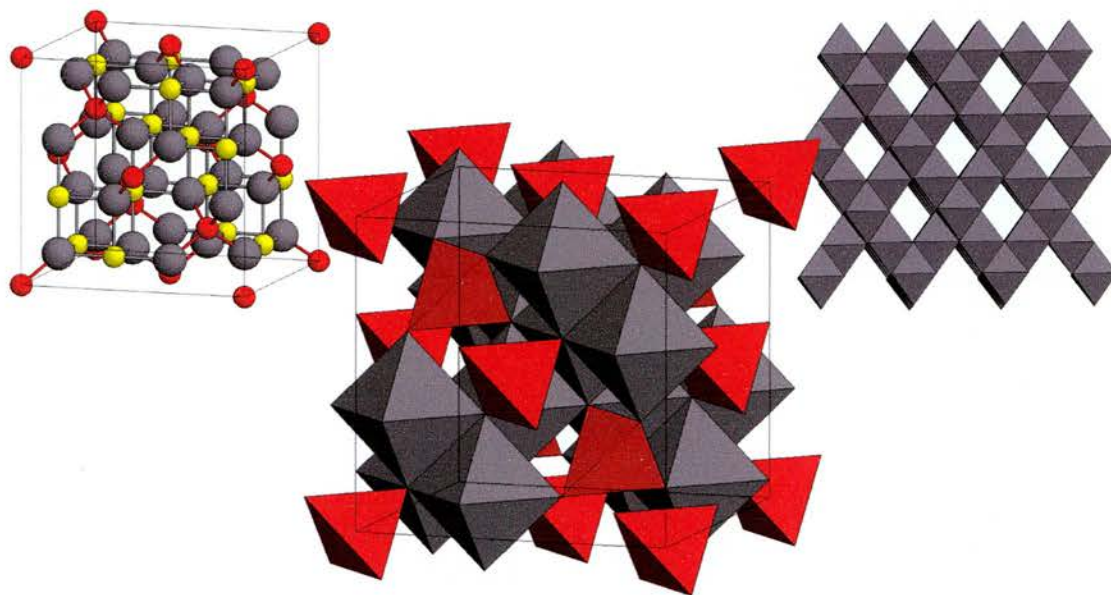


Figure 1-1: Depictions of the spinel structure with the A cations marked in red and the B cations marked in yellow, (a) *left*. The "ball and stick" model (b) *centre*. The "polyhedra" model. (c) *right* The open framework formed by the octahedra.

1.2.1 Cation distribution

Much of the interest in spinels stems from the wide range of cations known to form spinel type structures (Table 1-1), and their statistical distribution between the octahedral and tetrahedral sites. In spinel itself ($MgAl_2O_4$) it has been long determined that Al^{3+} occupies all of the octahedral 16d sites, and Mg^{2+} occupies all the 8a sites. However, it is often the case that A and B cations are not on separate sites, but instead co-occupy the tetrahedral and octahedral positions. This can lead to any number of possible cation distributions:

1. $A^{tet}B_2^{oct}O_4$ - normal spinel.
2. $B^{tet}[AB]^{oct}O_4$ - inverse spinel.
3. $[A_{1-x}B_x]^{tet}[A_xB_{2-x}]^{oct}O_4$ - intermediate spinel

Cation Charge					
1+	2+	3+	4+	5+	6+
Li	Zn	Ti	Ti	Sb	Mo
Na	Mn	Mn	Mn	Nb	W
K	Hg	Cr	Sn		
Cu	Cu	V	V		
Ag	Mg	Ga	Ge		
	Fe	Fe	Si		
	Cr	In			
	Co	Co			
	Ni	Rh			
	Sr	Al			
	Ba				
	Sn				
	Cd				

Table 1-1: Elements known to form spinel materials

This combination of "flexible" cation distribution and the broad selection of spinel-forming cations, means that a diverse number of interesting electrical and magnetic properties are known in spinels. It also means that accurate prediction and evaluation of the cation structural preferences is of great importance when designing and understanding new spinel compounds. Several factors need to be considered when evaluating such preferences:

1. Elastic energy.
2. Electrostatic (Madelung) energy.
3. Crystal field stabilisation energy.
4. Polarisation effects.

The first of these refers to the degree of distortion of the crystal structure due to the difference in ionic radii, assuming that ions adopted a spherical shape. Smaller cations (of 0.225-0.4Å) should occupy tetrahedral sites, whilst larger ones (0.4-0.73Å) should occupy octahedral sites. This leads to a minimum in the lattice strain.

The coulomb (Madelung) energy is the electrostatic energy contribution to the lattice energy, and is given by:

$$V_c = -M \frac{e^2}{a}$$

Where M is the Madelung constant and a is the lattice parameter.

Detailed calculations of the Madelung energy for spinels³² show that this energy is strongly dependent on the u parameter. The Madelung constant (as calculated by Verwey *et al*³²) as a function of the oxygen parameter u and the charge distribution between A and B sites, is presented in Figure 1-3(a). An alternative representation (as preferred by Gorter³³), where M is plotted as a function of q_A (q_A represents the average ionic charge on the A site) for different values of u , is also presented (Figure 1-3(b)).

Not surprisingly, the calculations based on these assumptions of spherical ions and coulombic-only interactions are often not in very good agreement with experiment, as they simply do not adequately represent the transition metal cations in most spinels. For a better understanding, the principles of crystal field stabilisation have to be applied, and indeed when they are, most of the results in spinels can be adequately explained.

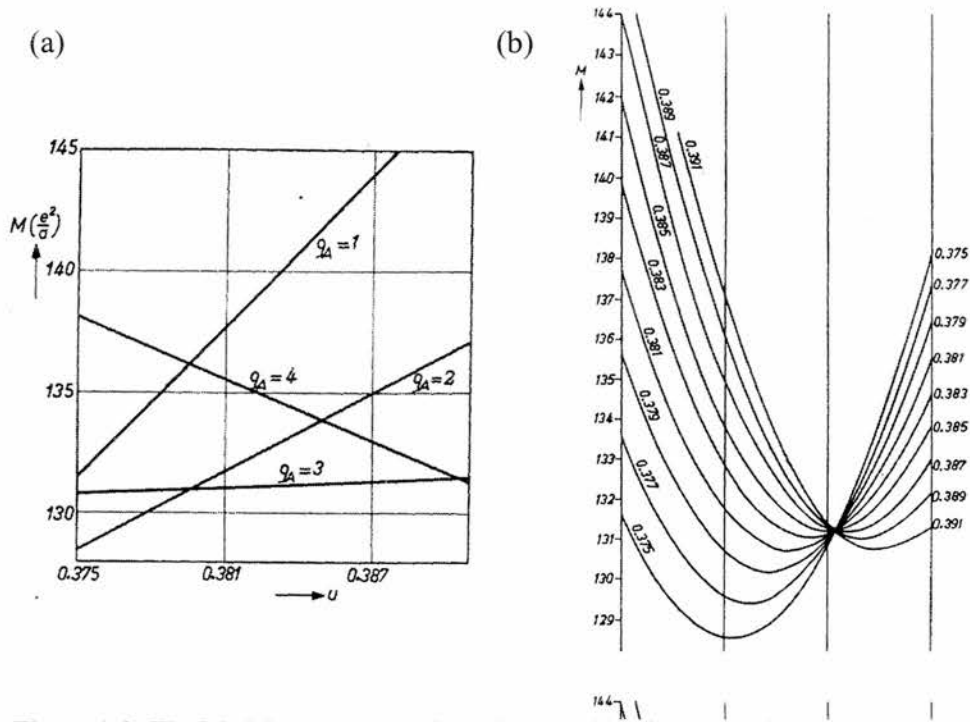


Figure 1-3: The Madelung constant for spinels as (a) a function of charge distribution between sites, and (b) as a function of q_A .

The application of crystal field theory to the understanding of cation site preference was first suggested by Romeijn³⁴. According to crystal field theory, the charge density of the cation d-orbitals interacts with the charge density in the environment in which the ion has been placed. Due to their different shape and distributions (Figure 1-4), the five d-orbitals are affected differently by the anion orbital charge and become no longer degenerate. The orbital energy is therefore "split" according to the environment in which they are placed, with some becoming higher and some lower in energy. It should be noted, though, that the total energy of the orbitals remains unchanged. The result of this is that in an octahedral field, the d_{xy} , d_{yz} and d_{zx} orbitals become lower in energy (because they point between anions) and the d_{z^2} and $d_{x^2-y^2}$ orbitals are raised in energy (because they point directly at anions). In a tetrahedral field this is reversed.

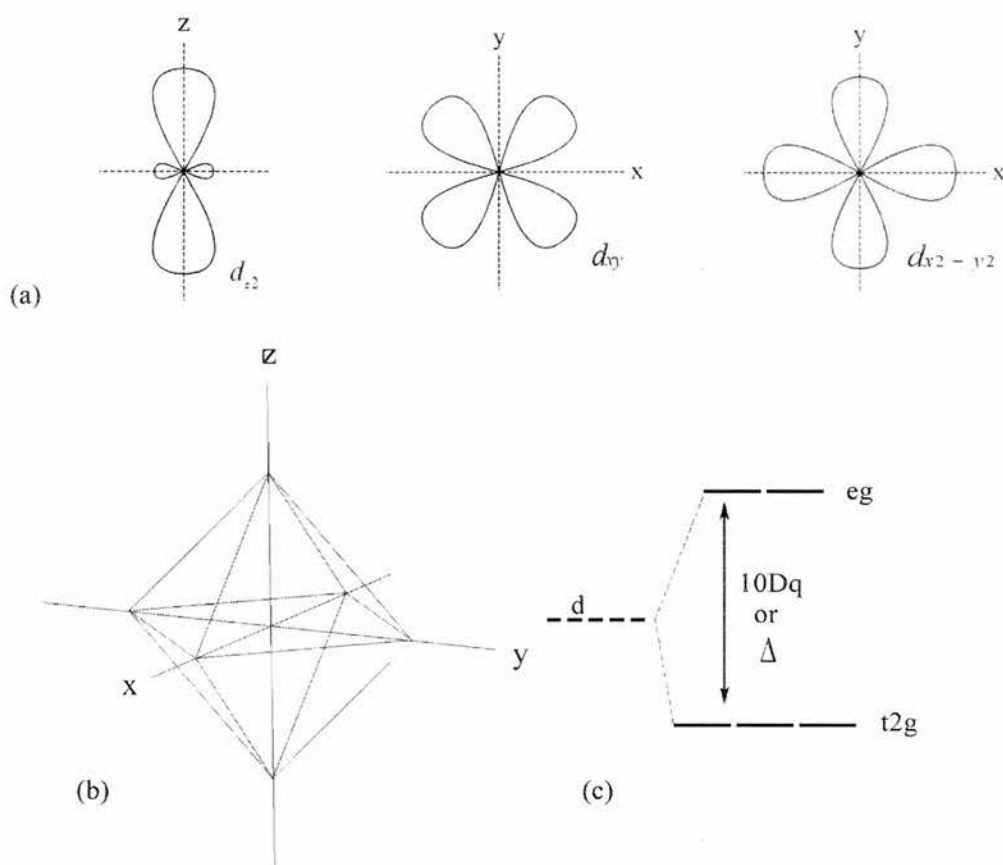


Figure 1-4: Crystal Field theory. (a) The d-orbital symmetries. (b) The octahedral environment and (c) the orbital energy splitting in an octahedral field.

Hunds' rules state that "the electron states with the greatest $(2S+1)$ are the most stable, and of those, the most stable is that with the greatest L ". Hence the electron configuration with the highest number of unpaired electrons (i.e. high spin) is of lowest energy and will be preferred. However if Δ is very large, it becomes more favourable to fill the lower levels (low spin), thus violating Hunds' rules by pairing electrons before the shell is full. The magnitude of Δ can therefore have important implications regarding both the magnetic and site preference properties of a cation. However, low spin states caused by large values of Δ are generally only seen for the heavier transition elements; first row transition metals are almost always in the high spin state, especially in oxides.

The final factor to be mentioned is polarisation. This can be regarded as simply the degree of distortion of the electron density around an ion, and it can arise for reasons such as high electronegativity, high ionic charge etc. The influence of

this effect on spinels is really only seen in cases where highly charged cations are incorporated in the material or for spherically symmetric cations (d^5 or d^{10}), which can show a degree of covalency when bonding, and so show a preference for tetrahedral sites³⁵.

1.2.2 Cation ordering

In any spinel in which more than one type of cation occupies the same set of crystallographic sites, *ordering* phenomena can be expected³³. This ordering takes the form of a superstructure formation on either the A or B sublattice, and is accompanied by a lowering of symmetry of the material, and often a distortion of the spinel away from cubic. Several types of ordering have been reported:

1. 1:1 order on the A sublattice as reported for $\text{Li}_{1/2}\text{Fe}_{1/2}\text{Cr}_2\text{O}_4$ ³³. The ordered structure remains cubic, but symmetry is lowered to F-43m.

2. 1:2 order on the A sublattice as reported for $\beta\text{-In}_2\text{S}_3$. This is a vacancy ordering: $\square_{1/3}\text{In}_{2/3}[\text{In}_2]\text{S}_4$ ³⁶. The unit cell is here tetragonally distorted.

3. 1:1 order on the B sublattice, as suggested by Verwey and Haaymann³⁷ for the $\text{Fe}^{2+}/\text{Fe}^{3+}$ ordering in Fe_3O_4 at low temperature. The ordered symmetry is changed from cubic to orthorhombic.

4. 1:3 order the B sublattice as found by Braun³⁸ for LiFe_5O_8 ³⁹. The structure remains cubic in this case, but the 16d site splits to become the 4b and 12d positions of the lower symmetry space group, $P4_332$ (or $P4_132$).

5. 1:5 order on the B sublattice, as described for $\gamma\text{-Fe}_2\text{O}_3$ ⁴⁰. Here the ordering is between vacancies and Fe^{3+} ions i.e. $\text{Fe}^{3+}[\square_{1/3}\text{Fe}^{3+}_{5/3}]\text{O}_4$. The c-axis is trebled, and structure becomes tetragonal.

1.2.3 Literature review - The phase diagram: “Li₃O₄”-“Ti₃O₄”- Fe₃O₄

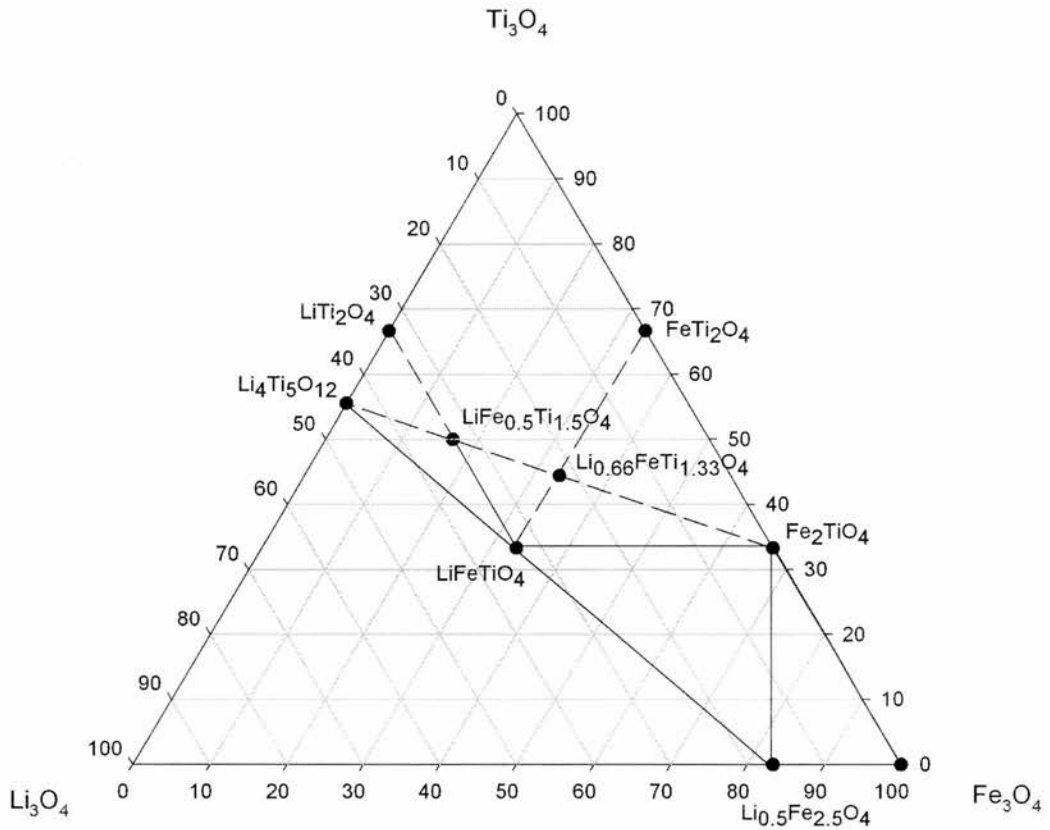


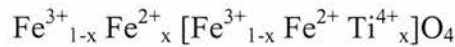
Figure 1-5: The “Li₃O₄”-“Ti₃O₄”-Fe₃O₄ phase diagram. Shown are the Fe³⁺ line joining Li₄Ti₅O₁₂ with LiFe₅O₈ and the Fe²⁺ line joining Li₄Ti₅O₁₂ with Fe₂TiO₄

1.2.3.1 The Fe₃O₄-“Ti₃O₄” system.

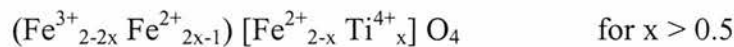
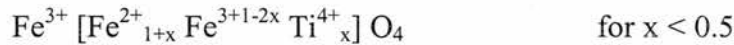
Fe₃O₄ was one of the first materials characterised as spinel^{30,31} and has subsequently proven to be one of the most interesting. It is a very unusual material in that being both partially reduced, and an inverse spinel, it contains both Fe³⁺ and Fe²⁺ on crystallographically identical sites. This leads to some interesting properties; the best known of which is the Verwey⁴¹ transition; below ~120K, magnetite has a low electrical conductivity whereas above this temperature it shows good semiconducting behaviour. To explain this transition, Verwey suggested that at low temperatures the octahedral Fe²⁺/Fe³⁺ ions order in alternate [110] directions. Above the critical temperature, thermal energy allows

the electrons to hop between the $\text{Fe}^{2+}/\text{Fe}^{3+}$ ions and so they become indistinguishable. Understandably, this finding attracted quite a lot of interest, and several techniques, including Mössbauer spectroscopy^{42,43}, electron and neutron diffraction^{44,45}, and NMR⁴⁶ have been employed to investigate this transition further.

The join from magnetite (Fe_3O_4) to ulvöspinel (Fe_2TiO_4) is an important one, with both compounds being important in rock magnetism. A continuous solid solution is known to exist⁴⁷ between these two end members, and much data on this solid solution has been published. Of greatest debate has been the distribution of the Fe^{2+} and Fe^{3+} ions within the solution. All authors agree that the method of substitution is one where $\text{Fe}^{2+}/\text{Ti}^{4+}$ replaces two Fe^{3+} i.e. the presence of Ti^{3+} is discounted (as found by Gorter⁴⁸ for some other reduced spinels), but beyond this there is little agreement, and several models of distribution have been proposed. The first of these was by Akimoto *et al*⁴⁹ who argued a preference of Ti^{4+} on octahedral sites and a linear substitution of $\text{Fe}^{2+}/\text{Fe}^{3+}$ on both tetrahedral and octahedral positions:



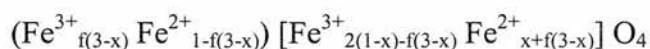
This distribution, while later partly corroborated^{50,51}, fails to take account of the empirical preference of Fe^{3+} for tetrahedral sites, as found by Verwey and Heilmann⁵². A second model by Néel⁵³, which does take this into consideration, proposed a two-stage substitution where Fe^{2+} preferentially fills octahedral sites and Fe^{3+} tetrahedral:



It has also been hypothesised by Gorter⁴⁸, and later reported by Forster *et al*⁵⁴ and Akimoto⁵⁵, that a very small quantity of Ti^{4+} could be occupying tetrahedral A sites. However, this contradicts a considerable weight of evidence^{56,57,58} that

Ti⁴⁺ only ever occupies the A sites in spinels if it is displaced from the B sites by cations with a very strong octahedral preference (like Ni²⁺). Neither high spin Fe²⁺ or Fe³⁺ can be said to have such a strong B site affinity.

A further three models have since been proposed ^{59,60,61}, all of which extend Néel's conclusion that Fe³⁺ shows a preference for tetrahedral coordination. The most recent of these models (by Hamdeh et al) is shown below, and serves as a good example of how difficult the cation distribution can be to ascertain:



Where:	$f = 0.333(1-0.25x)$	$\text{for } 0 \leq x \leq 0.2$
	$f = 0.35(1-0.57x)$	$\text{for } 0.3 < x \leq 0.5$
	$f = 0.50(1-x)$	$\text{for } 0.5 < x \leq 1$

1.2.3.2 The LiTi₂O₄–Li₄Ti₅O₁₂ system.

The solution Li_{1+x}Ti_{2-x}O₄ was first reported by Deschanvres *et al* ⁶² in 1971. A continuous solid solution, with cation distribution, Li^{tet}[Li_xTi_{2-x}]^{oct}O₄, was found to exist between LiTi₂O₄ and Li₄Ti₅O₁₂. Thus LiTi₂O₄ is a normal spinel, whereas Li₄Ti₅O₁₂ (x=0.33) is partly inversed. Investigations into the system ^{21,63,64} revealed that the end member LiTi₂O₄ undergoes a superconducting transition at ~13K. Whilst this is not high when compared to the more recent mercury cuprates, it is still one of the highest T_c's of any non-cuprate material. It was also found (as mentioned earlier) that on heating LiTi₂O₄ spinel above 950°C it undergoes a transition to the ramsdellite structure ^{21,22,23}.

Considering the similarities between the lithium titanates and the analogous lithium manganates, it is not surprising that they have also caught the attention of the lithium battery community. Sharing the same structure and cation distribution as the manganates, but not suffering the Jahn-Teller distortion problems of manganese, it was hoped that lithiated titanates would show the desirable

properties of the manganates, but without the unwanted distortions on reduction. This proved in part to be the case, with $\text{Li}_4\text{Ti}_5\text{O}_{12}$ demonstrating similar charge capacity, a very flat charge/discharge plateau, and good capacity retention over many cycles^{65,66,67,68}. Unfortunately, the voltage at which the lithium titanates cycle (1.43V for LiTi_2O_4 , 1.55V for $\text{Li}_4\text{Ti}_5\text{O}_{12}$) is a little high for application as a high power anode and too low for use as a cathode, so they are of limited commercial use. Nevertheless, $\text{Li}_4\text{Ti}_5\text{O}_{12}$ has found use both commercially and as a reference material by virtue of its very flat charge curve.

1.2.3.3 The LiFe_5O_8 - $\text{Li}_4\text{Ti}_5\text{O}_{12}$ system

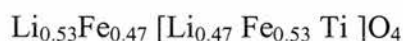
Structurally, it would be expected that with LiFe_5O_8 being a 1:3 octahedrally ordered spinel³⁸ (see earlier), and $\text{Li}_4\text{Ti}_5\text{O}_{12}$ being disordered⁶², the $\text{Li}_{0.5+0.5x}\text{Fe}_{2.5-1.5x}\text{Ti}_x\text{O}_4$ solid solution would be likely to show an ordered region toward the iron-rich end and a disordered region toward the titanium-rich end. Several investigations^{56,69,70} have shown that this is not the case, and the solution actually comprises two ordered regions ($0 \leq x \leq 0.33$, and $1.22 \leq x \leq 1.56$), with a disordered region between them. The end member $x=1.66$ ($\text{Li}_4\text{Ti}_5\text{O}_{12}$) is also disordered. The reason why the solution orders in such a fashion is unclear, as the generally accepted cation distribution between is independent of the ordered and disordered compositions:



What this model does make clear, however, is that the 1:3 ordering in the system originates from the Li:Fe/Ti ratio on the B sites. In the ordered materials lithium therefore occupies the 4b site, with the other cation(s) occupying the 12d site. In the disordered compounds there is instead a statistical disorder of all ions across the B sites. It is not surprising then that the ordering is a low temperature phenomenon, and that at high temperature the solution is entirely disordered⁷¹.

It is the case that several other lithium spinels⁷², including the $\text{LiFe}_{5-x}\text{Ga}_x\text{O}_8$ and $\text{LiFe}_{5-x}\text{Al}_x\text{O}_8$ systems^{73,74} show exactly the same kind of 1:3 ordering.

Interestingly, though, in these two systems there is no disordered region; all compositions show superstructure peaks. It has also been noted that although the nominal distribution in all these ordered spinels gives the 4b site as completely occupied by lithium, this is not always entirely accurate. In some cases⁷² a small quantity of lithium is actually displaced by a second cation, but without breaking down the long-range order. This can only occur for small values of substitution, because larger values of substitution will inevitably cause the long-range ordering to be lost. Recent neutron⁷⁵ and x-ray studies⁷⁶ on the disordered LiFeTiO_4 suggest that such substitution could in part explain the disordered region in the $\text{Li}_{0.5+0.5x}\text{Fe}_{2.5-1.5x}\text{Ti}_x\text{O}_4$ solution, as they give the cation distribution of this composition to actually be:



When reviewing the magnetic properties of the $\text{Li}_{0.5+0.5x}\text{Fe}_{2.5-1.5x}\text{Ti}_x\text{O}_4$ system it is necessary to also mention the zinc-substituted derivatives, as much of literature deals with the broader composition: $\text{Li}_{0.5(1-y+x)}\text{Zn}_y\text{Ti}_x\text{Fe}_{2.5-0.5(y+3x)}\text{O}_4$. This is because much of the work on LiFe_5O_8 and its derivatives has been concentrated on improving these materials' promising microwave properties, and the doping of zinc and titanium can reduce microwave losses and improve hysteresis properties.

Magnetically, the progression from $\text{LiFe}_5\text{O}_8 \rightarrow \text{Li}_4\text{Ti}_5\text{O}_{12}$ represents a gradual dilution of the magnetic Fe^{3+} with a diamagnetic Ti^{4+} on both tetrahedral and octahedral sites. Consequently, as the value of x increases, the number of magnetic A-B linkages falls. Work on similar systems, such as the Mg-Ti ferrites^{77,78}, suggest that as this dilution increases, effects such as spin-canting and superparamagnetic clustering can be expected. And indeed, these effects are seen in the $\text{Li}_{0.5+0.5x}\text{Fe}_{2.5-1.5x}\text{Ti}_x\text{O}_4$ solution; the superparamagnetism in the iron rich region ($0.2 \leq x \leq 0.6$)^{79,80}, and the spin canting at slightly higher levels of magnetic dilution ($0.735 \leq x \leq 1.25$)^{81,82,83,84}. In the Zn^{2+} substituted LiFe_5O_8 systems it should be noted that this spin canting occurs at much lower values of substitution ($z \geq 0.2$)^{75,85,86,87}. The reason being that Zn^{2+} substitutes only on A

sites (thus displacing Fe^{3+} to the B sites), whereas the Li/Ti substitution is divided between both sites. Therefore Zn^{2+} substitution simultaneously reduces A-B and increases B-B interactions, whereas increasing Li/Ti substitution reduces both similarly.

1.2.3.4 Other spinels - the lithium manganates

In its γ form, MnO_2 has for many years been the commercial cathode of choice in Leclanché type cells. With advent of Li-ion based batteries, it was logical that the development of manganese oxides would broaden to cover the other forms of MnO_2 , in particular the spinel, λ - MnO_2 allotrope. Several lithium containing derivatives of this material are now known ⁸, corresponding to general stoichiometry $\text{Li}_x\text{Mn}_{2-z}\text{O}_4$ ($0 \leq x \leq 1.33$, $0 \leq z \leq 0.33$). Of these, the solution, $\text{Li}_{1-x}\text{Mn}_{2-x}\text{O}_4$ (LiMn_2O_4 - $\text{Li}_4\text{Mn}_5\text{O}_{12}$) is probably the best characterised, and is known to be isostructural with the $\text{Li}_{1-x}\text{Ti}_{2-x}\text{O}_4$ solution mentioned earlier, so that $\text{Li}_4\text{Mn}_5\text{O}_{12}$ is partially inversed whilst LiMn_2O_4 is a completely normal spinel. This has important implications for these materials' electrode performance, as a stable MO_6 framework is essential for good charge cycling.

Compound	Cation distribution	Theoretical capacity mAh/kg
$\text{Li}_4\text{Mn}_5\text{O}_{12}$	$\text{Li}[\text{Mn}_{1.67}\text{Li}_{0.33}]\text{O}_4$	163
$\text{Li}_2\text{Mn}_3\text{O}_7$	$\text{Li}_{0.85}\square_{0.15}[\text{Mn}_{1.71}\text{Li}_{0.29}]\text{O}_4$	184
$\text{Li}_2\text{Mn}_4\text{O}_9$	$\text{Li}_{0.89}\square_{0.11}[\text{Mn}_{1.88}\square_{0.22}]\text{O}_4$	213
λ - MnO_2	$\square_{1.0}[\text{Mn}_2]\text{O}_4$	308

Table 1-2: Some spinels in the system $\text{Li}_x\text{Mn}_{2-z}\text{O}_4$. Figures taken from Thackeray et al ⁸.

Li/λ - MnO_2 cells discharge with two main voltage plateaus, the first at 4V vs Li (for the range $0 < x < 0.5$ in $\text{Li}_x\text{Mn}_2\text{O}_4$) ^{88,89} and the second at 3V (for the range $0.5 < x < 1$) ⁹⁰. The second of these steps is particularly interesting because the starting material, LiMn_2O_4 , is both cheap to manufacture and non-toxic. Unfortunately, the intercalation from LiMn_2O_4 to $\text{Li}_2\text{Mn}_2\text{O}_4$ corresponds to a reduction of Mn valence towards +3 (and an electron configuration of t_{2g}^3, e_g^1),

which results in a Jahn-Teller distortion. Furthermore this distortion occurs at very low values of intercalation ($x=0.08$ in $\text{Li}_{1+x}\text{Mn}_2\text{O}_4$), and causes a transformation of the spinel structure from cubic to tetragonal, with an increase of 16% in the c/a ratio. Such an increase is too large for the electrode to maintain structural integrity on cycling, and so the long-term performance of the electrode is severely compromised. To combat this, several approaches have been taken. Some groups have investigated the substitution of a small amount of Mn with a different valence metal (Ge, Fe, Co, Zn, Ni)^{91,92,93,94}, whilst others^{95,96,97} have tried to keep the manganese oxidation state above 3.5 by replacing some manganese with lithium ($\text{Li}_{1+\delta}\text{Mn}_{2-\delta}\text{O}_4$), or by synthesising defect spinels ($\text{Li}_{1-\delta}\text{Mn}_{2-2\delta}\text{O}_4$). These materials, whilst having lower theoretical capacities, do show better cycling characteristics as the onset of the Jahn-Teller distortion occurs much later in the discharge reaction.

More recently, following the development of more stable electrolytes⁹⁸, it has been possible to cycle cathode materials to much higher voltages than previously possible. Using these electrolytes LiMn_2O_4 has been shown to exhibit two more oxidation / reduction peaks⁹⁹ near 4.5V and 4.9V. Additionally, peaks at 4.9V, 4.8V, and 4.7V have been found for $\text{LiCu}_x\text{Mn}_{2-x}\text{O}_4$ ¹⁰⁰, $\text{LiCr}_x\text{Mn}_{2-x}\text{O}_4$ ¹⁰¹ and $\text{LiNi}_x\text{Mn}_{2-x}\text{O}_4$ ¹⁰² respectively, and a doped manganate ($\text{LiCoMn}_3\text{O}_8$) has recently been reported¹⁰³ as the first cathode to show an insertion plateau above 5V. Unfortunately, at the moment these cathodes' capacities at the higher voltages are quite low. Nevertheless, such high voltage cathode materials are of great commercial interest, because when optimised they could form the basis of a new generation of high power cells capable of providing power for applications such as electric vehicles.

1.3 Introduction to magnetism

Magnetism arises from the motion of electrons. In the same way as any moving electrical charge (such as a current through a wire) produces a magnetic field, the electrons orbiting a nucleus also produce a field. However, unlike the field

generated by a charge passing through a wire, the magnetic field produced by orbiting electrons is very difficult to describe as their motion is subject to the laws of quantum mechanics. The description of the magnetism of an atom or ion must therefore also be given in terms of quantum mechanics.

For each electron in an atom, four quantum numbers are required to describe its state:

n - the *principal quantum number*

l - the *angular momentum quantum number*

m_l - the *magnetic quantum number*

m_s - the *spin quantum number*

These numbers are applied as follows. The principal quantum number n , relates to the "shell" in which the electron resides, and takes a positive integer value $n=1,2,3\dots$

These shells are sometimes ascribed letters according to the following:

N	1	2	3	4.....
Shell	K	L	M	N.....

The *angular momentum quantum number* l , refers to the electronic subshell (or orbital) of the electron, and assumes values of 0 to $n-1$. As with n , the value of l is more commonly referred to by a letter:

L	1	2	3	4....
Orbital	s	p	d	f....

The m_l *magnetic quantum number* describes a further sub orbital of the l shell, and can take values $M_l=0, \pm 1, \pm 2, \pm l$. Its notation usually refers to the orbital orientation about the x, y and z axes i.e. p_x, p_y, p_z . The spin quantum number simply refers to the "spin" of the electron, and can take two values, $\pm \frac{1}{2}$.

As a complication, these terms in turn give rise to a further two quantum numbers j , and m_j , which are generated by the interaction of the *spin* and *orbital* momenta. These then describe the *total angular momentum* of the electron and its quantisation, and are simply the vector sum of the spin and orbital momenta. Thus j can take the values $l \pm 1/2$, describing the spin and orbital momenta when they are either opposed or parallel.

When several electrons are present, it is necessary to sum their individual orbital momenta in order to obtain the *total orbital angular momentum* L , and the *total spin angular momentum* S for the whole atom. The maximum values of L and S in a given atom are given by $\sum l_i$ and $\sum s_i$, but they can also take other values according to the following:

$$L = l_1 + l_2, l_1 + l_2 - 1, \dots, |l_1 - l_2|$$

$$S = s_1 + s_2, s_1 + s_2 - 1, \dots, |s_1 - s_2|$$

As in the single electron case, the values of L are commonly given as a letter rather than as a number. The translation being:

L	1	2	3	4....
	S	P	D	F....

Also, as in the single electron case, the angular and spin momenta can be summed to give a resultant total angular momentum J , which takes the values:

$$J = L + S, L + S - 1, \dots, |L - S|$$

In turn, each J state contains $2J + 1$ sub states which correspond to the different allowed values of M_J . In the absence of a field all these levels of M_J have the same energy. However, the application of a magnetic field separates the energies of these levels and removes their degeneracy.

It can be seen from this treatment that there are any number of possible states in which the electrons can lie. In order to ascertain which is lowest in energy (and so most stable), we have to apply Hund's rules. These state that:

1. Electrons occupy states with the maximum total spin number (consistent with Pauli's exclusion principle).
2. The next priority is to achieve maximum total orbital momentum L , consistent with the value obtained by rule 1.
3. The total angular momentum J is calculated as $J = |L-S|$ for an orbital which is less than $\frac{1}{2}$ full, and as $J = |L+S|$ for an orbital which is more than $\frac{1}{2}$ full. For an orbital exactly $\frac{1}{2}$ full, $L = 0$, $J = S$.

1.3.1 Magnetic moments and magnetisation.

Using these rules for quantised electronic orbitals, it is possible to derive several expressions for the magnetic moments, the magnetisation and susceptibility of an atom and of an assembly of atoms. The actual derivation of these expressions (being somewhat long and outside the scope of this work) will not be given here, only the relevant results. However, for the interested reader they are covered in depth by Crangle.¹⁰⁴

The first of these expressions is for the calculation of the magnetic moment of a single multi-electron atom. This is given by:

$$\mu_{\text{eff}} = g\mu_B [J(J+1)]^{1/2} \quad \text{Eq}^n \text{ 1.1}$$

Where:
$$g = \frac{3}{2} + \frac{S(S+1) - L(L+1)}{2J(J+1)}$$

This value g is called the Landé g -factor, and accounts for the difference in orbital and spin contribution to total orbital momentum. It has the value 2 when $L=0$, and the value 1 when $S=0$.

In the absence of an applied field all atoms having the same magnetic moment have the same energy. However, when a magnetic field is applied the energy depends on the statistical occupation of the $(2J+1)$ sub levels. By considering the population of these magnetic sub levels, it is possible to derive an expression which gives the total magnetic moment of an assembly of atoms (assuming no exchange interactions). This is called the Brillouin function and takes the form:

$$F(J,y) = (1 + \frac{1}{2}J) \coth[(1 + \frac{1}{2}J) y] - \frac{1}{2}J \coth(y/2J) \quad \text{Eq}^n \text{ 1.2}$$

Where: $y = Jg\mu_B B_0 / kT$

1.3.2 Comparison of theory with experiment

So how does this theory compare with the experimental data? Table 1-3 shows the calculated and experimental magnetic moments of a number of transition metal ions. From this it can be seen that for the first row transition elements the correlation between experimental data and the moment calculated according equation 1.1 is poor, but for the rare earth metals the correlation is good. The reason for this is that in transition metal salts the magnetic d-orbitals are also involved in bonding. Thus they are subjected to strong external fields produced by the surrounding anions i.e. they are affected by the ligand field. This is particularly pronounced in the first row transition metals, where the orbital moments can be effectively eliminated by the interaction of the bonding electrons with the ligand field if the magnetic ion is in either an A or E ground state (for T ground states though, this may not occur). This is called orbital quenching and means that there is little or no spin orbit coupling in many first row transition compounds. Hence, for these materials $g=2$, $L=0$, and the magnetism is determined only by the electron spins:

$$\mu_{\text{eff}} = 2[S(S+1)]^{1/2} \quad \text{Eq}^n \text{ 1.3}$$

Ion	Configuration	S	L	J	μ_J^a	μ_S^b	Exp.
Ti ³⁺ , V ⁴⁺	3d ¹	1/2	2	3/2	1.55	1.73	1.8
V ³⁺	3d ²	1	3	2	1.63	2.83	2.8
Cr ³⁺ , V ²⁺	3d ³	3/2	3	3/2	0.78	3.87	3.8
Cr ²⁺ , Mn ³⁺	3d ⁴	2	2	0	0	4.90	4.9
Fe ³⁺ , Mn ²⁺	3d ⁵	5/2	0	5/2	5.92	5.92	5.9
Fe ²⁺	3d ⁶	2	2	4	6.71	4.90	5.4
Co ²⁺	3d ⁷	3/2	3	9/2	6.63	3.87	4.8
Ni ²⁺	3d ⁸	1	3	4	5.59	2.83	3.2
Cu ²⁺	3d ⁹	1/2	2	5/2	3.55	1.73	1.9
Ce ²⁺	4f ¹	1/2	3	5/2	2.53	1.73	2.4
Pr ³⁺	4f ²	1	5	4	3.58	2.83	3.6
Nd ³⁺	4f ³	3/2	6	9/2	3.62	3.87	3.62
Pm ³⁺	4f ⁴	2	6	4	2.68	4.90	0
Sm ³⁺	4f ⁵	5/2	5	5/2	0.85	5.92	1.54
Eu ³⁺	4f ⁶	3	3	0	0	6.93	3.6
Gd ³⁺	4f ⁷	7/2	0	7/2	7.94	7.94	8.2
Tb ³⁺	4f ⁸	3	3	6	9.72	6.93	9.6
Dy ³⁺	4f ⁹	5/2	5	15/2	10.65	5.92	10.5
Ho ³⁺	4f ¹⁰	2	6	8	10.60	4.90	10.5
Er ³⁺	4f ¹¹	3/2	6	15/2	9.58	3.87	9.5
Tm ³⁺	4f ¹²	1	5	6	7.56	2.83	7.2
Yb ³⁺	4f ¹³	1/2	3	7/2	4.54	1.73	4.4

Table 1-3: Comparison of calculated and experimental magnetic moments of some transition metal ions. Taken from Kittel.¹⁰⁵

This orbital quenching does not occur for the rare earth compounds because the magnetic 4f electrons lie deep within the atoms, and so are well screened from the crystal fields by a significant outer electron distribution, including the 5s and 5p closed shells. Unlike the first row transition compounds then, the spin orbit coupling is stronger than the crystal field, and so the magnetic moment is generally in accord with the values predicted from the Landé treatment.

^a Calculated as $g[J(J+1)]2$

^b Calculated as $2[S(S+1)]3/2$

1.3.3 Magnetic order

A useful property in the characterisation of magnetic materials is the magnetic susceptibility χ . This is defined as the magnetisation M , divided by the applied magnetic field H :

$$\chi = M/H$$

The magnetic susceptibility has no units, and because it is a volume property it is also known as the volume susceptibility, although with appropriate conversion it can also be expressed in terms of mass (χ_m) or moles (χ_M).

1.3.3.1 Diamagnetism

All substances show some level of diamagnetism, but usually it is very weak and if other magnetism is present it will be masked. Basic diamagnetism is independent of temperature and is caused by the effect of a magnetic field on the inner electrons of the atom. When a field is applied, the electronic motion is modified and a current induced. This current, according to Lenz's law, in turn creates a field which opposes the applied field. Thus the induced magnetisation is negative and so is the susceptibility. Generally this is quite weak, with values typically in the -1×10^{-7} to -2×10^{-6} emu range. Superconductors, however, are perfect diamagnets ($\chi = -1$) and so the induced magnetisation exactly counters the applied field and all magnetic flux is excluded from the sample. This is called the Meissner effect and is commonly demonstrated by "hovering" a superconducting pellet over a magnet.

1.3.3.2 Paramagnetism

Paramagnets are materials which, while having intrinsic magnetic moments, do not have any magnetic order, and so don't exhibit any spontaneous magnetisation. On application of a field, however, they do become magnetised,

and this magnetisation depends linearly on the applied field. If the field is removed all magnetisation is lost. Most paramagnetic materials obey the Curie-Weiss law, which states that the magnetic susceptibility is inversely proportional to temperature:

$$\chi = C/(T-\theta_p)$$

Where: C is the Curie Constant
 T is temperature (K)
 θ_p is the Paramagnetic Curie temperature

Accordingly, it is common for inverse susceptibility to be plotted against T. The y axis intercept is then θ_p . For some materials, such as hydrated copper sulphate, $\theta_p = 0$ and this becomes the Curie law.

At this point it should be pointed out that ferromagnets, antiferromagnets and ferrimagnets all show paramagnetism above their respective Curie and Néel temperatures. Some typical plots of $1/\chi$ vs T are shown in Figure 1-6.

1.3.3.3 Ferromagnetism and Antiferromagnetism

A ferromagnetic material is one in which the magnetic dipoles are ordered in parallel and in such a way as to cooperatively reinforce one another (Figure 1-6). Ferromagnetic materials tend to show domain type magnetism and when subjected to field will continue to show spontaneous magnetisation, even after the field has been removed. Their magnetisation is also temperature dependent, as increasing temperature causes increasing disorder in the alignment of the magnetic spins due to kinetic effects. They show their maximum magnetisation therefore at 0K, and their minimum close to (usually just above) their Curie temperature, T_c , where they undergo a transition from the ferromagnetic state to paramagnetic. Fe, Co and Ni are the most common examples of ferromagnets.

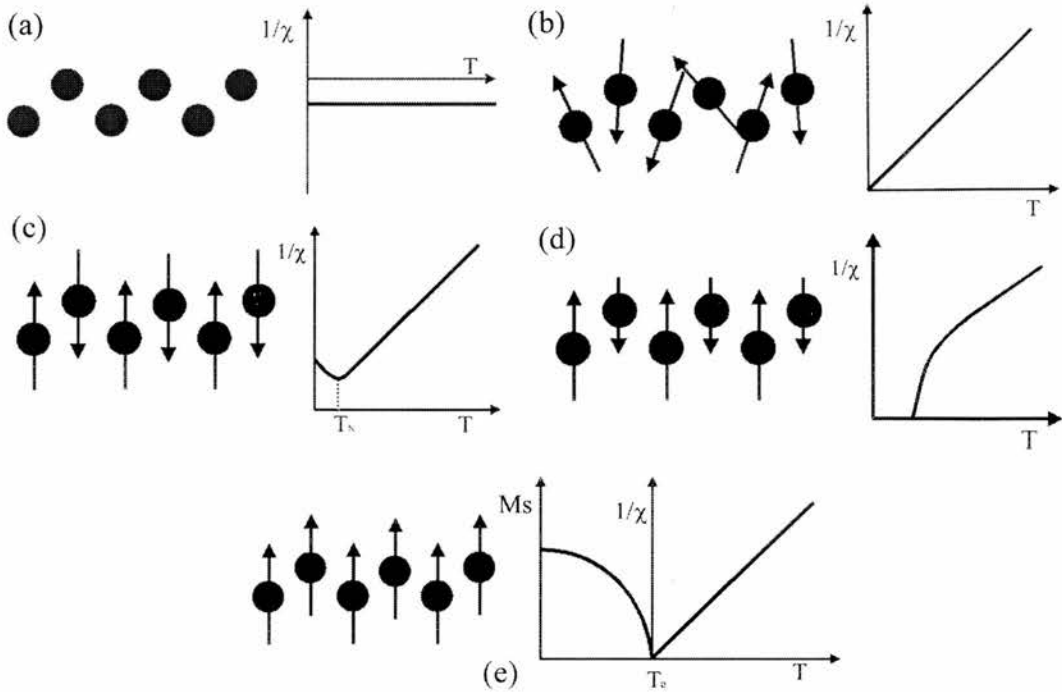


Figure 1-6: Magnetic ordering and typical inverse susceptibility curves for (a) a Diamagnet, (b) a Paramagnet, (c) an Antiferromagnet, and (d) a Ferrimagnet. (e) Shows the inverse susceptibility and magnetisation below the Curie point (T_c) for a Ferromagnet.

Antiferromagnetism is very similar to ferromagnetism, except that the magnetic dipoles are aligned antiparallel, rather than parallel, and so exactly cancel one another out. Antiferromagnets therefore show no spontaneous magnetisation, and are consequently very difficult to recognise. In simple cases, their paramagnetic state shows Curie-Weiss behaviour with a negative θ_p , and also a maximum in the susceptibility at the transition temperature (called the Néel temperature T_N) between paramagnetic and antiferromagnetic states. However, difficulties arise in that not all antiferromagnets show this maximum (though most ionic ones do), and that there are also some non-antiferromagnets which show a similar maximum in their susceptibility. The only conclusive proof of antiferromagnetism is obtained by neutron diffraction.

1.3.3.4 Ferrimagnetism

Ferrimagnetic materials are superficially very similar to ferromagnets in that they show spontaneous magnetic moments, and have similar hysteresis and domain properties. However, they actually have more in common with antiferromagnets, as they similarly show two opposing magnetic sublattices. The difference is that in a ferrimagnet these opposing moments are not equal, and so the material shows a spontaneous magnetic moment corresponding to the resultant of the opposing moments.

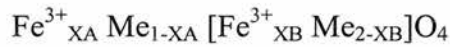
Ferrimagnets can be identified by the fact that above T_c they do not follow the Curie-Weiss law until relatively high temperatures are reached. Below T_c the temperature dependence of their spontaneous magnetisation is also often different to ferro and antiferromagnets, as the temperature dependence of each magnetic sublattice is generally different. Consequently a large variety of magnetisation vs temperature plots have been found for ferrimagnets, including some appearing to show false T_c 's, which are actually compensation points where the magnetic moments of the opposing sublattices are equal.

As this kind of magnetic order is generally shown by non-metallic ionic compounds, particularly the spinels and garnets, it is with ferrimagnetism this work is most concerned. Thus it seems appropriate to subject the reader to a more rigorous treatment of the topic, focusing on the spinels in particular.

1.3.3.5 The Néel theory of collinear Ferrimagnetism

Using data taken from several samples, including the paramagnetic normal ferrites of Zn and Cd, ferromagnetic inverse ferrites of Mn, Co, Ni, Cu and Mg, and the ferromagnet-like Fe_3O_4 , Néel, in 1948¹⁰⁶, was able to prove the hypothesis that a strong negative interaction exists between the ionic moments of the A and B sites in magnetic spinels, thus leading to the antiparallel orientation of these moments. At the same time he was also able to extend the molecular

field approximation of Weiss¹⁰⁷, in which the exchange forces exerted on an atom by its neighbours are represented by a fictitious magnetic field (the molecular field) which acts on that atom in addition to the applied field. Néel showed that the theory was also applicable to a system in which two different lattice sites are occupied by differing amounts of magnetic ions. Using this extended theory he was then able to show that the magnetic moment of $\text{Fe}^{3+}[\text{Fe}^{2+}\text{Fe}^{3+}]\text{O}_4$ should be $5+4-5=4$, a result that is in good agreement with experiment¹⁰⁸. He termed this behaviour "ferrimagnetism", though more accurately it should be described as non-compensated antiferromagnetism. A short overview of the theory now follows, using the general spinel:



Where: Me represents non-magnetic ions.

X_A and X_B are the number of ferric ions on A and B sites respectively

1.3.3.6 Behaviour below the Curie point

Below the Curie point, the temperature dependence of the magnetic moment per mole of each sublattice can be represented using the Brillouin function, and the total magnetic moment is the sum of the separate sublattice moments.

$$M_i(T) = M_i(0)F(J,y)_i$$

Where: $F(J,y)$ is the Brillouin function (see Eqn 1.2).

The i subscript refers to the particular magnetic sublattice.

For a spinel then (which has only two sublattices), the resultant magnetic moment per mole is given by the sum of the magnetic moments of the A and B sublattices:

$$M(T) = M_B(0)F(J,y)_B - M_A(0)F(J,y)_A \quad \text{Eq}^n \text{ 1.4}$$

Where: M_B and M_A are the B and A sublattice magnetisations respectively.

These magnetisations are given according to:

$$M_A = NgS\mu_B F(S, y_A) \quad \text{Eq}^n \text{ 1.5}$$

$$M_B = NgS\mu_B F(S, y_B) \quad \text{Eq}^n \text{ 1.6}$$

Where: $y_A = Sg\mu_B h_A / kT \quad \text{Eq}^n \text{ 1.7}$

$$y_B = Sg\mu_B h_B / kT \quad \text{Eq}^n \text{ 1.8}$$

Here: N is the number of magnetic atoms

g is the gyromagnetic ratio

S is the spin of the magnetic atom

μ_B is the Bohr-magneton

$h_{A/B}$ is the molecular field of the A or B sublattice

The values of the molecular fields of the A and B sublattices here can be given by:

$$h_A = n (-X_B M_B + \alpha X_A M_A) \quad \text{Eq}^n \text{ 1.9}$$

$$h_B = n (-X_A M_A + \beta X_B M_B) \quad \text{Eq}^n \text{ 1.10}$$

Where: $-\alpha$ and $-\beta$ are the ratios of AA:AB and BB:AB interactions respectively.

Note that the applied field (H) here is now the molecular field (h) (as $h \gg H$ at low temperatures), and that the value J has been replaced by S, as we are dealing with spin only magnetism.

From these equations it is obvious that the values of α and β have considerable importance regarding the relative sublattice magnetisations, and therefore on the

overall magnetisation. Néel saw this also, and speculated several possible magnetisation behaviours depending upon the ratio, X_A/X_B :

1. The first of these is for $X_A/X_B = 1$. At 0K, it can be seen from the Eqⁿ's above that each sublattice magnetisation is equal, and so the spontaneous magnetisation of the sample is 0. However, for this to remain so for all other temperatures h_A and h_B would also have to remain equal, and this only happens if $\alpha = \beta$. So if $\alpha \neq \beta$, $M_A \neq M_B$ except at 0K, and a magnetisation curve of the form shown in Figure 1-7 is found. Néel labelled this L type behaviour.
2. Néel calculated that near the Curie point (i.e. for small M_A and M_B) the slope of the M_S vs T curve, dM_S/dT , changes sign for $X_A/X_B = (1+\beta)/(1+\alpha)$. For this ratio of X_A/X_B , M_S is not zero at 0K and so M_S at the Curie point changes sign with respect to M_S at 0K. The range of X_A/X_B between 1 and $(1+\beta)/(1+\alpha)$, Néel labelled as N type behaviour.
3. Néel also suggested that the condition for which dM_S/dT changes sign near 0K, is $X_A/X_B = (1-\beta)/(1-\alpha)$. He noted that the magnetisation curve for this ratio is the same as for a ferromagnet, and denoted the region between $X_A/X_B = 1$ and $X_A/X_B = (1-\beta)/(1-\alpha)$ as P type.
4. For X_A/X_B further from 1 than $(1-\beta)/(1-\alpha)$ or $(1+\beta)/(1+\alpha)$ a magnetisation vs T curve of the forms *a* and *g* (Figure 1-7) were predicted. These regions Néel labelled as Q type.

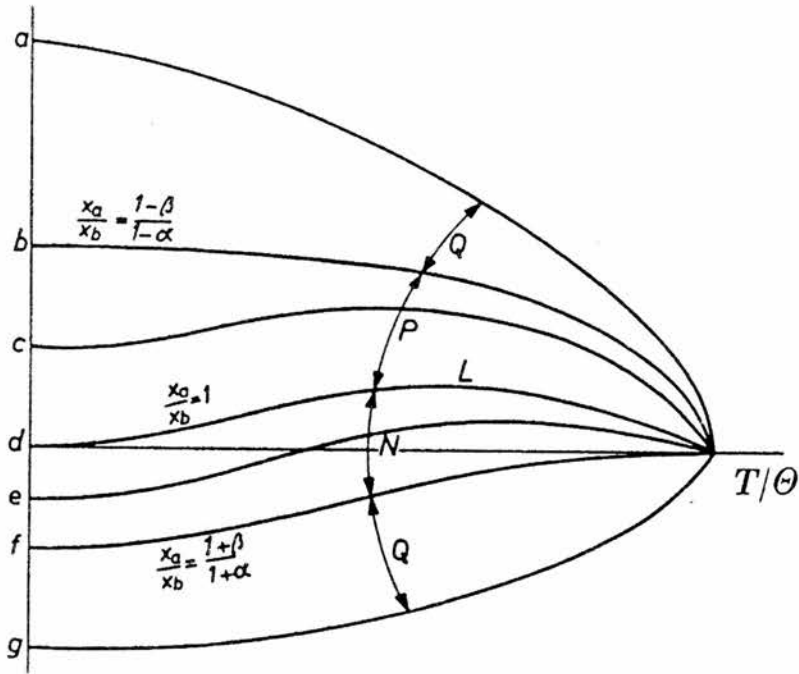


Figure 1-7: Predicted magnetisation curves according to Néel.

1.3.3.7 Behaviour above the Curie point

As with the treatment for behaviour below the Curie point, we can write that the total magnetisation is the sum of the magnetisations of each sublattice, and that for each sublattice there is a molecular field acting as a consequence of its interactions with the other sublattice:

$$M_s = X_A M_A + X_B M_B$$

and

$$h_A = n (-X_B M_B + \alpha X_A M_A)$$

$$h_B = n (-X_A M_A + \alpha X_B M_B)$$

We can also write that the partial magnetisations of each sublattice are:

$$M_A = C/T (H+h_A)$$

$$M_B = C/T (H+h_B)$$

Eliminating M_A , M_B , h_A and h_B from these equations gives:

$$\frac{H}{M_{\text{Mole}}} = \frac{T}{C_{\text{Mole}}} + \frac{n(2X_A X_B - \alpha X_A^2 - \beta X_B^2)}{(X_A + X_B)^2} - \frac{n^2 C_{\text{Mole}} X_A X_B [X_A(1 + \alpha) - X_B(1 + \beta)]^2 / (X_A + X_B)^4}{T - n C_{\text{Mole}} X_A X_B (2 + \alpha + \beta) / (X_A + X_B)^2}$$

or

$$\frac{1}{\chi_{\text{Mole}}} = \frac{T}{C_{\text{Mole}}} + \frac{1}{\chi_0} - \frac{S}{T - \theta}$$

This shows there is a hyperbolic relationship between $1/\chi$ and T , as is found experimentally.

It should be stressed here that this treatment is limited to systems of collinear order in which the AA and BB interactions are negligible with respect to the AB interactions. It is also inapplicable to systems such as MgFe_2O_4 where X_A/X_B (and hence the chemical formula) changes with temperature. Nevertheless, Néel was able to show qualitatively that for several ferrites $|\alpha|$ and $|\beta| \ll 1$, and so show that for these materials the AA and BB interactions are small with respect to the AB interaction. He also found that α and β , and thus the AA and BB interactions, are negative.

1.3.4 Exchange interactions

In the preceding sections we have covered some of the more important types of magnetism and magnetic order, often giving reference to interactions (e.g. AA, BB) which have hitherto not been fully explained. In this section an overview of these interactions will be given, again using the spinel structure as a reference.

To understand basic exchange interactions it is helpful to use a simple system as an initial example: take two atoms, a and b, each with one electron and place

close enough together that their electron wave functions overlap. The electron wave functions for this interacting system can then be expressed as many combinations of the original atomic wave functions. This is called the Heitler-London approximation, and allows us to express the total energy as:

$$E = E_a + E_b + Q \pm J_{ex}$$

Where: E_a and E_b are the energies of the electrons in atomic a and b.
 Q is the electrostatic interaction energy.
 J_{ex} is the exchange energy.

When such overlap occurs, the Pauli exclusion principle must be applied, and dictates that in the overlapping region no single electron state may be doubly occupied. Therefore, because of this region of overlap a correlation between the electron spins of the two atoms is imposed. The effect is as though there is an interaction energy between the spin vectors, and so the exchange energy (J_{ex}) arises. For positive values of J_{ex} , parallel (ferromagnetic) coupling occurs, and for negative J_{ex} antiparallel (antiferromagnetic or ferrimagnetic) coupling occurs.

Whilst this goes some way towards explaining the magnetic order in metals, the magnetic properties of oxides and similar materials are a little more difficult to explain. This is because the magnetic ions in these materials are generally too far separated to allow such direct orbital overlap, and it is often found that a non-magnetic ion, such as oxygen, lies directly between the magnetic ions. In order to explain magnetic order in such compounds, a mechanism called *superexchange* was proposed, in which the spins of magnetic cations are coupled indirectly via intervening anions.

Consider two magnetic cations separated by an oxygen anion (Figure 1-8). The O^{2-} has no magnetic moment as it has a full electron shell, with p-type orbitals outermost. If we take the p_x orbital, we know that it contains two electrons and that they must be of opposite spin, consistent with Pauli's principle. When a

magnetic cation is brought close to one lobe of this orbital, orbital overlap can only occur for antiparallel spins. Because the two electrons of the $2p_x$ orbital must also be antiparallel, this dictates that the interaction of the second p_x lobe with another magnetic cation will give rise to antiparallel moments between the two magnetic ions.

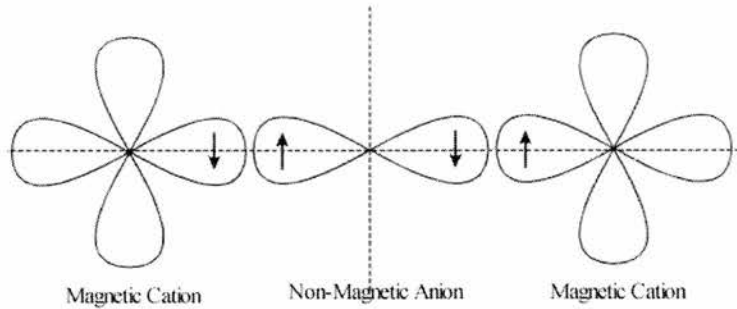


Figure 1-8: Magnetic superexchange via a non-magnetic anion such as O^{2-} .

When we apply this to spinels we can see that for an ideal spinel the bond angles and distances (Figure 1-9) are such that interaction between the A and B sites (AB interaction, or more accurately, A-O-B interaction) is considerably favoured over B-O-B interaction, due to the respective bond angles of 125° and 90° . It can also be seen from Figure 1-9 that there is no pathway through which such superexchange can occur between A sites. It should also be noted that with respective A-A. and B-B distances of $\frac{1}{4}a\sqrt{3}$ and $\frac{1}{4}a\sqrt{2}$ (or 3.68 \AA and 3.00 \AA for a typical spinel of $a = 8.5 \text{ \AA}$) there is unlikely to be significant direct interaction of magnetic cations.

References

- ¹ A. M. Bryström, *Acta. Chem. Scand.* 3, (1949), 163.
- ² J. Grins and A.R. West. *J. Solid State Chemistry.* 65, (1986), 265.
- ³ P.M. De Wolff. *Acta Cryst.* 12, (1959), 341.
- ⁴ J. Pannetier. *Prog. Batteries Battery Mater.* 11, (1992), 51.
- ⁵ J. Pannetier, Y. Chabre, C. Poinignon, *ISSI lett.* 12, (1990), 5.
- ⁶ Y. Chabre and J. Pannetier. *Prog. Solid State Chem.* 23, (1995), 1.
- ⁷ L.A.H. Maclean, C. Poinignon, J.M. Amarilla, F. Le Cras, P. Strobel. *J. Mater Chem.* 3(12), (1993), 227.
- ⁸ M.M. Thackeray, M.H. Roussouw, A. de Kock, A.P. de la Harpe, R.J. Gummow, K. Pierce, D.C. Liles. *Journal of Power Sources.* 43-44, (1993), 289.
- ⁹ L.A.H. Maclean, F.L. Tye. *J. Mater. Chem.* 7(6), (1997), 1029.
- ¹⁰ C. Poinignon, M. Amarilla, F. Tedjar. *J. Mater. Chem.* 3(12), (1993), 1227.
- ¹¹ C. Poinignon, J.M. Amarilla, F. Tedjar. *Solid State Ionics.* 70/71, (1994), 649.
- ¹² B. Zachau-Christiansen, K. West, T. Jacobsen, S. Skaarup. *Solid State Ionics.* 70/71, (1994), 401.
- ¹³ G.H. Jonker. *Traajos Reunion Intern. Reactividad Solidos, 3^o Madrid.* April 1956, 1 (1957), 423.
- ¹⁴ M. Lundberg, S. Andersson. *Acta Chem. Scand.* 18(3), (1964), 817.
- ¹⁵ B. E. Liebert and R. A. Huggins. *Proceedings of the second international meeting on solid electrolytes.* (1978).
- ¹⁶ J.B. Boyce, J.C. Mikkelsen, Jr. and B.A. Huberman. *Solid State Commun.* 29, (1979), 507.
- ¹⁷ J.B. Boyce and J.C. Mikkelsen, Jr. *Solid State Communications.* 31 (1979), 741.
- ¹⁸ C.J. Chen and M. Greenblatt. *Mater. Res. Bull.* 20(11), (1985), 1347.
- ¹⁹ S. Garnier, C. Bohnke, O. Bohnke, J.L. Fourquet. *Solid State Ionics.* 83, (1996), 323.
- ²⁰ M.E. Arroyo y de Dompablo, E. Morán, A. Várez, F. Garcia-Alavarado. *Mater. Res. Bull.* 32 (1997), 993.
- ²¹ D.C. Johnston. *J. Low Temp. Phys.* 25, (1976), 145.
- ²² J. Akimoto, Y. Gotoh, M. Sohma, K. Kawaguchi, Y. Oosawa and H. Takei. *J. Solid State Chem.* 110, (1994), 150.
- ²³ R.K.B. Gover, J.T.S. Irvine, A. Finch. *J. Solid State Chem.* 132, (1997), 382.
- ²⁴ J. Akimoto, Y. Gotoh, Y. Oosawa, N. Nonose, T. Kumagai, K. Aoki and H. Takei. *J. Solid State Chem.* 113, (1994), 27.
- ²⁵ B. Morosin and J.C. Mikkelsen Jr. *Acta Cryst.* B35, (1979), 798.
- ²⁶ I. Abrahams, P.G. Bruce, W.I.F. David and A.R. West. *J. Solid State Chem.* 78, (1989), 170.
- ²⁷ R.K.B. Gover and J.T.S. Irvine, *J. Solid State Chem.* 141, (1998), 365.
- ²⁸ J. Choisenet, M. Hervieu, B. Raveau, P. Tarte. *J. Solid State Chem.* 40, (1981), 344.
- ²⁹ P.H. Lacorre, M. Hervieu, J. Pannetier, J. Choisenet, B. Raveau. *J. Solid State Chem.* 50, (1983) 196.
- ³⁰ W.H. Bragg *Phil. Mag.* 30, (1915), 305

- ³¹ S. Nishikawa. *Proceedings of the mathematical and physical society of Tokyo*. 8, (1915), 199.
- ³² E.J.W Verwey, F. de Boer, J.H. van Santen. *J. Chem Phys.* 15, (1948), 1091.
- ³³ E.W. Gorter. *Philips Res Rep.* 9, (1954), 295.
- ³⁴ F.C. Romeijn. *Philips Res Rep.* 8, (1954), 304.
- ³⁵ R. Valenzuela. "*Magnetic Ceramics*". Cambridge press. (1994), 14.
- ³⁶ C.J.M. Rooymans. *J. Inorg. Nucl. Chem.* 11, (1959), 78.
- ³⁷ E.J.W. Verwey, P.W. Haayman. *Physica*, 8, (1941), 979.
- ³⁸ P.B.Braun. *Nature*. 170, (1952), 1123
- ³⁹ A. Tomas, P.Laruelle, J.L. Dormann, M. Nogués. *Acta Cryst.* C39, (1983), 1615.
- ⁴⁰ G.W. van Oosterhout, C.J.M. Rooymans. *Nature*. 181, (1958), 44.
- ⁴¹ E. J. W. Verwey, *Nature (London)*. 144, (1939), 327.
- ⁴² S. Umemura, S. Iida. *J. Phys. Soc. Japan*. 47, (1979), 458.
- ⁴³ K. Ôno, Y. Ishikawa, A. Ito, E. Hirahara. *J. Phys. Soc. Japan*, 17, Suppl B1, (1962), 125.
- ⁴⁴ T. Yamada, K.Suzuki, S.Chikazumi. *Appl. Phys. Lett.* 13, (1968), 172.
- ⁴⁵ G. Shirane, S. Chikazumi, J. Akimitsu, K. Chiba, M. Matsui, Y. Fuji. *J. Phys. Soc. Japan*. 39, (1975), 949.
- ⁴⁶ M. Mizoguchi. *J. Phys. Soc. Japan*. 44, (1978), 1501.
- ⁴⁷ A. Michel. *Ann Chimie*. 8, (1937), 317.
- ⁴⁸ E.W. Gorter. *Adv. Phys.* 6, (1957), 336.
- ⁴⁹ S. Akimoto, T. Katsura, M. Yoshida. *Geomagn. Geoelect.* 9, (1957), 165
- ⁵⁰ H. Tanaka, N. Kono. *J Geoelect.* 39, (1987), 463.
- ⁵¹ S.D. Jensen, P.N. Shive. *J. Geophys. Res.* 78, (1973), 8474.
- ⁵² E. J. W. Verwey, T. L. Heilmann, *J. Chem. Phys.* 15, (1947), 174.
- ⁵³ L. Néel. *Advan. Phys.* 4, (1955), 191.
- ⁵⁴ R.H. Forster, E.O. Hall. *Acta Cryst.* 18, (1965), 859.
- ⁵⁵ S. Akimoto. *J. Phys. Soc. Japan*. 17, Suppl. B1, (1962), 706.
- ⁵⁶ G.Blasse. *Philips Res. Rep. Suppl.* No.3. (1964).
- ⁵⁷ Y. Ishikawa, Y. Syono, S. Akimoto. *Ann. Prog. Rep. Rock Mag. Res. Group Japan.* (1964), 14.
- ⁵⁸ E.W. Gorter. *Philips Res Rep.* 9, (1954), 403.
- ⁵⁹ W. O'Reilly, S.K. Banerjee. *Phys Lett.* 17, (1965), 237.
- ⁶⁰ Z. Kakol, J. Sabol, J.M. Honig. *Phys. Rev. B.* 43, (1991), 649.
- ⁶¹ H.H. Hamdeh, K. Barghout, J.C. Ho, P.M. Shand, L.L. Miller. *J. Magn. Magn. Mater.* 191, (1999), 72.
- ⁶² A. Deschanvres, B. Raveau, Z. Sekkal. *Mater Res. Bull.* 6, (1971), 699.
- ⁶³ M. Dalton. *Ph.D Thesis*, Univ. of Cambridge (1992).
- ⁶⁴ M.R. Harrison, P.P. Edwards, J.B. Goodenough. *Phil. Mag.* 52, (1985), 679.
- ⁶⁵ E. Ferg, R.J. Gummow, A. De Kock. *J. Electrochem. Soc.* 141, (1994), L147.

- ⁶⁶ K.M. Colbow, J.R. Dahn, R.R. Haerin. *J. Power Sources*. 26, (1989), 397.
- ⁶⁷ T. Ohzuku, A.Ueda, N. Yamamoto. *J Electrochem. Soc.* 142, (1995), 1431.
- ⁶⁸ T. Ohzuku, A.Ueda, N. Yamamoto, Y. Iakoshi. *J. Power Sources*. 54, (1995), 99.
- ⁶⁹ M. Nogue, J.L. Dormann, M. Perrin, W. Simonet, P. Gibart. *IEEE Trans. Magn.* MAG-15, (1979), 1729.
- ⁷⁰ S. Scharner, W. Weppner, P. Schmid-Beurmann. *J. Solid State Chem.* 134, (1997), 170.
- ⁷¹ Y.C. Yau, J.M.Hughes. *J. Am. Ceram. Soc.* 66, No.7. (1983), 479.
- ⁷² H. Kawai. M. Tabuchi, M. Nagata, H. Tukamoto, A.R. West. *J. Mater Chem.* 8(5), (1998), 1273.
- ⁷³ J.A. Schulkes, G. Blasse. *J. Phys. Chem. Solids*. 24, (19F3), 1651.
- ⁷⁴ D.W. Strickler, R. Roy. *J. Am. Ceram. Soc.* 44, (1961), 225.
- ⁷⁵ S. Ligenza, M. Konwicki. *Phys. Stat. Sol. (a)*. 109, (1988), 319.
- ⁷⁶ M.A. Arillo. M.L. López, E. Perez-Cappe, M.L.Veiga. *Solid State Ionics*. 107, (1998), 307.
- ⁷⁷ E. De Grave, R. Vanleerberghe, C. Dauwe, J. De Sitter, A. Govaert. *J. Physique*. 37, (1976), 97.
- ⁷⁸ R.A. Brand, H. Georges-Gilbert, J. Hubsch, J. A. Heller. *J. Phys. F*. 15, (1985), 1987.
- ⁷⁹ P. Kishan, C. Prakash, J.S. Baijal, K.K. Laroia. *Phys. Stat. Sol (a)*. 84, (1984), 535.
- ⁸⁰ A.A. Yousif, M.E. Elzain, S.A. Mazen, H.H. Sutherland, M.H. Abdalla, S.F. Masour. *J. Phys. Condens. Matter*. 6, (1994), 5717.
- ⁸¹ J. L. Dormann. *J. de Physique*. C1, 41, (1980), 175.
- ⁸² J.L. Dormann, M.E.I. Haraoui, M. Nogue, J. Jove. *J. Phys C*. 20, (1987), L161.
- ⁸³ M.E.I. Haraoui, J.L. Dormann, M. Nogue, G. Villers, V. Caignaert, F. Bouree-Vigneron. *J. De Physique Colloque*, C8, 49, (1988), 1147.
- ⁸⁴ S.K. Kulshreshta. *J. Magn. Magn. Mater.* 53, (1986), 345
- ⁸⁵ M. Konwicki, S. Makolagwa. *J. de Physique Colloque*. C1, 38, (1977), C1-271.
- ⁸⁶ G.F. Dionne. *J. Appl. Phys.* 45, (1974), 3621.
- ⁸⁷ C.R. Abeledo, R.B. Frankel. *J. de Physique Colloque*. C1, 38, (1977), C1-135.
- ⁸⁸ J.M. Tarascon. D. Guyomard. *J. Electrochem. Soc.* 138, (1991), 2864.
- ⁸⁹ T. Ohzuku, M. Kitagawa, T. Hirai. *J. Electrochem. Soc.* 137, (1990), 769.
- ⁹⁰ M.M. Thckeray, W.I.F. David, P.G. Bruce, J.B. Goodenough. *Mater. Res. Bull.* 18, (1983), 461.
- ⁹¹ J.M. Tarascon, E. Wang, F.K. Shokoohi, W.R. McKinnon, S. Colson. *J. Electrochem. Soc.* 138, (1991) 2859.
- ⁹² R. Bittihn, R. Herr, D. Hoge. *J. Power Sources*. 43-44, (1993) 223.
- ⁹³ C. Sigala, A. Verbaere, J.L. Mansot, D. Guyomard, Y. Piffard, M. Tournoux. *J. Solid State Chem.* 132, (1997), 372.
- ⁹⁴ R. Stoyanova, E. Zhecheva, L. Zarkova. *Solid State Ionics*. 73 (1994), 233.
- ⁹⁵ R.J. Gummow, A. De Kock, M.M. Thackeray. *Solid State Ionics*. 69, (1994), 59.

-
- ⁹⁶ M.M. Thackeray, A. De Kock, M.H. Roussouw, D.C. Liles, R. Bittihn, D. Hoge. *J. Electrochem Soc.* 139, (1992), 363.
- ⁹⁷ A. De Kock, M.H. Roussouw, L. A. Picciotto, M.M. Thackeray, W.I.F. David, R.M Ibberson.. *Mater. Res. Bull.* 25, (1990), 657.
- ⁹⁸ J.M. Tarascon, D. Guyomard. *Solid State Ionics.* 69, (1994), 293.
- ⁹⁹ J.M. Tarascon, W.R. McKinnon, F. Coowar, T.N. Bowmer, G. Amatucci, D. Guyomard. *J. Electrochem. Soc.* 141, (1994), 2279.
- ¹⁰⁰ Y. Ein-Eli, W.F. Howard, S.H. Lu, S. Mukerjee, J. McBreen, J.T. Vauhey, M.M. Thackeray. *J. Electrochem. Soc.* 145, (1998), 1238.
- ¹⁰¹ C. Sigala, D. Guyomard, A. Verbaere, Y. Piffard, M. Tournoux. *Solid State Ionics.* 81, (1995), 167.
- ¹⁰² K. Amine, H. Tukamoto, H. Yasuda, Y. Fujita. *J. Electrochem. Soc.* 144, (1996), 1607.
- ¹⁰³ H. Kawai, M. Nagata, H. Tukamoto, A.R. West. *J. Mater. Chem.* 8(4), (1998), 837.
- ¹⁰⁴ J. Crangle. "Solid state magnetism". Chapter 2, 16. Edward Arnold, London.
- ¹⁰⁵ C. Kittel, "Introduction to solid state physics", 7th ed. John Wiley and Sons, New York, (1996)
- ¹⁰⁶ L. Néel . *Ann. Phys. Paris.* 3, (1948), 137.
- ¹⁰⁷ P. Weiss. *J. Phys.* 6 (4), (1907), 661.
- ¹⁰⁸ P. Weiss, R. Forrer. *Ann. Phys. Paris.* 12 (10), (1929), 279.

2 - Experimental

2	- EXPERIMENTAL	48
2.1	SAMPLE PREPARATION	50
2.1.1	<i>Powder Preparation</i>	50
2.1.2	<i>Pelletisation</i>	51
2.1.3	<i>Sintering</i>	52
2.2	STRUCTURAL CHARACTERISATION OF MATERIALS	54
2.2.1	<i>Diffraction and Bragg's law</i>	54
2.2.2	<i>Miller indices</i>	56
2.2.3	<i>Systematic absences</i>	58
2.2.4	<i>Form factors</i>	58
2.2.5	<i>The structure factor</i>	61
2.2.6	<i>Other factors influencing diffraction intensity</i>	62
2.2.7	<i>The powder x-ray diffraction experiment</i>	62
2.2.8	<i>The neutron diffraction experiment</i>	64
2.2.9	<i>Powder Pattern Analysis – The Rietveld Method</i>	65
2.2.10	<i>R-Factors</i>	66
2.3	THERMAL ANALYSIS	68
2.4	MAGNETIC CHARACTERISATION OF MATERIALS.....	69
2.4.1	<i>Mössbauer spectroscopy</i>	69
2.4.1.1	<i>The Mössbauer spectra</i>	71
2.4.1.2	<i>The Mössbauer Experiment</i>	74
2.4.2	<i>Vibrating Sample Magnetometer (VSM)</i>	75
2.5	LITHIUM BATTERY EVALUATION	76

2.1 Sample preparation

All samples and precursors presented in this work were prepared using traditional solid state synthesis techniques as detailed below.

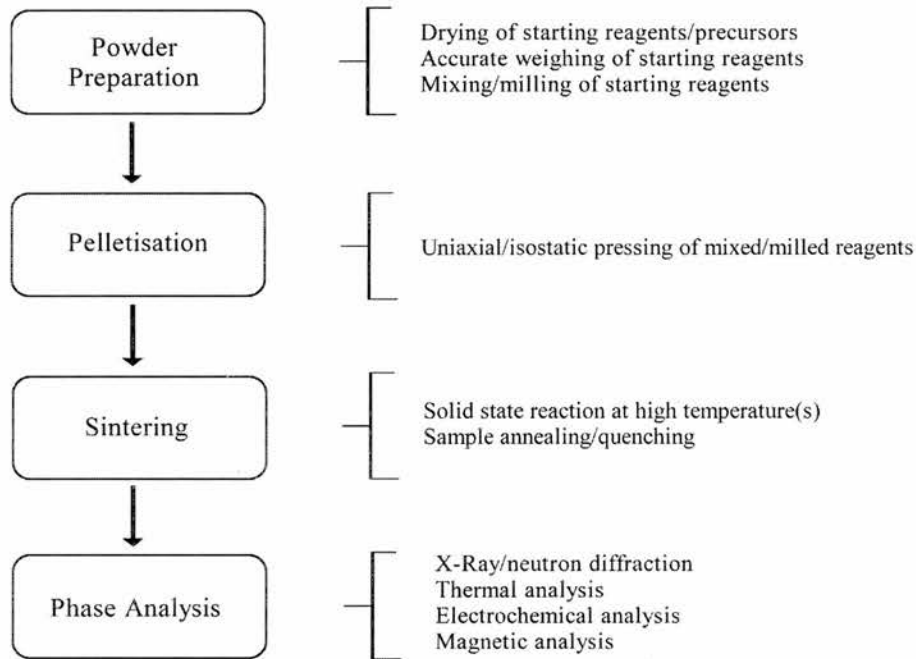


Figure 2-1: Schematic of the preparation and analysis of a typical ceramic material.

2.1.1 Powder Preparation

Prior to use, the starting materials TiO_2 (Aldrich) and Fe_2O_3 (Aldrich) were dried at 300°C in a muffle furnace for at least three hours. Li_2CO_3 (Aldrich) was dried for a similar length of time, but at the lower temperature of 150°C in order to prevent any decarbonation. Neither $(\text{MgCO}_3)_4 \cdot \text{Mg}(\text{OH})_2 \cdot 5\text{H}_2\text{O}$ (Aldrich) nor Ti metal (Aldrich) was dried, as such heat treatment would result in decarbonation or oxidation of the respective materials. Instead, they were used as received, although the Ti was stored in a vacuum dessicator when not in use. Following drying, the starting reagents were weighed using a stainless steel weighing boats upon an accurate ($\pm 0.1 \text{ mg}$) balance. The weighed materials

were then ground together, under acetone, for approximately 20 minutes using an agate pestle and mortar; ball milling being unavailable due to the possible contamination of the ball mill by (and consequential loss from the reactant mixture of) the Ti metal used in reduced samples.

2.1.2 Pelletisation

Oxidised samples were uniaxially pressed into pellets using a 13mm stainless steel die, at 1.5 tonnes/cm² pressure. Such a low pressure was used because high density pellets were not required for the subsequent sample analyses, and because pellets pressed at higher pressures showed a tendency to form a "cap", and the pellets disintegrate during sintering (Figure 2-1).

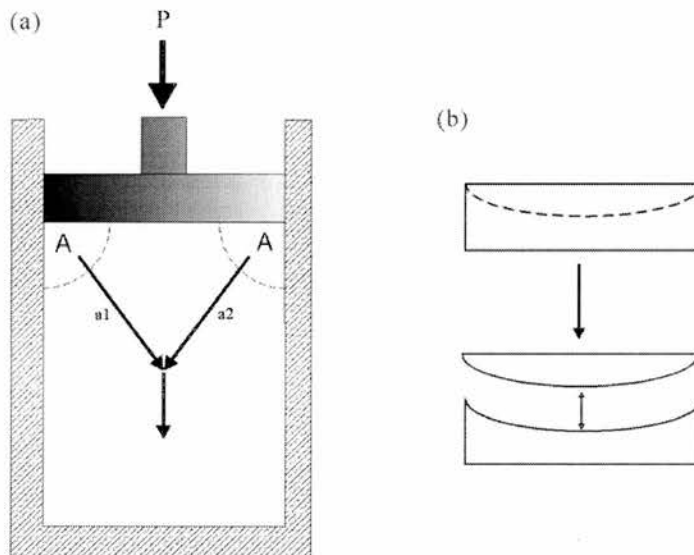


Figure 2-2: Stress in uniaxial pressing¹. (a) The friction between particles and the die walls, sections A, results in a shear stress along a1 and a2. (b) Pellets tend to form "caps" and disintegrate on firing.

Reduced samples were similarly pelleted at 1.5 tonnes/cm², but using a smaller, 8 mm die. In both cases an appropriate amount of powder was left unpressed, and was used as a "bedding" upon which the pellets were placed so as to prevent any reaction with the vessel in which they were fired.

2.1.3 Sintering

The pelleted reactant mixtures for oxidised samples were pre-fired at 700°C, overnight in order to decarbonate, and were then removed, reground and repelleted before being fully reacted in a muffle furnace, using an appropriate temperature/time regime (Table 2-1).

For reduced samples, a slightly different processing was applied. These samples were wrapped (again using a quantity of the ground mixture as bedding) in copper foil, placed in an alumina boat, and fired in a tube furnace of the design shown in Figure 2-3. The advantage of this type of furnace over the muffle design, is that a variety of gases (e.g. Ar, 5%H₂ in Ar, N₂) can be flowed continuously through the tube as the sample is fired, thus giving considerable control over the oxidation state of the sample. As before, a decarbonation step was initially included in the firing, but due to the smaller pellet size it was found that there was no apparent improvement in either pellet density or sample purity if the samples were removed, reground and repelleted after decarbonation, and so this step was later omitted.

Sample	Starting reagents	Oxidised/Reduced	Firing Temperature	Firing Time
LiFeTiO ₄	Li ₂ CO ₃ , Fe ₂ O ₃ , TiO ₂	Oxidised	1000°C	24Hrs
LiFe _x Ti _{2-x} O ₄ (0.5 ≤ x < 1)	Li ₂ CO ₃ , Fe ₂ O ₃ , TiO ₂ , Ti	Reduced	970°C	20Hrs
Li ₄ Ti ₅ O ₁₂	Li ₂ CO ₃ , TiO ₂	Oxidised	930°C	36Hrs
Li ₂ Ti ₃ O ₇	Li ₂ CO ₃ , TiO ₂	Oxidised	970°C	24Hrs
Li _{2-x} Ti _{2-2x} O ₄ ²	Li ₄ Ti ₅ O ₁₂ , TiO ₂ , Ti	Reduced	970°C	20Hrs

Table 2-1: Sample starting reagents and reaction regimes.

In order to obtain high temperature polymorphs of some samples, a vertical quench furnace (Figure 2-3) was used. This is similar to the horizontal tube furnace in that it allows reaction/annealing of the samples under almost any atmosphere, but differs in that the vertical geometry allows samples to be

"dropped" onto a bed of copper turnings while still at high temperature. In this way samples can be quenched from reaction temperature to room temperature in a matter of seconds, allowing the synthesis of high purity samples of high temperature phases.

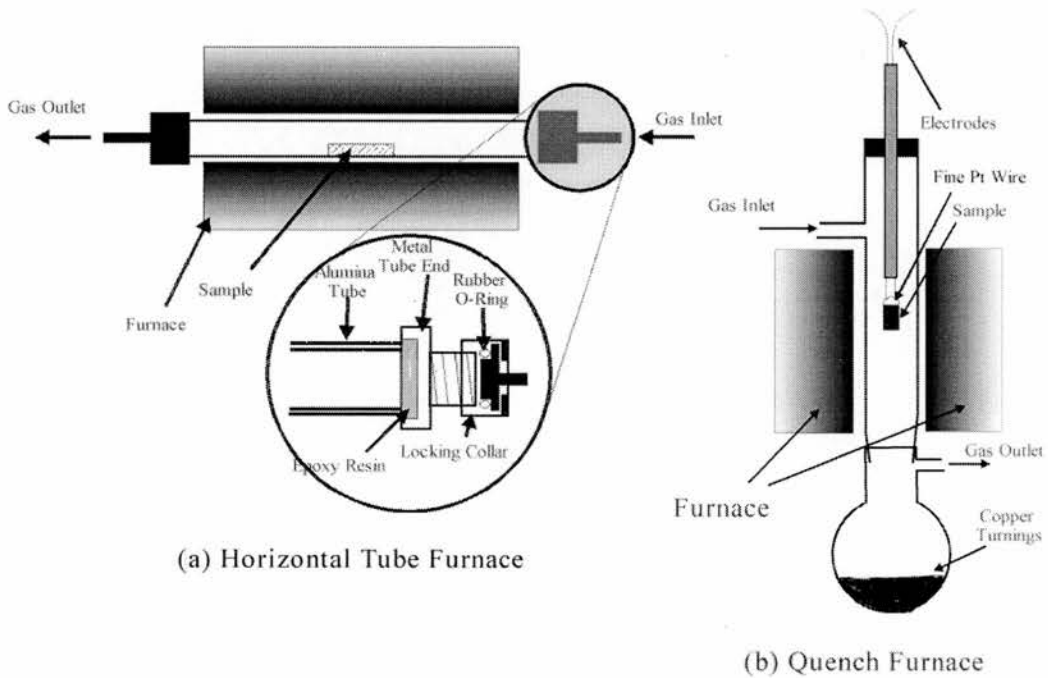


Figure 2-3: The horizontal tube (a) and vertical quench (b) furnace designs used in sample preparation

2.2 Structural Characterisation of Materials

2.2.1 Diffraction and Bragg's law

Consider a simple diffraction grating (Figure 2-4). A wavetrain approaches the grating and is coherent, and when it reaches the grating, it passes through both slits at precisely the same time. However, it does not pass through unchanged. Instead, each slit acts as a “secondary source” of radiation and effectively new waves propagate from each slit. This then gives us two wavetrains propagating from the grating, and when they overlap they interfere. This then causes an intense maximum to be generated when the waves constructively interfere (meet in phase) or a minimum to be generated where they destructively interfere (meet exactly out of phase). If a piece of card is placed behind the grating, a *diffraction pattern* (or *interference pattern*) will be produced upon the card.

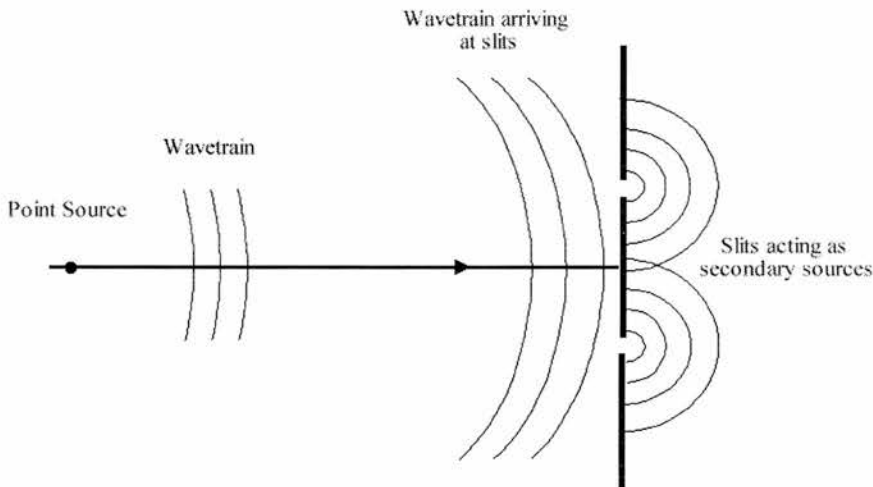


Figure 2-4: How diffraction gratings act as secondary sources.

In 1912, Laue³ suggested that a crystal could be similarly regarded as a three-dimensional diffraction grating for electromagnetic waves of a wavelength comparable to the atomic spacing ($\sim 1\text{\AA}$). However, the mathematics of this approach are quite convoluted, and were fortunately made redundant a year later,

when W.L.Bragg ⁴ provided an easier way to describe the diffraction of radiation by crystals. Rather than viewing the crystal as a three dimensional diffraction grating, he envisaged crystals in terms of layers, or planes, of atoms which behaved as reflecting planes. This approach is much simpler, and while not physically accurate - planes of atoms do not reflect radiation as such - it is correct in a geometrical sense, and leads to an elegantly simple expression by which crystal structures are still analysed:

$$n\lambda=2d\sin\theta$$

Where n is the order of the reflection (usually n=1)
 λ is the wavelength of radiation
 d is the interplanar spacing
 θ is the Bragg angle

When this law is satisfied, the diffracted beams 1' and 2' (Figure 2-5(b)) are in phase and constructively interfere. When the law is not satisfied, the beams are out of phase and destructively interfere. Thus, by keeping λ constant and varying 2θ, a graph of constructive interference intensity can be plotted against angle. This is a diffraction pattern, and the Bragg law allows us to directly relate the intensity peaks with the interatomic spacing d, giving valuable information about the structure of the crystal.

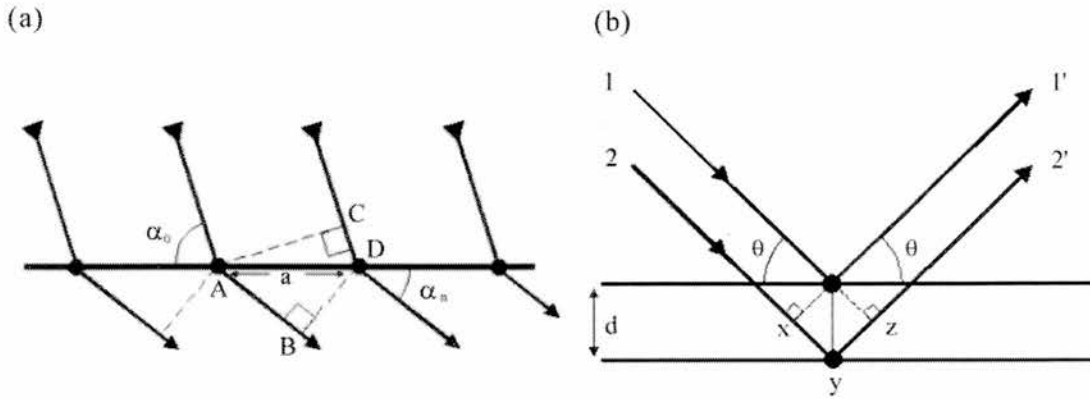


Figure 2-5 (a) Diffraction from a lattice row along the x-axis, as envisioned by Laue. The incident and diffracted beams are at angles α_0 and α_n to the row. The path difference between the diffracted beams is $(AB-CD)$. (b) Diffraction from lattice planes as envisioned by Bragg. The path difference between the diffracted beams is XYZ .

2.2.2 Miller indices

Examination of almost any crystal diffraction pattern will show that there are usually several peaks, all of differing d . In order to explain why one material exhibits several diffraction peaks, and thus several atomic planes, we have to use the idea of Miller indices, so named after W.H. Miller who first suggested their use, in 1839.

Figure 2-6(a) shows how a simple square grid of dots can be divided into parallel rows (or planes). It is visually obvious that each set of planes has a different interplanar spacing (or d -spacing), and that any one point can be associated with many sets of planes. Figure 2-6(b) shows how this translates into three dimensions.

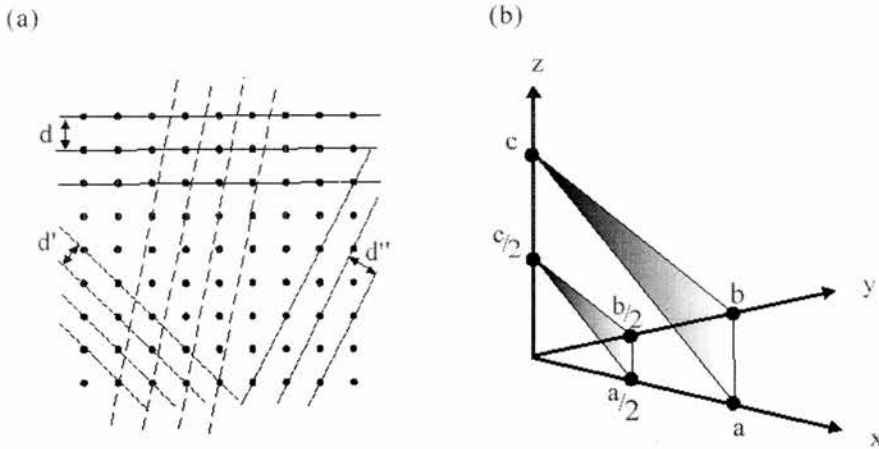


Figure 2-6: (a) How a square array of dots can be divided into planes of different interplanar spacing. (b) Lattice planes in three dimensions.

Obviously, in order to differentiate these planes it is necessary to label them, and to do this the intercepts of the plane of a family nearest to the origin are taken. In the case shown in Figure 2-6(b) these would be at $\frac{1}{2}a$, $\frac{1}{2}b$ and $\frac{1}{2}c$. Now the reciprocals of these fractions are taken and the numbers written in round brackets, without commas, in the form (hkl) . This is the Miller index of the plane (thus in the case of the example given above, the (222) plane is shown). For an orthogonal crystal system (i.e. $\alpha = \beta = \gamma = 90^\circ$), the Miller indices can be related to the unit cell dimensions (a, b, c) and the interplanar d -spacing in the following way:

$$\frac{1}{d_{hkl}^2} = \frac{h^2}{a^2} + \frac{k^2}{b^2} + \frac{l^2}{c^2}$$

Where: h, k and l are the Miller indices
 $a, b,$ and c are the unit cell edges
 d is the interplanar d -spacing

2.2.3 Systematic absences

Although the relationship between this and Bragg's law imposes strict conditions on where constructive diffraction can occur, they only represent a minimum condition for diffraction from a crystal - they merely state that diffraction can occur, not that it will.

In practice, it is found that the symmetry of the crystal plays an important part in the scattering of the radiation. If the lattice type is non-primitive, or if elements of space symmetry, such as a screw axis, are present, certain peaks will be absent from the diffraction pattern. As an example, take cubic α -Fe (Figure 2-7), with a body centred lattice (I). It is found experimentally that reflections from the (100) plane are systematically absent, whilst reflections from the (200) plane are present. This is because, at the Bragg angle for the (100) reflection, the body centred atom lies precisely midway between the (100) planes and so diffracts radiation exactly 180° out of phase relative to the corner atoms, and thus completely cancels out the radiation diffracted from these atoms. The (200) diffraction peak is present however, because all atoms lie in the (200) planes.

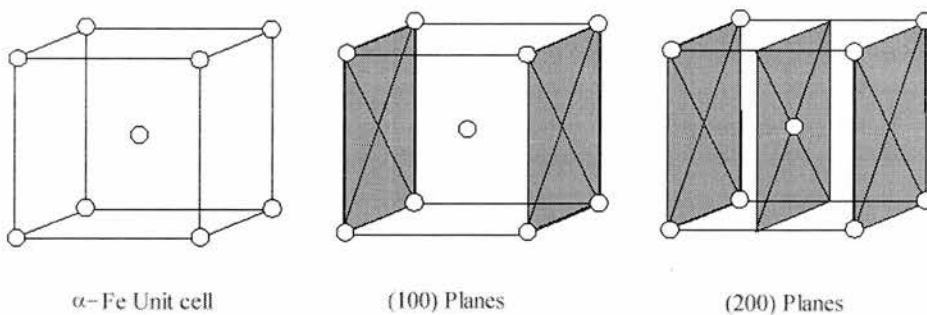


Figure 2-7: Systematic absences in α -Fe.

2.2.4 Form factors

In order to fully understand the nature of diffraction and the information contained within a diffraction pattern, it is necessary to understand the factors

which determine the intensity, as well as the angle, of diffracted radiation. In order to do this, the nature of the interaction of the radiation with the crystal must be considered.

For x-rays, diffraction occurs as a result of the interaction of the x-ray photons with the electron density (Thompson scattering). Essentially, the x-ray elastically interacts with the electron density to set it vibrating, a second photon is generated and re-emitted in a fashion coherent to the incident radiation. The atom effectively acts a secondary source of x-rays. Unfortunately, because the electron shell of an atom is not a point charge, but is distributed over a volume of diameter comparable to the x-ray wavelength, partial destructive interference can occur between x-rays diffracted from different parts of the electron shell (Figure 2-8(a)). Consequently, the intensity of x-ray scattering from a sample decreases significantly with increasing values of 2θ .

A further consequence of this mode of interaction is that the intensity of x-rays scattered from an atom increases with the number of electrons present, and hence with increasing atomic number. The practical result of this is that in compounds containing both heavy and light atoms, such as PbO , the heavy atom dominates the x-ray scattering from the crystal, and it becomes difficult to "see" the lighter atoms.

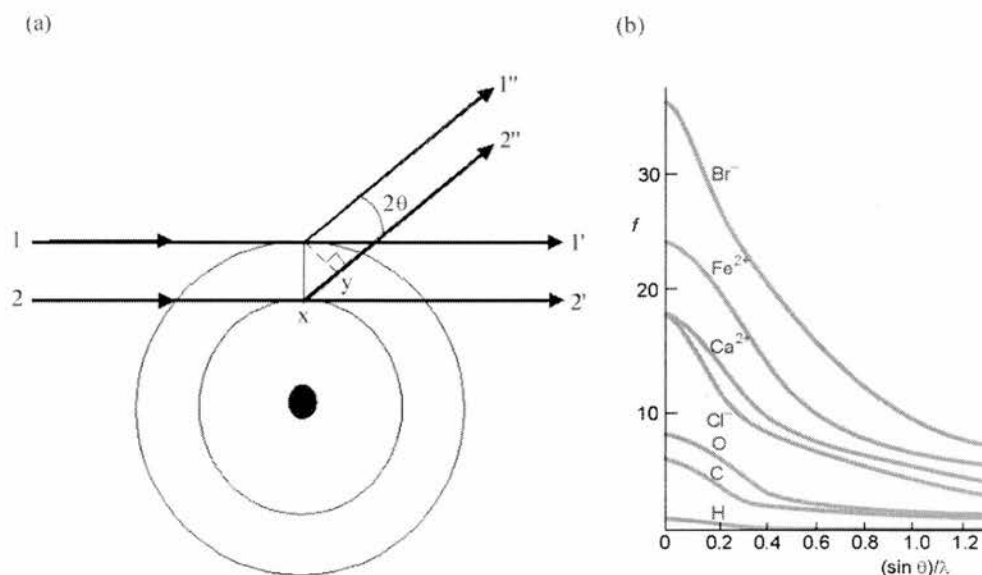


Figure 2-8: (a) Destructive interference between x-ray beams scattered from different parts of an electron shell. (b) Some typical values of x-ray scattering factors (form factors) in terms of $(\sin \theta)/\lambda$. (Taken from Atkins⁵)

This dependence of x-ray scattering with angle and atomic number is described quantitatively by a value known as the *form factor*. Each element has its own form factor which, excluding resonance effects, can be regarded as wavelength independent. These are usually given in terms of $(\sin \theta)/\lambda$. Some typical form factors are given in Figure 2-8(b).

Where neutron radiation is used instead of x-ray, the mechanism by which neutrons are scattered is somewhat more complex. Instead of being diffracted by the electron cloud, neutrons scatter primarily from an interaction between the neutron and the atom nucleus. There is no simple relationship between atomic number and scattered intensity, as there is in the x-ray case. Indeed, different isotopes of the same element (e.g. hydrogen and deuterium) can have completely different scattering factors. Also, because the mechanism of scattering from the nucleus is different, neutron radiation does not suffer the intensity fall-off with angle that is present when x-rays are used. Neutron diffraction can therefore give considerably more information at higher angles of 2θ (shorter d-spacing).

Neutron radiation has yet another advantage over x-rays - neutrons possess a magnetic moment, which can interact with the unpaired electrons in the magnetic materials, giving rise to extra "magnetic" peaks in the diffraction pattern.

Although theorised 10 years previously^{6,7}, this property was first used by Schull *et al*⁸ in 1949 to detect magnetic diffraction in MnO, and to later solve its antiferromagnetic structure. Since then, neutron diffraction has become an important tool in the study of magnetism, and still remains the only method of conclusively proving antiferromagnetism.

2.2.5 The structure factor

So far it has been explained how diffraction from a crystal comes about, and how the angles and intensities of diffraction peaks are different with different elements and crystal types. In order to draw these factors together, and so fully explain the scattering from an array of atoms (or a crystal), we must define the relationship between them. This relationship is given by the *structure factor*, F_{hkl} , and is the same whether neutron or X-ray radiation is used:

$$F_{hkl} = \sum_{r=1}^N f_r \exp 2\pi i(hx_r + ky_r + lz_r)$$

or

$$F_{hkl} = \sum_{r=1}^N f_r [\cos 2\pi(hx_r + ky_r + lz_r) + i \sin 2\pi(hx_r + ky_r + lz_r)]$$

Where: f_r is in the form factor for atom type r .
 h, k and l are the Miller indices for the reflection.
 x_r, y_r and z_r are the fractional coordinates for atom r .

Using this relationship, the diffraction pattern of any normal crystal can be calculated, and by comparing calculated patterns with the observed one, the structure of a compound can be derived.

2.2.6 Other factors influencing diffraction intensity

1. *Temperature factors* - The thermal vibrations of atoms can cause a decrease in the scattered intensity of diffracted radiation and an increase in background scattering. High resolution diffraction techniques can be used to give a measure of such thermal motion.

2. *Preferred orientation* - In powder diffraction it is imperative that the powder crystallites be randomly oriented. If the crystals are needle or plate-like, they may tend to pack in a specific manner, and then the intensity of some peaks will be disproportionately high or low depending on the sample orientation. Preferred orientation effects can be considerably reduced by using a rotating sample holder.

3. *Peak multiplicities* - In powder diffraction, the intensity of a diffraction line is affected by the number of Miller planes contributing to that reflection. For example, in a cubic material, the (100), ($\bar{1}00$), (010), ($0\bar{1}0$), (001) and ($00\bar{1}$) all have the same d-spacing, and so all contribute to the same diffraction line. In single crystal diffraction this is not a problem, as the sample is oriented so that diffraction from each plane can be analysed separately.

4. *Polarization factors* - While the x-rays produced by the diffractometer tube are unpolarized, a crystal does not reflect waves vibrating in all directions with equal efficiency, and so the reflected beam is partially polarized. Because the beam intensity is reduced by a factor of $(1 + \cos^2 2\theta)/2$, this causes the intensities at very low and very high Bragg angles to be enhanced relative to those at intermediate values.

2.2.7 The powder x-ray diffraction experiment

The geometry of a typical reflectance mode powder diffractometer is given in Figure 2-9. Reflectance is the most common geometry for powder diffraction instruments, as it gives fast scans and good pattern intensities, but a second mode

is also sometimes used - transmission. In transmission mode, the diffracted x-ray beams pass through the sample, rather than being reflected, and so the thickness of the sample used must be judged carefully.

In a typical diffraction scan, the source remains still while the detector moves around the sample on an arc centred on the sample, as shown in Figure 2-9. Additionally, the sample is rotated to ensure that the incident angle of the radiation remains equal to the angle of diffraction. In this way, the detector rotates an angle of 2θ around the sample, whilst the sample is rotated by θ . This is called a 2θ - θ scan. Samples for reflectance diffraction are generally mounted in specially hollowed metal plates, and carefully smoothed off to ensure an accurate zero point. For transmission mode diffraction, a thin layer of sample is "stuck" to a Mylar disc, using Vaseline or something similar. This is then mounted in a rotating sample holder, which minimises any preferred orientation effects.

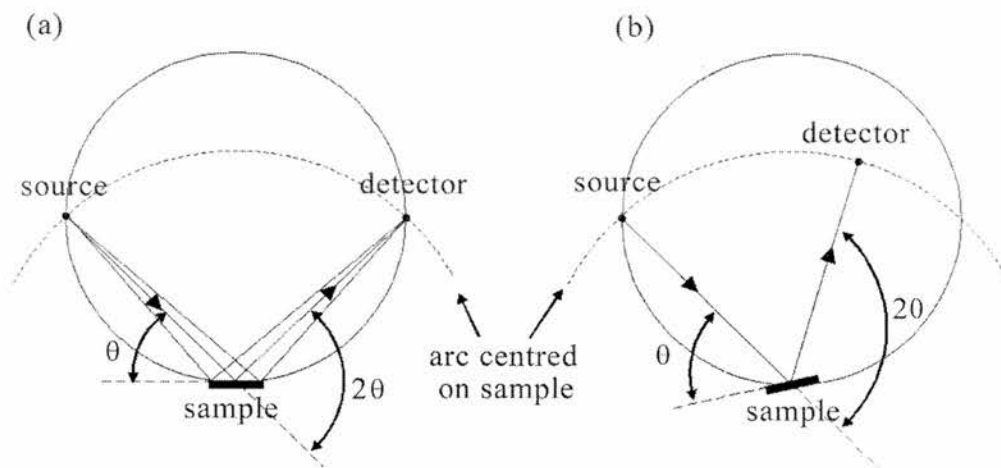


Figure 2-9: The geometry of a powder x-ray diffractometer. During a scan, the detector moves through the angle 2θ , whilst the sample is rotated by θ . This is shown in (b). Note that the source and the detector are both mounted on a circle which is centred on the sample. This is to ensure that the x-rays remain focused when they reach the detector.

Three diffractometers were used to collect data for this work; a Philips PW3810 reflectance diffractometer, using Cu- K_{α} radiation, and two STOE STADI P

transmission diffractometers, one using Cu-K_{α1} radiation and the other using Fe-K_α.

2.2.8 The neutron diffraction experiment

Two very different ways are available for the generation of neutrons for diffraction work. The first of these uses a nuclear reactor to source the neutrons, by means of fission. These neutrons are produced continuously, and after thermalising in a moderator surrounding the reactor core, a steady supply of neutrons is available with a broad range of wavelengths. Selection of wavelengths for diffraction is then achieved by Bragg scattering from a crystal monochromator. The sample for analysis is then mounted in a vanadium "can", similar in shape to a small cigar tube, and the beam enabled by means of lifting a large "shutter". The diffraction pattern is collected over a range of 2θ , in a similar way to an XRD pattern (Figure 2-10(a)).

The second method of neutron generation is by spallation. In this technique, neutrons are generated by bombarding a uranium or tantalum target with high-energy protons. As these protons are not continuous, but are released from a synchrotron in pulses, the neutrons are similarly generated in pulses. These pulses then pass through a chopper (a rotating metal disc with a section missing) in order to remove undesirable wavelengths and to give a zero point in the time of flight (TOF) of the neutrons. The pulses are then diffracted by the sample and the neutron TOF counted using a static detector of known angle to the sample and neutron beam (Figure 2-10(b)). Because the TOF is proportional to the wavelength of the neutron, and the distance from chopper to detector is known, the detected neutrons can then be processed to give a diffraction pattern. The time of flight of the neutrons can then be converted into d-spacing using the following relationship:

$$d = \frac{ht}{2m_n l \sin \theta}$$

Where: d is the interplanar d-spacing.
 h is Planck's constant
 t is the time of flight
 m_n is the mass of the neutron
 l is the distance between chopper and detector
 θ is the angle between the beam and the detector

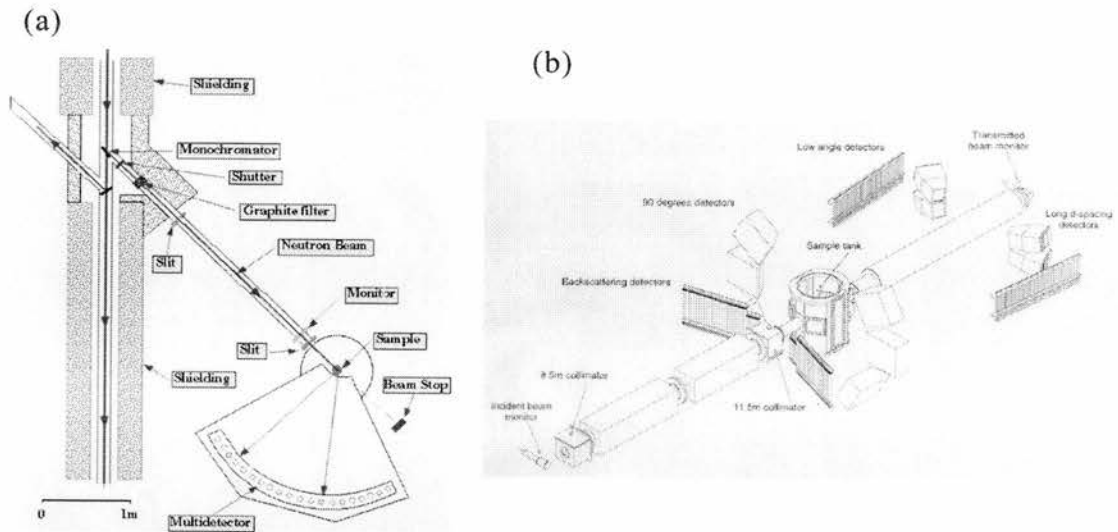


Figure 2-10: The layout of (a) a constant wavelength neutron diffractometer (D1B, ILL), and (b) a TOF diffractometer (Polaris, ISIS)

Neutron diffraction data for this work were obtained using both these techniques. Time of flight data were collected on the Polaris and HRPD instruments at the ISIS facility in Didcot, Great Britain, and at Argonne National Laboratories, Chicago, USA, using the GPPD and SEPD instruments. Constant wavelength diffraction data were obtained using the D2B instrument at Institut Laue Langevin (ILL), Grenoble, France.

2.2.9 Powder Pattern Analysis – The Rietveld Method

Whilst the growth of large single crystals has always been preferable for structure solution purposes, in many cases it is often difficult or impossible to achieve. For structure solution and refinement of polycrystalline samples then, a technique of extracting accurate information from powder diffraction data had to

be developed. The technique most commonly applied to this problem is the Rietveld ^{9,10} method.

In Rietveld analysis, a model is fitted to the entire diffraction pattern by means of curve fitting and least squares methods, rather than by fitting the intensity maxima. By taking this approach, the intensity of each data point is taken into account in the calculation, and so diffraction optics, instrument geometry, and even second phases can be factored into a refinement in order to more accurately characterise a sample. Obviously these kinds of calculation require a considerable quantity of computing power, and until recently such refinements had to be carried out on expensive workstations or computer clusters. However, with the explosion in the computing power of desktop PC's it is now possible to carry out such refinements on ordinary laboratory computers. Several pieces of software, capable of processing both x-ray and neutron (constant wavelength and TOF) diffraction data are available for the PC. In this work, the GSAS ¹¹ (General Structure and Analysis Software) and FULLPROF ¹² packages were used.

It should be noted, however, that the Rietveld method makes no effort in advance to allocate diffraction intensity to Bragg reflections, nor to resolve overlapping peaks. Before refinement can begin, a good starting model, consisting of at least space group, unit cell and atom occupancies, is therefore required. Additionally, the technique is not a replacement for crystallographic knowledge and experience - it is often easier to fit a physically impossible model than a realistically feasible one. Therefore, at least some basic knowledge of crystallography is required to ensure that the refinement results are sensible.

2.2.10 R-Factors

As well as providing a visual measure of the quality of the refined model in the form of a difference curve, Rietveld software also provides a quantitative measure of the closeness of fit in terms of R factors, or Residual factors. There are four commonly used R factors:

1. Profile R factor, R_p
2. Weighted R factor, R_{wp}
3. Intensity or Bragg R factor, R_I
4. Expected R factor, R_E

These are defined as follows:

$$R_p = \frac{\sum_i |Y_i(obs) - Y_i(calc)|}{\sum_i Y_i(obs)}$$

$$R_{wp} = \left[\frac{\sum_i |Y_i(obs) - Y_i(calc)|^2}{\sum_i W_i Y_i^2(obs)} \right]^{1/2}$$

Where: Y is the intensity of the point on the powder diffraction profile
 W is a weighting factor

$$R_I = \sum_k \left| I_k(obs) - \frac{1}{c} I_k(calc) \right| \sum_k I_k(obs)$$

Where: I is the peak intensity.

The intensity R factor is helpful in determining the structural fit since it is related to the peak area and not the peak shape.

$$R_E = \left[\frac{N - P}{\sum_i W_i Y_i^2(obs)} \right]^{1/2}$$

Where: N is the number of observations.
 P is the number of variables.
 C is the number of constraints.

Another guide to the quality of a refinement is χ^2 , which is calculated using the following relationship:

$$\chi^2 = \left[\frac{R_{wp}}{R_E} \right]^{1/2}$$

For an ideal refinement then, the weighted and expected R factors should be identical, and hence a value of 1 obtained for χ^2 . However, a number of things can affect the value of χ^2 , and hence the value should not be used solely on its own as a guide to the quality of a refinement. It is also important to examine the observed and calculated profiles at each stage of refinement in order to assess the progress and future strategy of the refinement. The R factors obtained during the course of a refinement are the best guide to the quality of the fitted profile.

It should be noted though, that the value of R may be artificially high for a number of reasons, such as short counting times (leading to a systematic error in the background, poor peak separation, etc.). The use of specialist equipment such as a furnace or cryostat can also contribute to the background of the collected profile, and hence influence the expected R factor. Factors such as these must be considered when reporting the R factors obtained from a refinement.

2.3 Thermal Analysis

In order to investigate the thermal properties of some samples, thermal analysis¹³ was employed. This is a group of techniques in which a property of the sample is monitored as a function of time and/or temperature, while the temperature of the sample is altered. The sample is kept in a controlled, specified atmosphere for the duration of the experiment. For this work, two thermal analysis techniques were employed.

Thermogravimetric analysis (TGA) is a technique in which the mass of the sample is monitored against its temperature, for a specified temperature program.

The rate of heating/cooling can be varied, and the temperature held constant for a specified length of time, if desired. TGA is thus commonly used to study decomposition, dehydration and oxidation.

Differential thermal analysis (DTA) is a technique where the difference in temperature between the sample and a reference (usually alumina) is monitored as a function of temperature and/or time. DTA can thus detect endotherms or exotherms of the sample and is commonly used to study phase changes and reactions. It should be noted, though, that DTA does not directly give sufficiently good data for accurate, qualitative analysis of heat capacities or enthalpy changes. For this, Differential Scanning Calorimetry must be used.

Thermal analysis measurements for this work were performed on two machines, a TA Instruments 2960 simultaneous TGA/DTA, and a Rheometric Scientific TG 1000M+.

2.4 Magnetic Characterisation of Materials

2.4.1 Mössbauer spectroscopy

Lying in the high-energy end of the electromagnetic spectrum, beyond x-rays, γ radiation is extremely penetrating, but with low ionising power relative to α and β radiation. When rays pass through matter they interact a little with electrons (and are diffusely scattered), and with the nucleus of the atoms through which they pass. A gamma beam thus loses intensity primarily by absorption of individual γ rays by the nuclei of the matter through which it passes.

However, as nuclear energy levels are very sharply defined, only γ rays of discrete energies can be absorbed by any given nucleus. Consequently, for any technique using the nuclear absorption of gamma rays, a monochromatic beam of radiation is required, of energy specific to the atom under investigation.

In 1958, Rudolf Mössbauer found that certain gamma emitting radioactive isotopes could be used as sources of gamma radiation of correct energy to be absorbed by non-radioactive isotopes of the same element. This is called the Mössbauer effect (Figure 2-11).

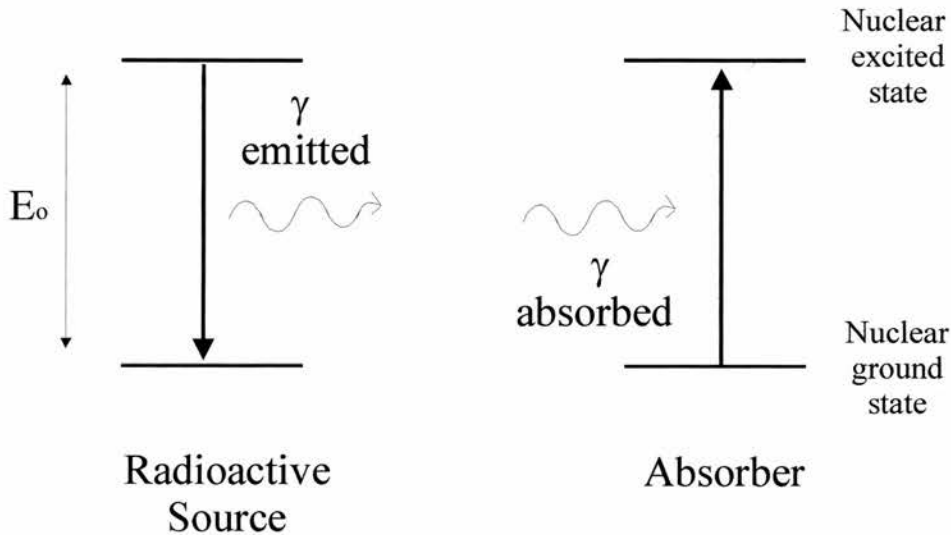


Figure 2-11: The Mössbauer Effect

He also showed, both theoretically and practically, that this only worked if radioactive nucleus is bound in a solid, because there would be a significant increase in the number of *recoil-less* emissions. This is important, as when a γ ray is emitted, conservation of momentum requires that the emitting nucleus "recoil" in the opposite direction with approximate energy:

$$E_r = E_\gamma / 2Mc^2$$

Where: M is the nuclear mass
 E_r is the recoil energy loss

This result is in a loss of energy of the emitted γ ray relative to the nuclear transition which generated it. Although this reduction is small (generally 10^{-2} to 10^{-3} eV for transitions used in Mössbauer spectroscopy), it is significantly larger than the width of a nuclear energy level, and so a γ ray produced by a non-recoil less transition between two levels cannot be then absorbed by the reverse

transition as its energy is incorrect. It follows then, that only gamma rays emitted by a recoil less process can be resonantly absorbed by nucleus of the same type.

2.4.1.1 The Mössbauer spectra

There are basically two types of information that can be obtained from the Mössbauer spectroscopy: the isomer (or chemical) shift, and the hyperfine coupling parameters of the material.

The isomer shift is best thought of as a displacement of the energy levels of the atom under investigation, so that the overall energies of the ground and excited states are both "shifted", but the difference between them remains the same (Figure 2-12).

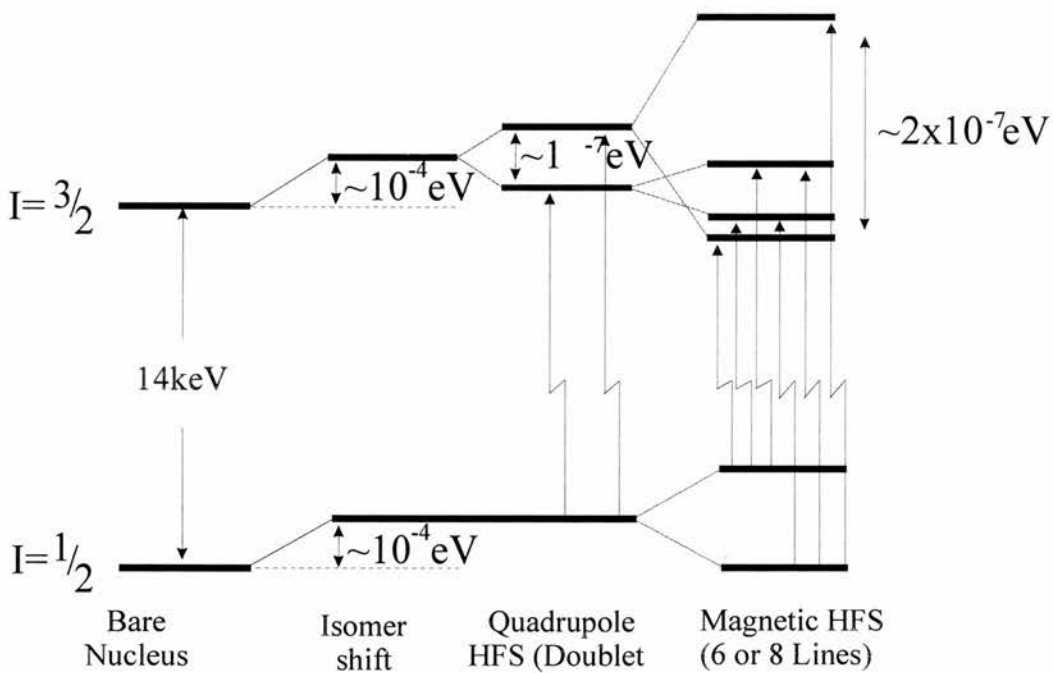


Figure 2-12: Energy level diagram for ^{57}Fe showing isomer shift and hyperfine splitting.

This effect arises from the electrostatic interaction of the nucleus with the electric field due to the orbital electrons, particularly the s-electrons. It should be noted, though, that the "measured" isomer shift is not the total energy perturbation of

the atom under investigation, but the difference in transition energies between the source and the sample.

There are two basic mechanisms by which the valence of the ion being studied can affect the isomer shift. The first is a direct change in the electron density at the nucleus due to the absence or presence of valence s-electrons. This is the case for systems such as Sn, where the +2 and +4 oxidation states correspond to $5s^2$ and $4d^{10}$ configurations respectively. The second mechanism applies more to transition elements, where the change in charge at the nucleus is caused by a change in the shielding by the d-electrons upon oxidation or reduction. This is the case in Fe, where the loss of a 3d electron causes the 4s electrons to be "pulled" in more tightly, thus causing a change in the electronic charge at the nucleus. This means that we can study valence changes even in systems in which the s-electrons are not valence electrons.

In addition to energy changes caused by the isomer shift, energy levels can be split by electric-quadrupole and magnetic-dipole hyperfine interactions.

Quadrupole coupling occurs from the fact that the nucleus is not necessarily spherical, but can be ellipsoidal, elongated or flattened (Figure 2-13). This then gives two different energies to the nuclear states; one corresponding to the nucleus pointing towards the surrounding ligands (low E) and one where the nucleus lies at 90 degrees to the ligands (high E). As the two "ends" of the nucleus have the same charge distribution, coupling energy of the "spin up" ($I = +1/2, +3/2$) configurations will be the same as the "spin down" ($I = -1/2, -3/2$). This means that the levels $1/2$ and $3/2$ will be degenerate, as will the levels $-1/2$ and $-3/2$. This explains why a doublet is observed in the Mössbauer spectra of ^{57}Fe and ^{119}Sn : the $I=3/2$ excited nuclear state splits into $\pm 3/2$ and $\pm 1/2$, whilst the ground state $I=1/2$ remains unsplit.

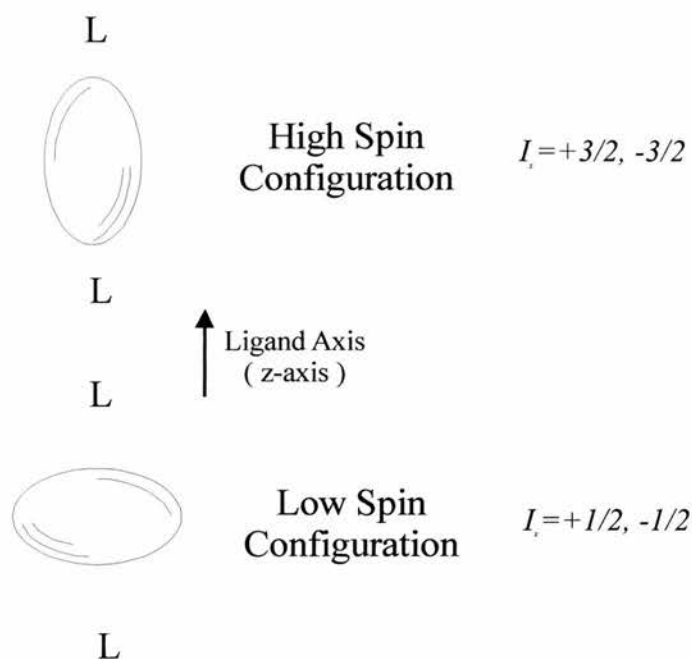


Figure 2-13: Coupling of the nuclear quadrupole moment with nearby charges. Note the low energy configuration is obtained with the nuclear axis pointing towards the ligands. The difference in energy between the two configurations is quadrupole splitting.

The magnetic hyperfine interaction (or nuclear Zeeman effect) arises from coupling of the nuclear magnetic moment with the effective magnetic fields at the nucleus. The result of this is a splitting of the nuclear ground and excited states, if they have spin $I > 0$.

The hf (or internal) field is usually given the term B_{hf} , and the energy by which nuclear energy levels are perturbed by magnetic interaction alone is given by:

$$\Delta E_m = B_{hf} \mu \left(\frac{I_z}{I} \right)$$

Where: μ is the magnetic moment of the nuclear state

I and I_z are the spin of the nuclear state and its projection along the z-axis from $-I$ to $+I$.

As I_z varies in steps of one unit, this gives $2I+1$ equally spaced energy levels which arise from the magnetic splitting.

The splitting itself occurs from several sources:

1. If the ion under study is magnetic, densities of “spin-up” and “spin-down” electrons at the nucleus will be different, and there will be a net spin polarisation. The interaction of the nucleus with the electron spin polarisation is called the Fermi contact interaction and can be thought of as an effective magnetic field at the nucleus.
2. In insulating materials, hf fields can be generated by polarisation of magnetic ligands.
3. Externally applied fields can be used to produce magnetic splitting of nuclear energy levels.

Whilst hf splitting generally arises from more than one of these sources, in magnetically ordered systems the first one tends to be dominant.

2.4.1.2 The Mössbauer Experiment

In order to measure a spectrum from a real sample, a small spread of γ ray energies is obviously required as, by definition, the isomer shift is the difference between the source and absorber energies. This is achieved by using the Doppler effect: the γ ray source is mounted on a specially designed vibrator coil which can be tuned to give different energies and waveforms depending on the sample and the information required.

As the measurement is taken in transmission, the thickness of the sample is very important: too little sample and the spectra will contain little information, too much and the transmitted intensity will be faint. For this work samples were contained between two pieces of ordinary clear sticky tape, and were mounted in a non-magnetic sample holder. In order to allow measurements of spectra at various temperatures, this was contained within an Oxford Cryosystems cryostat, with an operating temperature range of 2K to room temperature. A ^{57}Fe source

was used, and spectra were collected over roughly 8-10 hrs, depending on the sample.

Following collection, the data were normalised to an Iron standard (taken at the same time as the sample spectra), and then fitted using the Recoil software package.

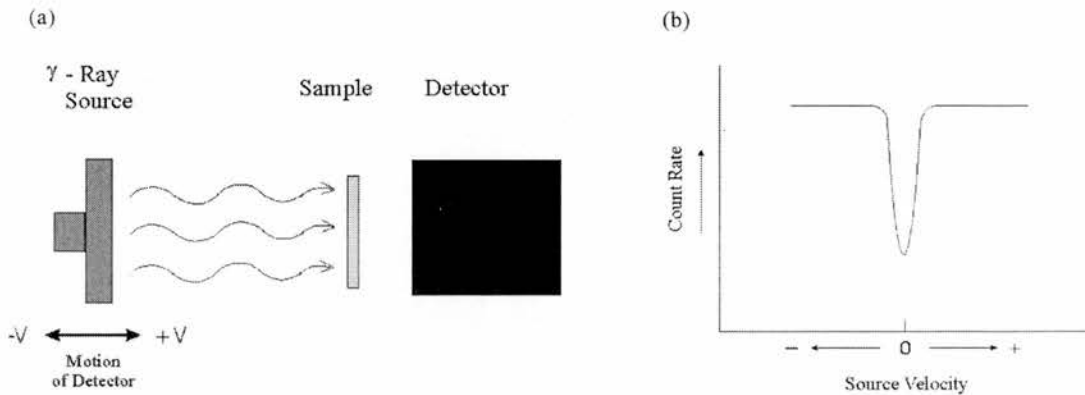


Figure 2-14: (a) Schematic of a Mössbauer Spectrometer and (b) an example pattern showing how velocity is plotted against counts.

2.4.2 Vibrating Sample Magnetometer (VSM)

If a magnetic dipole, placed in the centre of a coil, is then moved a voltage ε is induced in that coil. The time integral of this, $\int \varepsilon dt$, is then equal to the flux produced by the dipole. The total flux ϕ is then given by $\int B dS$, where dS is an element of the area. As the induction is given by $B=B_0+\mu_0 M$, if the applied field B_0 is known accurately, or if it can be compensated for, the magnetisation is given directly from ϕ .

The Vibrating Sample Magnetometer (VSM) is a convenient and popular application of the inductive method described above, in which the sample under

investigation is placed in a uniform magnetic field and subjected to a mechanical vibration. In this way an alternating signal is induced in the pick-up coils, which is dependent on the magnetic moment, amplitude of vibration and vibration frequency. As long as the sample weight, molecular weight and magnetising field are known, this measured magnetisation can give a great deal of information regarding the magnetic properties of the sample. It is most common for thus collected data to be converted into magnetic susceptibility for further analysis. This can be done via the expression:

$$\chi_m = \frac{M_s (Mw)_s}{B_a W_s}$$

Where: χ_m is the molar magnetic susceptibility

$(Mw)_s$ is the sample molecular weight

B_a is the applied magnetic field

W_s is the weight of the sample

Additionally, by using an electromagnet to generate the field, and by placing the apparatus in a cryostat, it is possible to perform these magnetisation measurements as a function of temperature, magnetic field, magnetic field ramp rate and crystallographic orientation.

Data presented in this work were obtained using an Oxford Instruments 12 Tesla VSM, located in the School of Physics and Astronomy, University of St. Andrews.

2.5 Lithium Battery Evaluation

Primary (or one-use) cells, such as the Alkaline batteries produced by Duracell and Ever Ready, have long been established in the marketplace. They have high capacities and good discharge characteristics, but can only be used once as the reactants are consumed irreversibly on discharge. This makes them an inherently

wasteful source of power, as they have to be discarded after use, and in an increasingly environmentally conscious society this is unacceptable.

Secondary (or rechargeable) cells have suffered in the past from a higher initial purchase cost and lack of capacity compared to the Alkaline primary cells, and also from the fact that, until recently, most batteries were used in occasional-use devices, such as Walkmans. However, there is an increasing market in devices, such as mobile phones, which have to run from a battery all day, every day. This has led to an explosion in the market for rechargeable cells and demands for higher capacity, light-weight batteries.

In secondary cells the demands on both the anode and cathode are much greater than for primary cells. As well as the discharge reaction described above, the electrodes must be capable of the reverse reaction (charging) and must be able to do these repeatedly, without loss of structure or capacity, and without side reaction with the electrolyte. Whilst cathode materials such as MnO_2 demonstrate the required qualities for use as secondary cell electrodes, suitable anode materials have also to be found. Lithium metal, as used in primary cells, cannot be used as an anode for secondary cells. This is because it reacts with the electrolyte in the cell, forming a *passivation layer* on the surface of the anode, which can cause lithium to be deposited unevenly on the anode during the charging process and lead to the formation of dendrites which ultimately short circuit the cell.

What is required therefore, is a material with a high energy density which can uptake and release lithium with good cyclability. Carbon (as both coke and graphite) has been the commercial material of choice, demonstrating higher energy capacity than many transition metal oxides, and an operating voltage close to that of metallic lithium. For the next generation of anodes, however, focus has moved back to the oxides, in particular the amorphous tin oxide materials reported by Fujifilm Celltech^{14,15}. These are thought to insert Li via an alloying (rather than insertion) process, but circumvent the limitations of

previous alloy electrodes (such as large volume change) by maintaining the active electrode material (microfine Sn metal) within an inert matrix (Li_2O).

In this work we have investigated several spinel and ramsdellite materials for use in lithium battery anode applications. To test these materials we made them up into porous “Bellcore”¹⁶ type electrodes. These were prepared in the form of a slurry of 11.6% by weight, active material, 1.4% Super S carbon (to aid electronic conduction), 5.5% PVDF, 9.5% Propylene carbonate and 72% acetone. This as prepared slurry was stirred at 50°C for 4hrs in order to ensure full dissolution of the PVDF binding agents, and then doctor-bladed onto a glass plate at a thickness of roughly 0.3mm. The electrode sheet was allowed to dry and from it were cut 6mm diameter electrodes for testing purposes. Each of these discs was then immersed in ether in order to remove the PC and dry, leaving a porous electrode for testing purposes.

From this electrode sheet, 6mm diameter electrodes were cut and made up into model 2325 coin cells from the NRC, Canada. The counter electrode used was a 7mm diameter disc of Li. The electrodes were separated with a 17mm glass fibre (Whatman) disc and either LiClO_4 in EC-DMC or LiPF_6 in EC-DMC used as the electrolyte, depending on the voltage ranges being used. The Li electrode, it should be noted, is slightly larger than the test electrode. This is in order to optimise the Li-ion transfer and so ensure that the cell performance is affected only by the test electrode, and not by any rate-limiting factors of the Li electrode.

In order to perform in-situ XRD measurements on our test materials, a series of modified coin cells were produced which would allow the transmission of x-rays through the sample in order to obtain a diffraction pattern of the test material without dismantling the cell. To accomplish this, a 5mm hole was punched in the middle of both coin cell cases and in the centre of the metal spacer. In order to maintain a sealed system, plastic “windows” were then fixed over these holes. At the cathode end a 0.125mm thick piece of Kapton was fixed using “Roscoe” adhesive. At the anode end, stronger PET was used due to the higher pressure

exerted on the window. In this case, “Torr Seal” epoxy was the adhesive. A schematic of the cell is shown below:

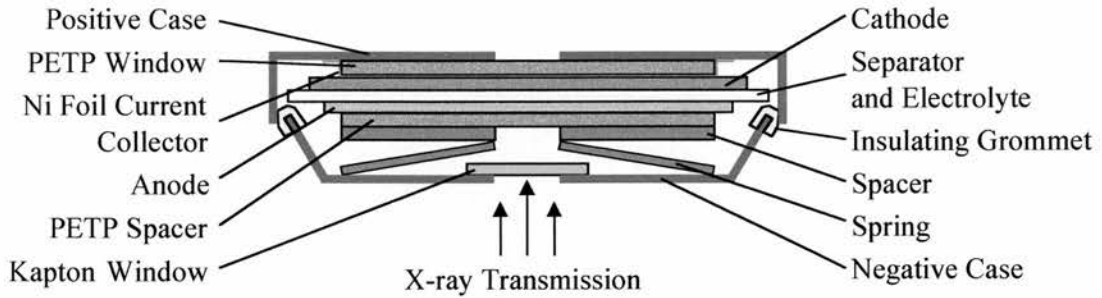


Figure 2-15: Schematic of the transmission mode in situ XRD cell.

Cycling of the test cells was carried out using Maccor™ 2200 and Macpile II™ controllers to regulate voltage and current, and to collect the cycling data. Cycling was carried out in both potentiostatic (constant voltage) and galvanostatic (constant current) modes, with rates of 10mV/hr and 0.05mA used respectively.

References

- ¹ R. Valenzuela. *"Magnetic Ceramics"*. Cambridge Press. (1994), 60.
- ² R.K.B. Gover and J.T.S. Irvine, *J. Solid State Chem*, 141, (1998), 365.
- ³ M. von Laue. *Ann Physik*, 41, (1912), 989.
- ⁴ W.L. Bragg. *Proc Cambridge Phil. Soc.* 17, (1913), 43.
- ⁵ P.W. Atkins. *"Physical Chemistry, 6th Ed."* Oxford University Press.
- ⁶ F. Bloch. *Phys Rev.* 50, (1936), 259.
- ⁷ O. Halpern, M.H. Johnson. *Phys Rev.* 55, (1939), 898.
- ⁸ C.G. Schull, J. S. Smart. *Phys Rev.* 76, (1949), 1256.
- ⁹ H.M, Rietveld, *Acta Cryst.* 21, (1966), A228.
- ¹⁰ H.M, Rietveld. *J. Appl. Crystallogr.* 2, (1969), 65.
- ¹¹ A.C. Larson, R.B. Von Dreele. *Los Alamos National Laboratory, Report.* No LA-UR-86-748, (1987).
- ¹² J. Rodriguez-Carvajal. *15th C.Int.Un.Cryst.* (1990), 127.
- ¹³ A.R. West, *"Solid State Chemistry and its Application"*, John Wiley and Son, Chichester, (1984), 102.
- ¹⁴ Y. Idota, M. Nishima, Y. Miyaki, T. Kubota, T. Miyasaki. *Eur Pat Appl.* 651450 A1 950503, (1995).
- ¹⁵ Y. Idota, T. Kubota, A. Matsufuji, A. Maekawa, T. Miyasaki. *Science*, 276, (1997), 1394.
- ¹⁶ A.S. Gozdz, C.N. Schmutz, J.M. Tarascon, P.C. Warren, *U.S. Patent* 5,552,339, (1996).

**Chapter 3 - Studies on ramsdellite lithium
titanates**

CHAPTER 3 - STUDIES ON RAMSDELLITE LITHIUM TITANATES	81
3.1 INTRODUCTION.....	83
3.2 EXPERIMENTAL.....	84
3.3 NEUTRON POWDER DIFFRACTION STUDIES ON LiTi_2O_4 AND $\text{Li}_{1.1}\text{Ti}_{1.8}\text{O}_4$	87
3.3.1 <i>Introduction</i>	87
3.3.2 <i>Results</i>	87
3.3.3 <i>Discussion</i>	101
3.4 LOW TEMPERATURE STUDIES ON LiTi_2O_4	103
3.4.1 <i>NMR and Magnetic studies</i>	103
3.4.1.1 <i>Introduction</i>	103
3.4.1.2 <i>Results</i>	104
3.4.2 <i>X-ray diffraction studies</i>	110
3.4.2.1 <i>Introduction</i>	110
3.4.2.2 <i>Results</i>	110
3.4.3 <i>Discussion</i>	115
3.5 STUDIES ON DELITHIATED LiTi_2O_4	116
3.5.1 <i>Introduction</i>	116
3.5.2 <i>Experimental</i>	116
3.5.3 <i>Results and Discussion</i>	117
3.6 ELECTROCHEMICAL STUDIES ON RAMSDELLITE LiTi_2O_4 AND TiO_2	123
3.6.1 <i>Introduction</i>	123
3.6.2 <i>Electrochemical cycling results</i>	124
3.6.2.1 <i>Results for LiTi_2O_4</i>	124
3.6.2.2 <i>Results for $\text{TiO}_2(\text{R})$</i>	130
3.6.3 <i>In-situ X-ray diffraction</i>	137
3.6.3.1 <i>Introduction and experimental</i>	137
3.6.3.2 <i>Results</i>	138
3.6.4 <i>Discussion</i>	142
3.7 SUMMARY.....	145

3.1 Introduction

The first reported synthesis of a ramsdellite structured lithium titanate came in 1957, when Jonker ¹ reported the existence of a phase of composition $\text{Li}_2\text{Ti}_3\text{O}_7$, but as no structural data were given full characterisation of the material had to wait until 1964 when Lundberg and Andersson ² confirmed it as having the ramsdellite structure more commonly seen in the Manganese dioxide systems.

Following this report, $\text{Li}_2\text{Ti}_3\text{O}_7$ has been the primary focus of the work performed on the lithium titanate ramsdellites, with neutron and x-ray diffraction studies on the material ^{3,4}, along with conductivity studies ^{5,6,7} suggesting it is a good, highly anisotropic, though not one-dimensional, ionic conductor, the primary conduction route being down the structural channels. Several other ramsdellites have been since reported though, most lying in the LiFeO_2 - SnO_2 - TiO_2 ternary system ^{8,9,10,11,12} though an interesting, reduced solid solution joining $\text{Li}_2\text{Ti}_3\text{O}_7$ with LiTi_2O_4 was recently reported by Gover and Irvine ^{13,14} along with a study of the transition of LiTi_2O_4 from spinel to ramsdellite at high temperature ¹⁵.

With the recent explosion in the mobile electronics market, and the corresponding need for lighter, higher capacity power sources, their relation to the widely used manganese dioxide systems, along with the excellent cycling characteristics of the lithium titanate spinels, has made the titanate ramsdellites obvious candidates for Li-ion battery applications. Accordingly, much of the recent work on the systems has been their electrochemical evaluation, though with the focus again on $\text{Li}_2\text{Ti}_3\text{O}_7$ ^{16,17,18}. This work has all demonstrated that the good capacity and cycling characteristics of the lithium manganates extends to the polymorphic titanates.

It is therefore a little surprising, considering their potential importance as Li-ion battery materials, to find that the mechanism of ionic conduction, and environment of the channel sited lithium in these materials are not very well

understood. It is known that several very similar sites exist within the structural channels, but which of these are occupied is still the subject of some uncertainty, with structural studies on these and similar materials^{3,4,8,13,15} reporting different lithium environments and high thermal displacement parameters.

The focus of this work then, is to expand on the previous results on the $\text{Li}_{1+x}\text{Ti}_{2-2x}\text{O}_4$ system by Gover and Irvine, extending the structural investigations to lower temperatures, expanding on previous NMR and magnetic investigations and evaluating the materials for lithium battery applications.

3.2 Experimental

Samples of the $\text{Li}_{1+x}\text{Ti}_{2-2x}\text{O}_4$ series were synthesised according to the methods described in chapter 2. Additionally, a sample of LiTi_2O_4 was delithiated by the action of weak $\text{HCl}_{(\text{aq})}$ according to the method of Akimoto *et al*¹⁹. A sample of this delithiated LiTi_2O_4 was also relithiated using n-butyl lithium as a lithiating agent. Phase identification and purity was established using two diffractometers: a Philips PW3810 reflection mode machine using $\text{CuK}\alpha$ radiation and a high resolution Stöe StadiP diffractometer using monochromated $\text{CuK}\alpha_1$ radiation. Low temperature XRD data were collected using a Bruker D8 diffractometer, courtesy of Dr. John Evans at Durham University.

Indexing of patterns was carried out initially using the LATREF routine and later using the proprietary Stöe Winxpow software. Rietveld refinements of the data were carried out using GSAS^a.

Two x-ray diffractometers were used to establish phase purity because whilst the Stöe offers higher resolution, Ti in these samples was found to fluoresce slightly in the $\text{CuK}\alpha$ radiation, making accurate detection of any second phases difficult. The Philips diffractometer in contrast, offered lower resolution, but is fitted with

^a A.C Larsen and B. von Dreele, Los Alamos Laboratory.

a detector end monochromator, which filters any fluorescence and leaves a very flat background to the data. This proved to be important for this series of samples, as with ramsdellite being a high temperature form of LiTi_2O_4 it is common to find that traces of the lower temperature spinel polymorph have formed during the cooling phase of the sample preparation:

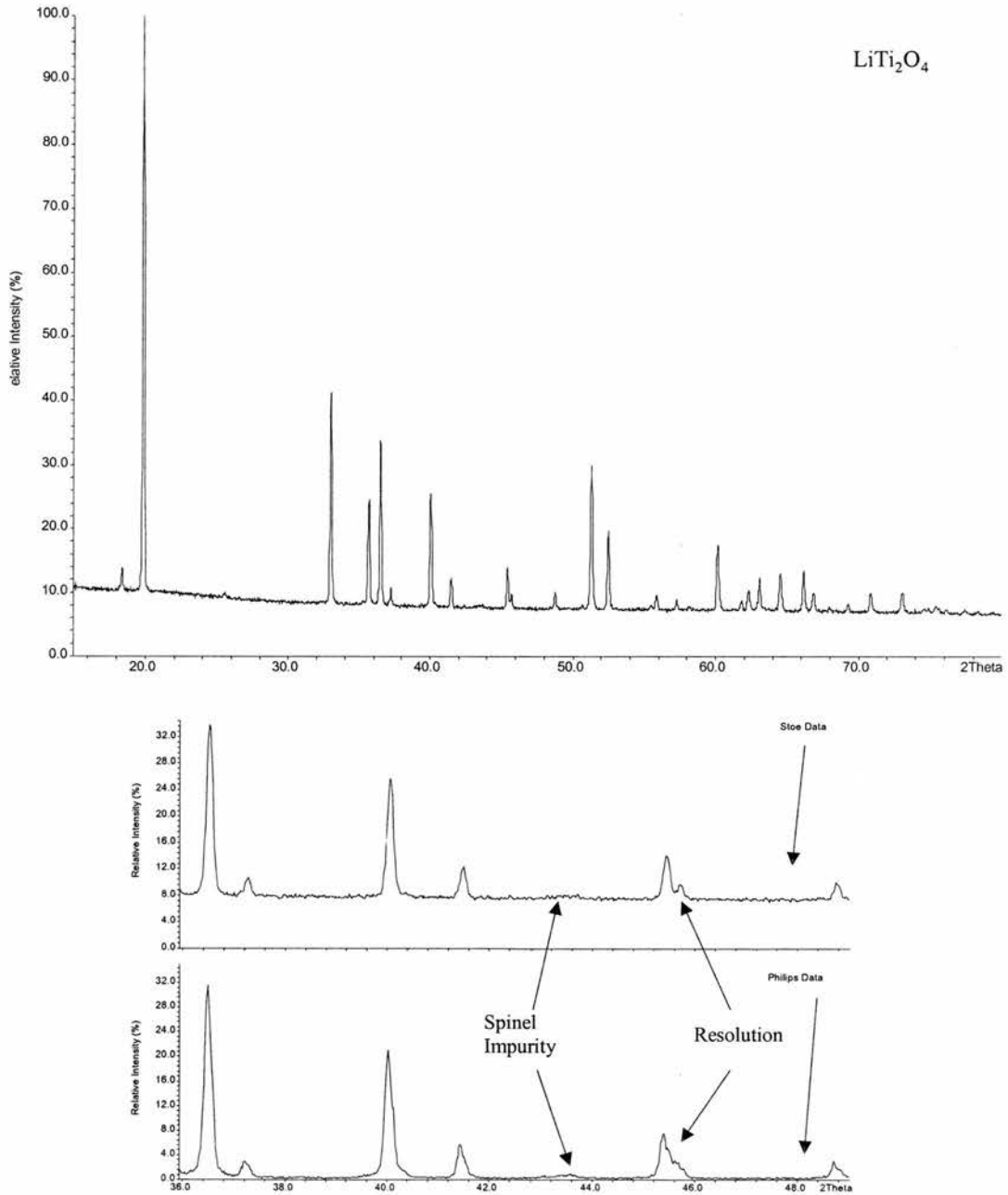


Figure 3-1: A typical XRD of LiTi_2O_4 ramsdellite (above) and the resolution of the Stoe and Philips diffractometers (below).

High resolution, high temperature neutron diffraction data presented here were collected at the IPNS facility, Argonne National laboratories, Chicago. For multi-temperature high resolution studies on LiTi_2O_4 and $\text{Li}_{1.1}\text{Ti}_{1.8}\text{O}_4$, the General Purpose Powder Diffractometer (GPPD) instrument was used, the sample being heated in-situ using a vanadium walled furnace. Data on the delithiated LiTi_2O_4 sample were collected using the SEPD instrument. As with the x-ray data, Rietveld refinement was carried out using the GSAS^a refinement software.

Solid state ^7Li Magic Angle Spinning NMR data on LiTi_2O_4 were collected between 170K and 340K by Shannon Brown and Dr. David Tunstall using a Bruker MSL-500MHz NMR Spectrometer. A Bruker MAS probe was used, with spinning rates in the 6kHz range.

Thermal Analysis of the delithiated LiTi_2O_4 sample was performed under a variety of flowing gases using a TA Instruments 2960 simultaneous DTA/TGA, whilst Li battery electrochemical testing and in-situ XRD of the materials was carried out using the Li cycling equipment described in chapter two.

^a A.C Larsen and B. von Dreele, Los Alamos Laboratory.

3.3 Neutron Powder Diffraction Studies on LiTi_2O_4 and $\text{Li}_{1.1}\text{Ti}_{1.8}\text{O}_4$

3.3.1 Introduction

In previous work by Gover¹⁵ investigating the transition of LiTi_2O_4 from spinel to ramsdellite, it was found that the channel sited lithium exhibited surprisingly high thermal displacement parameters, an observation that is echoed in the data published on other lithium ramsdellites, as mentioned earlier. Unfortunately, in all these studies the focus of investigation has been upon structure determination, with the data not being collected with close investigation of a mobile atom in mind. For a better investigation of the channel environment, much higher quality data is required.

To this end, neutron diffraction data on two samples, LiTi_2O_4 and $\text{Li}_{1.1}\text{Ti}_{1.8}\text{O}_4$, were collected for 13 hours at each of four temperatures; 25°C, 75°C, 150°C and 300°C. The experiments were carried out in an in-situ environment, using a vanadium walled furnace, with the samples being allowed 25 minutes to equilibrate at each temperature. The diffraction data obtained were analysed using the GSAS^a software to give a full Rietveld refinement of the data, including in particular, anisotropic temperature factors for all atoms, as analysis of the lithium thermal motion could give an indication of extra structural sites and possible paths of conduction.

3.3.2 Results

The data were refined using the Akimoto²⁰ model of LiTi_2O_4 with one channel lithium site positioned at $x=-0.057$, $y=0.473$, $z=0.25$, first to give unit cell edges

^a A.C Larsen and B. von Dreele, Los Alamos Laboratory.

and isotropic thermal displacement information. Then, the site occupancies were refined to check for any non-stoichiometry, and the thermal displacement factors for each site were in turn refined anisotropically, before being allowed to all refine together.

The as-refined unit cell edges, atomic positions, occupancies and isotropic thermal parameters were found to be in good agreement with previous work (see appendix 1 for tabulated data). Our results are presented graphically below, along with sample refined diffraction patterns:

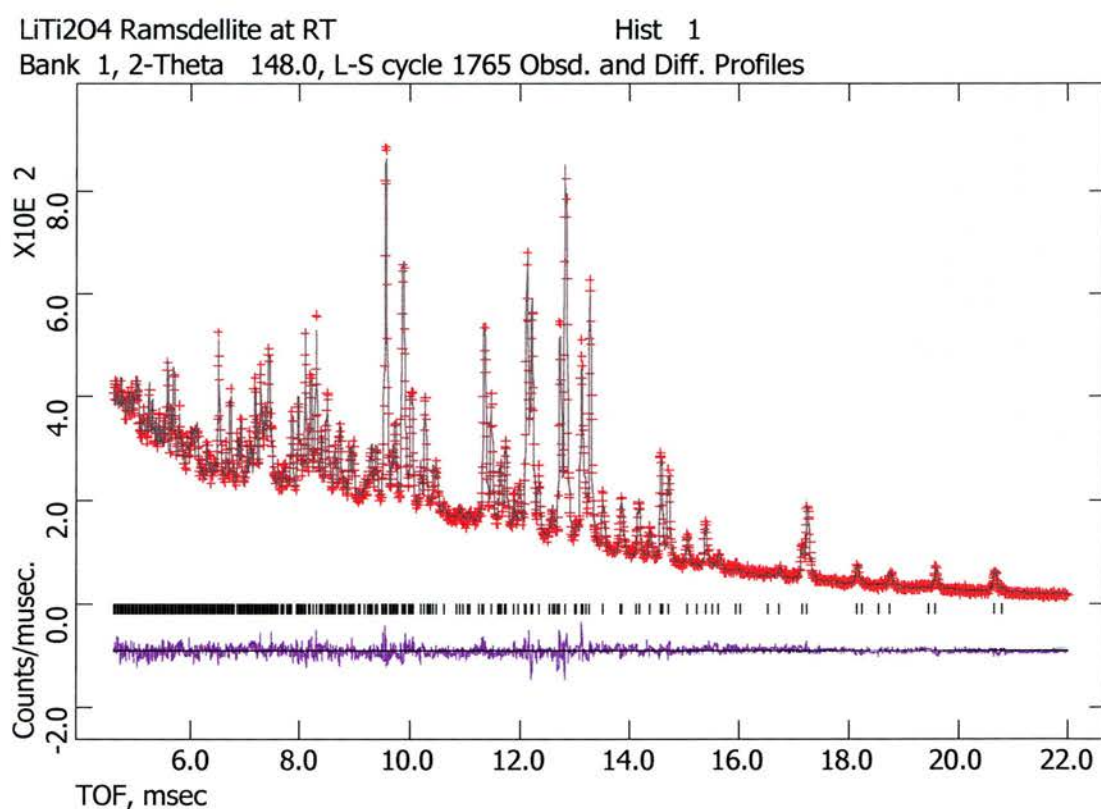


Figure 3-2: As refined neutron diffraction data for LiTi₂O₄ at 25°C

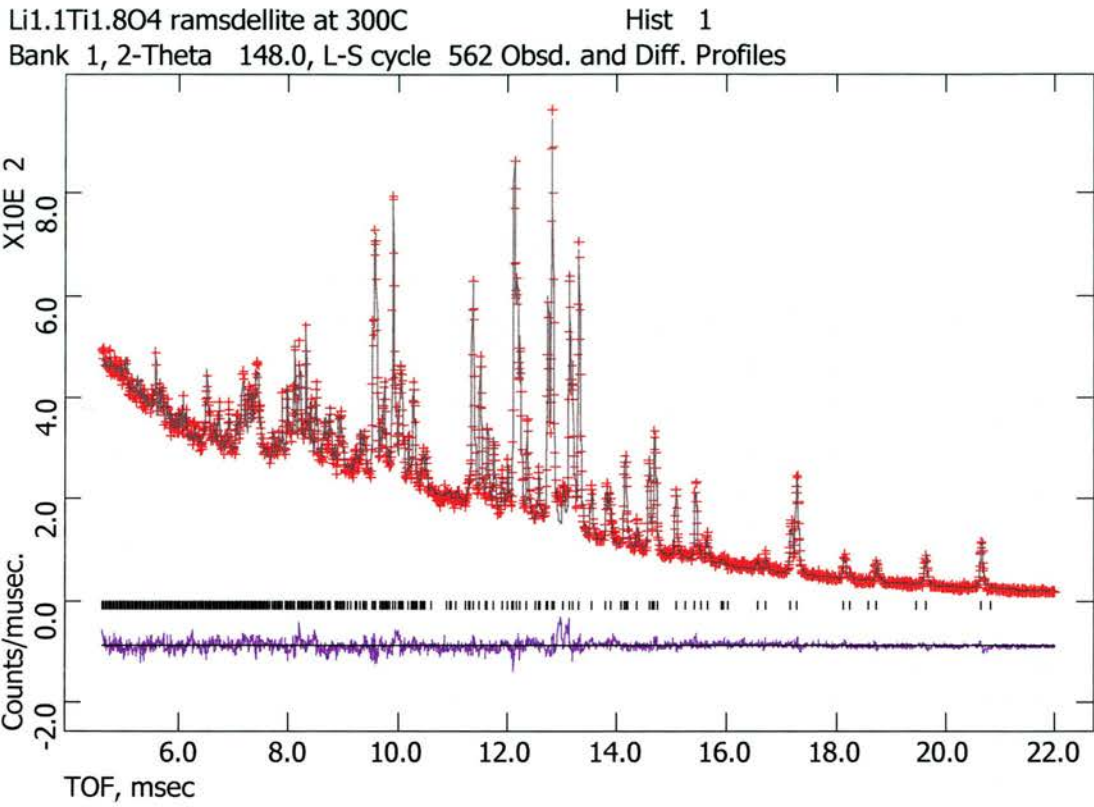


Figure 3-3: As refined neutron diffraction data for Li_{1.1}Ti_{1.8}O₄ at 300°C

Graph of unit cell "a" vs Temperature for LiTi₂O₄ and Li_{1.1}Ti_{1.8}O₄

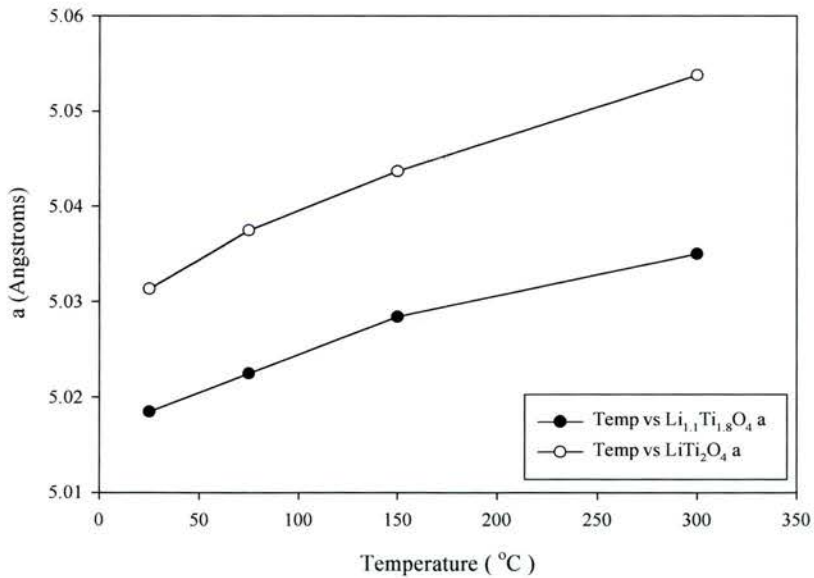
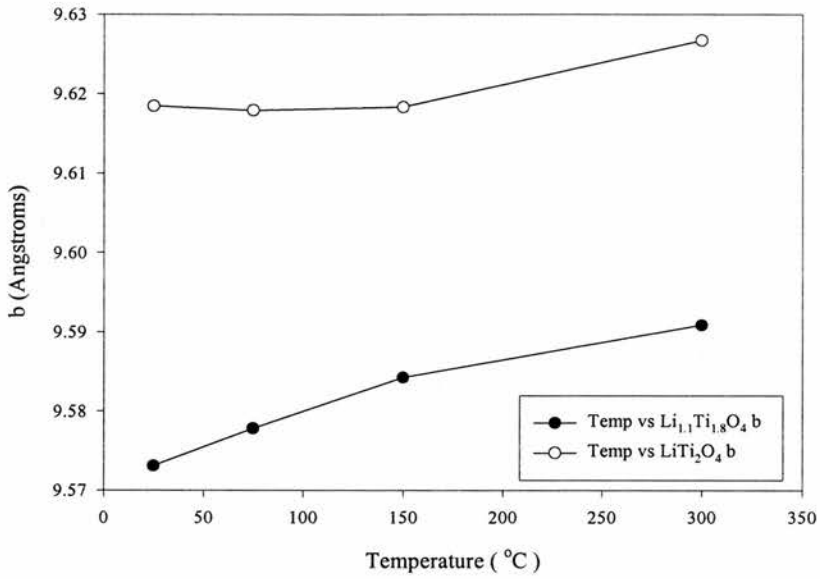
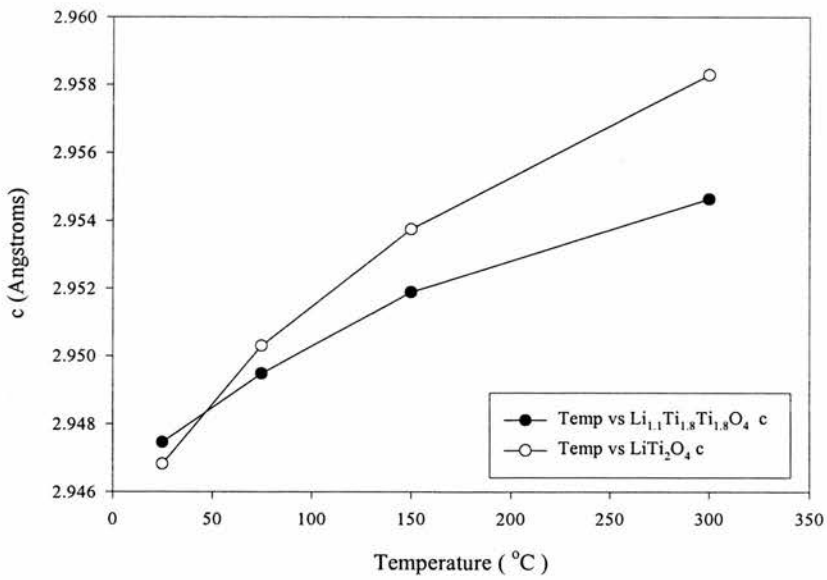


Figure 3-4 Variation in temperature for the unit cell "a" for LiTi₂O₄ and Li_{1.1}Ti_{1.8}O₄

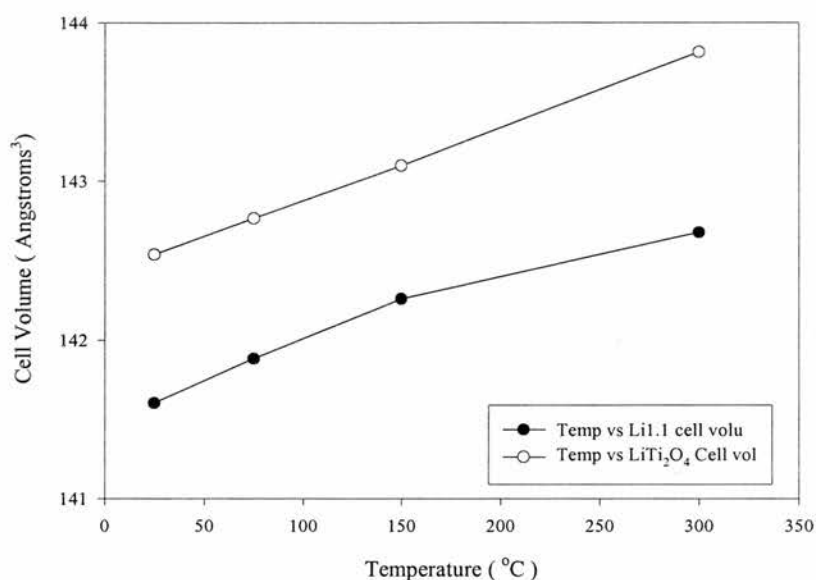
Graph of Unit cell "b" vs Temperature for LiTi_2O_4 and $\text{Li}_{1.1}\text{Ti}_{1.8}\text{O}_4$ Figure 3-5 Variation in temperature for the unit cell "b" for LiTi_2O_4 and $\text{Li}_{1.1}\text{Ti}_{1.8}\text{O}_4$ Graph of Unit cell "c" vs Temperature for LiTi_2O_4 and $\text{Li}_{1.1}\text{Ti}_{1.8}\text{O}_4$ Figure 3-6 Variation in temperature for the unit cell "c" for LiTi_2O_4 and $\text{Li}_{1.1}\text{Ti}_{1.8}\text{O}_4$

Temp (°C)	LiTi ₂ O ₄			Li _{1.1} Ti _{1.8} O ₄		
	Rwp(%)	Rp(%)	Chi ²	Rwp(%)	Rp(%)	Chi ²
25	4.87	3.46	1.826	4.4	3.11	1.718
75	4.87	3.45	1.454	4.39	3.07	1.759
150	4.91	3.48	1.478	4.19	2.93	1.582
300	5.14	3.73	1.539	4.55	3.1	1.832

Table 3-1: Quality of Fit data for LiTi₂O₄ and Li_{1.1}Ti_{1.8}O₄

Beginning with the refined unit cell parameters we can see that for both samples the a, b and c axes increase in a manner expected with increasing temperature, though with a small fall-off from linearity as the temperature increases. That the Li_{1.1}Ti_{1.8}O₄ sample shows consistently smaller unit cell axes than LiTi₂O₄, is to be expected as the 1/10th of the structural framework Titanium has been replaced by a smaller lithium ion in this sample, and the channel sites are also lower occupied due to the lower cation stoichiometry.

The LiTi₂O₄ sample exhibits somewhat more interesting behaviour in that the b parameter doesn't show the expected temperature dependence, but remains reasonably constant between 25°C and 150°C. Indeed there is a small contraction along b between 25°C and 75°C. The c parameter also appears to show greater sensitivity to temperature in LiTi₂O₄, expanding considerably faster than in Li_{1.1}Ti_{1.8}O₄ (between 25°C and 300°C thermal expansion coefficients for LiTi₂O₄ and Li_{1.1}Ti_{1.8}O₄ are $1.419 \times 10^{-5} \text{ K}^{-1}$ and $8.932 \times 10^{-6} \text{ K}^{-1}$ respectively.). Surprisingly, these observed variations in unit cell edge don't appear to affect the unit cell volume, which increases linearly with temperature for both samples. This is an indication that the cell is in some way constrained, with contraction in one direction forcing expansion in another, as might be expected from a hinged structure.

Graph of Unit cell volume vs Temperature for LiTi_2O_4 and $\text{Li}_{1.1}\text{Ti}_{1.8}\text{O}_4$ **Figure 3-7: The temperature dependence of the Unit cell volume for LiTi_2O_4 and $\text{Li}_{1.1}\text{Ti}_{1.8}\text{O}_4$**

Examination of the atomic positions in LiTi_2O_4 (Appendix 1) shows no obvious movement of any atoms off-site to account for this, and no cation deficiencies were detected for the framework Ti and O positions. Thermal parameters for these sites also appear to behave in an expected manner, increasing reasonably with temperature. This is mirrored by the $\text{Li}_{1.1}\text{Ti}_{1.8}\text{O}_4$ sample.

In contrast, the isotropic thermal parameters for the channel sited Li are exceptionally high for both samples, a result reported previously for similar samples. However, unlike in previous reports, we were able to obtain good stable refinements for the anisotropic motion of the channel lithium. A 3D representation of the temperature dependence of the anisotropic temperature factors is given below (again, tabulated data is given in Appendix1):

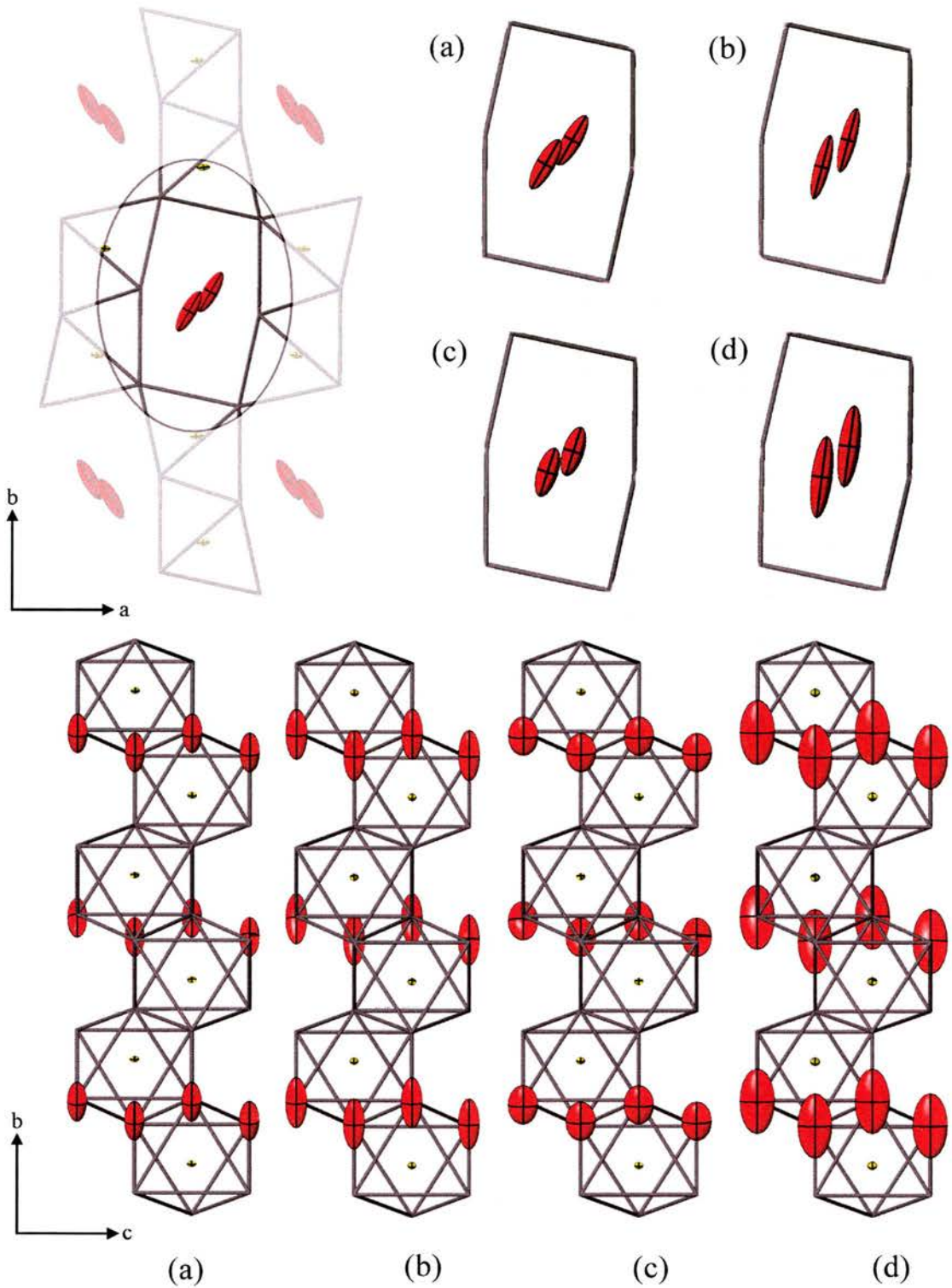


Figure 3-7: Anisotropic temperature factors for LiTi_2O_4 plotted as thermal ellipsoids for the x-y plane (top) and the x-z plane. Four temperatures are shown: 25°C, 75°C, 150°C, and 300°C. These correspond to (a), (b), (c) and (d) respectively. Ellipsoids are presented showing the 50% contour.

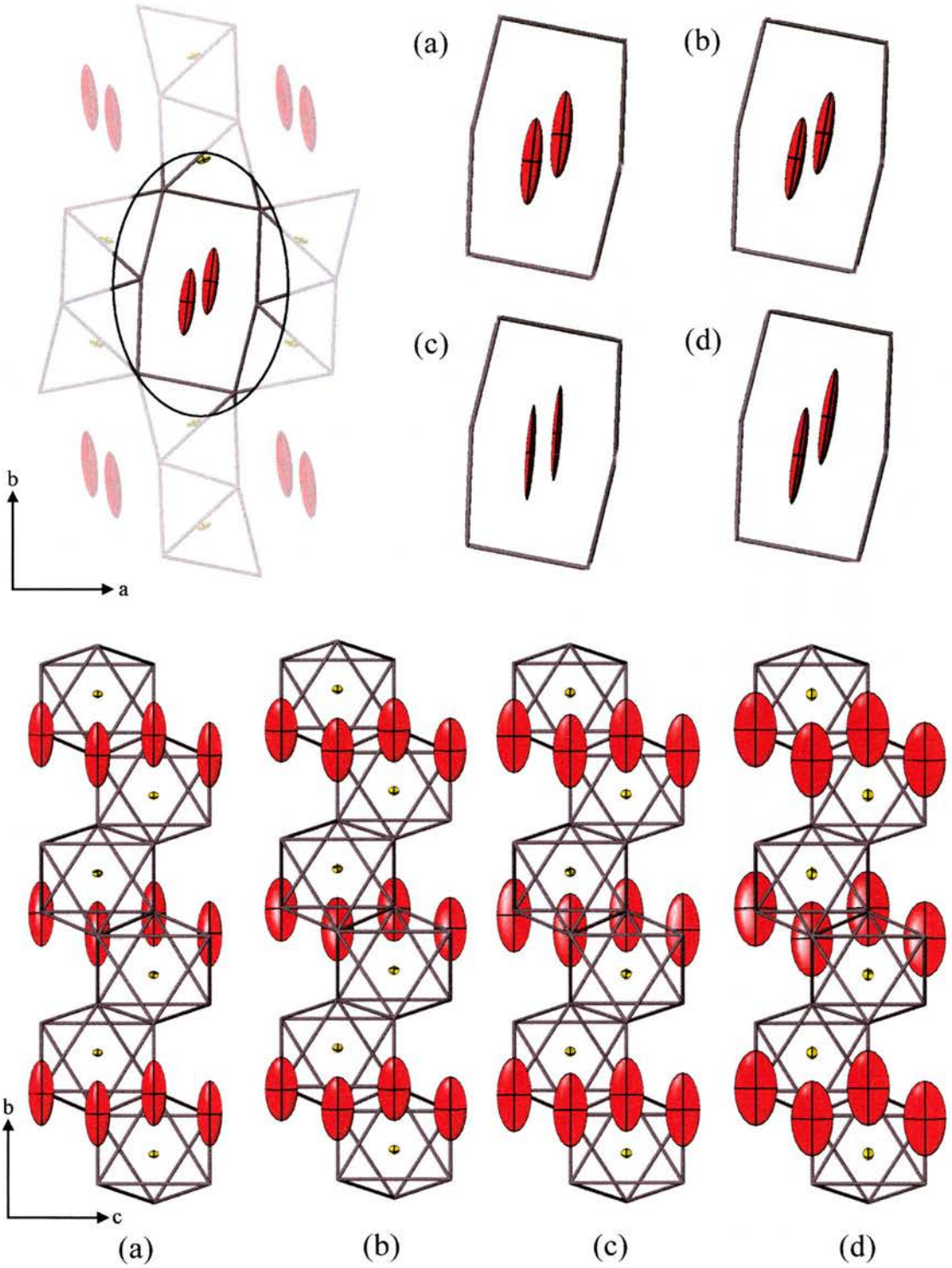


Figure 3-8: Anisotropic temperature factors for $\text{Li}_{1.1}\text{Ti}_{1.8}\text{O}_4$ plotted as thermal ellipsoids for the b-a plane (top) and the b-c plane. Four temperatures are shown: 25°C, 75°C, 150°C, and 300°C. These correspond to (a), (b), (c) and (d) respectively. Ellipsoids are presented showing the 50% contour.

Examination of these plots shows that the samples are obviously very similar, but at the same time quite different. For both samples the thermal motion of channel lithium is very high in comparison to the oxygen and titanium framework cations, with the $\text{Li}_{1.1}\text{Ti}_{1.8}\text{O}_4$ sample showing consistently greater thermal motion both across and along the channels than LiTi_2O_4 . The plotted temperature factors obviously also indicate a preferential mode of vibration in the b-a plane for both samples, with the thermal ellipsoids pointing primarily in the b-direction. For $\text{Li}_{1.1}\text{Ti}_{1.8}\text{O}_4$, there appears to be a fairly consistent temperature dependence to the motion also, with motion both along and across the channels increasing visibly with increasing temperature. The LiTi_2O_4 sample, however, shows a markedly different behaviour than $\text{Li}_{1.1}\text{Ti}_{1.8}\text{O}_4$, particularly in the 25°C to 150°C temperature range. Between 25°C and 75°C it can be seen that the thermal ellipsoids for LiTi_2O_4 “rotate” to point much more along the b direction, and between 75°C and 150°C they then appear to shrink in the b-a plane whilst continuing to expand along c. Interestingly, this rotation moves the direction of thermal motion through a possible path of conduction between the channels via the passage of a lithium through an empty tetrahedral site between the channels. This would involve passing through two faces of the tetrahedron, but with the distance from the corner oxygen’s to the tetrahedron face centre about 1.6Å this is far from impossible.

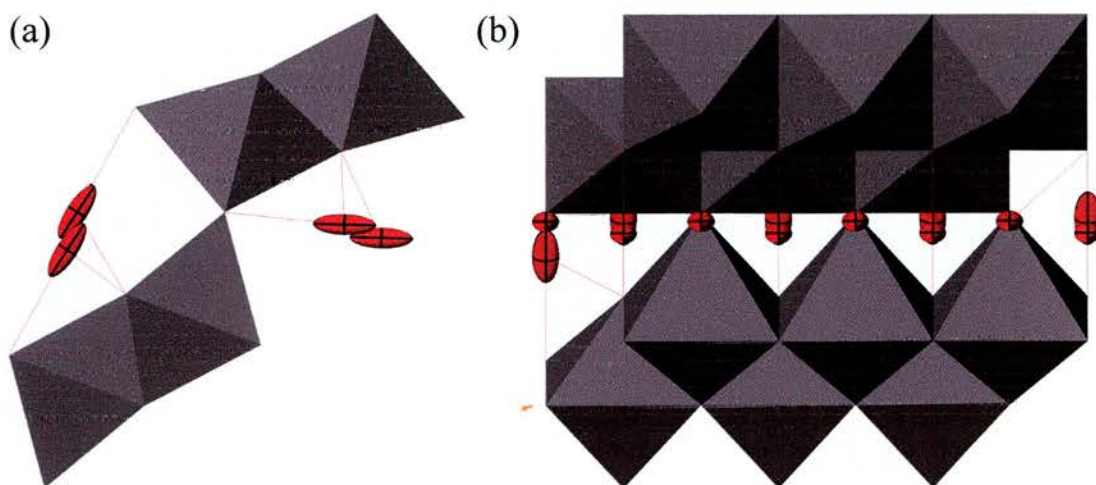


Figure 3-10: Thermal motion of channel lithium in LiTi_2O_4 at 25°C, showing possible conduction route between the channels

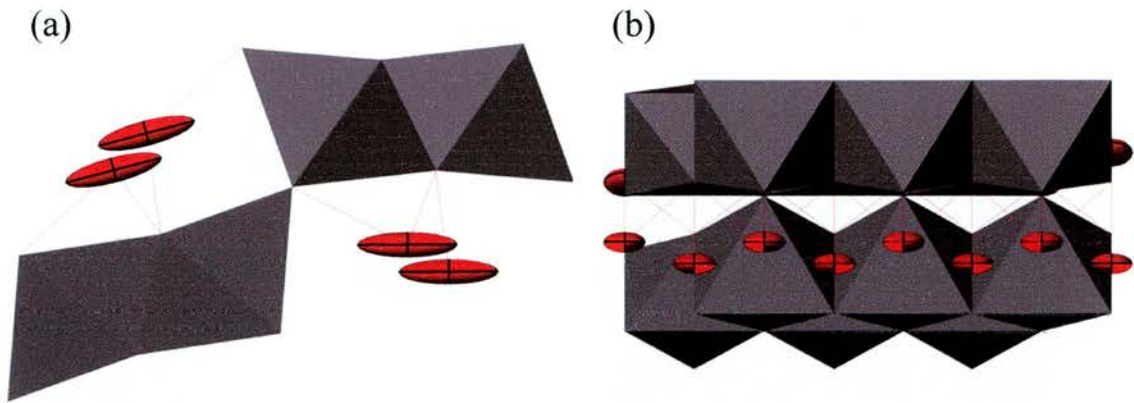
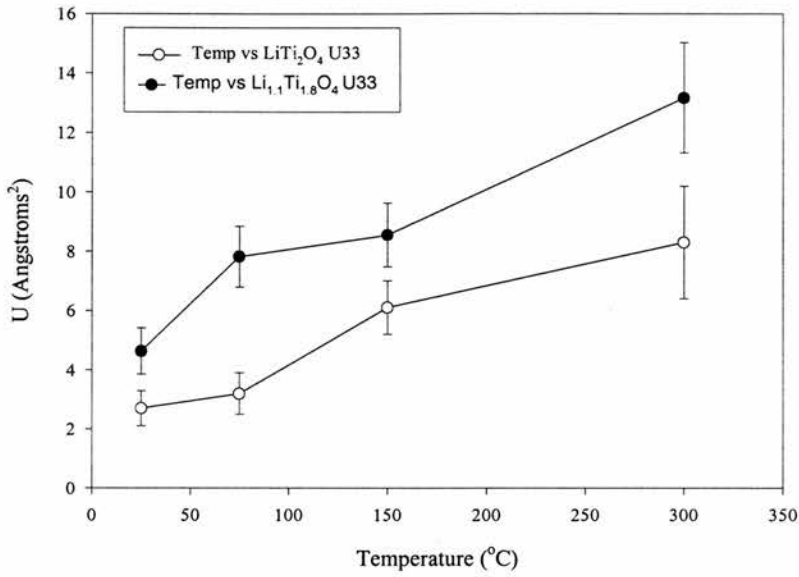
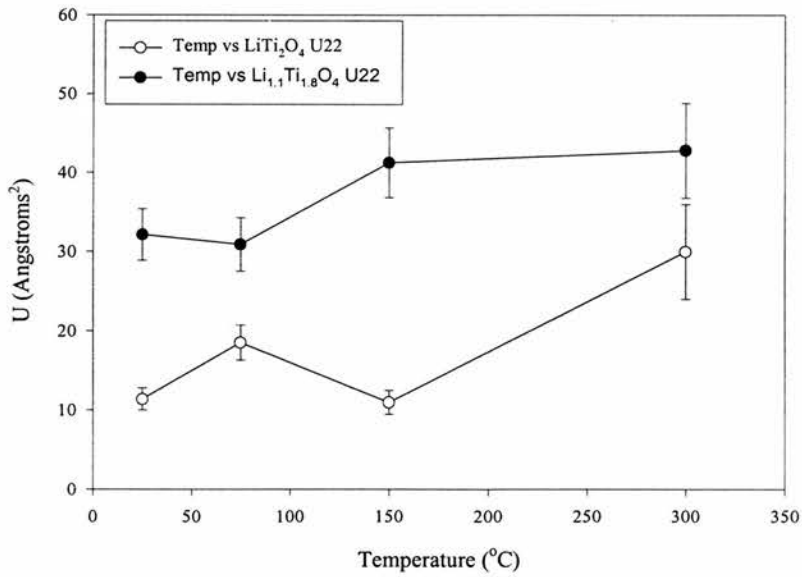


Figure 3-11: Thermal motion of channel lithium in LiTi_2O_4 at 300°C , showing how the ellipsoids have moved through the possible conduction route between the channels

Plotting the individual thermal parameters graphically confirms these observations: U_{33} , which is the measurement of motion along the c -direction, increases steadily for both samples, whilst the plots of U_{22} and U_{12} , which determine the degree of “rotation” and the magnitude of the ellipsoid in the b - a plane, show a minimum at 150°C for LiTi_2O_4 .

Graph of U33 vs Temperature for LiTi_2O_4 and $\text{Li}_{1.1}\text{Ti}_{1.8}\text{O}_4$ Figure 3-12: Variation of U33 with temperature for LiTi_2O_4 and $\text{Li}_{1.1}\text{Ti}_{1.8}\text{O}_4$ Graph of U22 vs Temperature for LiTi_2O_4 and $\text{Li}_{1.1}\text{Ti}_{1.8}\text{O}_4$ Figure 3-13: Variation of U22 with temperature for LiTi_2O_4 and $\text{Li}_{1.1}\text{Ti}_{1.8}\text{O}_4$

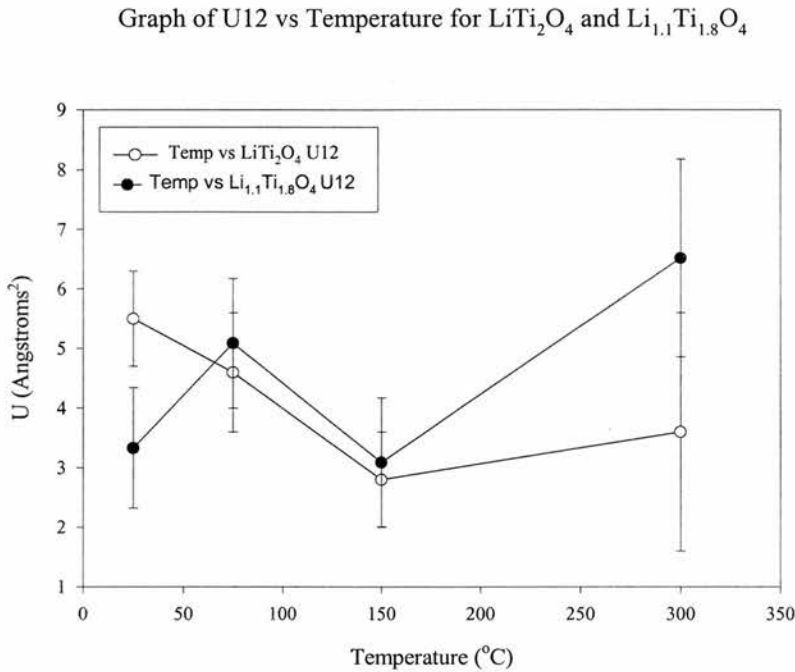


Figure 3-14: Variation of U12 with temperature for LiTi_2O_4 and $\text{Li}_{1.1}\text{Ti}_{1.8}\text{O}_4$

As these results clearly demonstrate that the channel-sited lithium is exceptionally mobile, and as such high thermal parameters are usually an indication of disorder, or a sign that the structural model is not correctly describing the atomic site in question, we went on to test the structural models proposed in the literature for similar materials. A brief synopsis of these is given below, along with a pictorial representation for clarity.

1. Akimoto²⁰, Gover and Irvine¹³: Lithium situated on one 4c channel site (as shown above) at $x=-0.058$, $y=0.467$, $z=0.25$.

2. Morosin and Mikkelson³: Lithium distributed across two 4c channel sites at $x=-0.060$, $y=0.451$, $z=0.25$ and $x=0.532$, $y=0.050$, $z=0.25$.

3. Abrahams and Bruce *et al.*⁴: Effectively the Morosin and Mikkelson model given above, but with the first 4c site split into an 8c site of coordinates $x=-0.058$, $y=0.445$, $z=0.181$.

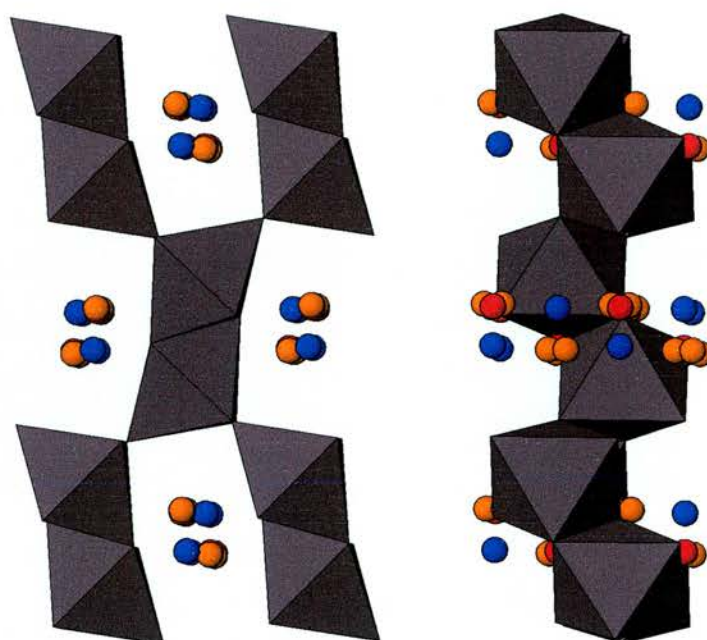


Figure 3-15: The Ramsdellite structure, showing the reported channel lithium sites. Models 1, 2 and 3 are respectively: Red, Red and Blue, Orange and Blue.

For reasons of stability, and to ensure consistent comparison, refinements using these models were carried out with the temperature factors all set to be isotropic.

The calculated fit parameters for each model are given below:

Temp (°C)	Model 1		Model 2		Model 3	
	Rwp	Chi ²	Rwp	Chi ²	Rwp	Chi ²
25	5.12	2.01	5.06	1.964	Unrefineable	Unrefineable
75	5.16	1.63	5.09	1.587	Unrefineable	Unrefineable
150	5.24	1.66	5.17	1.64	Unrefineable	Unrefineable
300	5.63	1.837	5.55	1.785	Unrefineable	Unrefineable

Table 3-2: Fit parameters for different lithium distribution models in LiTi₂O₄

Temp (°C)	Model 1		Model 2		Model 3	
	Rwp	Chi ²	Rwp	Chi ²	Rwp	Chi ²
25	4.74	1.99	4.61	1.878	Unrefineable	Unrefineable
75	4.72	2.032	4.62	1.947	4.6	1.93
150	4.6	1.904	4.48	1.81	4.46	1.79
300	5.04	2.238	4.92	2.14	4.89	2.114

Table 3-3: Fit parameters for different lithium distribution models in Li_{1.1}Ti_{1.8}O₄

As before, we can see similar and yet differing behaviour for the two samples. There is a definite improvement in both Rwp and Chi² for both samples when an extra site is introduced into the refinement, suggesting that the high temperature factors might indeed be due to some lithium disorder. This is reinforced by the fact that, whilst still high, the lithium thermal parameters are considerably lowered on the split sites (see Table 3-4). Additionally, a plot of the as-refined Morosin and Mikkelson model for LiTi₂O₄ shows that the second site added to our refinements moves considerably with temperature, effectively following the rotation of the ellipsoids calculated for the single site model. However, in both models 2 and 3 the Li sites within the b-a plane are very close together at 0.98Å for the Li(1)-Li(2) sites, with the intersite distances for the split 8c site in the Abrahams and Bruce *et al* model being 0.28Å.

Temp (°C)	Model 1	Model 2	
	Li(1) Uiso x100 (Å ³)	Li(1) Uiso x100 (Å ³)	Li(2) Uiso x100 (Å ³)
25	8.31(42)	2.57(32)	4.91(50)
75	9.44(47)	3.59(40)	5.54(55)
150	10.67(54)	4.75(48)	4.78(49)
300	12.89(80)	6.47(69)	4.24(52)

Table 3-4: As refined isotropic temperature factors for Li_{1.1}Ti_{1.8}O₄

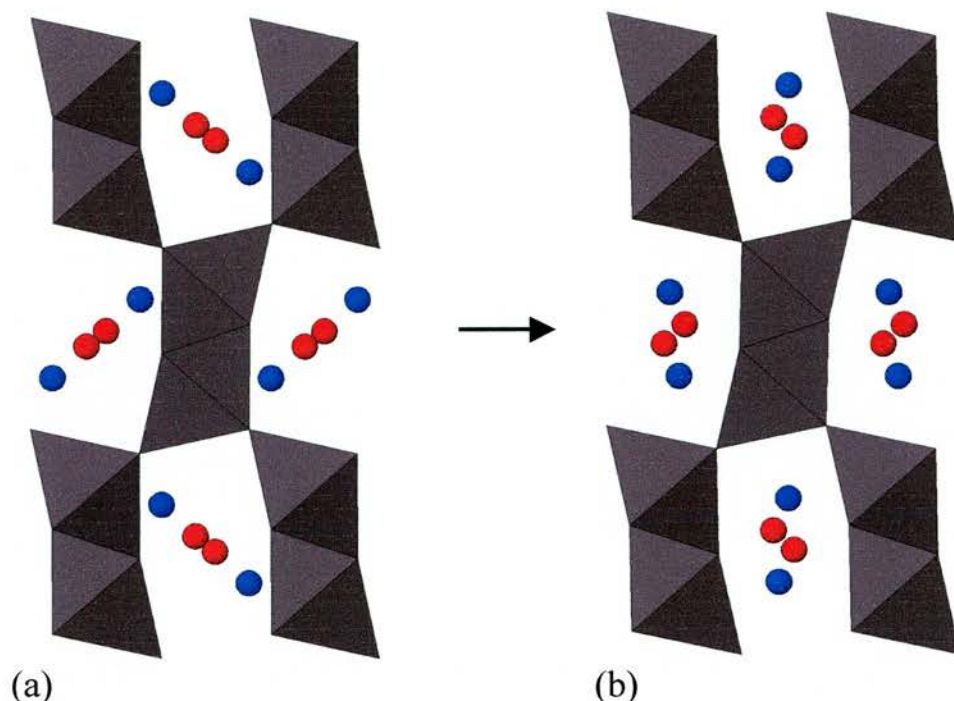


Figure 3-16: Refined atom positions for LiTi_2O_4 using the Morosin and Mikkelson model. Note the movement of the second site (blue) between 25°C (a) and 300°C (b).

3.3.3 Discussion

Drawing these results together, several observations can be made. The first and foremost is that the channel lithium in these systems is highly mobile (with $\text{Li}_{1.1}\text{Ti}_{1.8}\text{O}_4$ the more so), a result in accordance with the previous structural studies on these systems, and with the conductivity studies on $\text{Li}_2\text{Ti}_3\text{O}_7$. However, the preferred direction of motion is not along the channels, as might be expected from the conductivity studies, but across the channels, though with motion along the channels still relatively high. The direction of this thermal motion across the channels “points” in a general sense towards a conductivity path between the channels, though the movement of the LiTi_2O_4 thermal ellipsoids away from this route suggests that it is not an energetically easy conduction route, despite the relatively large tetrahedral faces through which the conduction would occur. In this respect, our thermal displacement results correlate well with the conductivity data of Boyce and Mikkelson⁷, who reported the anisotropic conductivity of $\text{Li}_2\text{Ti}_3\text{O}_7$ as being of the ratios $\sigma_c/\sigma_b=7$ and

$\sigma_b/\sigma_a=4$. We are also able to suggest that the cross channel conduction does not occur via the structural octahedra, as they suggested, but possibly via unoccupied tetrahedra lying at the channel corners.

Whilst the thermal parameters for the refinements are constrained to be isotropic, we can see that using two sites to describe the lithium rather than one yields a slight improvement in R-factors, coupled with a reduction in the thermal parameters for each site. However, comparison of the results of the two site model with those from the anisotropically calculated one site model shows that the additional second site simply lies within the volume of the thermal ellipsoid calculated for one site only, suggesting that they are simply two ways of describing the same phenomenon: A combination of static disorder across sites and dynamic disorder from the high mobility of lithium between these sites. As the R-factors for the anisotropically refined single site model are significantly better, this seems the statistically better description.

Of the two samples, LiTi_2O_4 is clearly the more interesting, as rather than the anisotropic thermal factors increasing steadily with temperature as those of $\text{Li}_{1.1}\text{Ti}_{1.8}\text{O}_4$ do, in both the one and two site models the direction of lithium disorder “rotates” within the channel with increasing temperature to assume a similar mode of motion as $\text{Li}_{1.1}\text{Ti}_{1.8}\text{O}_4$ shows for all temperatures. From this it could be implied that $\text{Li}_{1.1}\text{Ti}_{1.8}\text{O}_4$ demonstrates the “natural” motion for the system and that LiTi_2O_4 is in some way frustrated. That this rotating of the motion is coupled with a lack of thermal expansion along the b axis, is also surprising as it would be expected that the increase in motion in the b direction would be coupled with an anomalous increase in the b-axis, not an anomalous lack of expansion. Indeed, from the thermal displacement data an anomalous contraction along the a axis would seem more likely.

3.4 Low Temperature studies on LiTi_2O_4

3.4.1 NMR and Magnetic studies

3.4.1.1 Introduction

In the course of their solid state Li NMR investigations into the spinel to ramsdellite transition of LiTi_2O_4 , Kartha *et al*²¹ found that while LiTi_2O_4 spinel shows a chemical (Knight) shift characteristic of an insulating oxide, on transformation to ramsdellite the lithium spectra changed from a sharp resonance at -2.1 ppm to a broad, fast relaxing peak at -1.1 ppm. Comparing this chemical shift with that of $\text{Li}_2\text{Ti}_3\text{O}_7$ (~0.3 ppm) and with the data of Gover, who reported LiTi_2O_4 ramsdellite as non-metallic, the authors concluded that the large shift of -1.1 ppm in ramsdellite LiTi_2O_4 was probably due to the proximity of the lithium to a magnetic moment, presumably located on the framework titanium. They were, however, unable to characterise this further.

In this work, then, we extend the investigation of Kartha *et al*, collecting ^7Li NMR and SQUID data of a sample of LiTi_2O_4 ramsdellite over a broad range of temperatures in an effort to understand further the nature of the large chemical shift of lithium in the material.

For this, a sample of LiTi_2O_4 was synthesised according to the method described in chapter 2, but using carbon as a wrapping material, not copper. The reason for this was simply to allow a higher synthesis temperature to be used. At synthesis temperatures above 1000°C, copper was found to degrade appreciably, and in an effort to minimise the formation of spinel in the sample we wanted to synthesise the material at a slightly higher temperature of 1020°C. The minimisation of spinel formation was largely successful, with only a small trace being evident on XRD and NMR. However, in an attempt to remove the spinel phase entirely, we chose to further anneal the sample using a vertical quench furnace. This was done because it was felt that the residual spinel in the sample was being formed on the cooling phase of preparation, and whilst the sample was not quenched, the

lower thermal mass and poorer insulation of the quench furnace means that it cools much more quickly than our horizontal tube furnaces. The sample we produced in this way was found to be completely free of any detectable spinel phase.

To collect the NMR data, a Bruker MSL 500 solid state NMR spectrometer equipped with a DOTY Magic Angle Spinning probe was used. Spin rates in the 6kHz region were employed, with dry N₂ being used to spin the sample. The SQUID data were collected courtesy of Prof. Andrew Harrison at the University of Edinburgh. Both of these sets of data were collected and analysed for us by Shannon Brown.

3.4.1.2 Results

Below is presented a selection of fitted NMR spectra, along with an analysis of peak positions, areas and FWHM's.

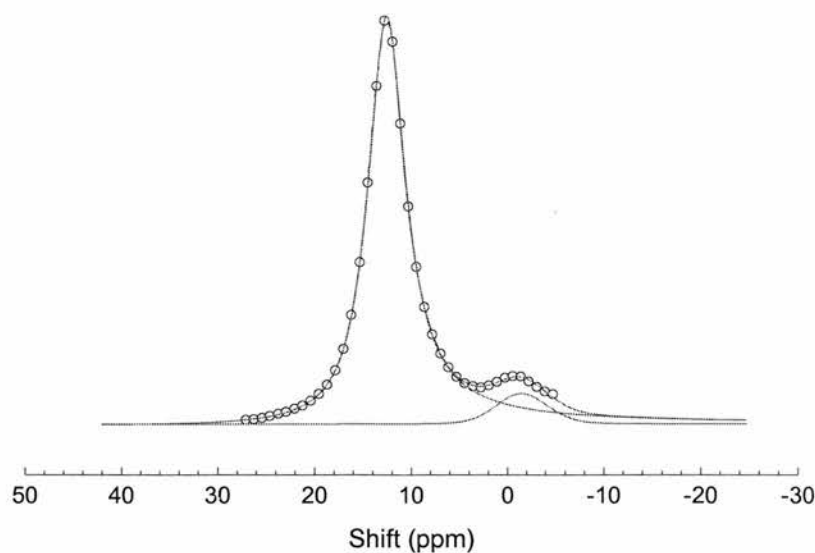


Figure 3-17: Fitted spectrum taken at 290K

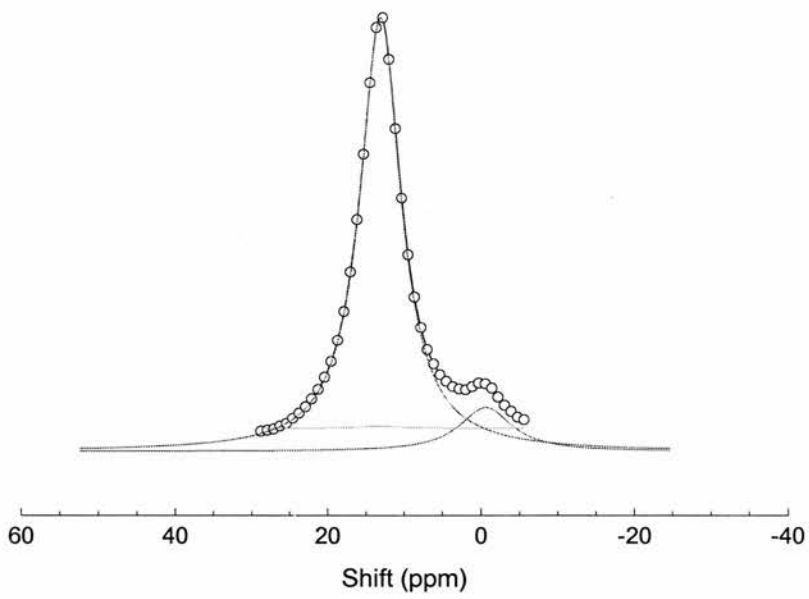


Figure 3-18: Fitted spectrum taken at 250K

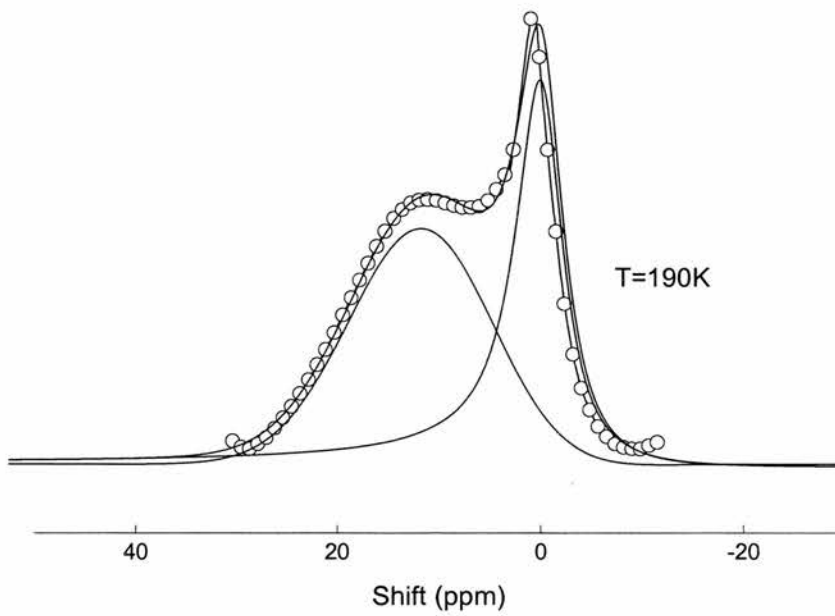


Figure 3-19: Fitted spectrum taken at 190K

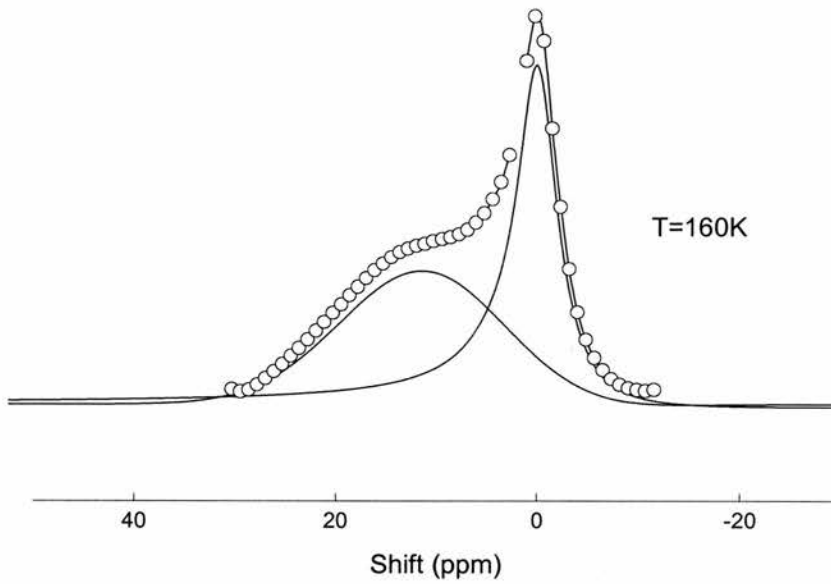


Figure 3-20: Fitted spectrum taken at 160K

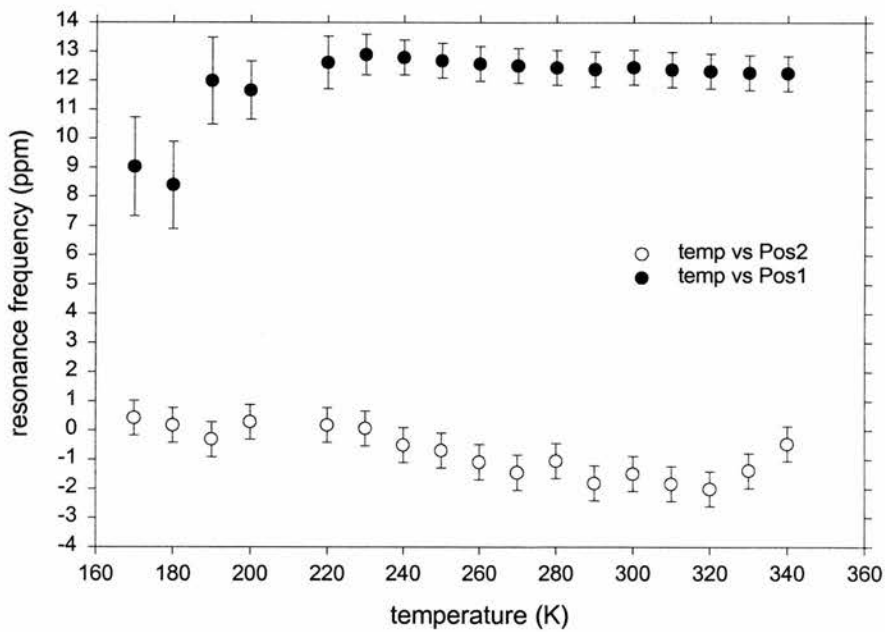


Figure 3-21: Peak positions as a function of temperature.

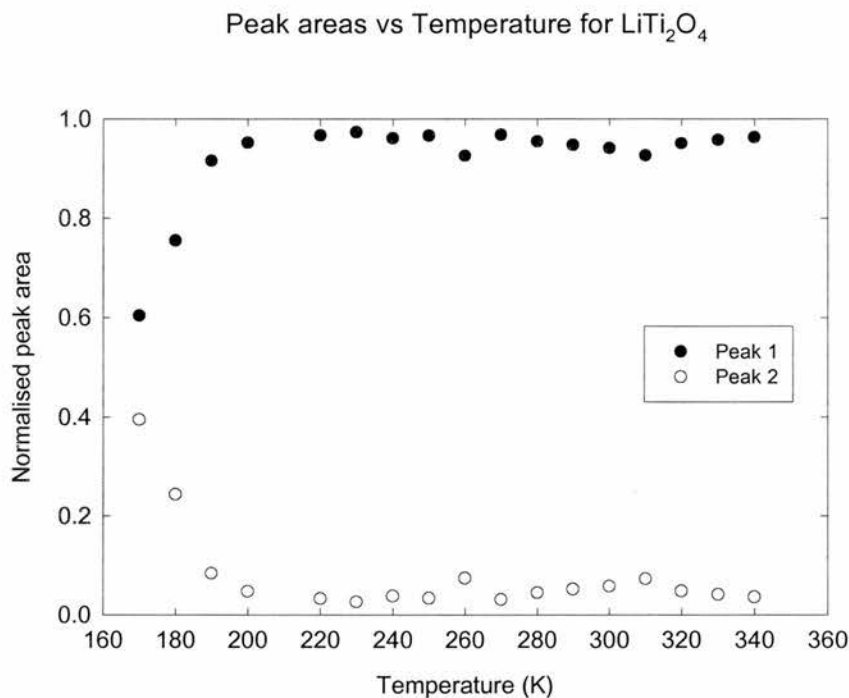


Figure 3-22: Normalised area beneath each of the two peaks as a function of temperature.

At high temperature we observe that the spectra of the material are dominated by an intense peak at -12ppm , with a smaller peak evident at -0.3ppm . This second peak is very close to that expected for a spinel impurity, but after comparison of our measured T1 relaxation time ($126.8 \pm 1.8\text{ ms}$) with that of LiTi_2O_4 spinel ($\sim 10\text{sec}$ ²²) we assigned it as being due to a second environment in the ramsdellite phase.

As the temperature is lowered, we see a broadening of the -12ppm peak down to 200K , but no apparent change in either peak position. Fitting of the data shows that there is also no change in the relative peak intensities, though the combination of the peak overlap and the -12ppm peak broadening gives the visual impression that there might be.

Below 200K we do see a change in the relative peak areas, with the -12ppm weakening considerably at the expense of the -0.3ppm peak. This continues down to the lower limit of our probe at 160K . There is additionally a little apparent variation in the position of the -12ppm peak, but this may be an artefact

caused from the fact that the breadth of the peak makes accurate assessment of its position difficult.

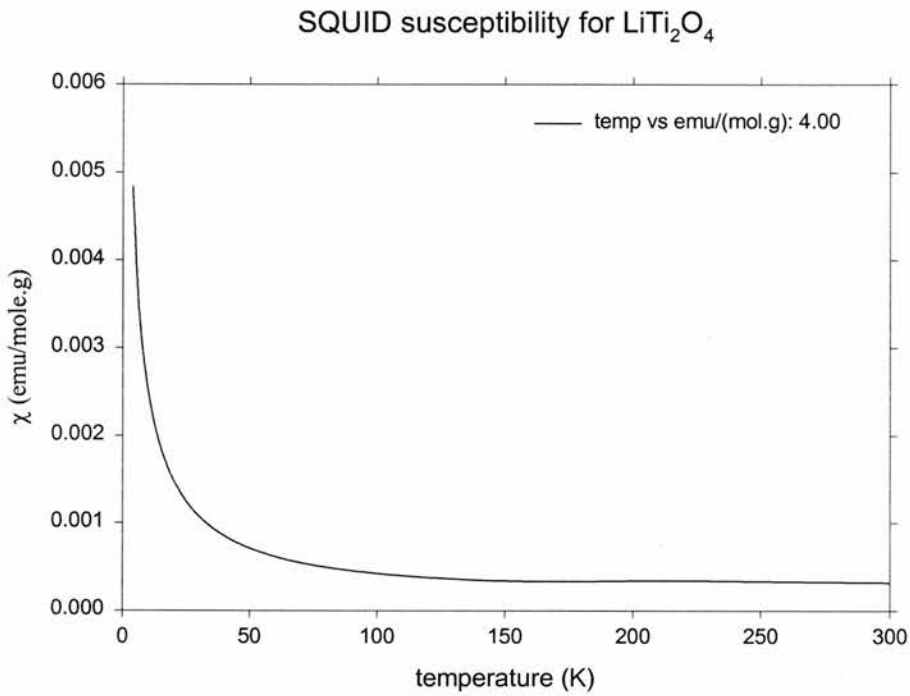


Figure 3-23: SQUID susceptibility for LiTi_2O_4 .

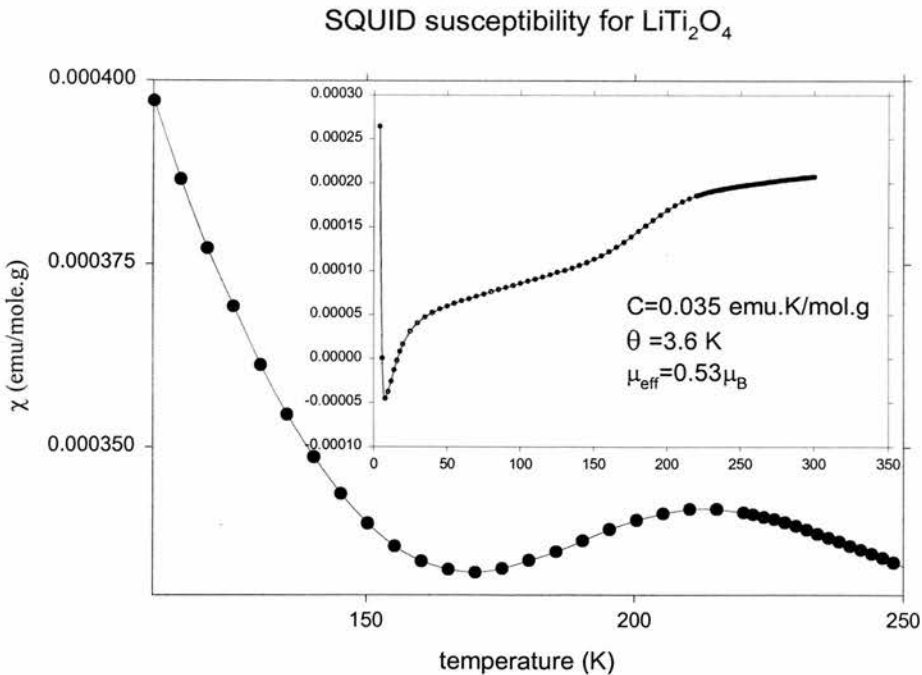


Figure 3-24: Close up and residual plot from fitting LiTi_2O_4 SQUID data to Curie-Weiss behaviour.

The SQUID susceptibility data confirms the findings of Gover¹³ that the material is predominantly paramagnetic. Fitting the data to Curie-Weiss behaviour we found a similar value of μ_{eff} ($0.53\mu_{\text{B}}$ vs. $0.52\mu_{\text{B}}$), but from the plot of the residual fit we discovered a magnetic anomaly between 130K and 220K. This is shown in Figure 3-24.

3.4.2 X-ray diffraction studies

3.4.2.1 Introduction

In investigating the origin of the unusual NMR results reported above, we collected x-ray diffraction data at a series of temperatures down to 90K. These data were collected at Durham University by Dr. Richard Gover using a Bruker D8 diffractometer equipped with a custom temperature stage. At each temperature the sample was allowed to equilibrate for 3 minutes before a 26 minute scan was taken between 10° and $90^{\circ} 2\theta$. The data were then analysed using the GSAS^a Rietveld refinement software.

3.4.2.2 Results

A selection of the data collected for this sample is presented below in its raw form. Close examination of this revealed that several peaks were seen to split on cooling, the most obvious and most intense of these is the (130) peak, the temperature dependence of which is given below, along with a similar plot for the (024) reflection (Figure 3-26 and Figure 3-27 below).

^a A.C Larsen and B. von Dreele, Los Alamos Laboratory.

Diffraction patterns taken of LiTi_2O_4 between 350K and 230K

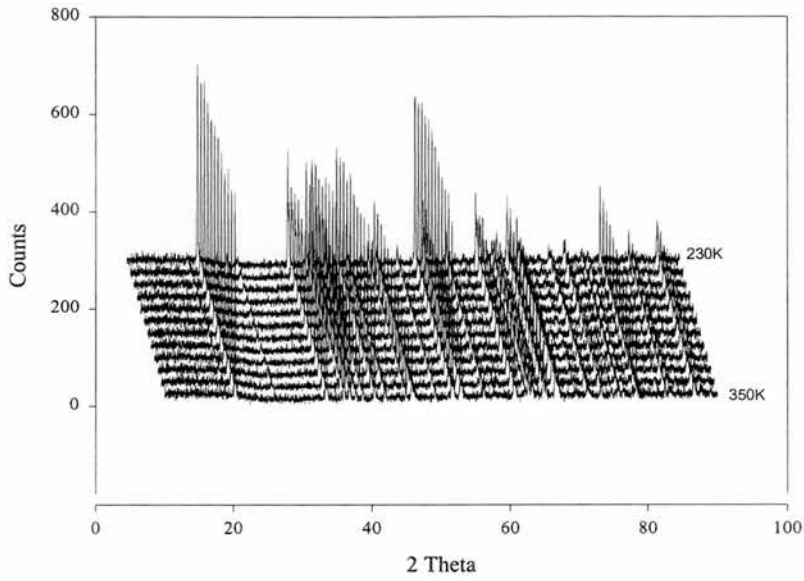


Figure 3-25: Raw data between 350K and 230K

The splitting of the (130) peak of LiTi_2O_4 ramsdellite with temperature

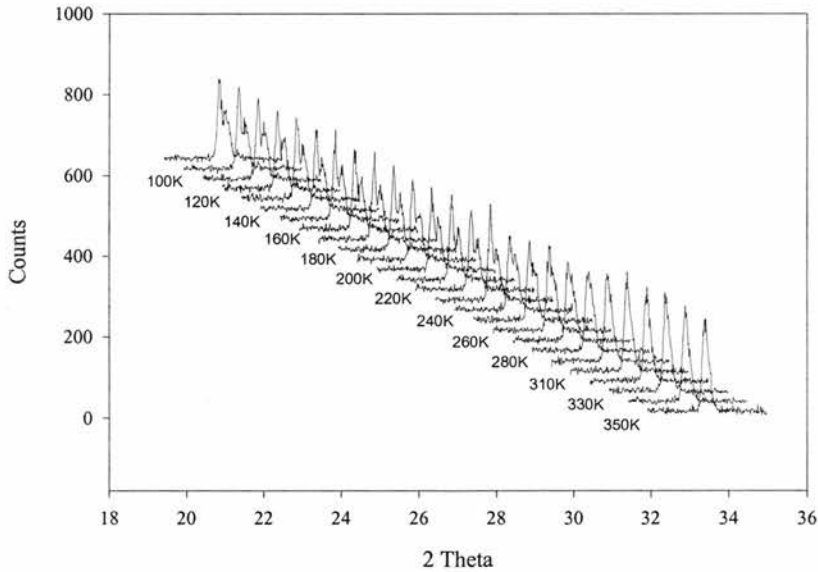


Figure 3-26: The splitting of the (130) peak of LiTi_2O_4 with temperature. Note that the intensities and diffraction angles are offset for clarity.

The splitting of the (240) peak of LiTi_2O_4 ramsdellite with temperature

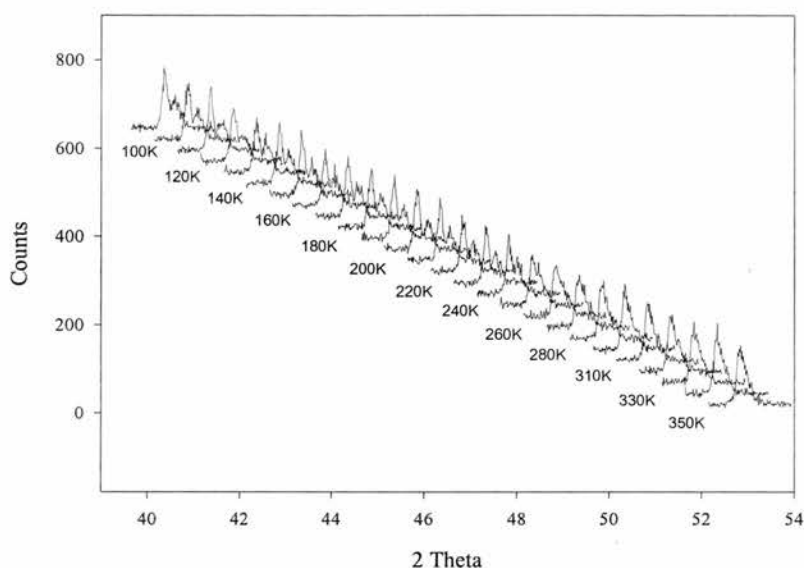


Figure 3-27: The splitting of the (240) peak of LiTi_2O_4 with temperature. Note that the intensities and diffraction angles are offset for clarity.

From the figures above it can be seen that the sample undergoes a considerable change with decreasing temperature, with several peaks splitting below about 260K, in addition to the (130) and (240) shown. Many of these diffraction peaks arise from the contribution of planes of more than one Miller index. The (130) however, does not, and so the splitting of the peaks indicates a change in symmetry for the system: The sample appears to undergo a phase transition in the 260-280K range. From the peak splittings observed a change of symmetry from orthorhombic to monoclinic seems most likely, but as, at the time of writing, no space group has been accurately assigned, this cannot be regarded as certain.

Fitting the low temperature data to the high temperature ramsdellite structural model we also observe unusual behaviour in the unit cell axes for the sample with temperature (Figure 3-28, Figure 3-29, and Figure 3-30). For all three axes there is a change in behaviour in the visually observed transition region, but for the “b” axis we also observe a steady contraction above 200K, which then

flattens out towards 350K. Similarly, the “flattening off” of the c axis expansion observed in the higher temperature neutron data presented earlier (Figure 3-6) is also seen here. These results are therefore complementary to this data, and give confirmation that the trends are real, and not an artefact from fitting the data to the incorrect space group.

Graph of unit cell "a" vs Temperature

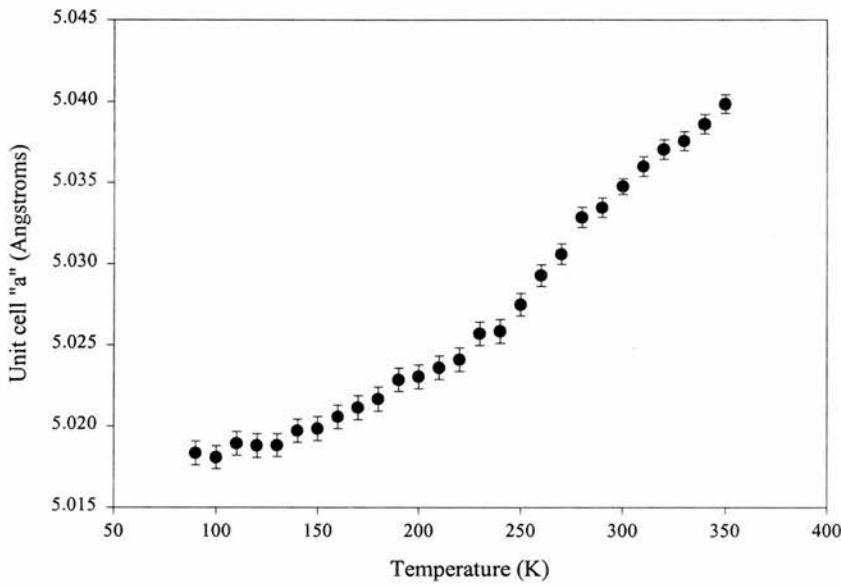


Figure 3-28: The temperature dependence of the unit cell “a”.

Graph of unit cell "b" vs Temperature

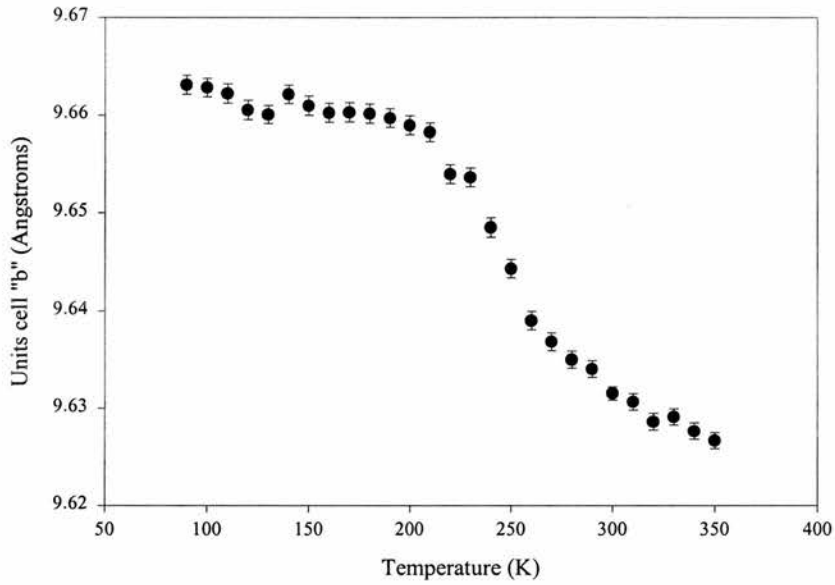


Figure 3-29: The temperature dependence of the unit cell "b".

Graph of unit cell "c" vs Temperature

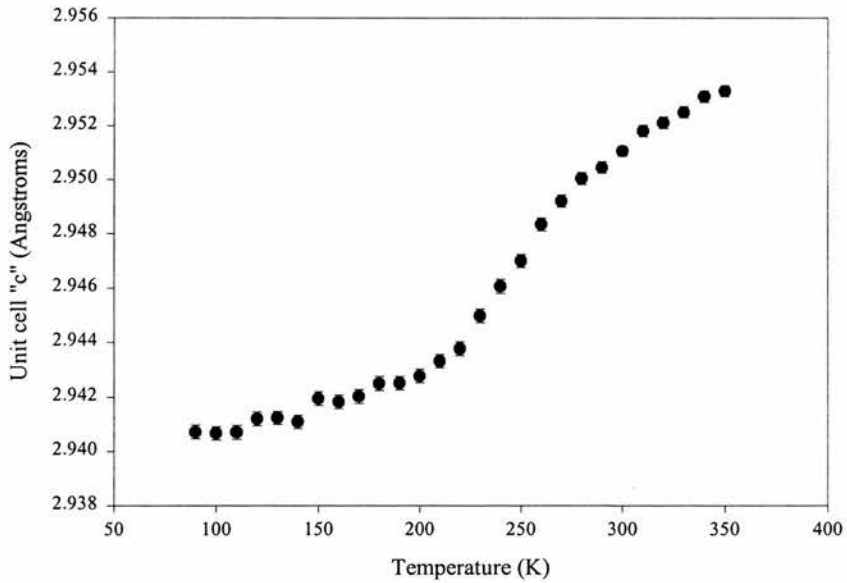


Figure 3-30: The temperature dependence of the unit cell "c".

3.4.3 Discussion

From the NMR and XRD data we see that there are a number of changes in LiTi_2O_4 ramsdellite on cooling to low temperature. At $\sim 280\text{K}$ XRD indicates what appears to be a structural transition, accompanied by a change in symmetry, probably to monoclinic, and at $\sim 200\text{K}$ the NMR and SQUID susceptibility indicate a magnetic transition of some kind. Close inspection of the unit cell behaviour with temperature suggests that the structural transition actually takes place over the temperature range 200K to 280K rather than at the higher temperature alone. If this is the case it allows us to correlate the two transitions and so seems more reasonable than suggesting that the structure could undergo a major transformation without affecting the magnetism of the system. Bringing together the NMR and XRD data is still difficult however, as even accepting that the structural transition begins at 200K , we have the difference that the magnetism clearly changes below 200K and the structure above; the magnetic transition seems to follow on from the completion of the structural.

The magnetic transition itself is interesting in that it would perhaps be more usual to observe magnetic order being lost on heating rather than on cooling. The nature of transition is also slightly odd, as we see two distinctly different lithium sites seemingly begin to change to become one, the obvious interpretation of which is that the lithium physically migrates from one site to the other on cooling, possibly facilitated by the structural distortion. However, this could also be interpreted as the magnetic transition causing a major change in the -12ppm site environment, leaving two separate sites of similar ppm. It is hoped that with the solution of the low temperature structure, and possibly some further low temperature studies, we will be able to explain this more fully.

3.5 Studies on delithiated LiTi_2O_4

3.5.1 Introduction

As part of their studies on the topotactic oxidation of reduced lithium titanates, Akimoto *et al*¹⁹ reported that on reaction with weak hydrochloric acid all the lithium in LiTi_2O_4 could be removed whilst leaving the ramsdellite framework intact, a reaction facilitated by the fact that the removal of lithium from the sample corresponds exactly to the oxidation of titanium from a nominal oxidation state of +3.5 to +4. The thus formed polymorph of TiO_2 they reported as stable at room temperature, but when heated a transformation to the brookite structure was observed. Since this report no further work on $\text{TiO}_2(\text{R})$ has been reported and so this work is concerned with extending the work of Akimoto *et al*.

3.5.2 Experimental

Samples of LiTi_2O_4 were prepared as described elsewhere in this work, and analysed for purity using x-ray diffraction. Delithiation was achieved by reaction of the samples with 1M hydrochloric acid for a period of 36 hours. During this time the sample was occasionally stirred, but no constant mixing or heat was applied. On reaction the sample was seen to change colour from black to light grey as the lithium was removed and the titanium oxidised. At the end of the reaction the sample was filtered using a sintered glass filter, washed with distilled water and ethanol, and dried under vacuum. At this point it was noticed that the powder of $\text{TiO}_2(\text{R})$ obtained was considerably finer than that of the starting LiTi_2O_4 .

In order to test the stability of the ramsdellite framework, a sample of the as-prepared $\text{TiO}_2(\text{R})$ was chemically relithiated using n-butyl lithium. This reaction was done in large excess of the lithiating agent so as to ensure that as much lithium was reinserted as possible. During the reaction the sample was observed to change colour from light grey to dark grey/black. Following reaction the

excess n-butyl lithium was neutralised using isopropanol and the sample washed and dried under vacuum.

3.5.3 Results and Discussion

Example diffraction patterns for both the as-made $\text{TiO}_2(\text{R})$ and relithiated $\text{Li}_x\text{TiO}_2(\text{R})$ are presented below, along with a pattern of the $\text{TiO}_2(\text{R})$ following two years storage in a dessicator. Unit cell parameters are given in Table 3-5.

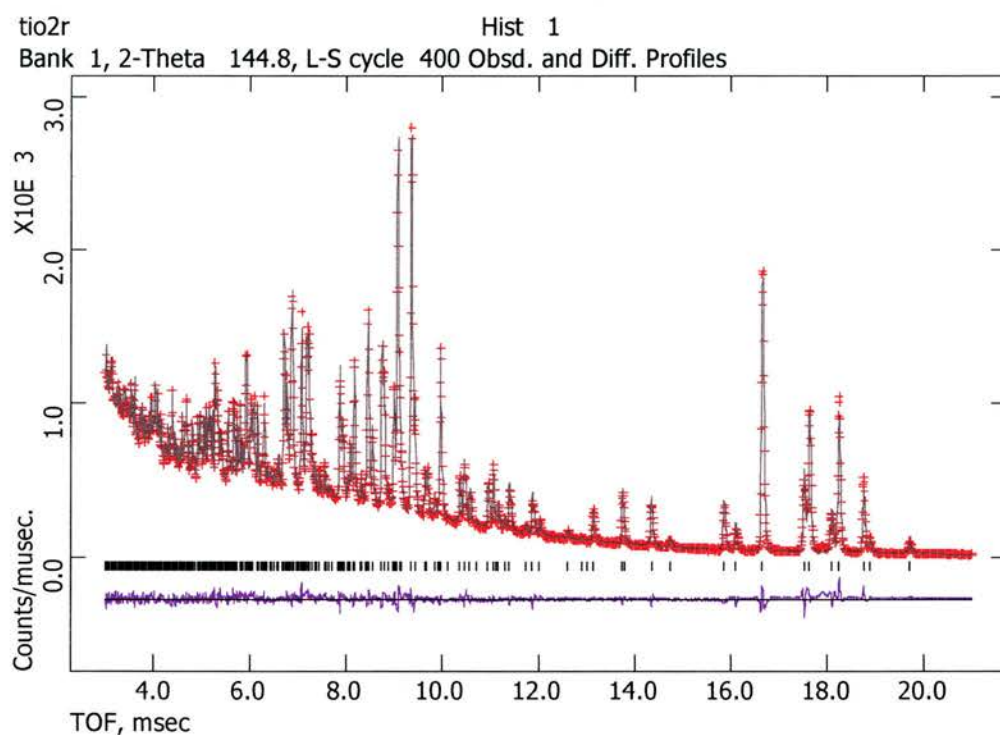


Figure 3-31: Refined neutron diffraction data for $\text{TiO}_2(\text{R})$.

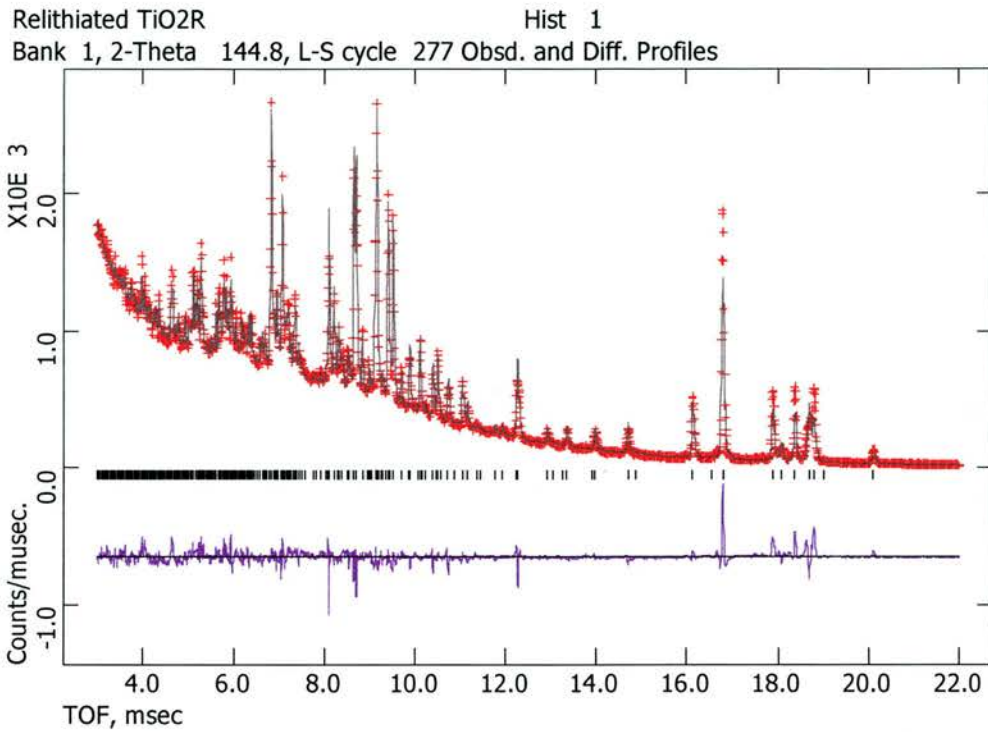


Figure 3-32: Refined neutron diffraction data for relithiated TiO₂(R)

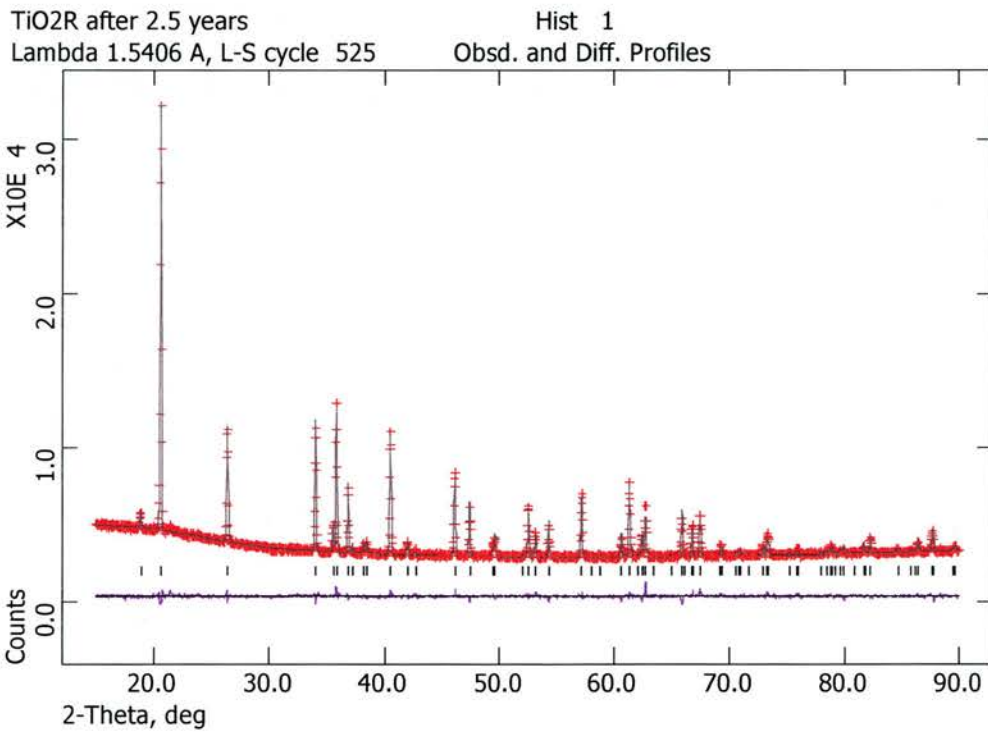


Figure 3-33: XRD pattern of the sample of TiO₂(R) after 2.5 years in a dessicator

Sample	Cell Axis (Å)			Unit cell vol (Å ³)
	a	b	c	
LiTi ₂ O ₄	5.0329(1)	9.6291(1)	2.9460(1)	142.76
TiO ₂ (R)	4.8436(3)	9.4453(6)	2.9656(2)	135.67
Relithiated TiO ₂ (R)	5.00129(14)	9.57646(26)	2.95519(8)	141.53
TiO ₂ (R) after 2.5 yrs*	4.83848(8)	9.42275(13)	2.960059(35)	134.95

Table 3-5: Unit cell parameters for samples of LiTi₂O₄ before and after delithiation and relithiation, with confirmation of the stability of TiO₂(R) after 2.5 years. * Indicates parameters obtained from XRD data. Other data are from neutron diffraction results.

From the above data it is clear that on reaction with acid, LiTi₂O₄ undergoes a considerable reduction in unit cell volume (~5%), as would be expected with the removal of Li, contracting considerably along a and b, though surprisingly expanding slightly along c. It can also be seen that the ramsdellite TiO₆ framework is very stable to the removal of the channel lithium, maintaining its structural integrity for the initial lithium removal and then remaining intact for 2.5 years without appreciable degradation.

As has been discussed earlier, the accurate analysis of the lithium in these samples can be difficult, but nevertheless efforts were made to try to locate lithium within the sample. Initially, scattering density (DELF) maps were used, but no “missing” atoms were observed. Following this we added a small quantity of channel sited lithium to the refinement and monitored the residual fit parameters for the refinement. These did not improve at all, and efforts to refine the lithium position and thermal displacement resulted in instability in the refinement. Thus we conclude that any lithium left in the sample is below the detection threshold of the neutron diffraction technique.

Similar difficulties were presented in trying to ascertain the lithium content and placement in the relithiated sample of TiO₂(R). Making the reasonable assumption that the unit cell volume and edge parameters will vary reasonably linearly with lithium content, we can infer that roughly 80% of the original lithium content is restored on the reaction with n-butyl lithium, giving a nominal stoichiometry Li_{0.8}Ti₂O₄. However, the accurate locating of this lithium is hampered by the fact that the sample has now undergone two structure-changing

chemical reactions. In addition to a slight loss of crystallinity being expected, it is not unlikely that, despite drying under a heavy vacuum, there may be some residual solvent present in the sample. The electrochemistry results presented in section 3.6, additionally suggest that the sample could be a mixture of line compositions. These factors are reflected in the quality of the visual fit shown in Figure 3-32. Nevertheless, similar efforts as for $\text{TiO}_2(\text{R})$ were made to isolate the reinserted lithium. As with that sample, Fourier difference maps were of no help, showing no missing scattering density. However, adding the 0.8 Li calculated as being inserted earlier resulted in a drop in the fitted residuals as shown below. It can be seen that whilst we cannot conclusively differentiate between the one and two site models on the basis of R-factors, it is clear that the addition of lithium to the refinement causes a considerable improvement to the quality of fit.

Sample	Rwp	Cell Axis (Å)		
		a	b	c
$\text{TiO}_2(\text{R})$	5.28	4.83966(7)	9.43328(12)	2.96297(4)
$\text{Li}_x\text{Ti}_2\text{O}_4$ no lithium	7.03	5.00130(14)	9.57646(26)	2.95519(8)
$\text{Li}_x\text{Ti}_2\text{O}_4$ one lithium site	6.86	5.00134(14)	9.57630(26)	2.95519(8)
$\text{Li}_x\text{Ti}_2\text{O}_4$ two lithium sites	6.8	5.00137(14)	9.57631(26)	2.95517(8)

Table 3-6: Unit cell and fit parameters for neutron diffraction on delithiated and relithiated ramsdellite. Full data available in appendix 1

Thermal analysis of the $\text{TiO}_2(\text{R})$ sample (Figure 3-36) showed that in common with the results of Akimoto *et al*, there is a phase change in the 523K (250°C) region, but the second transition they reported at 640K is not visible in our results. In order to confirm this we took XRD patterns of the sample after heating just past the first phase transition (300°C / 573K), at a point that would be past the second phase transition (400°C / 673K) and at 1000°C where the thermal analysis run finished. These are presented below.

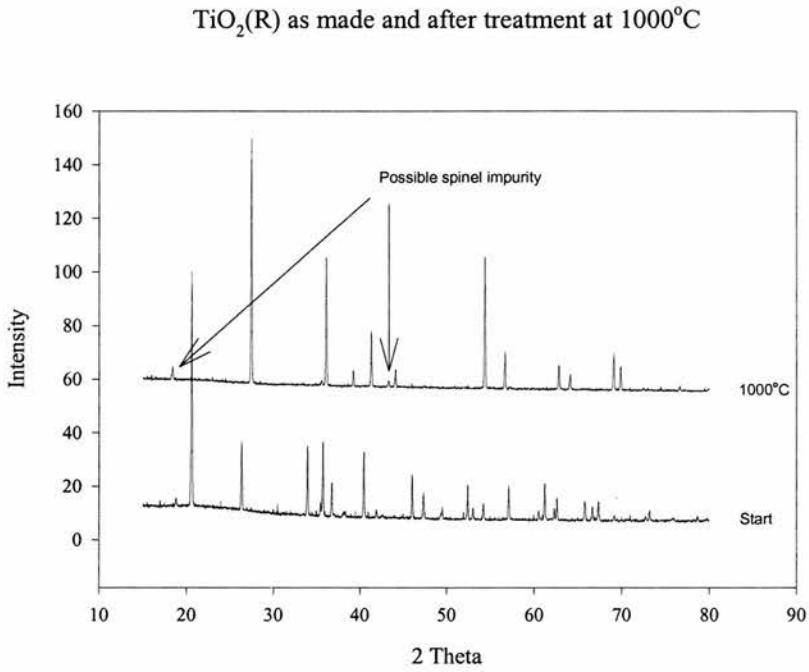


Figure 3-34 XRD patterns of $\text{TiO}_2(\text{R})$ as made (bottom) and after heating to 1000°C (top).

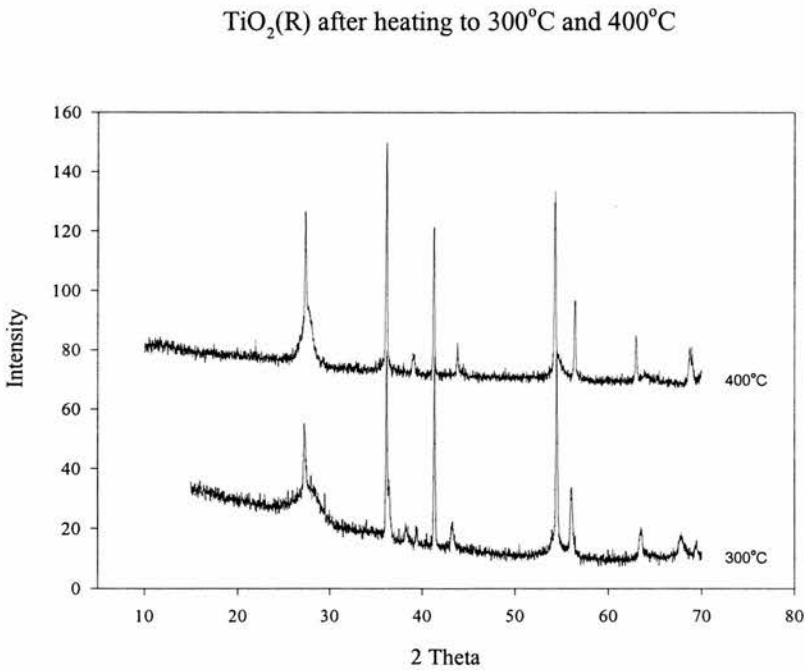


Figure 3-35: XRD patterns of $\text{TiO}_2(\text{R})$ after heating to 300°C (bottom) and 400°C (top)

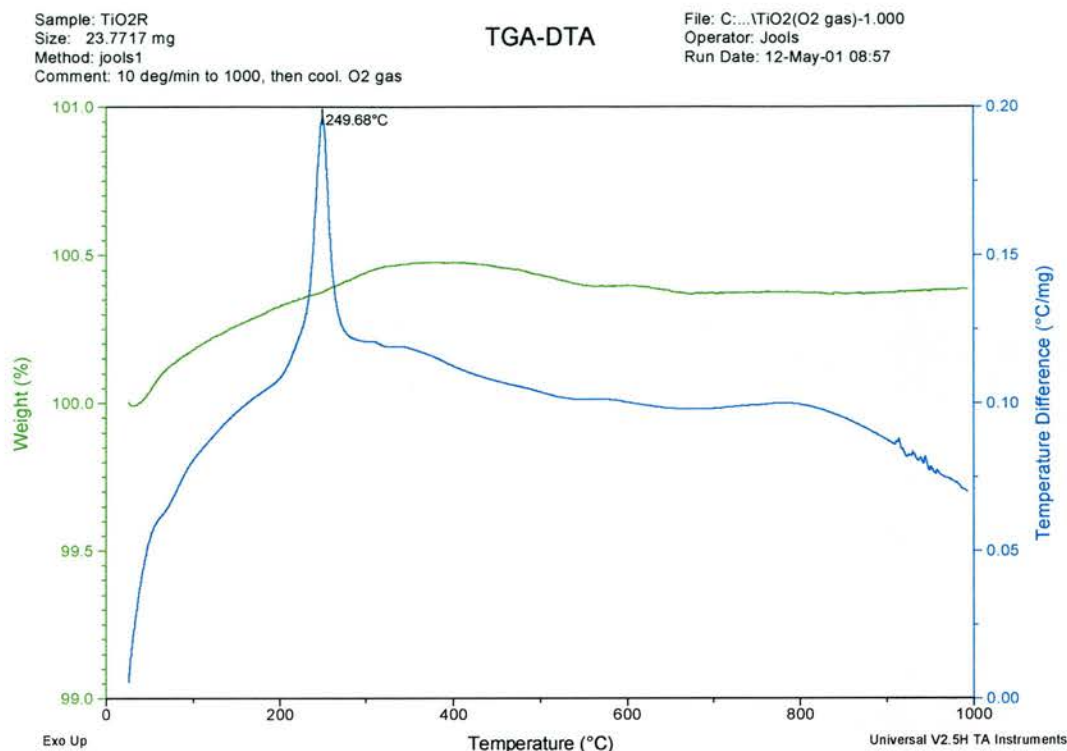


Figure 3-36: TGA/DTA of TiO₂(R) showing the structural transition at 250°C/523K.

These results clearly show that the transition at 520K is the structural transition of the ramsdellite TiO₂ into a form identified from the XRD pattern as rutile, and that between this temperature and 1000°C the only changes are the improvement in the crystallinity of the rutile, and the appearance of a small second phase. There is no evidence of a brookite being formed as reported by Akimoto *et al*, and no evidence of a phase change at 640K, though there is a small second phase evident, the exact nature of which cannot be accurately ascertained, but as the visible diffraction peaks coincide well with those of a spinel, it could be suggested that the phase could well be an Li₄Ti₅O₁₂ type phase resulting from the presence of a small quantity of residual lithium in the sample. It can also be seen that there is no sign of significant weight loss upon heating, so the sample can be regarded as being completely dry and stable, containing no residual water or solvent within the structure.

3.6 Electrochemical studies on ramsdellite LiTi_2O_4 and TiO_2

3.6.1 Introduction

In the form of $\gamma\text{-MnO}_2$ the ramsdellite structure has long been known as a stable insertion host framework for small cations, being for many years used in primary Leclanchè type cells before being investigated extensively for use in Li-ion secondary cells^{23,24,25}. Similarly, the titanium oxides have been seen to show very favourable cycling characteristics with regard to Li-ion cell applications, particularly the spinel $\text{Li}_4\text{Ti}_5\text{O}_{12}$ ^{26,27} and the ramsdellite $\text{Li}_2\text{Ti}_3\text{O}_7$ ^{16,17,18}. It was therefore a logical extension of our work on the ramsdellite lithium titanates to evaluate them for use as Li-ion cell electrodes.

To test these materials, we produced Bellcore²⁸ type electrodes (see chapter 2 for details) from the as prepared samples of LiTi_2O_4 and $\text{TiO}_2(\text{R})$ and cycled them in 2325 model coin cells as described in section 2.2. MacpileTM and MaccorTM controllers were used to regulate voltage and current, and to collect the cycling data. For all results presented here the galvanostatic current was set at 0.05mA. Potentiostatic cycling was carried out at a rate of 10mV/h. No optimisation of the sample particle size etc was performed before cycling.

In-situ X-ray diffraction patterns were taken of the materials at varying stages of cycling using two different in-situ cell arrangements. The first of these was the transmission XRD cell described in section earlier, the second was a reflection mode cell used courtesy of Dr. Antonio Fernandez at the Universidad Autonoma de Nuevo Leon, Monterrey, Mexico. For this cell, diffraction patterns were collected using a reflection mode Siemens diffractometer.

Ex-situ X-ray diffraction patterns of electrode materials were taken on some electrodes after several cycles using the Philips PW3810 diffractometer described earlier.

3.6.2 Electrochemical cycling results

3.6.2.1 Results for LiTi_2O_4

Galvanostatic cycling of the LiTi_2O_4 and $\text{TiO}_2(\text{R})$ materials was carried out between a series of potential windows in the 0.2V to 5V range. The results for LiTi_2O_4 are shown below:

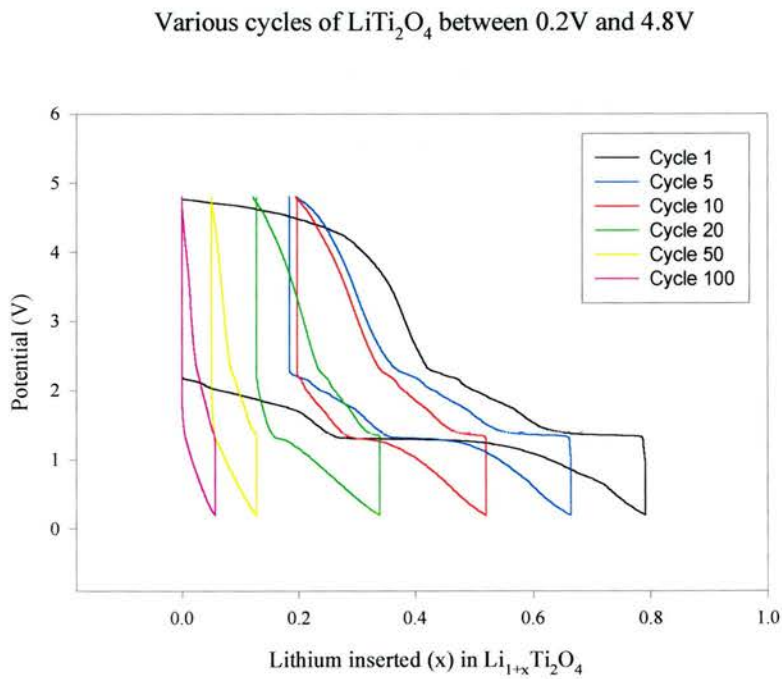
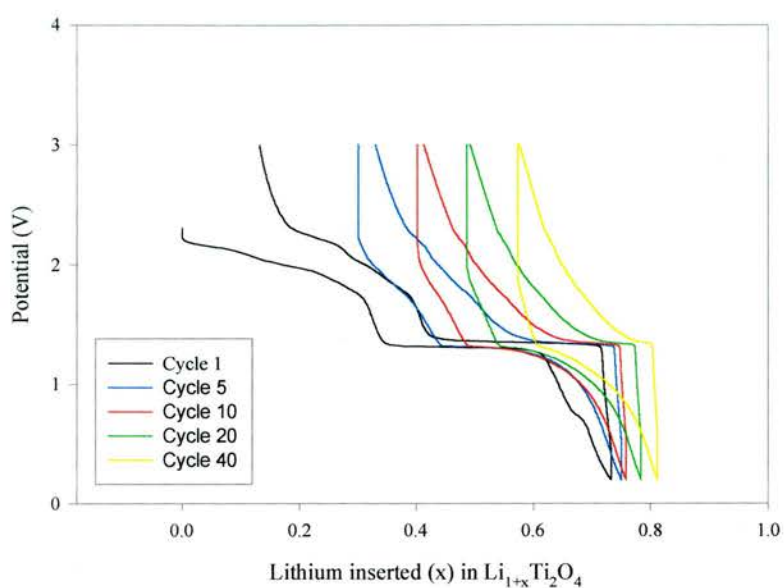
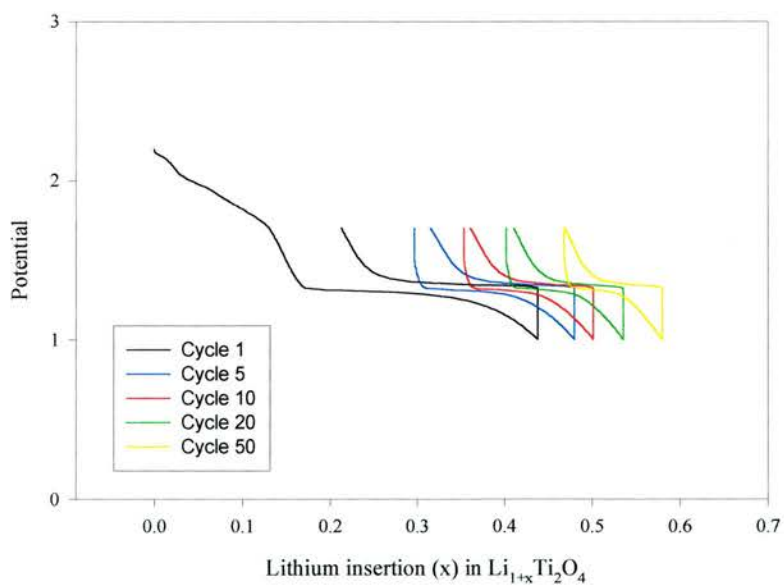
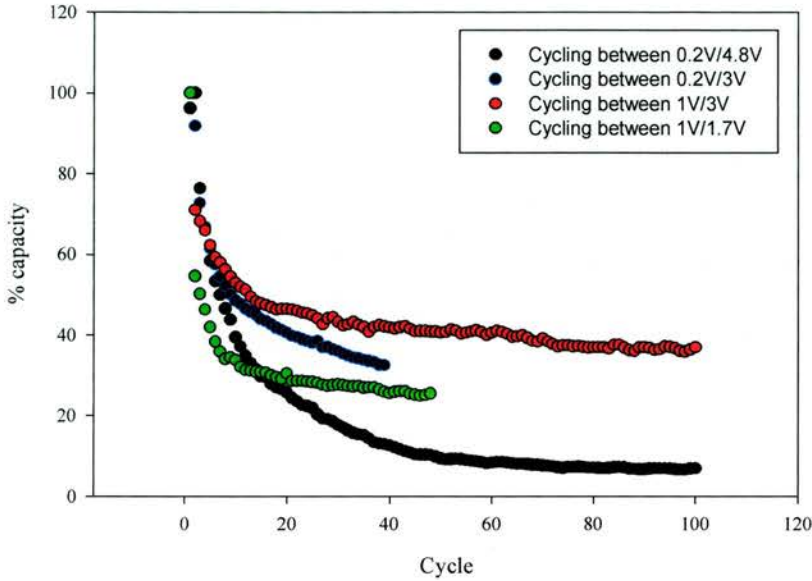


Figure 3-37: Cycling of LiTi_2O_4 between 0.2V and 4.8V. The sample was reduced on the initial step, lithium being inserted.

Various cycles of LiTi_2O_4 in the 0.2V/3V voltage range**Figure 3-38: Cycling of LiTi_2O_4 between 0.2V and 3V. Lithium was inserted on the initial cycling step**Various cycles of LiTi_2O_4 between 1V and 1.7V**Figure 3-39: Cycling of LiTi_2O_4 between 1V and 1.7V. Lithium was inserted on the initial cycling step**

Capacity fade with cycling for different voltage regimes

Figure 3-40: Percentage capacity retained with cycling for LiTi_2O_4 .

Voltage range	1st insertion capacity (mAh/g)	1st deinsertion capacity (mAh/g)	2nd insertion capacity (mAh/g)	5th insertion capacity (mAh/g)	% capacity retained after 5 cycles
0.2/4.8V	127.12	127.12	132.19	77.16	61
0.2/3V	117.83	106.95	108.21	72.41	61
1/3V	77.32	50.63	54.85	48.1	62
1/1.7	113.95 (79.97*)	58.63	62.16	47.75	42 (60*)

Table 3-7: Insertion capacities for LiTi_2O_4 over various cycling voltages. * indicates the capacity below 1.7V on first cycle, as initial OCV is $\sim 2.7\text{V}$ for this material.

From this galvanostatic data we can draw several observations:

- Insertion occurs in three distinct stages. First there is a steady drop in voltage from OCV to 1.3V during which roughly half of the lithium insertion occurs. This is followed by a plateau at 1.3V at which about 0.26Li are inserted. The remaining capacity is below 1V, some of

which may be due to the carbon current collector used in the electrode preparation.

- Only around 80% of the theoretical 160mAh/g (calculated for the reduction of Ti +3.5 to +3) capacity is being realised on first insertion. Whilst this is poor in comparison to the best of the insertion oxides, such as the lithium manganates, which cycle closer to 200mAh/g²⁹, this non-optimised capacity compares much more favourably with materials such as $\text{Li}_4\text{Ti}_5\text{O}_{12}$ (150mAh/g)³⁰, LiFePO_4 (160mAh/g)³¹, and the commercially used LiCoO_2 (100mAh/g)³².
- Whilst the cells cycled many times, the material does not appear to cycle well. In every voltage window, 40% of the initial capacity is lost by the 5th cycle. Confining the voltage limits to between 1 and 3V helps longer cycling considerably, with the capacity stabilising at about 40% of its initial value. Likewise, confining the voltage to allow cycling of the 1.3V plateau also assists in cyclability. (Note that in this case Figure 3-40 is misleading as the residual capacity is calculated according to an initial insertion cycle starting at ~2.7V whilst the following cycles are only from 1.7V. If the figure is recalculated with only the capacity below 1.7V accounted, the curve is “shifted up” about 22% and very similar curve to that of the 1V/3V cycles is observed.).
- Only the lithium electrochemically inserted into the material is removed at the deinsertion step. The lithium already present in the material is not removed even when the cell is cycled to 5V.

Examination of the potentiostatic cycling data for this material (below) contrasts somewhat the galvanostatic data. In this case, the cell was cycled to 5V initially, and then down to 0.2V. It can be seen clearly that in cycling in this way a quantity of lithium equivalent to the amount expected from the nominal LiTi_2O_4 formula is removed between 4V and 5V, although some caution should be taken in the exact value removed as the cell electrolyte is approaching the limit of stability at these potentials, and the apparent removal of lithium could instead be the degradation of the electrolyte. Nevertheless, the removal of Li realises greater

capacity in the material for the insertion step, with 1.8Li being inserted on reduction of the sample. This corresponds to a capacity of approximately 290mAh/g. Interestingly, it can be seen that the insertion profile is very similar in appearance to that of the galvanostatic cells which had not been cycled to 5V initially, with the regions of insertion simply extended over a larger value of x . It can also be seen that on the first deinsertion from low voltage, both the 1.3V plateau and the 1.4V-2.5V regions of cycling are considerably shortened with respect to the initial insertion step, with much of the lithium removal occurring at higher voltage than insertion occurred.

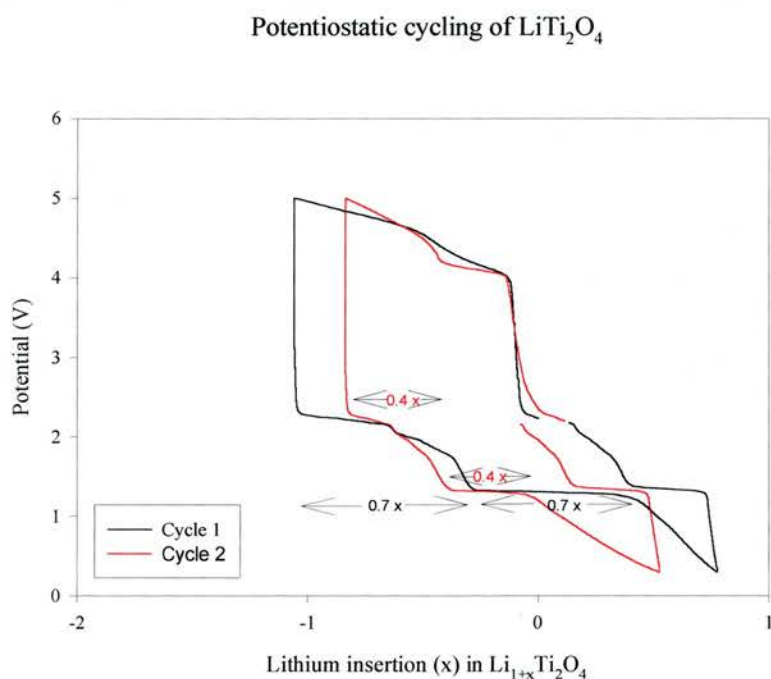


Figure 3-41: 1st and 2nd potentiostatic cycles for LiTi_2O_4 . Shown on the plot are the values of x for the insertion regions between 3V and 1V.

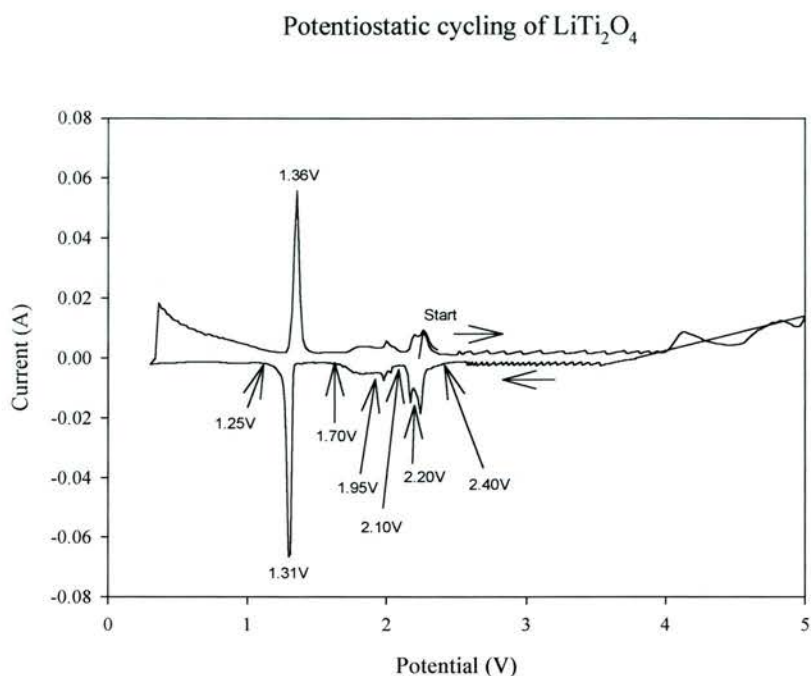


Figure 3-42: Current/voltage plot for LiTi_2O_4 . Marked are the potentials of stable phases

Close up of the 1st cycle potentiostatic reduction of LiTi_2O_4 .

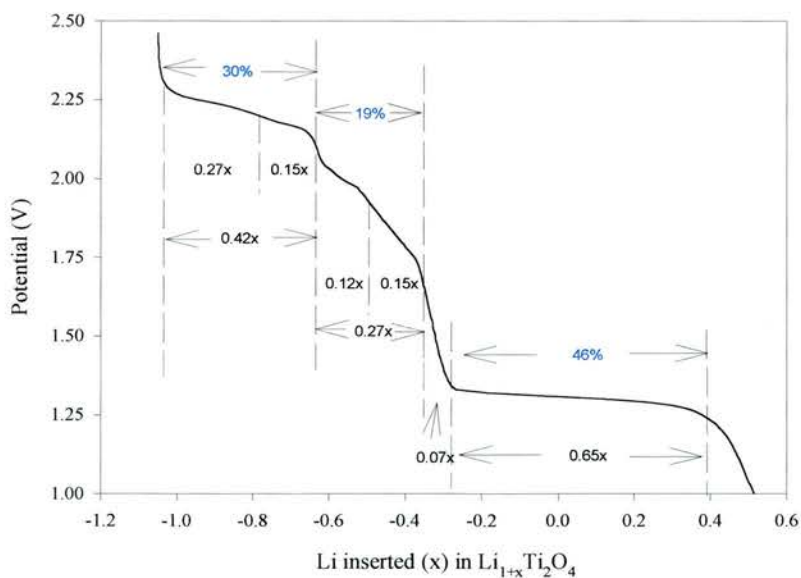


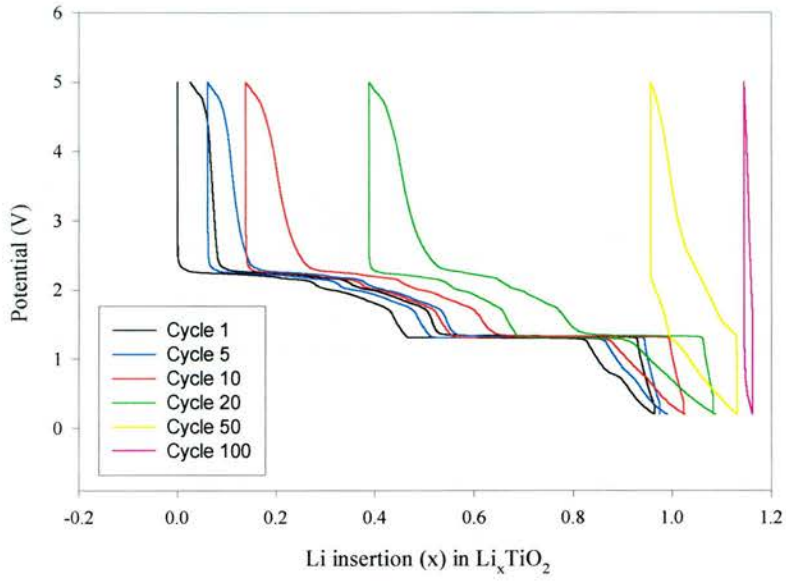
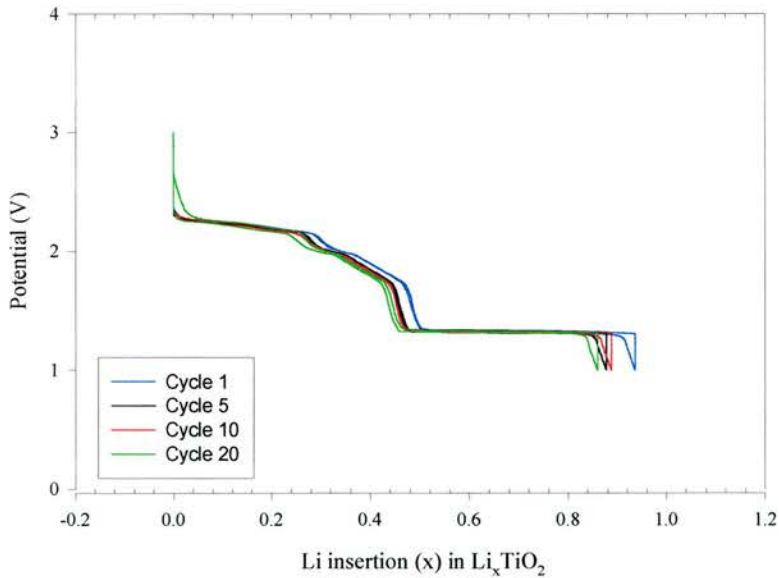
Figure 3-43: Close up of the first potentiostatic insertion cycle into LiTi_2O_4 . Marked in black on the graph are the values of x inserted between each of the voltages marked on the I-V curve above. In blue are the relative percentage uptakes for each region.

Further, it can be seen that capacity of the sample is lost all across the voltage window, not in any one part of it. Though more marked in potentiostatic mode, this agrees well with the galvanostatic data, where the capacity drops similarly for both the 1V/3V and 1V/1.7V data sets, suggesting that the capacity drop is not tied to any particular voltage range, but to the sample as a whole.

Analysis of the Potential vs Current plot for LiTi_2O_4 (Figure 3-42) shows several peaks in the region below 2.5V, the largest at 1.31V. Each of these peaks represents a phase change in the system, during which lithium is inserted into the material, and so each of the troughs then relates to a stable phase. Comparing the data with the Potential vs Insertion plot (Figure 3-43) we can thus describe a series of stable compositions being formed on reduction of the sample. These are summarised along with the data from $\text{TiO}_2(\text{R})$ in Table 3-9 on page 136.

3.6.2.2 Results for $\text{TiO}_2(\text{R})$

As with LiTi_2O_4 , a sample of $\text{TiO}_2(\text{R})$ was evaluated using our lithium battery cycling equipment. Presented below are the results from galvanostatic cycling of this material in various voltage windows between 0.2V and 5V:

Various plots of TiO_2R cycled between 0.2V and 5V**Figure 3-44: Cycling of TiO_2R between 0.2V and 5V. Lithium was inserted on the initial cycling step**Various plots of TiO_2R cycled between 1V and 3V**Figure 3-45: Cycling of TiO_2R between 1V and 3V. Lithium was inserted on the initial cycling step.**

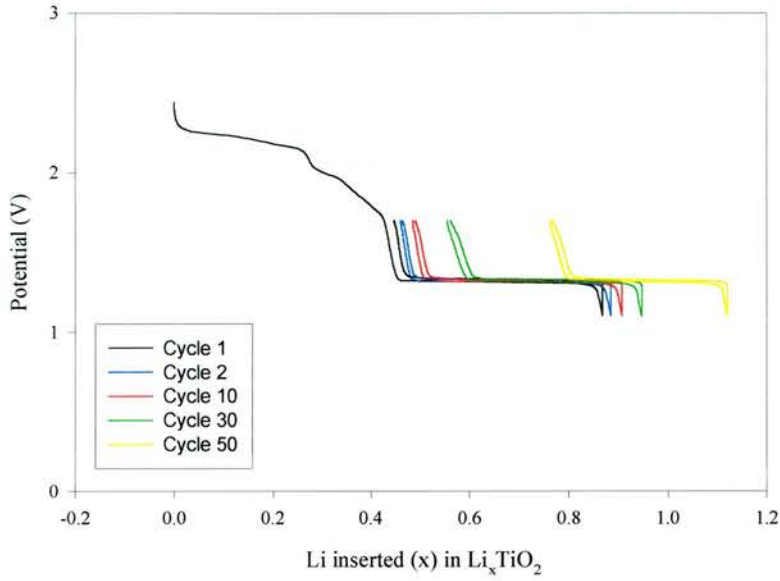
Various plots of TiO_2R cycled between 1V and 1.7V

Figure 3-46: Cycling of $\text{TiO}_2\text{(R)}$ between 1.1V and 1.7V. Lithium was inserted on the initial cycling step.

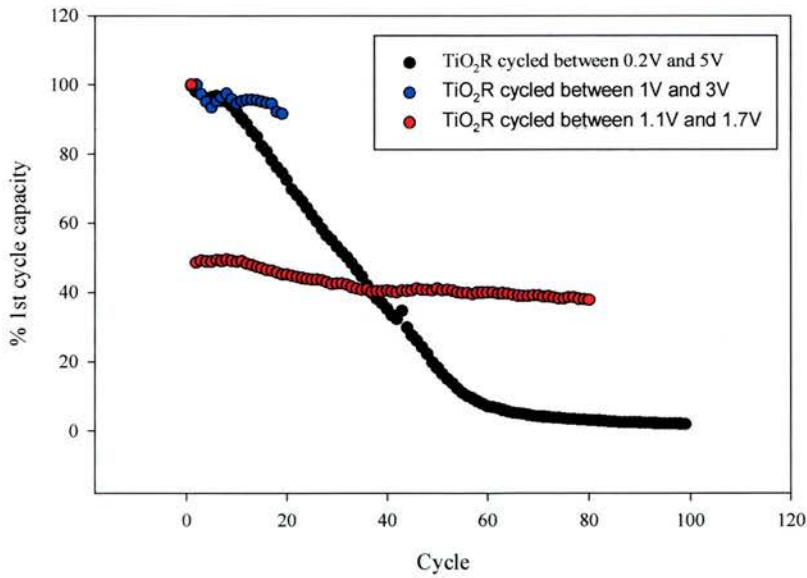
Capacity retention with cycle for TiO_2R 

Figure 3-47: Percentage capacity retained with cycling for LiTi_2O_4

Voltage range	1st insertion capacity (mAh/g)	1 st deinsertion capacity (mAh/g)	2nd insertion capacity (mAh/g)	5th insertion capacity (mAh/g)	% capacity retained after 5 cycles
0.2V/5	323.6	314.88	317.47	311.85	96
1V/3V	314.16	314.16	315.26	294.31	94
1.1V/1.7V	291.34 (148.27*)	141.55	141.61	142.33	49 (96*)

Table 3-8: Insertion capacities for TiO₂(R) over various cycling voltages. * indicates the capacity below 1.7V on first cycle, as initial OCV is ~2.4V for this material

From this data we can see that whilst at first glance the cycling profiles appear very similar to the results from the LiTi₂O₄ sample, comparison of the two data sets shows several notable differences between the results from LiTi₂O₄ and TiO₂(R):

- The initial insertion capacity of the TiO₂(R) sample is more than twice that of LiTi₂O₄, though the voltage profile is very similar, with a decreasing voltage region of insertion between 2.5V and 1.3V, followed by a plateau at 1.3V. The sample also shows considerably lower polarisation than LiTi₂O₄, with oxidation curves overlaying the reduction almost perfectly.
- Whilst the voltage profiles of the two samples are very similar, each of the two insertion regions has twice the capacity for TiO₂(R) compared to LiTi₂O₄. Note that this was also seen in the potentiostatic data of LiTi₂O₄ where lithium was removed initially, thus effectively forming TiO₂(R) in-situ.
- The initial insertion capacity of 323mAh/g represents the availability of 96% of the theoretical capacity of 335mAh/g for this material (assuming reduction of Ti to +3) on first charge, compared to the 80% found for LiTi₂O₄.
- Cyclability of TiO₂(R) is considerably better than for LiTi₂O₄. Whilst cycling in a high voltage window between 0.2V and 5V results in a steady drop of capacity over the first 50 cycles (probably caused by

the degradation of the electrodes/electrolyte due to the high voltage used), constraining the cell to cycle in the main insertion/deinsertion regions between 1V and 3V results in excellent cyclability. It can be seen that for the 1.1V/1.7V voltage window, only 11% of the electrode capacity (calculated against initial insertion capacity) is lost between the 2nd and 80th cycles.

Potentiostatic cycling of the $\text{TiO}_2(\text{R})$ was carried out in a similar fashion as for LiTi_2O_4 , with the electrode again being initially oxidised to remove any lithium present within the sample. From Figure 3-48 below we can see that only a very small amount of lithium is removed from the electrode in the high potential range, suggesting that the acid delithiation does indeed remove almost all the lithium from LiTi_2O_4 . We can also see that, in contrast to the LiTi_2O_4 cycles, there is no large loss of capacity in the 1.4V to 2.5V region on deinsertion from low voltage, and that there is no obvious deinsertion step above 4V as seen in LiTi_2O_4 . Instead, insertion and deinsertion reactions occur at almost identical potentials.

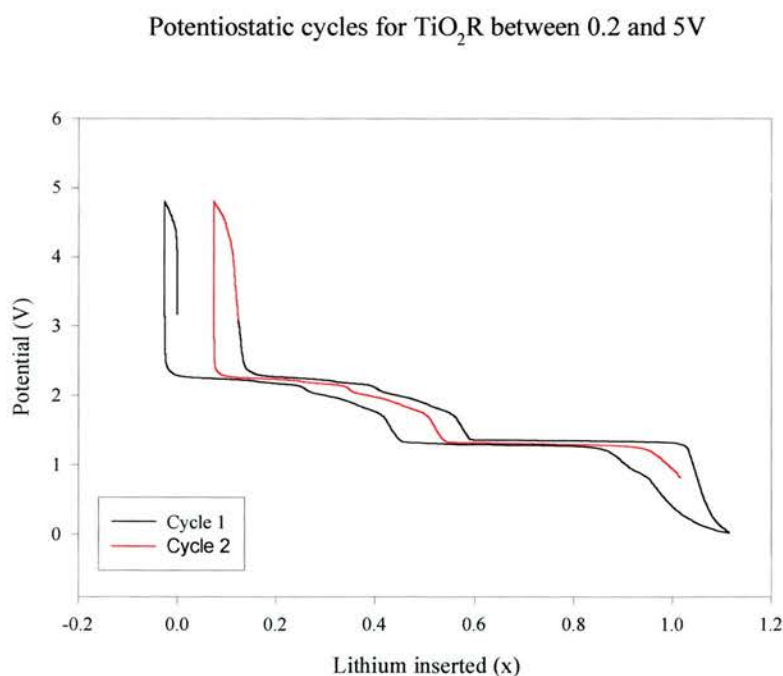


Figure 3-48: Potentiostatic cycling of $\text{TiO}_2(\text{R})$ between 5V and 0.2V

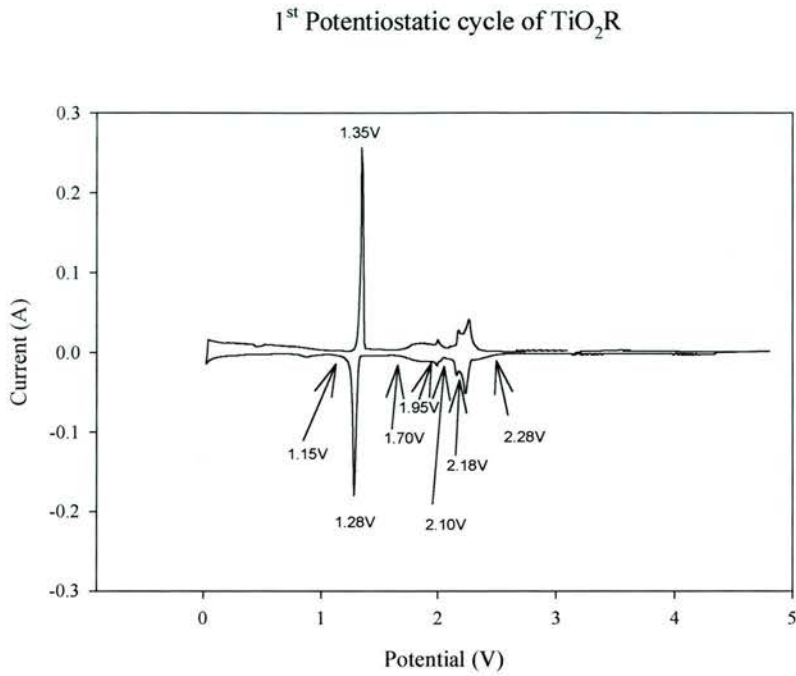


Figure 3-49: Current/voltage plot for $\text{TiO}_2\text{(R)}$. Marked are the potentials of stable phases.

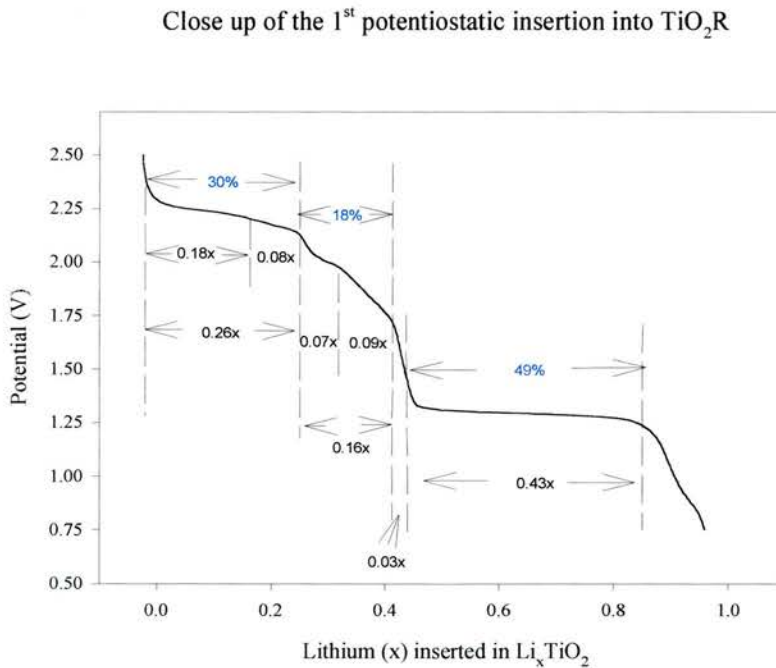


Figure 3-50: Close up of the first potentiostatic insertion cycle into $\text{TiO}_2\text{(R)}$. Marked in black on the graph are the values of x inserted between each of the voltages marked on the I-V curve above. In blue are the relative percentage uptakes for each region.

Analysis of the Current vs Potential and insertion data again shows a series of stable phases being formed on reduction. It can be seen that these occur at almost identical potentials as for LiTi_2O_4 , (see Table 3-9 below) though the compositions in this case are richer in lithium at each stage, a result that correlates with the overall higher capacity of this sample and demonstrates that the higher capacity is not related to any one region of insertion, but to the sample as a whole.

LiTi_2O_4 sample		$\text{TiO}_2(\text{R})^*$ sample	
Potential	Composition	Potential	Composition
>2.40V	$\text{Li}_0\text{Ti}_2\text{O}_4$	>2.28V	$\text{Li}_0\text{Ti}_2\text{O}_4$
2.20V	$\text{Li}_{0.27}\text{Ti}_2\text{O}_4$	2.17V	$\text{Li}_{0.36}\text{Ti}_2\text{O}_4$
2.1V	$\text{Li}_{0.42}\text{Ti}_2\text{O}_4$	2.10V	$\text{Li}_{0.52}\text{Ti}_2\text{O}_4$
1.95V	$\text{Li}_{0.54}\text{Ti}_2\text{O}_4$	1.95V	$\text{Li}_{0.66}\text{Ti}_2\text{O}_4$
1.70V	$\text{Li}_{0.69}\text{Ti}_2\text{O}_4$	1.70V	$\text{Li}_{0.84}\text{Ti}_2\text{O}_4$
<1.25V	$\text{Li}_{1.41}\text{Ti}_2\text{O}_4 - \text{Li}_{1.84}\text{Ti}_2\text{O}_4$	<1.15V	$\text{Li}_{1.76}\text{Ti}_2\text{O}_4 - \text{Li}_{2.3}\text{Ti}_2\text{O}_4$

Table 3-9: Stable phases in the reduction of LiTi_2O_4 and $\text{TiO}_2(\text{R})$. * Note that the insertion compositions for $\text{TiO}_2(\text{R})$ have been normalised to stoichiometry $\text{Li}_x\text{Ti}_2\text{O}_4$ for easier comparison of the two data sets.

3.6.3 In-situ X-ray diffraction

3.6.3.1 Introduction and experimental

In order to extend provisional work by Elias³³ investigating some of the structural aspects of the electrochemical results shown above, we used specially modified electrochemical cells to allow x-ray diffraction to be carried out on our electrodes without dismantling the cells at each stage. As already discussed, two different cell types were used in this work; for the LiTi_2O_4 sample a transmission type cell was utilised, for the $\text{TiO}_2(\text{R})$ sample a reflection mode cell was used. As with many bespoke solutions, both of these approaches had their failings, most notably a considerable loss of resolution and diffraction intensity caused by the need for the x-rays to pass through the casings of the electrochemical cells. Additionally, in the case of the transmission cell, the seals holding the x-ray transparent “windows” are prone to failure and leakage, causing both a high rate of cell failures and a very limited life for those cells which are successfully constructed. For the reflection mode cell, a beryllium window caused greater intensity loss than the Kapton windows of the transmission cell, and as measurements were carried out during a short visit to the Universidad Autonoma de Nuevo Leon, time was also a limiting factor.

Diffraction patterns for both cells were taken before cycling and then at several points on the discharge curves of the materials. For LiTi_2O_4 XRD patterns were taken at 1.1V (just after the insertion plateau), 0.6V and then at 2.5V following deinsertion. It was hoped that more could be taken for this sample, but the unreliability of the cell design forced a compromise on the data that could be collected. For $\text{TiO}_2(\text{R})$, patterns were obtained at 1.4V, 1V, 0.2V and at 1.5V on the return insertion. In both cases the cells were cycled potentiostatically so as to give better control over the finishing voltage of each step. After cycling the cell was allowed to relax for at least an hour before a diffraction pattern was taken.

Calculation of the unit cell parameters from these patterns was carried out in two ways. For the data obtained for LiTi_2O_4 from the Stöe diffractometer, the

proprietary Stöe Winxpow software was used to calculate the unit cell parameters. For the Siemens diffractometer data collected for $\text{TiO}_2(\text{R})$, the poor peak intensities and background made it necessary to calculate the unit cell by hand. For this, the (110), (111) and (130) peaks were used.

3.6.3.2 Results

Presented below are the in-situ XRD patterns taken at different points in the cycling of the LiTi_2O_4 and $\text{TiO}_2(\text{R})$ samples, along with ex-situ XRD patterns taken after 100 cycles. The calculated unit cell parameters for each point of the in-situ data are presented below these.

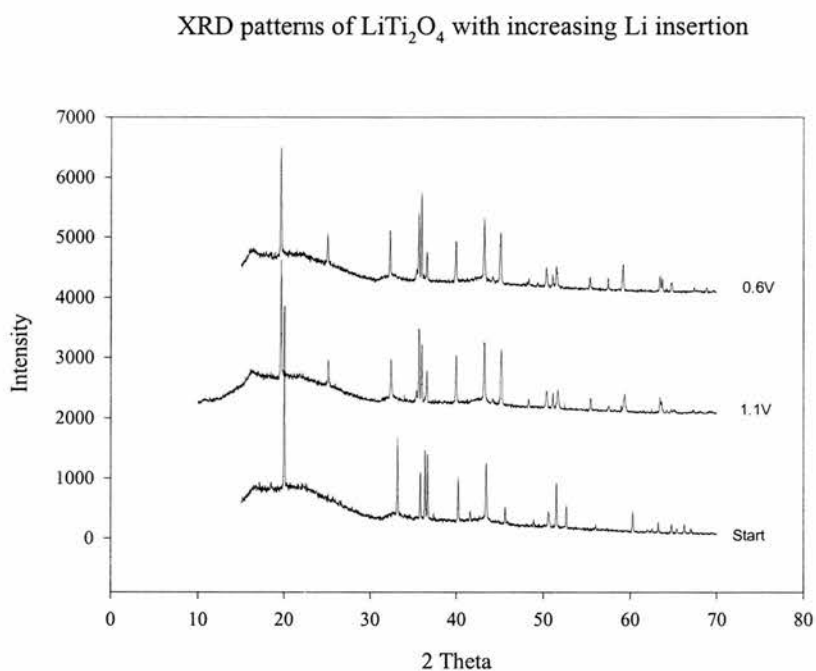


Figure 3-51: XRD patterns of LiTi_2O_4 before cycling, and after insertion to 1.1V and 0.6V

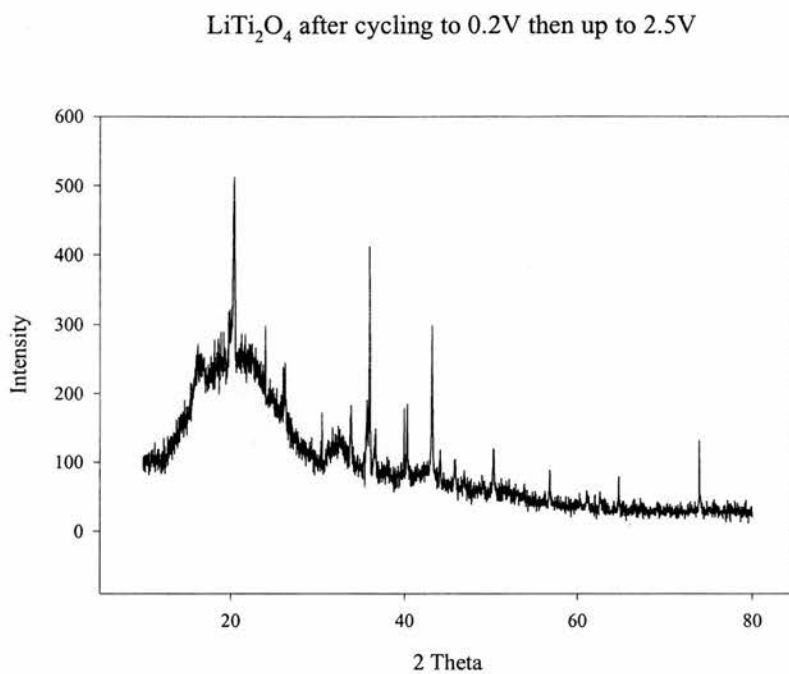


Figure 3-52: XRD patterns of LiTi_2O_4 after cycling to 0.2V and then back up to 2.5V

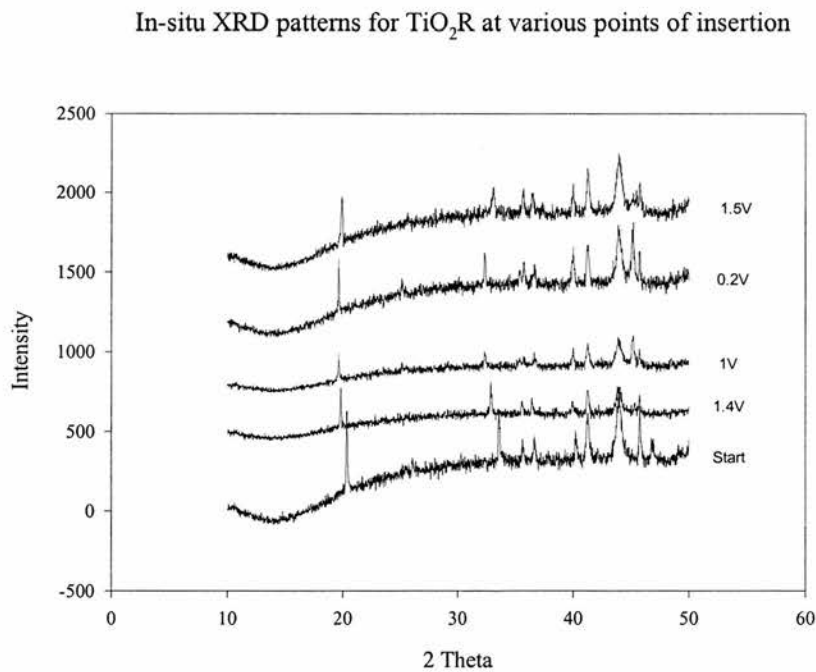


Figure 3-53: XRD patterns of $\text{TiO}_2\text{(R)}$ before cycling and after cycling to various voltages.

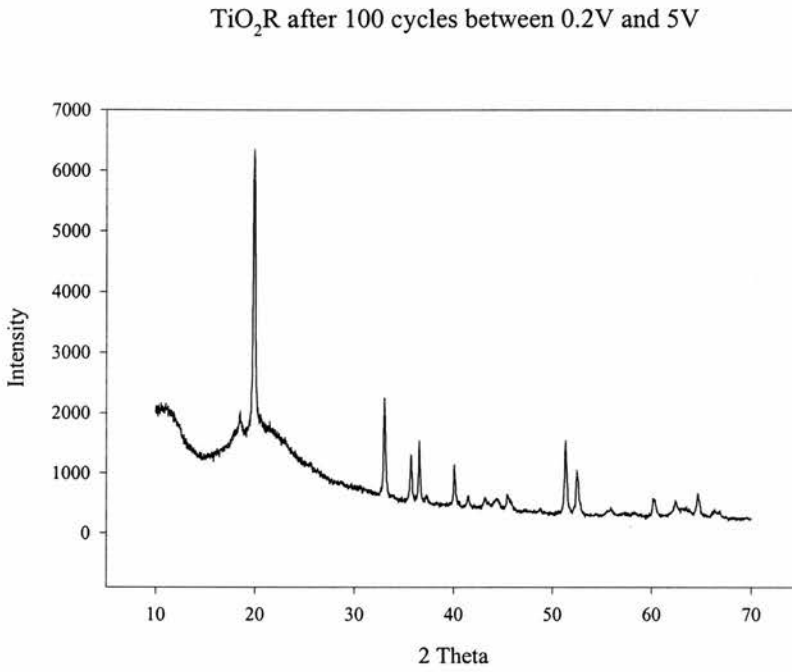


Figure 3-54: Ex-situ XRD pattern for $\text{TiO}_2\text{(R)}$ after 100 cycles between 0.2V and 5V.

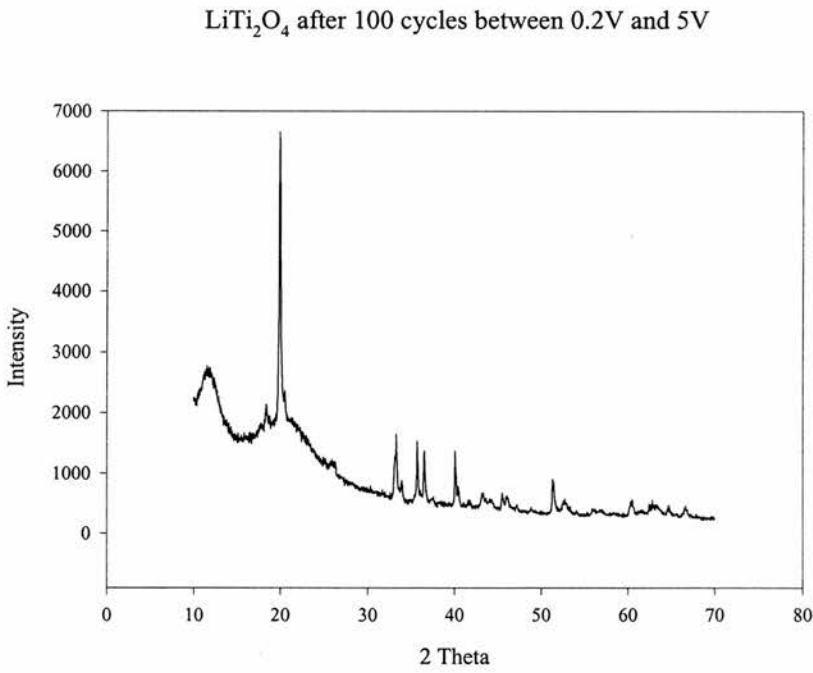


Figure 3-55: Ex-situ diffraction pattern of LiTi_2O_4 after 100 cycles between 0.2V and 5V.

Unit Cell Axis	TiO ₂ (R)				LiTi ₂ O ₄			
	Start	1.4V	1V	1.5V	Start	1.1V	0.6V	2.5V
a	4.91Å	5.0Å	5.07Å	5.02Å	5.05Å	5.07Å	5.08Å	4.86Å
b	9.5Å	9.69Å	9.87Å	9.61Å	9.68Å	9.85Å	9.9Å	9.44Å
c	2.96Å	2.95Å	2.92Å	2.95Å	2.93Å	2.93Å	2.92Å	2.9Å

Table 3-10: Unit cell parameters for LiTi₂O₄ and TiO₂(R) measured in-situ the electrochemical cell.

We can see clearly from these results that on cycling the ramsdellite structure is retained for both the initial insertion and deinsertion steps and for many cycles afterwards, a not unexpected result considering that the structure has already been shown to be stable to chemical relithiation. It is noticeable, however, that while the patterns for TiO₂(R) are all of similar quality, the data obtained from the LiTi₂O₄ sample after reinsertion to 2.5V is noticeably worse. We initially attributed this to a degradation of the sample on reinsertion, but the ex-situ XRD of as made LiTi₂O₄ after 100 cycles suggests that this is not the case, so perhaps the poor diffraction pattern is a sign that the in-situ cell began to fail on the reinsertion step.

For the TiO₂(R) sample it can be seen that for both the 2.5V-1.4V and the 1.4V-1V steps there is a considerable enlargement of the unit cell in the a and b directions with the insertion of lithium into the structure. As each of these steps represents the insertion of ~0.5Li into the TiO₂ stoichiometry, at 1.4V we can regard the material as being nominally LiTi₂O₄ (Li_{0.5}TiO₂) and at 1V, Li₂Ti₂O₄ (LiTiO₂). It is therefore not surprising that the unit cell parameters at 1.4V correspond quite well to the starting parameters of the LiTi₂O₄ cell, and that after the 1.3V insertion plateau, both materials have expanded in a similar fashion and demonstrate almost identical unit cell parameters. On removal of lithium, the TiO₂(R) sample fares better, contracting roughly as would be expected according to the lithium removed. As mentioned above however, the LiTi₂O₄ sample appears to have degraded somewhat, and consequently the calculated unit cell parameters may well be misleading.

3.6.4 Discussion

Drawing the electrochemistry results together we can conclude that, in common with their manganate brethren, the ramsdellite lithium titanates are promising Li-ion battery electrode materials. Both LiTi_2O_4 and $\text{TiO}_2(\text{R})$ have been shown to reversibly insert lithium over many cycles, with $\text{TiO}_2(\text{R})$ being the better of the two samples. On restriction of the cycling windows to 1V/3V and 1V/1.7V we have shown that in excess of 80% of the initial insertion capacity is retained after 100 cycles. For the 1V/3V window this corresponds to long term cycling in the region 250 – 320mAh/g, for the 1V/1.7V window, 110mAh/g – 140mAh/g. The former of these is a considerable improvement over even the best insertion oxides, and compares well with the carbon anode materials presently used commercially. The latter compares very well with other insertion oxides such as LiCoO_2 , $\text{Li}_4\text{Ti}_5\text{O}_{12}$ and LiFePO_4 and the flat plateau is ideal for use in a secondary battery. The 1.3V plateau is admittedly a little higher than ideal for an insertion anode, limiting the power output of any cell based upon it. However, for lower power cells, and for applications where safety is the primary issue the high voltage plateau is ideal as the material cycles well above the potential at which metallic lithium might be formed in-situ.

Insertion into LiTi_2O_4 and $\text{TiO}_2(\text{R})$ occurs in two voltage stages, the first over a steady decrease between about 2.2V and 1.3V in which roughly 50% of the materials' capacity is located. The second stage is a voltage plateau, reminiscent of $\text{Li}_2\text{Ti}_3\text{O}_7$ ¹⁸ located at 1.3V, and accounts for ~45% of the cell capacity. Potentiostatic data indicates that the first region is a series of small phase changes, corresponding to the insertion of increasing amounts of lithium into the ramsdellite framework. XRD data taken at the end of this potential region indicates that the ramsdellite framework is retained on lithium insertion undergoing a ~2% increase in both the a and b directions. Kuhn *et al*³⁴ recently reported that this first stage of insertion into $\text{TiO}_2(\text{R})$ could be described in terms of the sequential filling of the T1 channel sites as described by Abrahams *et al*⁴, with the 1.3V plateau due to the filling of the less stable T2 sites. De Dompablo *et al*³⁵, however, described the equivalent process in $\text{Li}_2\text{Ti}_3\text{O}_7$ as being

accompanied by a structural transformation. Our XRD results support the former proposition, that between 2.2V and 1.3V a series of close composition line phases are formed followed by a large insertion at 1.3V correlated to the filling of a different type of lithium site.

Another interesting result from our data is that LiTi_2O_4 behaves differently depending on the initial direction of cycling:

- If lithium is first inserted into the material, the structural lithium already present is effectively “locked in” and cannot be removed electrochemically, thus limiting the theoretical capacity of the sample to 160mAh/g. That there is no obvious change in the voltage profile of the as-made LiTi_2O_4 , (ie it doesn't start to cycle over just one of the insertion stages after the 1st cycle) is very interesting, and unusual, as it indicates that the “locked in” lithium is distributed over both the sites proposed above, and that the cycling of the material then proceeds over these, already part occupied, sites.
- If the material is oxidised initially, the stoichiometric lithium is removed in the 4V-5V region, and a capacity and voltage profile similar to that of $\text{TiO}_2(\text{R})$ is realised for the insertion step. In contrast to $\text{TiO}_2(\text{R})$, however, the deinsertion step above 4V remains for the second oxidation.

We also see that the cyclability and polarisation of the $\text{TiO}_2(\text{R})$ is different to LiTi_2O_4 , with the former showing excellent capacity retention and overlapping reduction/oxidation curves, whilst the latter degrades quickly with cycling. Due to the nature of the capacity loss in LiTi_2O_4 (it occurs across all voltage windows), we suspect that both this and the higher polarisation are probably due simply to the difference in particle size between the LiTi_2O_4 and the chemically treated $\text{TiO}_2(\text{R})$. It is also possible that the 4V deinsertion plateau of LiTi_2O_4 could be linked to the particle size, as the ramsdellite TiO_2 formed by electrochemical removal of Li from LiTi_2O_4 should chemically be little different from that formed by acid delithiation.

Further consideration of the in-situ XRD's and the voltage profiles also leads to the conclusion that the "LiTi₂O₄" produced electrochemically is not the same as that produced by the high temperature synthesis, as the voltage insertion profiles of the two samples differ between the LiTi₂O₄ and Li₂Ti₂O₄ electrochemical compositions: TiO₂(R) (both chemically and electrochemically produced) inserts across a single plateau whilst as-made LiTi₂O₄ inserts with the two stage profile, showing a similar series of line phases as for TiO₂(R), but with lower levels of insertion at each stage. The logical conclusion from this is that the high temperature synthesis route favours lithium distribution over two electrochemically different sites, whereas the low temperature electrochemical insertion favours sequential insertion into those same sites.

3.7 Summary

In the research presented here we have been able to considerably extend the work of Akimoto *et al*^{19, 20} and Gover *et al*¹³ on the reduced ramsdellite lithium titanate system. Four materials have been synthesised, LiTi_2O_4 , $\text{Li}_{1.1}\text{Ti}_{1.8}\text{O}_4$, $\text{TiO}_2(\text{R})$ and relithiated $\text{TiO}_2(\text{R})$. These have been studied and evaluated using a variety of techniques.

Structural studies using high resolution neutron diffraction have shown conclusively that the channel sited lithium is extremely mobile even at room temperature, and that much of this mobility stems from disorder across more than one channel site. We have also shown that the primary mode of movement of the lithium is in the a-b plane, predominantly in the b axis direction, a surprising result considering that ionic conduction has been shown to be along the channels, not between them. We have also shown the existence of a possible new conduction route between channels via unoccupied tetrahedra at the channel corners.

Low temperature SQUID investigations have shown a weak anomaly in the χ vs T curve, possibly arising from localised/short range antiferromagnetic coupling of the Ti. This is correlated with a considerable change in the environment of the channel sited Li according to NMR, giving the possibility of some sort of magnetic ordering in the 200K region. XRD data taken in the same temperature range show that this is probably correlated to a structural transition in the 200K-260K region, though we are unsure how at the present. As this part of our work is very much ongoing, and the data presented here preliminary, it is on the low temperature evaluation of LiTi_2O_4 that future work on the system is planned to focus. Further NMR and SQUID experiments are already planned, and efforts are continuing to solve the structural transition observed in the 200K-260K region.

Electrochemical evaluation of LiTi_2O_4 and the chemically delithiated $\text{TiO}_2(\text{R})$ confirms that the ramsdellite titanates are very promising secondary Li-ion

battery anodes, with $\text{TiO}_2(\text{R})$ in particular showing the kind of capacity and cyclability required of a commercial electrode. The comparatively poor performance of LiTi_2O_4 is almost certainly due to the larger particle size of the as-made sample compared to $\text{TiO}_2(\text{R})$. Some work optimising this may be undertaken to confirm this, along with an evaluation of different delithiation techniques for the manufacture of $\text{TiO}_2(\text{R})$.

In conclusion then, we can say that we have considerably extended our knowledge of the reduced ramsdellite lithium titanates and have been able to answer many questions posed by earlier work, particularly the issue of the channel lithium environment. However, we still have little understanding of the magnetism of the system and how this relates to the low temperature structural transition, so much remains to be done.

References

- ¹ G.H. Jonker. *Traajos Reunion Intern. Reactividad Solidos, 3^o Madrid*. April 1956, 1 (1957), 423.
- ² M. Lundberg, S. Andersson. *Acta Chem. Scand.* 18, No.3, (1964), 817.
- ³ B.Morosin and J.C. Mikkelson Jr. *Acta Cryst*, B35, (1979), 798.
- ⁴ I. Abrahams, P.G. Bruce, W.I.F. David and A.R. West. *J. Solid State Chem.* 78, (1989), 170
- ⁵ B. E. Liebert and R. A. Huggins. *Proceedings of the second international meeting on solid electrolytes*. (1978).
- ⁶ J.B. Boyce and J.C. Mikkelson, Jr. *Solid State Communications*. 31 (1979), 741
- ⁷ J.B. Boyce, J.C. Mikkelson, Jr. and B.A. Huberman. *Solid State Communications*. 29, (1979), 507.
- ⁸ P.H. Lacorre, M. Hervieu, J. Pannetier, J. Choisenet, B. Raveau. *J. Solid State Chem*, 50, (1983) 196
- ⁹ J.Grins and A.R. West. *Journal of Solid State Chemistry*. 65, (1986), 265
- ¹⁰ M. Greenblatt, E. Wang, H. Eckert, N. Kimura, R.H. Herber, J.V. Waszczak. *Inorg Chem*, 24. (1985), 1661
- ¹¹ A. Watanabe, H. Yamamura, Y. Matsui, Y. Moriyoshi, S. Shirasaki. *J. Mater. Sci Lett*, 1, (1982), 116.
- ¹² S.A. Petrov, S.K. Filatov, L.F. Grigor'eva, T.G. Kostyreva. *Neorganicheskie Materialy*, 28, No.5, (1992), 1070.
- ¹³ R.K.B. Gover, *PhD Thesis*, Univ. of St. Andrews, (1997)
- ¹⁴ R.K.B. Gover and J.T.S. Irvine, *J. Solid State Chem*, 141, (1998), 365.
- ¹⁵ R.K.B. Gover, J.T.S. Irvine, A. Finch. *J. Solid State Chem.* 132, (1997), 382.
- ¹⁶ C.J. Chen and M. Greenblatt. *Mater. Res. Bull.* 20(11), (1985), 1347
- ¹⁷ S. Garnier, C. Bohnke, O. Bohnke, J.L. Fourquet. *Solid State Ionics*. 83, (1996), 323
- ¹⁸ M.E. Arroyo y de Dompablo, E. Morán. A. Varez, F. Garcia-Alvarado. *J. Solid State Chem.* 153, (2000), 132.
- ¹⁹ J Akimoto, Y Gotoh, Y Oosawa, N Nonose, T Kumagai, K Aoki and H Takei. *J. Solid State Chem.* 113, (1994), 27.
- ²⁰ J. Akimoto, Y. Gotoh, M. Sohma, K. Kawaguchi, Y. Oosawa and H. Takei. *J. Solid State Chem.* 110, (1994), 150
- ²¹ J.P. Kartha, D.P. Tunstall, J. T. S. Irvine. *J. Solid State Chem.* 152, (2000), 397
- ²² M. Dalton, D.P. Tunstall, J. Todd, S. Arumugam, P.P. Edwards. *J. Phys. Cond. Matt*, 6, (1994), 8859.
- ²³ M.M. Thackeray, M.H. Roussouw, R.J. Gummow, D.C. Liles, K. Pearce, A. De Kock, W.I.F David, S. Hull. *Electrochimica Acta*, Vol. 38, No. 9, (1993), 1267.

-
- ²⁴ B. Zachau-Christiansen, K. West, T. Jacobsen, S. Skaarup. *Solid State Ionics*, 70/71, (1994), 401.
- ²⁵ L.A.H MacLean, C. Poinson, J.M. Amarilla, F.Le Cras, P. Strobel. *J. Mater Chem*, 5(8), (1995), 1183.
- ²⁶ D.W. Murphy, R.J. Cava, S.M. Zahurak, A. Santoro. *Solid State Ionics*, 9/10, (1983), 413.
- ²⁷ K.M. Colbow, J.R. Dahn, R.R. Haering, *J. Power Sources*, 26, (1989), 397.
- ²⁸ A.S. Gozdz, C.N. Schmutz, J.M. Tarascon, P.C. Warren, *U.S. Patent* 5,552,339, (1996).
- ²⁹ T. Ohsuku, A. Ueda, T. Hirai. *Chem. Express*, 7, (1992), 193.
- ³⁰ S. Bach, J.P. Pereira-Ramos, N. Baffier. *J. Mater. Chem.* 8(1), (1998), 251.
- ³¹ A. Yamada, S.C. Chung, K. Hinokuma. *J. Electrochem. Soc.* 148(3), (2001), A224.
- ³² R. Alcántara, P. Lavela, J.L. Tirado. *J. Solid State Chem.* 134, (1997), 265.
- ³³ M. Elias, *Honours project*, Univ. of St. Andrews, 2000.
- ³⁴ A. Kuhn, R. Amandi, F. García-Alvarado. *J. Power Sources.* 92, (2001), 221
- ³⁵ M.E. Arroyo y de Dompablo, A. Várez, F. García-Alvarado. *J.Solid.State Chem*, 153, (2000),

**Chapter 4 - Studies on some new lithium titanium
ferrites**

CHAPTER 4 - STUDIES ON SOME NEW LITHIUM TITANIUM FERRITES	149
4.1 INTRODUCTION.....	151
4.2 STRUCTURAL STUDIES ON THE M_3O_4 (M=Li, Fe, Ti) TERNARY PHASE DIAGRAM.....	152
4.2.1 <i>Introduction</i>	152
4.2.2 <i>Results</i>	154
4.2.2.1 XRD studies on the “ Li_3O_4 ”-“ Ti_3O_4 ”- Fe_3O_4 phase diagram.....	154
4.2.2.2 Results.....	156
4.2.2.3 X-ray diffraction and high temperature neutron diffraction studies on the $LiFe_xTi_{2-x}O_4$ solid solution	161
4.2.3 <i>Discussion</i>	173
4.3 LOW TEMPERATURE STUDIES OF THE $LiFe_xTi_{2-x}O_4$ SOLID SOLUTION.....	176
4.3.1 <i>Results for $LiFe_{0.5}Ti_{1.5}O_4$</i>	176
4.3.2 <i>Results for $LiFe_{0.75}Ti_{1.25}O_4$ and $LiFeTiO_4$</i>	182
4.3.3 <i>Discussion</i>	192
4.4 ELECTROCHEMICAL STUDIES OF THE $LiFe_xTi_{2-x}O_4$ SOLID SOLUTION	194
4.4.1 <i>Introduction</i>	194
4.4.2 <i>Results</i>	195
4.4.3 <i>In-situ and ex-situ XRD studies</i>	205
4.4.3.1 Introduction and experimental.....	205
4.4.3.2 Results.....	205
4.4.4 <i>Electrochemistry conclusions</i>	208
4.5 SUMMARY	209

4.1 Introduction

The area of science relating to ferrite spinels is a very extensive and well studied one, with work dating back more than 50 years. Undoubtedly the best known, and probably most extensively investigated, spinel ferrite is magnetite, Fe_3O_4 , with literally countless Mössbauer, X-ray and Neutron diffraction studies being published in the search for better understanding of the charge ordering Verwey transition ¹.

Less well known, but almost as well characterised, are the technologically important family of lithium ferrites. Lithium ferrite itself, LiFe_5O_8 , along with its Ti, Mn and Zn doped derivatives, has found application in microwave electronics ^{2,3}, as well as showing promise as a lithium intercalation host ⁴. Considering the technological importance of these materials, it is therefore not surprising that there has been a great deal of work published in the area, particularly in the area with which we are concerned - titanium substituted derivatives. In particular, much work has focussed on the LiFe_5O_8 - $\text{Li}_4\text{Ti}_5\text{O}_{12}$ solid solution. Blasse ⁵, in 1964, first reported the existence of the solid solution, and based on magnetic and structural data proposed a model of cation substitution for the system, $(\text{Li}_{0.5x}\text{Fe}_{1-0.5x})^{\text{tet}}[\text{Li}_{0.5}\text{Fe}_{1.5-x}\text{Ti}_x]^{\text{oct}}\text{O}_4$. Also reported were two areas of cation ordering in the system, lying at $0 \leq x \leq 0.33$, and $1.22 \leq x \leq 1.56$. Rather surprisingly though, given the extensive investigation of these materials, there appears to be little literature relating to reduced titanium or lithium ferrites. Indeed, the only reports on reduced materials that we can find are related to magnetite and the solid solution linking it to Ulvöspinel.

In this work, then, we present the results of our investigations on the ternary, spinel stoichiometry, “ Li_3O_4 ”- Fe_3O_4 -“ Ti_3O_4 ” phase diagram. We have chosen not to repeat studies on the $\text{Li}_4\text{Ti}_5\text{O}_{12}$ - LiFe_5O_8 solid solution, instead taking the results of previous studies and combining them with our new work on the reduced stoichiometries. We present below a general structural study of the area of the phase diagram lying between the Fe^{3+} and Fe^{2+} lines, along with more in depth studies on a new solid solution lying within the phase diagram, $\text{LiFe}_x\text{Ti}_{2-x}\text{O}_4$.

4.2 Structural studies on the M_3O_4 ($M=Li, Fe, Ti$) ternary phase diagram.

4.2.1 Introduction

The cation distribution in spinels has long been the subject of intense investigation, as with understanding of the site preference of different cations, the properties of any given material can be tailored to a surprising degree. Historically, this has been most applicable for the ferrite spinels, with many materials being carefully optimised for application in microwave electronics, power transformers and magnetic recording media in particular ⁶. More recently though, focus has moved towards the optimisation of materials such as the lithium manganates and lithium titanates for use in Li-ion batteries ^{7,8}.

For all of these applications the distribution of cations across the two crystallographic cation sites is of critical importance in determining the material's properties. In the ferrites for example, Fe is known to happily occupy both tetrahedral and octahedral sites, but this can be carefully altered by judicious doping of cations such as Zn^{2+} or Ni^{2+} , which exhibit a stronger preference for octahedral or tetrahedral coordination. With such substitutions, the magnetism of a material can be carefully tailored by the dilution of Fe on one or both sublattices, with at high dilution levels, weakening of the superexchange forces between the 8a and 16d sites, leading to the formation of canted and spin-glass type magnetism.

A further feature of the spinels is the possibility of cation ordering. Several forms of ordering are possible (see chapter 1), but by far the most common is the 1:3 octahedral ordering first reported for $LiFe_5O_8$ ⁹, in which the disordered 16d octahedral site orders to form a 4b and a 12d site (shown below in Figure 4-1). The symmetry of the system becomes primitive, though it remains cubic. Many 1:3 octahedrally ordered spinels are known, involving a variety of cations including Zn, Mg, Ti, Co and Ni ¹⁰, as well as the more thoroughly investigated systems joining $LiFe_5O_8$, $LiMn_2O_4$ ¹¹, $LiGa_5O_8$ ¹² and

LiAl_5O_8 ¹³. In all cases though, the driving force for the ordering appears to be the separation of octahedral lithium onto the new ordered 4b sites.

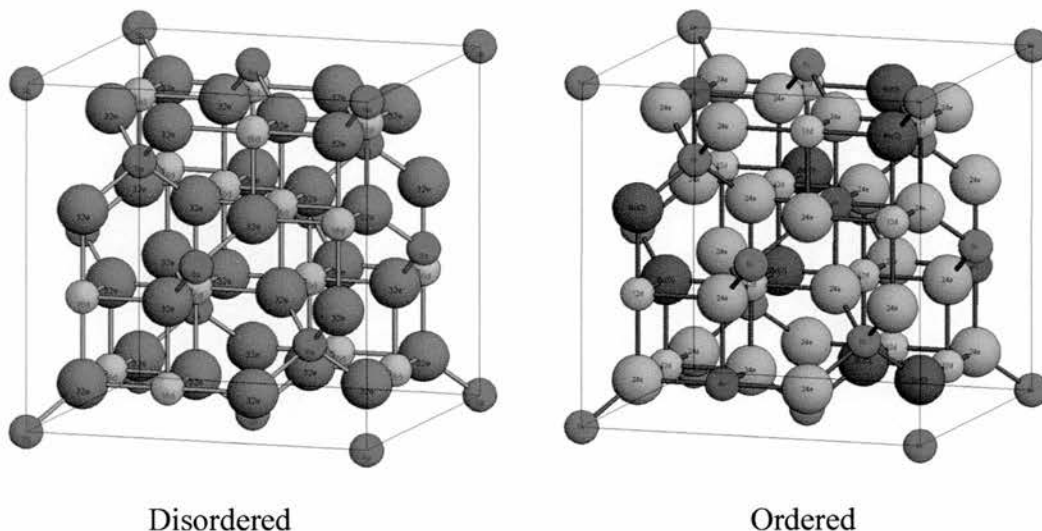


Figure 4-1: A comparison of the disordered and 1:3 octahedrally ordered spinels.

In this work, we have concerned ourselves with the lithium titanium ferrites, particularly the $\text{Li}_{0.5+0.5x}\text{Fe}_{2.5-1.5x}\text{Ti}_x\text{O}_4$ solid solution and its reduced derivatives.

In our studies of the reduced derivatives of this system we have made a provisional XRD structural study of an area of the spinel stoichiometry “ Li_3O_4 ”- Fe_3O_4 ”-“ Ti_3O_4 ” ternary phase diagram, along with a more detailed XRD, neutron diffraction, and magnetic study of a solid solution, $\text{LiFe}_x\text{Ti}_{2-x}\text{O}_4$, lying within the phase diagram. The focus of the work has been to characterise the ordering and cation distribution in the system rather than to evaluate the possible applications of the materials from a magnetic perspective. Nevertheless, a neutron diffraction study of the magnetic ordering has been attempted, along with some provisional Mössbauer and magnetic susceptibility studies.

For this work all samples were prepared in the manner described in chapter 2, from oxide starting materials. Phase identification for all materials was carried out using a Philips PW3810 reflectance diffractometer, equipped with a detector end monochromator. For accurate evaluation of the cation distribution in the $\text{LiFe}_x\text{Ti}_{2-x}\text{O}_4$ series, two Stöe StadiP diffractometers were used, one equipped with a monochromated Cu x-ray source, the other with an Fe x-ray source. These two radiation sources were

employed in order to try to minimise the impact of x-ray fluorescence on our results: Fe fluoresces in Cu radiation, Ti in Fe radiation. Neutron diffraction data were collected at two facilities: High temperature data, for determination of cation occupancies, were collected using the Polaris instrument at Rutherford Appleton Laboratories, England. Low temperature, magnetic, neutron data were collected using the D2B instrument at the Institut Laue Langevin, Grenoble. The reason for the high temperature data was that the samples are magnetically ordered at room temperature, and so for accurate structural characterisation data above the materials' respective Curie temperatures was required. For these samples, the data were collected at $\sim 180^\circ\text{C}$.

4.2.2 Results

General XRD results for the phase diagram are presented first, followed by high temperature neutron studies and high resolution XRD studies on the $\text{LiFe}_x\text{Ti}_{2-x}\text{O}_4$ solid solution series. Finally, the results of our low temperature neutron diffraction, magnetic susceptibility and Mössbauer studies will be presented.

4.2.2.1 XRD studies on the “ Li_3O_4 ”-“ Ti_3O_4 ”- Fe_3O_4 phase diagram

We present below the results of our structural studies on the “ Li_3O_4 ”-“ Ti_3O_4 ”- Fe_3O_4 phase diagram. It should be noted that the results presented for the $\text{Li}_4\text{Ti}_5\text{O}_{12}$ -join LiFe_5O_8 (except for LiFeTiO_4) are taken from the literature ¹⁴.

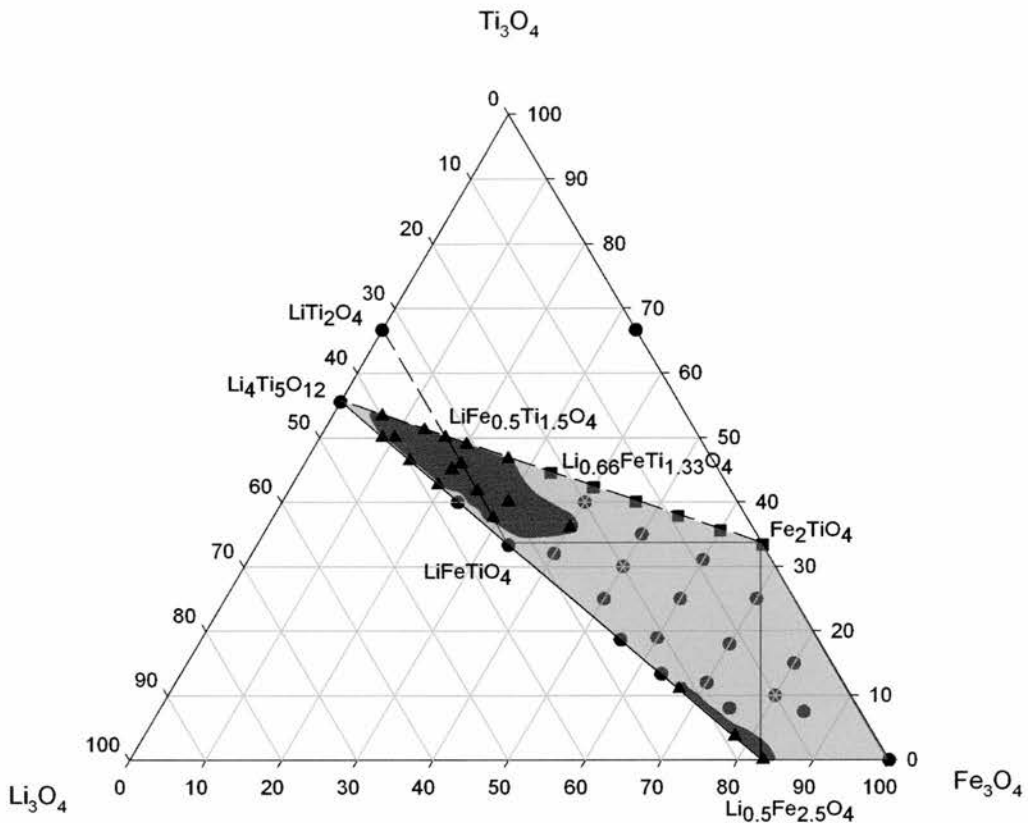


Figure 4-2 : The “ Li_3O_4 ”-“ Ti_3O_4 ”- Fe_3O_4 phase diagram. The lightly shaded area is disordered spinel, the dark areas are 1:3 octahedrally ordered spinel. The filled circles indicate disordered spinel compositions, triangles indicate ordered spinel and squares indicate disordered spinel with ilmenite impurity.

For the phase diagram we found two regions of order to exist, with much of the rest of the phase diagram exhibiting the more usual disordered spinel structure, space group $Fd-3m$. It should be noted that some samples exhibited a small quantity of a second phase thought to be rutile from the position of the strongest peak at $\sim 28^\circ 2\theta$. This is not unusual for samples of this kind, and has been reported before¹⁴. The impurity was not found to be dependent on composition or firing regime, and where more than one sample was made of a given stoichiometry, the impurity peaks often varied in intensity, sometimes disappearing entirely.

For samples in the $\text{Li}_{4/3x}\text{Fe}_{2-2x}\text{Ti}_{1+2/3x}\text{O}_4$ solid solution (end members $\text{Li}_4\text{Ti}_5\text{O}_{12}$ and Fe_2TiO_4), it was found that for values of $x \leq 0.5$, a quantity of ilmenite impurity was observed. As Fe_2TiO_4 is reported phase pure elsewhere in literature, the presence of this

impurity is thought to be linked to the firing temperature of the samples: Fe_2TiO_4 is reported as being made at 1200°C , whereas our samples were all fired at 1000°C . Similar behaviour has been seen in other spinels, such as Mg_2TiO_4 , and likely indicates that at this temperature the stoichiometry is in a two phase region of the phase diagram.

With regard to the ordered samples, the region lying near LiFe_5O_8 we will cover no further here as the data are taken from the literature¹⁴, and no ordering was found for the reduced samples. Instead we will focus on the region lying towards the Fe poor end of the phase diagram. It can be seen that this region extends over a large range of stoichiometries and also from the Fe^{3+} line to the Fe^{2+} line. The region of the ordering is a little surprising, in respect to both the samples which order and those which do not: It is normally only expected that such ordering occurs where there is a clear 1:3 ratio of cations on the octahedral sites. In this phase diagram, there is clearly enough lithium in many disordered samples to enable ordering to occur. Indeed the LiFeTiO_4 composition has been found previously to have a composition and cation distribution almost ideal for ordering to occur¹⁵, and yet it does not.

4.2.2.2 Results

Plotting relevant peak intensities and FWHM's (Full Width at Half Maximum) for the $\text{Li}_{4/3x}\text{Fe}_{2-2x}\text{Ti}_{1+2/3x}\text{O}_4$ and $\text{LiFe}_x\text{Ti}_{2-x}\text{O}_4$ solid solutions we can see some interesting trends:

- The unit cell for the $\text{Li}_{4/3-4/3x}\text{Fe}_{2x}\text{Ti}_{5/3-2/3x}\text{O}_4$ series is seen to increase linearly with Fe content, and decrease similarly with increasing Ti and Li contents.
- The (220) peak intensity increases steadily with increasing Fe substitution for the $\text{Li}_{4/3-4/3x}\text{Fe}_{2x}\text{Ti}_{5/3-2/3x}\text{O}_4$ series, from $\text{Li}_4\text{Ti}_5\text{O}_{12}$ ($x=0$) to $\text{Li}_{0.66}\text{FeTi}_{1.33}\text{O}_4$ ($x=0.5$) before flattening off for $x > 0.5$. For the $\text{LiFe}_x\text{Ti}_{2-x}\text{O}_4$ series it is seen to remain fairly constant despite the substitution of Fe with Ti and the changing oxidation states related to this.
- The intensity of the ordering peaks (210) and (211) show a maximum for $\text{LiFe}_{0.5}\text{Ti}_{1.5}\text{O}_4$, with intensity decreasing sharply when moving in any direction away from this composition on the phase diagram. The peak

widths are seen to behave in a very similar fashion, being sharpest for $\text{LiFe}_{0.5}\text{Ti}_{1.5}\text{O}_4$ and steadily broadening as composition moves towards the disordered region.

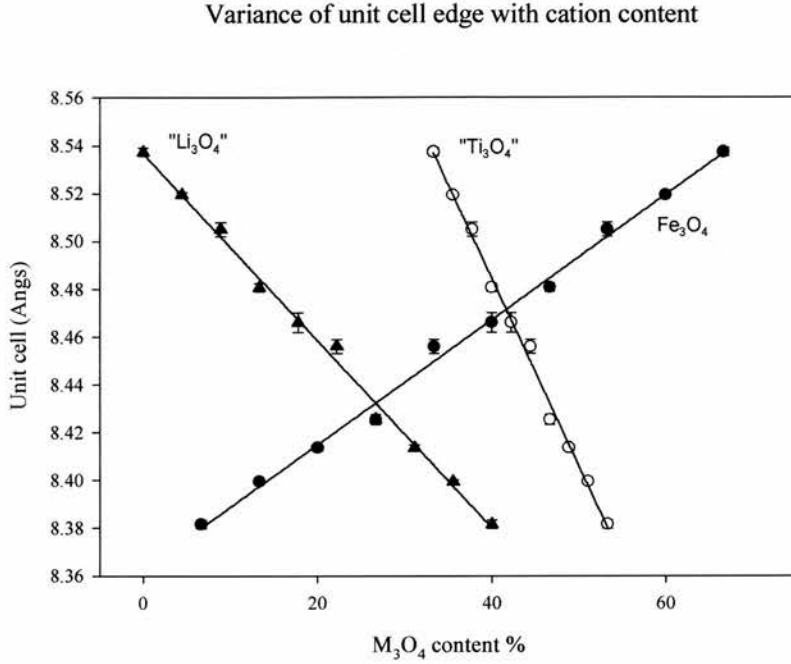


Figure 4-3: The variation of unit cell with changing cation stoichiometry for the $\text{Li}_{4/3-4/3x}\text{Fe}_{2x}\text{Ti}_{5/3-2/3x}\text{O}_4$ solid solution.

Variation of (210), (211) and (220) intensity with Fe content in the $\text{Li}_4\text{Ti}_5\text{O}_{12}\text{-Fe}_2\text{TiO}_4$ and $\text{LiFe}_{0.5}\text{Ti}_{1.5}\text{O}_4\text{-LiFeTiO}_4$ solid solutions

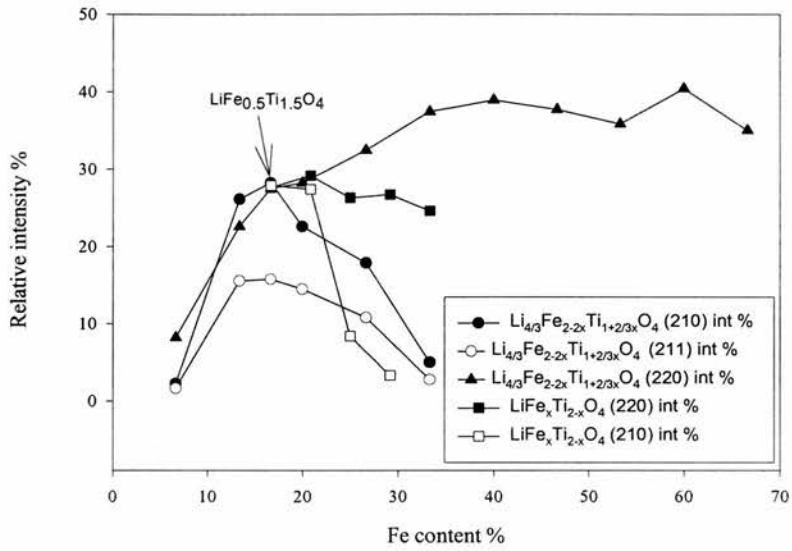


Figure 4-4: Variation of the (210), (211) and (220) peak intensities with Fe content for the $\text{Li}_{4/3}\text{-}4/3x\text{Fe}_{2x}\text{Ti}_{5/3-2/3x}\text{O}_4$ and $\text{LiFe}_x\text{Ti}_{2-x}\text{O}_4$ solid solutions.

Plot of (210) FWHM's for the $\text{Li}_{4/3}\text{Fe}_{2-2x}\text{Ti}_{1+2/3x}\text{O}_4$ and $\text{LiFe}_x\text{Ti}_{2-x}\text{O}_4$ solid solutions

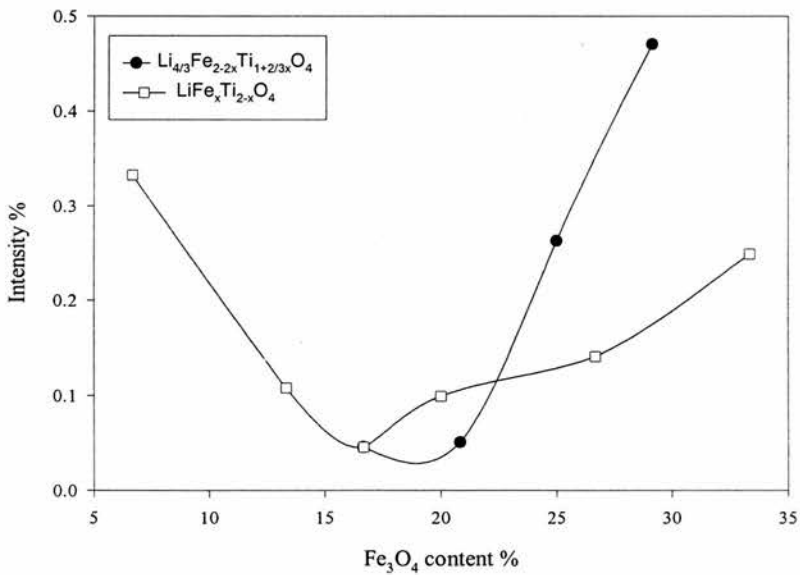


Figure 4-5: Variation of the FWHM for the (210) ordering peaks of the $\text{Li}_{4/3-4/3x}\text{Fe}_{2x}\text{Ti}_{5/3-2/3x}\text{O}_4$ and $\text{LiFe}_x\text{Ti}_{2-x}\text{O}_4$ solid solutions with changing Fe_3O_4 content.

Extending this to include the (220) peak intensities and unit cell edges for the phase diagram as a whole, we see that the observations for the $\text{Li}_{4/3-4/3x}\text{Fe}_{2x}\text{Ti}_{5/3-2/3x}\text{O}_4$ solid solution hold true for the rest of the phase diagram. The (220) peak intensities are predominantly dependent on the Fe content of the sample, with a flattening off at higher Fe contents, whilst the unit cell edges are dependent mainly on the lithium content of the sample, increasing with decreasing Li content.

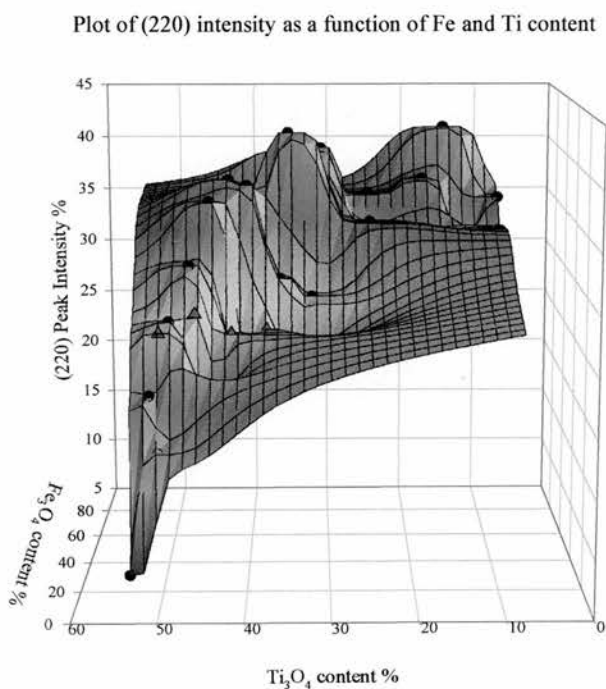


Figure 4-6: Variation of (220) peak intensities with Fe and Ti content for the “ Li_3O_4 ”-“ Ti_3O_4 ”- Fe_3O_4 phase diagram. For comparison the $\text{LiFe}_x\text{Ti}_{2-x}\text{O}_4$ solid solution is shown in blue.

Plot of (220) intensity as a function of Fe and Li content

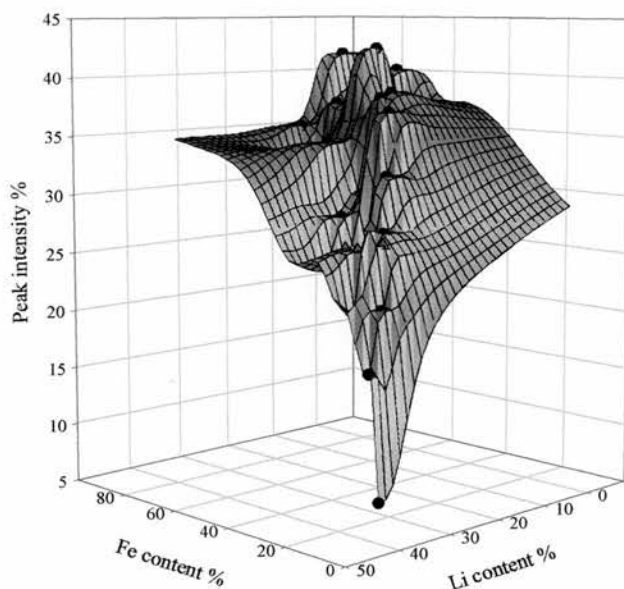


Figure 4-7: Variation of (220) peak intensities with Fe and Li content for the “ Li_3O_4 ”-“ Ti_3O_4 ”- Fe_3O_4 phase diagram. For comparison the $\text{LiFe}_x\text{Ti}_{2-x}\text{O}_4$ solid solution is shown in blue.

Unit cell as a function of Li and Fe content

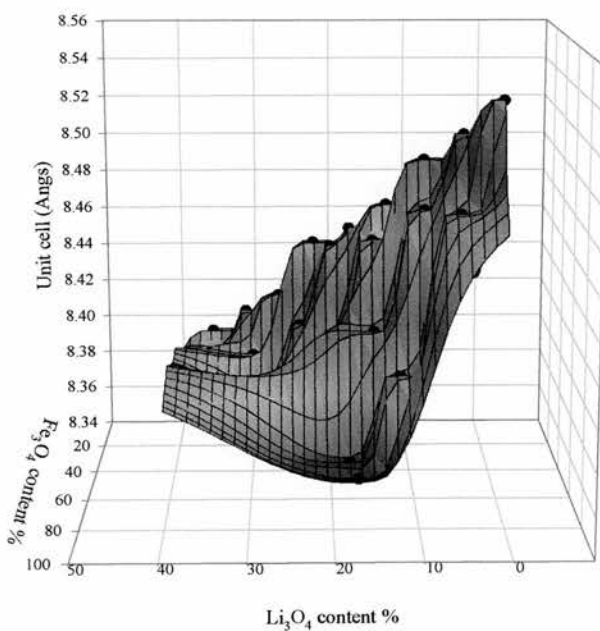


Figure 4-8: Variation of unit cell edge with Fe and Li content for the “ Li_3O_4 ”-“ Ti_3O_4 ”- Fe_3O_4 phase diagram.

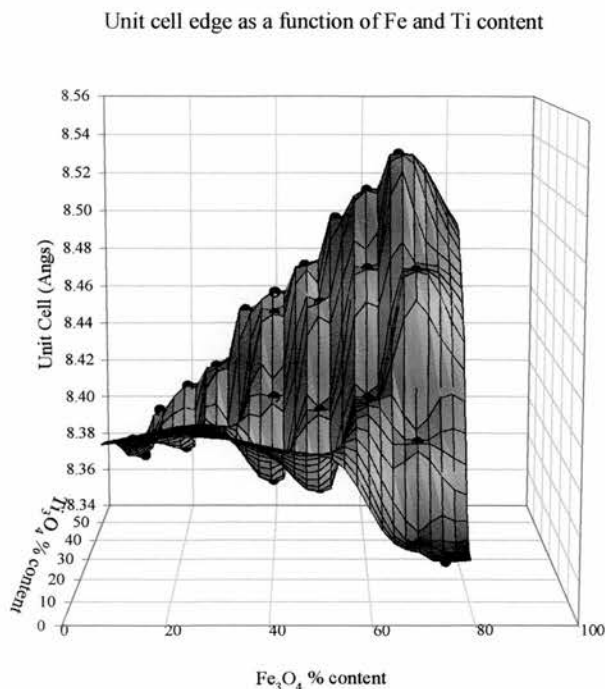


Figure 4-9: Variation of unit cell edge with Fe and Ti content for the “Li₃O₄”-“Ti₃O₄”-Fe₃O₄ phase diagram

4.2.2.3 X-ray diffraction and high temperature neutron diffraction studies on the LiFe_xTi_{2-x}O₄ solid solution

As mentioned earlier, in order to more accurately probe the cation distribution in this system, particularly across the ordered 4b and 12d octahedral sites, high resolution XRD and neutron diffraction data were obtained, using two Stöe StadiP X-ray diffractometers and the Polaris neutron diffraction instrument at Rutherford Appleton Labs. It was intended that the two techniques would be used in a complementary fashion, but with a weighting towards the neutron data due to its larger d-spacing range and ability to differentiate well between Fe and Ti.

During the course of our initial refinements however, it became apparent that there were several difficulties which made the structure evaluation somewhat harder than was originally expected:

- A very high and noisy background was found for the XRD data collected using both Fe and Cu radiation. This was attributed to be fluorescence of the sample Fe and Ti in respectively Cu and Fe radiation, and made it difficult to obtain accurate 8c, 4b and 12d occupancies for the system using just this data. Attempts were made to counter the fluorescence by placing Ni foil in front of the detector to act as a filter, but the loss of intensity this caused was unacceptable. As we could find no other solution we chose to use the Fe and Cu radiation in such a way as to minimise the effect: Data on $\text{LiFe}_{0.5}\text{Ti}_{1.5}\text{O}_4$ were collected using Cu radiation, whilst the rest were collected using an Fe source.
- It was found for the neutron diffraction data collected for LiFeTiO_4 that neither 16d Uiso's or occupancies could be refined without the refinement becoming very unstable. This was rather surprising, as the quality of the visual fit (Figure 4-10 below) was excellent, and a Rwp of 1.5% was being reported for the refinement:

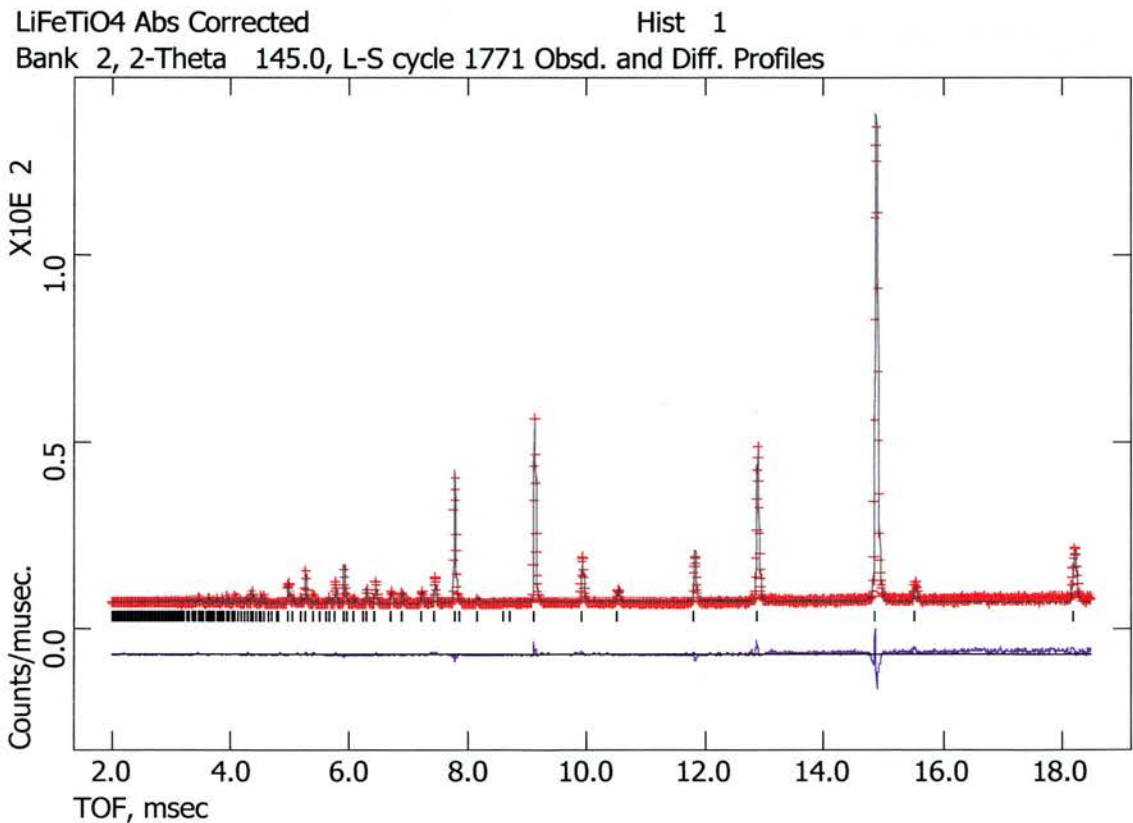


Figure 4-10: Refined tof neutron diffraction pattern for LiFeTiO_4 , according to the model of Arillo *et al.*

The source of this difficulty was eventually traced using Fobs and Fcalc maps generated for the refinement, which show that there is effectively no scattering from the 16d site for this material. A short “back of an envelope” calculation using the weighted scattering factors for Li, Fe and Ti according to the Arillo model¹⁵, shows how this comes about:

$$\begin{aligned}\text{Scattering from site} &= F_{Li}(SOF_{Li}) + F_{Fe}(SOF_{Fe}) + F_{Ti}(SOF_{Ti}) \\ &= -1.9 (0.266) + 9.4 (0.234) + -3.4 (0.5) \\ &\approx \mathbf{0.006.....}\end{aligned}$$

The calculated scattering from the 16d site in this sample is thus effectively zero, explaining why the refinement software is unable to vary parameters on this site: There is no scattering density for the calculation to “work with”. It should be noted here that this in itself is a “proof” of the model of Arillo *et al*, and as both the XRD data and neutron refined occupancies for 8a agreed well with the model, we concluded that their model is essentially correct with respect to our data.

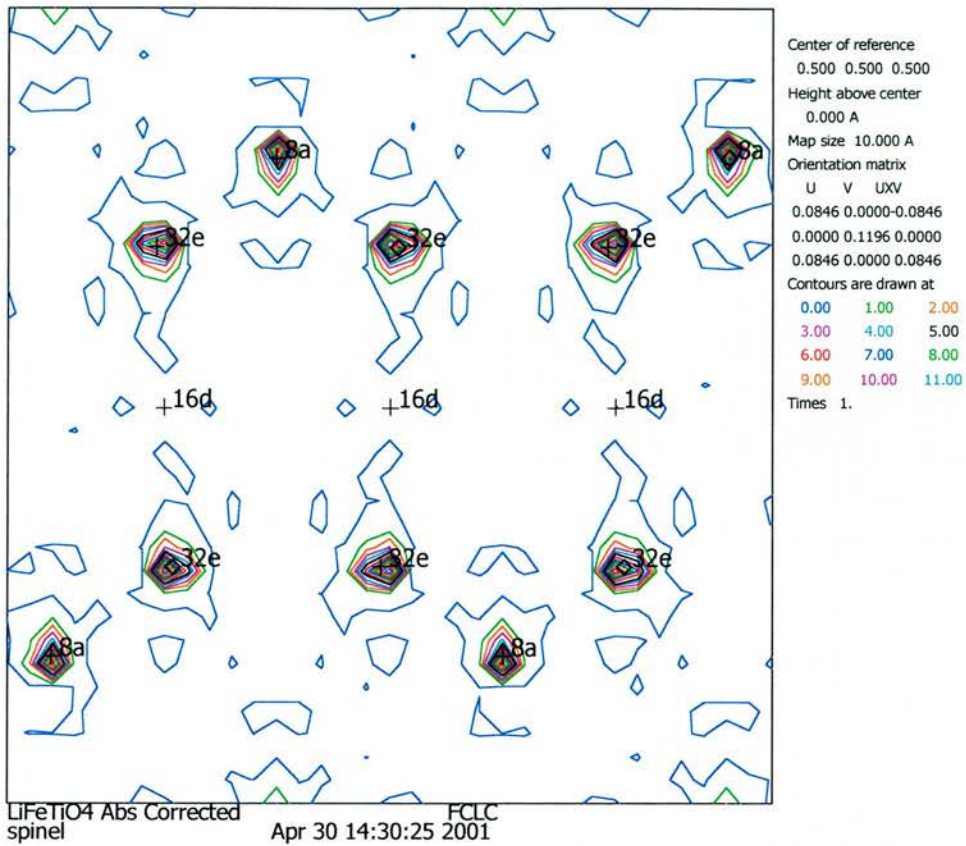


Figure 4-11: Fcalc map for LiFeTiO_4 showing the absence of scattering from 16d.

In addition to the scattering difficulties encountered for the disordered LiFeTiO_4 , it was found for the ordered samples in the solid solution that the strong ordering peaks evident in the XRD patterns (see Figure 4-12 below) were almost entirely absent in the neutron patterns, which caused problems when attempting to refine the cation occupancies of the 4b and 12d sites. The effect was so marked that even the data for strongly ordered $\text{LiFe}_{0.5}\text{Ti}_{1.5}\text{O}_4$ could be fitted almost as well to the disordered $Fd-3m$ space group as to the ordered $P4_332$ (see Figure 4-13 below).

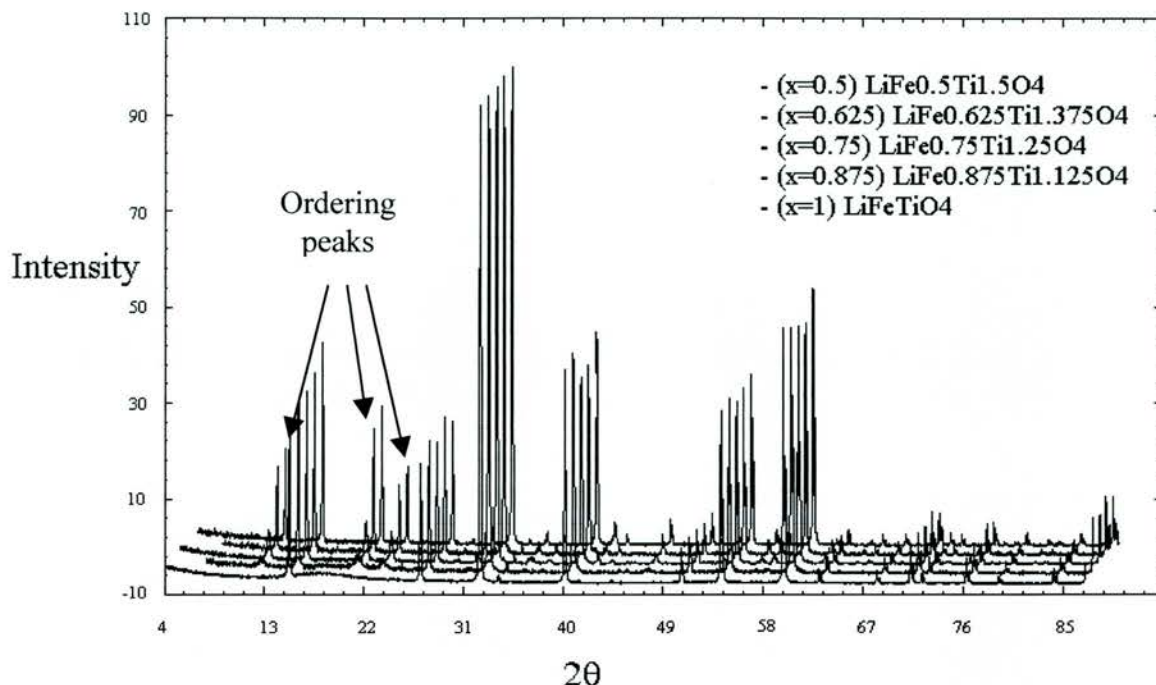


Figure 4-12: (Philips) XRD patterns for the $\text{LiFe}_x\text{Ti}_{2-x}\text{O}_4$ solid solution, plotted with x decreasing from front (LiFeTiO_4) to back ($\text{LiFe}_{0.5}\text{Ti}_{1.5}\text{O}_4$). The growth of the ordering peaks with decreasing x can be clearly seen.

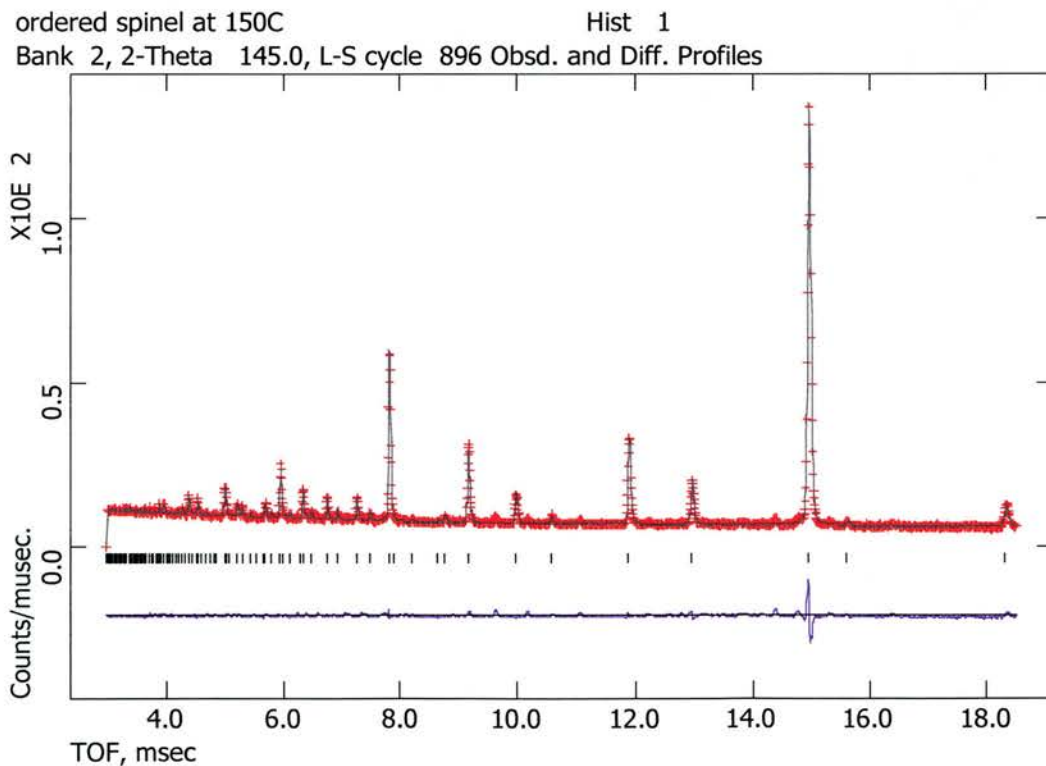


Figure 4-13: Neutron diffraction pattern of as-made $\text{LiFe}_{0.5}\text{Ti}_{1.5}\text{O}_4$ refined to space group Fd-3m .

Initially it was suspected that this might be a repeat of the phenomenon in LiFeTiO_4 , but investigation of the Fourier maps for these refinements showed that this was not the

case. It was found instead, that this problem was related to the calculated scattering factors for the ordering peaks, which whilst strong in x-ray radiation, were found to be weak in neutron radiation. This was confirmed both by hand calculation and by the generation of a theoretical “expected” pattern using our expected structural model, $(\text{LiFe})^{8c}(\text{Li})^{4b}(\text{Ti})^{12d}\text{O}_4$.

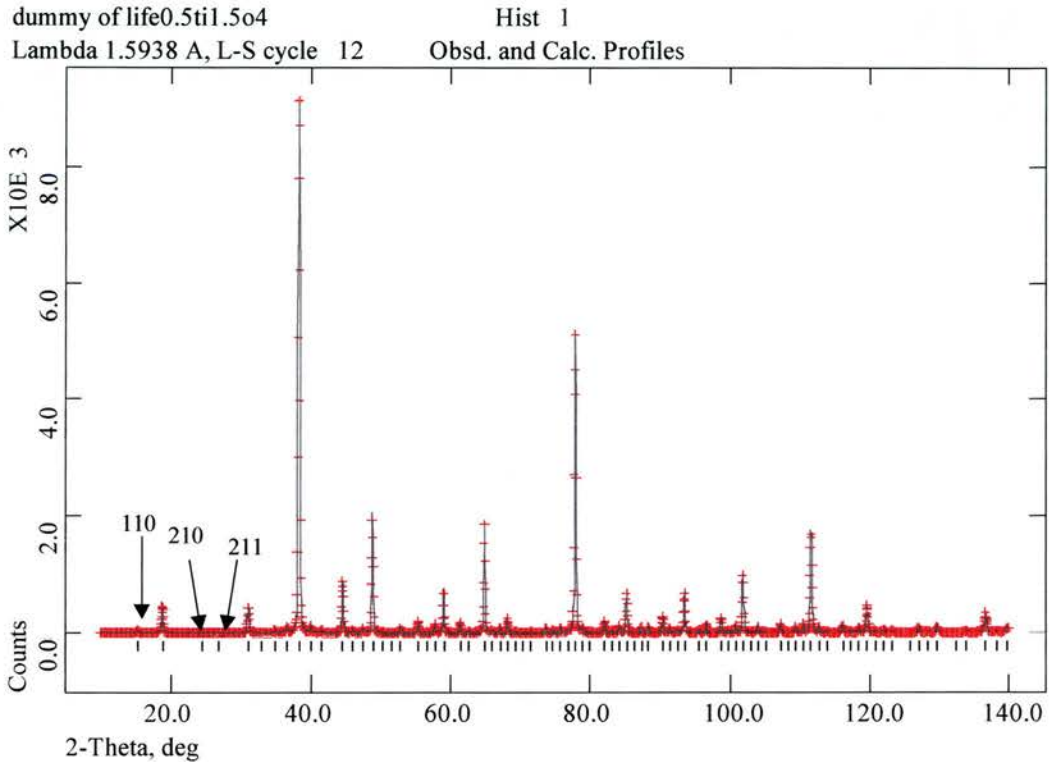


Figure 4-14: Calculated expected diffraction pattern using constant wavelength radiation for clarity. Three of the “absent” ordering peaks are labelled.

From here it was deemed that a new approach was required to obtain the cation occupancies for the system, as direct refinement of 4b/12d sites was impossible using either XRD or neutron diffraction, and the former would give no information regarding Fe/Ti ratios anyway, owing to the similar scattering factors of Fe and Ti.

To overcome these problems a new approach was used. Firstly, the stoichiometries of the samples were checked by refining the neutron data using the Fd-3m disordered space group. These were found to be in good agreement with expected values.

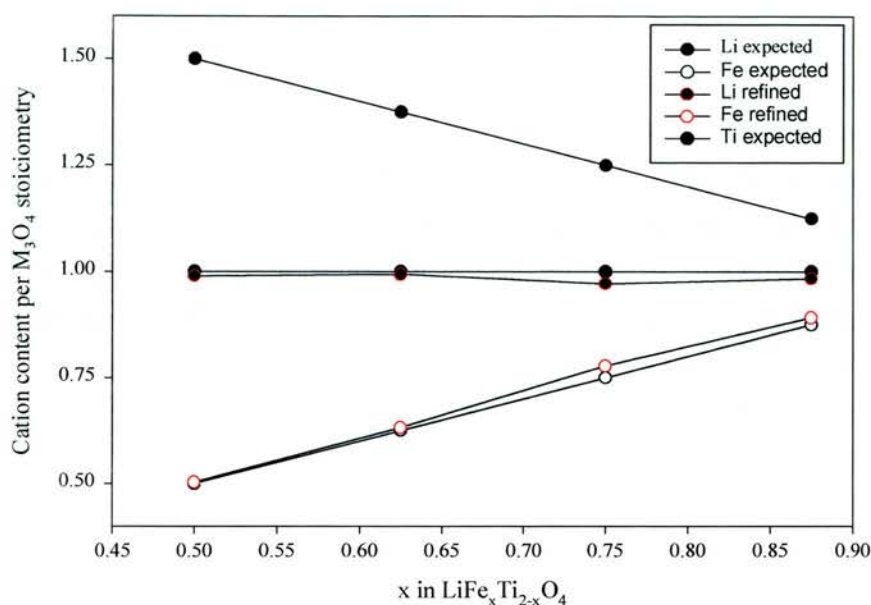


Figure 4-15: Refined and expected cation stoichiometries for Li and Fe in $\text{LiFe}_x\text{Ti}_{2-x}\text{O}_4$. Ti was held steady for the refinements.

Following this, the neutron data were further refined to give good A site occupancies, as scattering from the site was found to be strong in all samples (see F_{calc} map for LiFeTiO_4 earlier). This was carried out for both ordered and disordered space groups to ensure that the result was not influenced by trying to fit the weak ordering peaks of the $P4_332$ space group. It was found that, with the exception of most highly ordered sample, $\text{LiFe}_{0.5}\text{Ti}_{1.5}\text{O}_4$, there was excellent agreement between the results for the two space groups. Even for this sample there is reasonable agreement, and after some consideration the value obtained for the ordered space group refinement was used in the next stage of refinements.

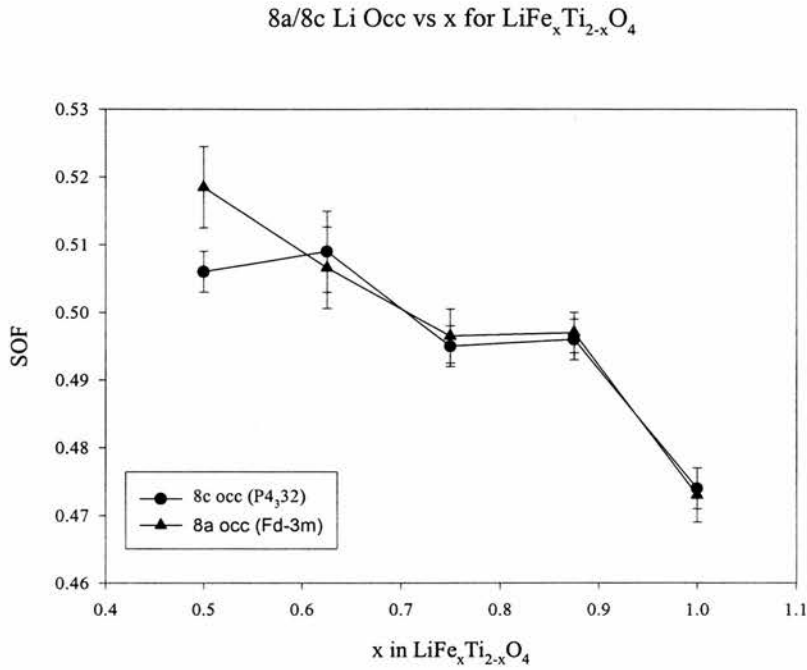
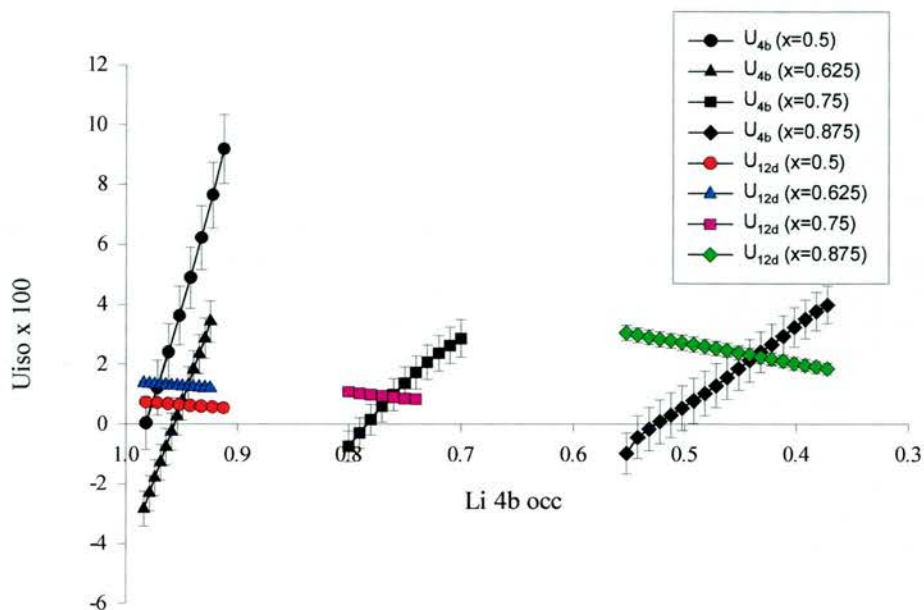


Figure 4-16: Refined A site occupancies for $\text{LiFe}_x\text{Ti}_{2-x}\text{O}_4$ for both disordered and ordered space groups.

The A site occupancies thus obtained were then inputted into the XRD refinements and held whilst the Li/M (where M=Fe/Ti) ratios on the 4b and 12d were manually changed and the temperature factors refined. The goal here being to infer sensible occupancies from the refined Uiso's. The results of this are shown in Figure 4-17.

4b and 12d Uiso's as a function of Li occupancy on 4b (XRD data)

**Figure 4-17: Refined 4b and 12d Uiso's as a function of Li 4b occupancy.**

At this point it was necessary to apply a consistent and realistic model that related the temperature factors with the site occupancies, and which could be applied to both XRD and neutron diffraction data. It was obviously impossible to assign occupancies based upon absolute Uiso's, as the increasing disorder and weakened neutron B site scattering with increasing Fe content caused both 12d and 4b thermal factors to rise rapidly with increasing x , especially in the neutron diffraction data (see Figure 4-18 below). It was therefore decided that a model based upon relative Uiso's was more applicable.

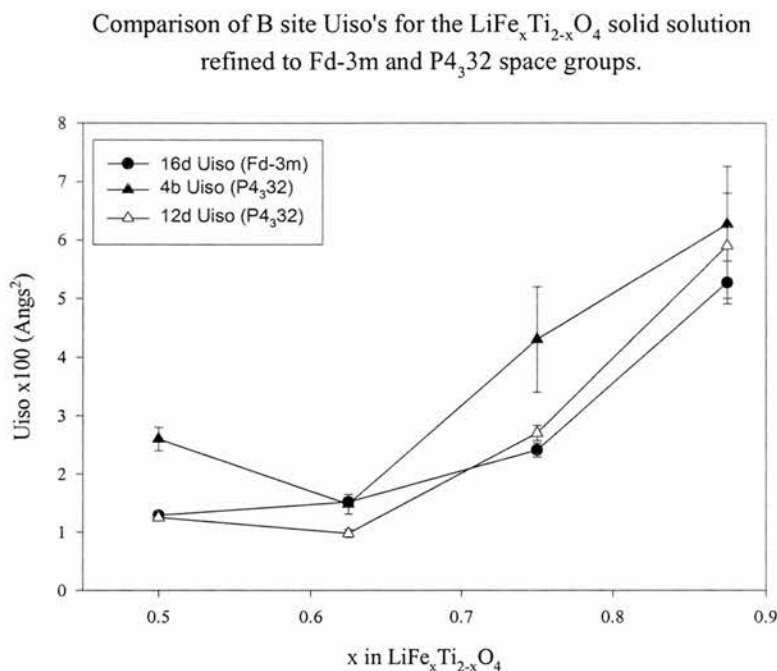


Figure 4-18: Refined temperature factors for the B site of the $\text{LiFe}_x\text{Ti}_{2-x}\text{O}_4$ solid solution as a function of x.

A review of the literature yielded values for several materials where Li entirely occupies the 4b site, and in these cases the 4b Uiso's are generally several times those of 12d^{16,17}. However, in materials such as LiAl_5O_8 ¹⁸, $\text{Li}_2\text{MgTi}_3\text{O}_8$ and $\text{Li}_2\text{CoGe}_3\text{O}_8$ ¹⁰ where greater cation disorder is evident across the B sites, this gap rapidly drops with increasing disorder and the values become more comparable. After considering these published values in conjunction with our data we formulated a model based upon a sliding scale of relative Uiso's going from $U_{4b}=2U_{12d}$ at $x=0.5$ through to a nominal value of $U_{4b}=U_{12d}$ for $x=1$ (which is fully disordered, and so 4b and 12d are equivalent). Accordingly we took values for the B site Li/M ratios ($M=\text{Fe}/\text{Ti}$) from the XRD data, put these back into the neutron diffraction data and in a similar fashion to above, refined the 4b and 12d temperature factors as a function of the Fe/Ti ratios (see Figure 4-19 below). This then gave final cation distributions for the system. These are shown graphically in Figure 4-20 and Figure 4-21 and are tabulated in Table 4-1.

This approach was obviously less than ideal in that there was no direct refinement of the cation site occupancies for 4b and 12d, and so the values obtained were the product

of informed speculation. Thus we have not as such calculated a unique solution, but have instead calculated a range of sensible solutions and picked the best. Despite this, though, it can be seen clearly from the plots that the ranges in which we are working are very small (< 0.05 SOF), and not far from the resolution which could be expected if the occupancy parameters were refineable.

A further consequence of the method is that assessment of the error in the occupancies was difficult, as not having refined the occupancy variables, there were no direct calculated statistics to use. We again took a speculative approach, and assessed a sensible limiting factor to be the occupancy at which $U_{4b}=U_{12d}$. The difference between this occupancy and our “chosen” one was taken to be a sensible error. These calculated errors are plotted on Figure 4-20 and Figure 4-21.

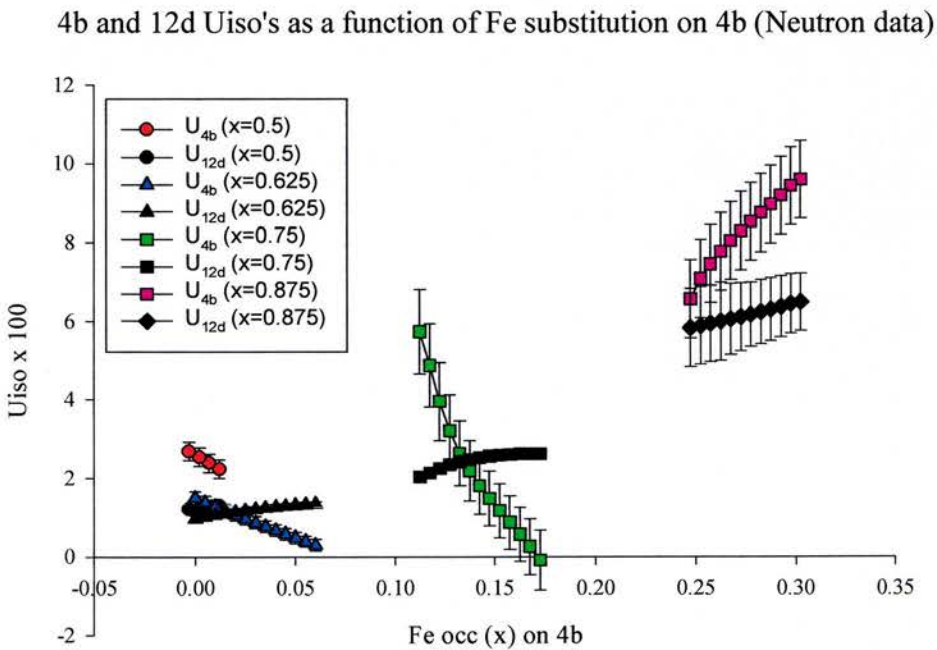


Figure 4-19: Refined 4b and 12d Uiso's as a function of Fe 4b occupancy.

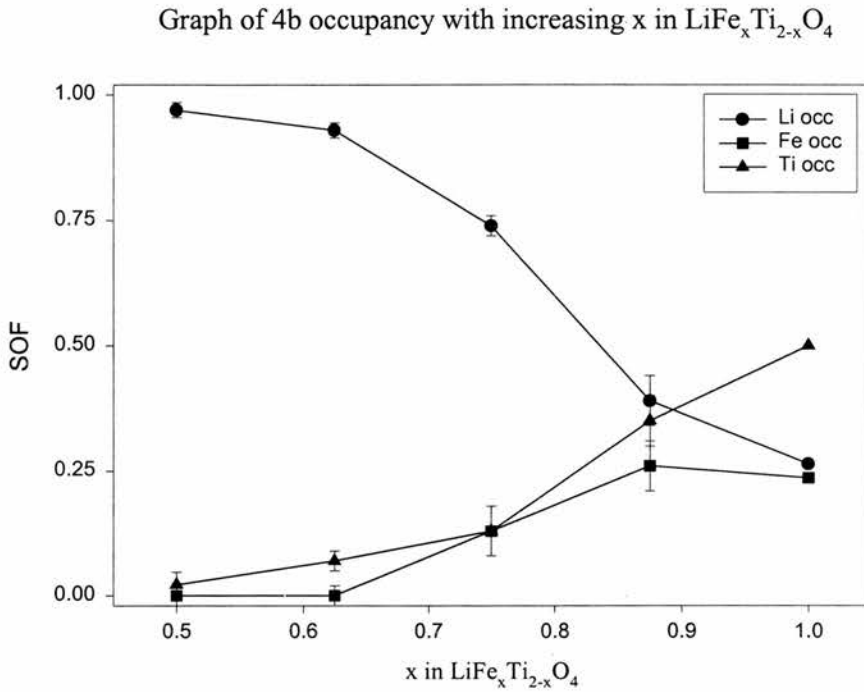


Figure 4-20: 4b cation occupancies as a function of x for the $\text{LiFe}_x\text{Ti}_{2-x}\text{O}_4$ solid solution. Note that values for x=1 are added for comparison.

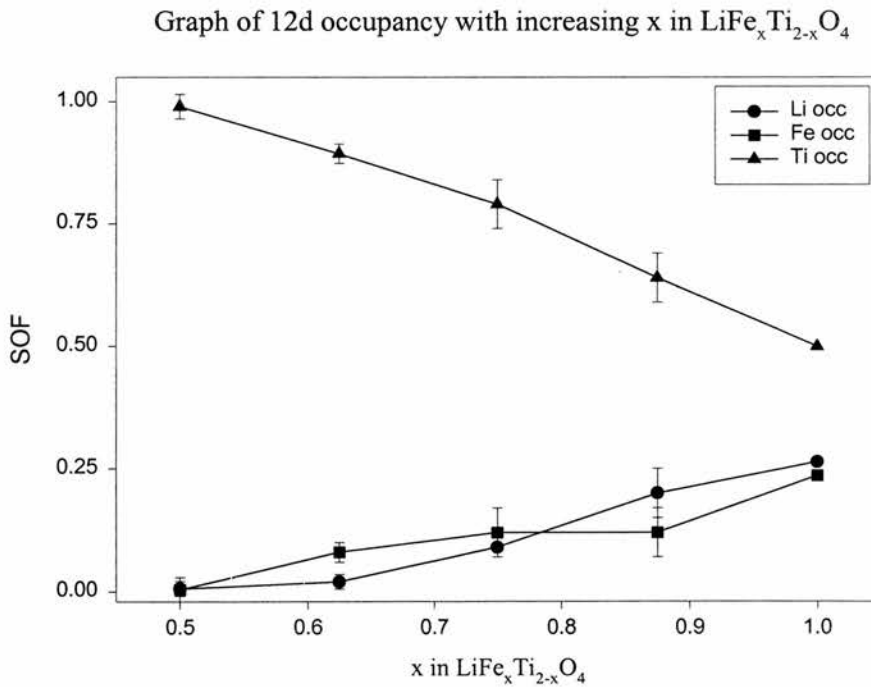


Figure 4-21: 12d cation occupancies as a function of x for the $\text{LiFe}_x\text{Ti}_{2-x}\text{O}_4$ solid solution. Note that values for x=1 are added for comparison.

Sample	x in $\text{LiFe}_x\text{Ti}_{2-x}\text{O}_4$	Cation Distribution
$\text{LiFe}_{0.5}\text{Ti}_{1.5}\text{O}_4$	0.5	$(\text{Li}_{0.506}\text{Fe}_{0.494})^{8c}[(\text{Li}_{0.97}\text{Ti}_{0.03})^{4b}(\text{Li}_{0.006}\text{Fe}_{0.004}\text{Ti}_{0.99})^{12d}]\text{O}_4$
$\text{LiFe}_{0.625}\text{Ti}_{1.375}\text{O}_4$	0.625	$(\text{Li}_{0.509}\text{Fe}_{0.491})^{8c}[(\text{Li}_{0.93}\text{Ti}_{0.07})^{4b}(\text{Li}_{0.02}\text{Fe}_{0.08}\text{Ti}_{0.8933})^{12d}]\text{O}_4$
$\text{LiFe}_{0.75}\text{Ti}_{1.25}\text{O}_4$	0.75	$(\text{Li}_{0.495}\text{Fe}_{0.505})^{8c}[(\text{Li}_{0.74}\text{Fe}_{0.13}\text{Ti}_{0.13})^{4b}(\text{Li}_{0.09}\text{Fe}_{0.12}\text{Ti}_{0.79})^{12d}]\text{O}_4$
$\text{LiFe}_{0.875}\text{Ti}_{1.125}\text{O}_4$	0.875	$(\text{Li}_{0.496}\text{Fe}_{0.504})^{8c}[(\text{Li}_{0.39}\text{Fe}_{0.26}\text{Ti}_{0.35})^{4b}(\text{Li}_{0.20}\text{Fe}_{0.16}\text{Ti}_{0.64})^{12d}]\text{O}_4$
LiFeTiO_4	1	$(\text{Li}_{0.473}\text{Fe}_{0.527})^{8a}[\text{Li}_{0.264}\text{Fe}_{0.236}\text{Ti}_{0.5}]^{16d}\text{O}_4$

Table 4-1: Cation distributions for the $\text{LiFe}_x\text{Ti}_{2-x}\text{O}_4$ solid solution

Sample	Rwp XRD (P4 ₃ 32)	Rwp Neutrons (P4 ₃ 32)	Rwp Neutrons (Fd-3m)
$\text{LiFe}_{0.5}\text{Ti}_{1.5}\text{O}_4$	1.80%	2.87%	1.49%
$\text{LiFe}_{0.625}\text{Ti}_{1.375}\text{O}_4$	2.65%	3.11%	1.93%
$\text{LiFe}_{0.75}\text{Ti}_{1.25}\text{O}_4$	3.51%	2.26%	1.63%
$\text{LiFe}_{0.875}\text{Ti}_{1.125}\text{O}_4$	6.09%	1.65%	1.63%
LiFeTiO_4	3.47%	1.88%	N/A

Table 4-2: Fit parameters for the $\text{LiFe}_x\text{Ti}_{2-x}\text{O}_4$ system.

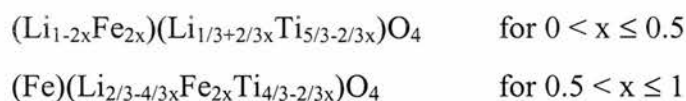
4.2.3 Discussion

In an “ideal” spinel with $u = 0.25$, the (220) peak arises solely from the scattering of the tetrahedral A sites. Whilst in “real” spinels the deviation of u away from ideal (and in our case the loss of symmetry with ordering) causes a small contribution to this reflection from the 32e site, it still remains an excellent measure of the A site occupancy. In particular, for a system such as ours, where the A sites are occupied by cations of strongly contrasting scattering factors, the (220) peak intensity can be of great use in giving information regarding cation distribution.

Analysing the (220) scattering for the $\text{Li}_{4/3-4/3x}\text{Fe}_{2x}\text{Ti}_{5/3-2/3x}\text{O}_4$ solid solution we see two distinct regions of behaviour either side of the $x=0.5$ composition. For lower Fe contents, there is a steady increase in the (220) intensity from $x=0$ to $x=0.5$, for contents with $x>0.5$, the scattering appears to flatten off up to the composition Fe_2TiO_4 . From this we can draw some conclusions regarding the substitution mechanism, the most important of which is that the substituting Fe^{2+} prefers to enter the tetrahedral A site, contradicting the result that would be expected from basic crystal field theory. That the

A site scattering comes from Fe, and not Ti is confirmed by the results of the neutron diffraction study on $\text{LiFe}_{0.5}\text{Ti}_{1.5}\text{O}_4$ which found the A site occupancy to be roughly $\frac{1}{2}$ Fe and $\frac{1}{2}$ Li, with Ti remaining octahedral.

We also observe that the plateau in the (220) intensities above $x=0.5$ extends to Fe_2TiO_4 , the A site of which is known to be occupied by Fe^{2+} only. Correlating this with the results for $\text{LiFe}_{0.5}\text{Ti}_{1.5}\text{O}_4$ we can tentatively propose a two stage substitution mechanism for the series:



Admittedly, there is likely to be some error in this model arising from the fact that samples of composition $x > 0.5$ contain a small ilmenite second phase, but the linearity of the unit cell increase with Fe content and the good agreement of our Fe_2TiO_4 unit cell edges with literature values (8.537\AA vs 8.53\AA ¹⁹) lend validity to the model.

In a fashion similar to the (220) peak giving information relating to the A site occupancies, the (210) and (211) peaks can be used to give a direct measure of the ordering of the sample as they arise predominantly from the difference in scattering between the 4b and 12d sites. Thus, a strong (210) peak indicates the 4b site is predominantly occupied by weakly scattering Li, whilst the 12d is occupied by the heavier Fe and/or Ti. The broadening we see of these peaks for some compositions is not directly a result of increasing cation disorder across the two sites, but is likely to be related, as it probably occurs from a change in the length scale of the ordering, which again is an indication of disorder in the system.

Applying these observations to our data, we can see that for $\text{LiFe}_{0.5}\text{Ti}_{1.5}\text{O}_4$ the (210) peak is strong and of similar width to the main structural peaks, indicating that ordering is consistent and long range. Indeed, this is probably the most strongly ordered sample on the phase diagram. Moving away from this stoichiometry, both the Philips XRD studies on the $\text{Li}_{4/3-4/3x}\text{Fe}_{2x}\text{Ti}_{5/3-2/3x}\text{O}_4$ series, and the higher resolution neutron and X-ray diffraction studies on the $\text{LiFe}_x\text{Ti}_{2-x}\text{O}_4$ solid solution, show that even small changes in

stoichiometry from this composition cause considerable changes in the strength and length scale of the ordering. Nevertheless, the breakdown of the ordering is not an “on-off” effect, but a gradual process which can be characterised in terms of increasing cation disorder and a breakdown in the distance over which the ordering is coherent.

Indeed, the neutron and X-ray diffraction results for the $\text{LiFe}_x\text{Ti}_{2-x}\text{O}_4$ system give a very good picture of how this disordering occurs. With increasing x , the peak widths for this system increase dramatically, showing a trend towards infinity approaching the disordered $x=1$ composition. In tandem with this there is a consistent disordering of the octahedral Li, Fe and Ti, with the ratios of the ions on the ordered 4b and 12d sites moving towards a point of convergence again at the fully disordered $x=1$.

4.3 Low temperature studies of the $\text{LiFe}_x\text{Ti}_{2-x}\text{O}_4$ solid solution.

Complementary to the structural investigations of the $\text{LiFe}_x\text{Ti}_{2-x}\text{O}_4$ solution we carried out a series of low temperature Mössbauer, neutron diffraction, and magnetic susceptibility studies on samples in the system, with a view to probing the nature of magnetism. These studies are, it should be stressed, still ongoing and the results presented here are limited and preliminary.

For this work, magnetic data were collected for us by Karin Garcia, using an Oxford Instruments Vibrating Sample Magnetometer (VSM), courtesy of Prof. Bob Cywinski. Mössbauer spectra were obtained using a ^{57}Fe source Mössbauer spectrometer, courtesy of Dr. Sue Kilcoyne and, for the neutron diffraction, the D2B instrument at the ILL, Grenoble was used. For the analysis of the neutron data, thanks go to Dr Andrew Wills.

4.3.1 Results for $\text{LiFe}_{0.5}\text{Ti}_{1.5}\text{O}_4$

Presented below are our data and results for the $\text{LiFe}_{0.5}\text{Ti}_{1.5}\text{O}_4$ sample. Included among these are the sample susceptibility data, the raw Mössbauer data for all temperatures along with example fitted data, and an example fitted neutron pattern.

The susceptibility data (Figure 4-22) clearly shows that the sample is paramagnetic down to low temperatures, though a small deviation from linearity in the $1/\chi$ vs temperature plot is observed. Fitting the data to Curie Weiss behaviour gives $C=1.9985(0.026)$ emu.K/mol.g, $\theta = -18.034(0.279)$ K. From this was calculated a value of $\mu_{\text{eff}} = 5.65\mu_{\text{B}}$.

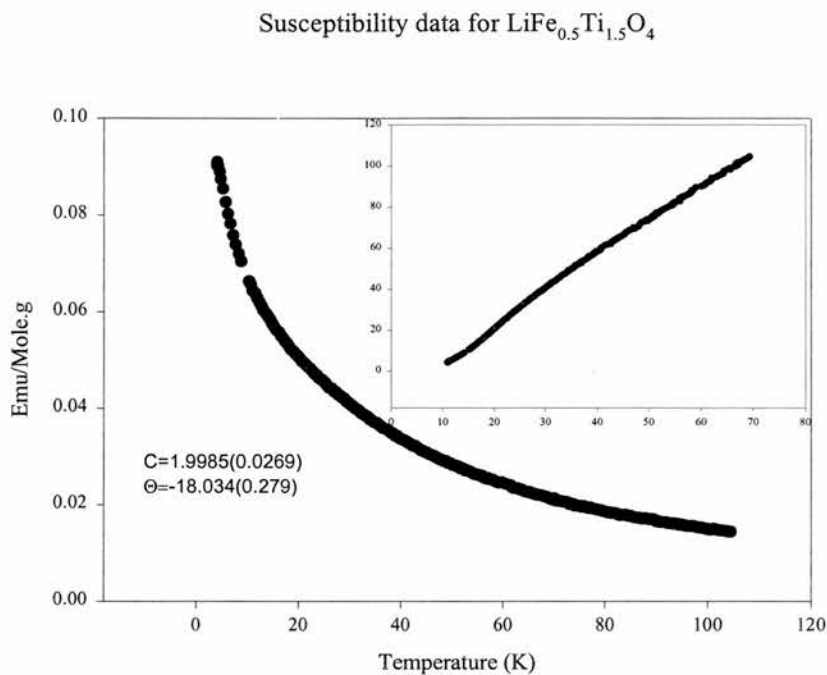


Figure 4-22: Magnetic Susceptibility data for $\text{LiFe}_{0.5}\text{Ti}_{1.5}\text{O}_4$. Inset is the $1/\chi$ vs temperature behaviour.

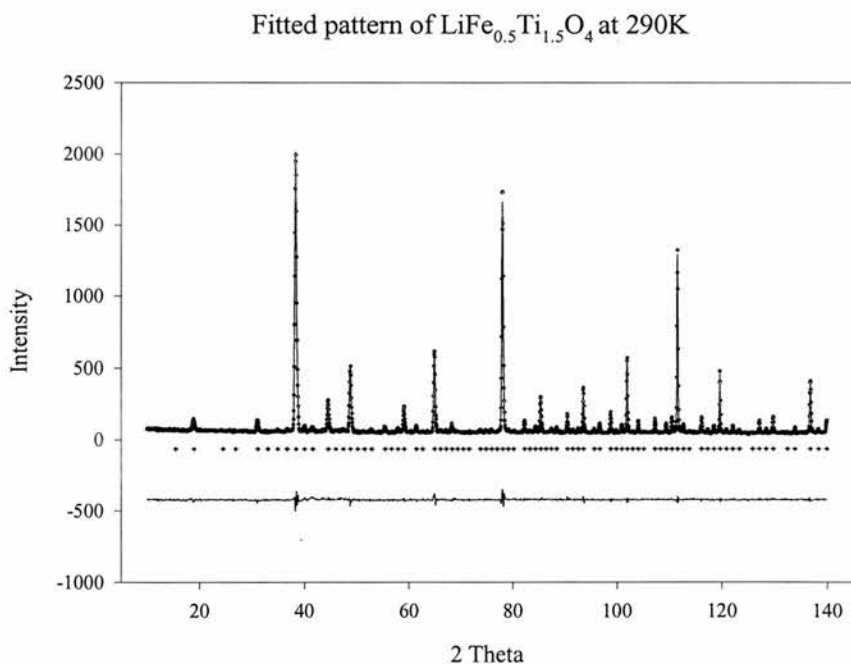


Figure 4-23: Fitted Neutron diffraction pattern for $\text{LiFe}_{0.5}\text{Ti}_{1.5}\text{O}_4$ at 290K

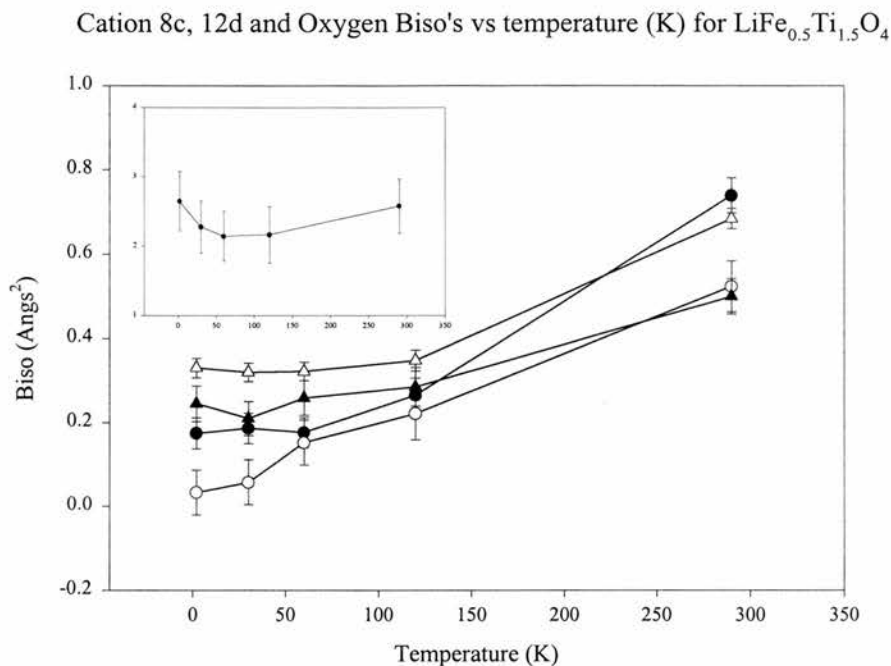


Figure 4-24: Temperature dependence of the site B_{iso} 's for $\text{LiFe}_{0.5}\text{Ti}_{1.5}\text{O}_4$

The results of the neutron diffraction were found to confirm the structural model derived from the high temperature data, with good fits being obtained at all temperatures. The unit cell (Figure 4-37 below) is seen to contract steadily down to 70K, after which it flattens off, suggesting a limit to the material's contraction. Thermal parameters for the 4b site are seen to behave a little strangely compared to those of the other sites. Several refinements were made using different cation distribution models, but as the same trends were also seen in these it was not felt to indicate any obvious deficiency in our structural model.

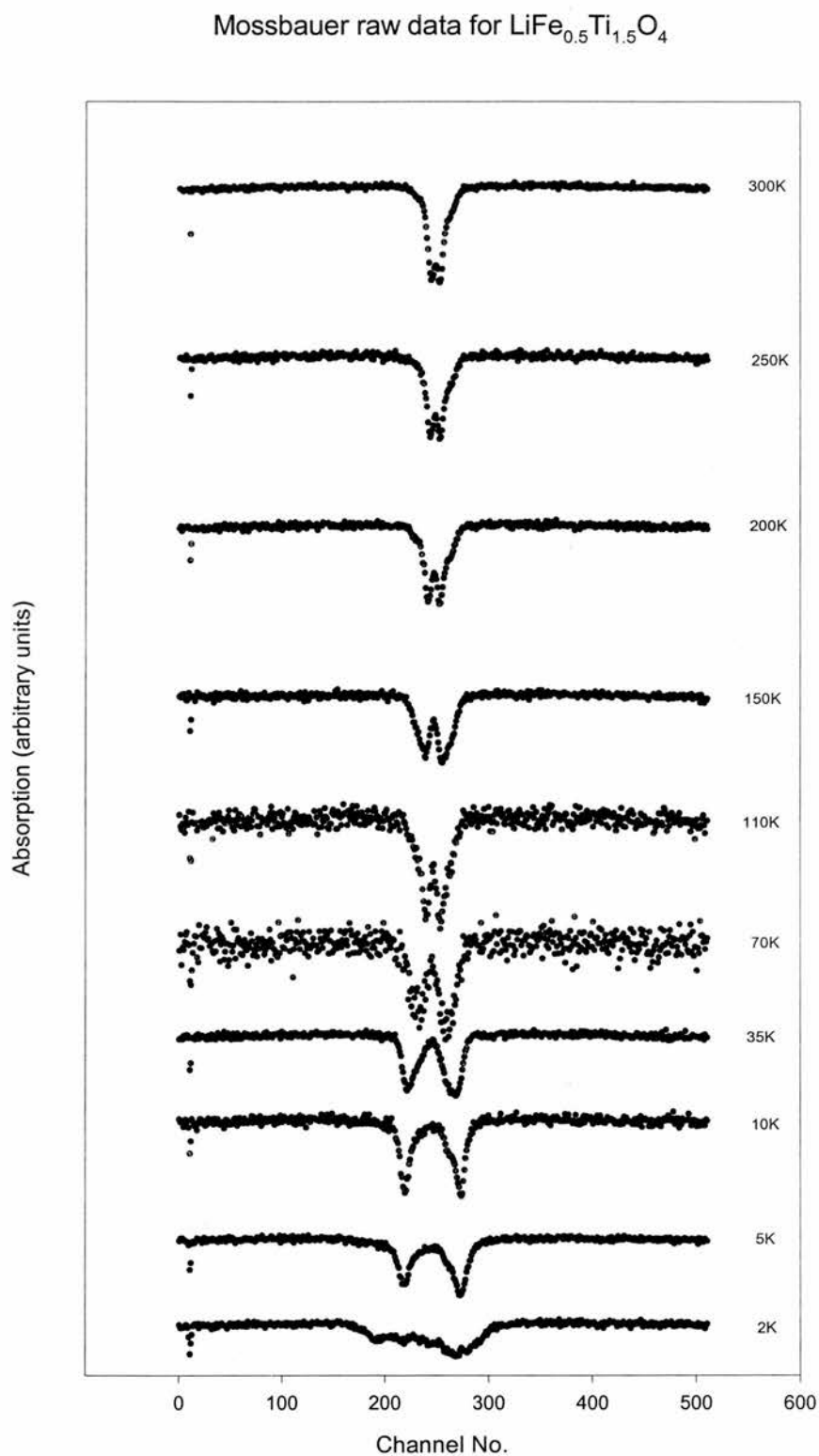


Figure 4-25: Raw Mössbauer data for $\text{LiFe}_{0.5}\text{Ti}_{1.5}\text{O}_4$

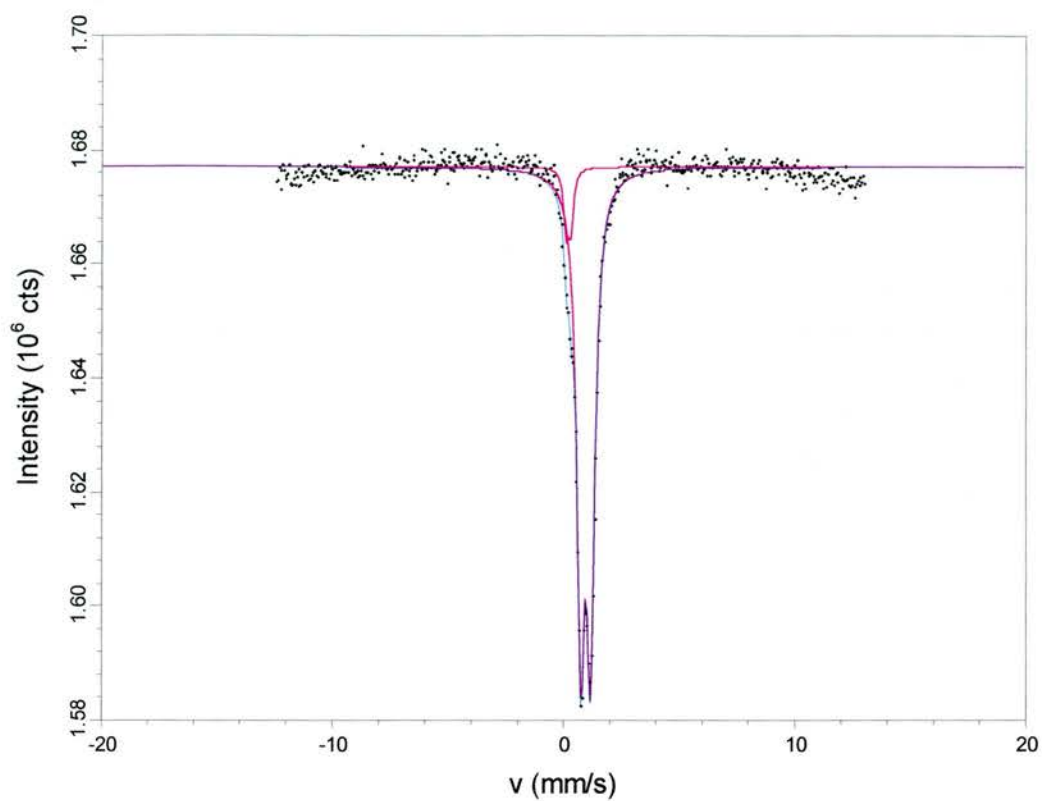


Figure 4-26: Fitted Mössbauer data for $\text{LiFe}_{0.5}\text{Ti}_{1.5}\text{O}_4$ at 300K

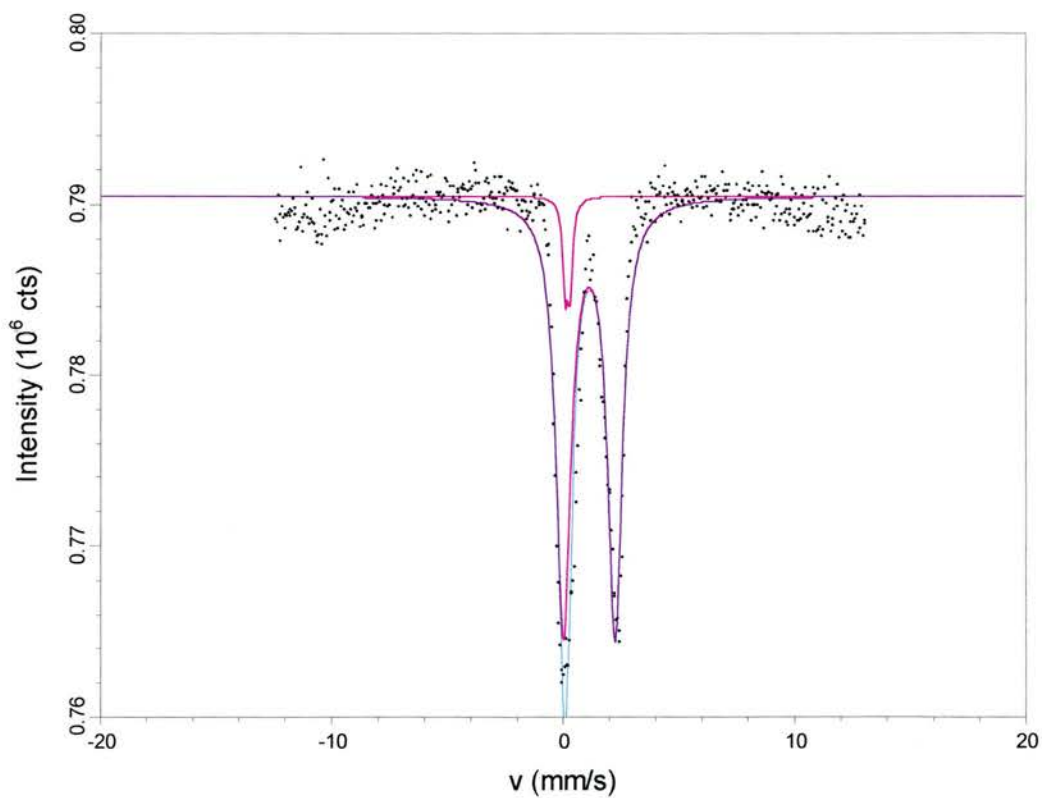


Figure 4-27: Fitted Mössbauer data for $\text{LiFe}_{0.5}\text{Ti}_{1.5}\text{O}_4$ at 35K.

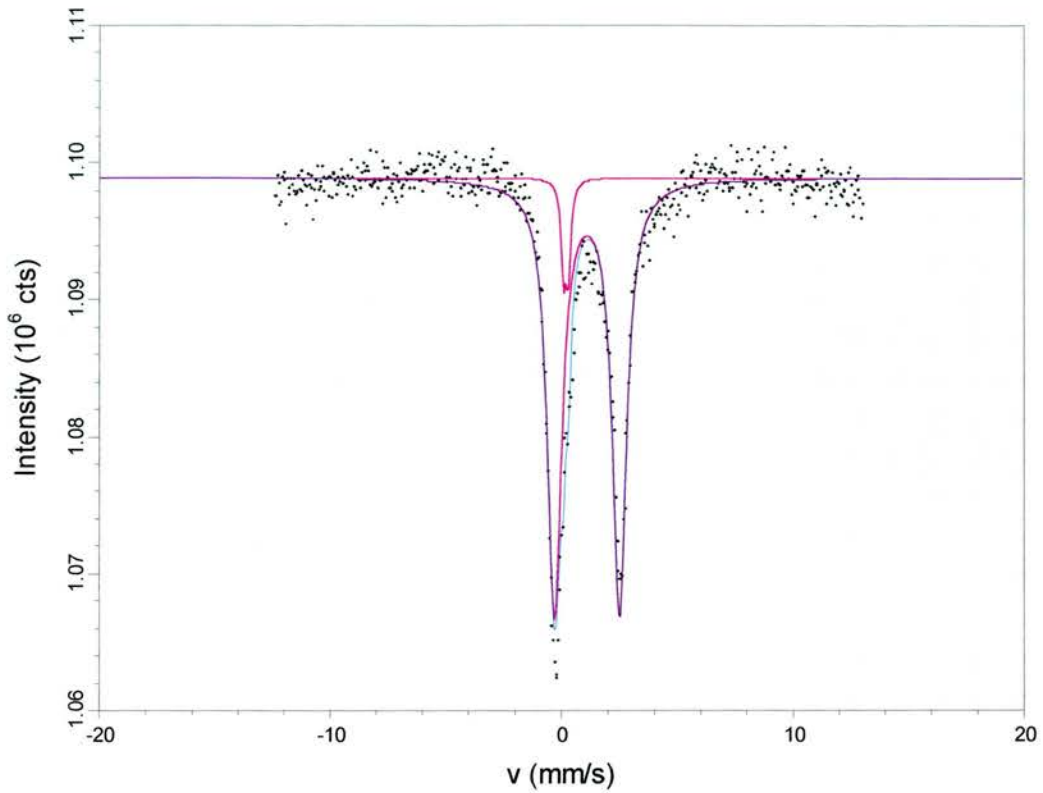


Figure 4-28: Fitted Mössbauer data for $\text{LiFe}_{0.5}\text{Ti}_{1.5}\text{O}_4$ at 5K

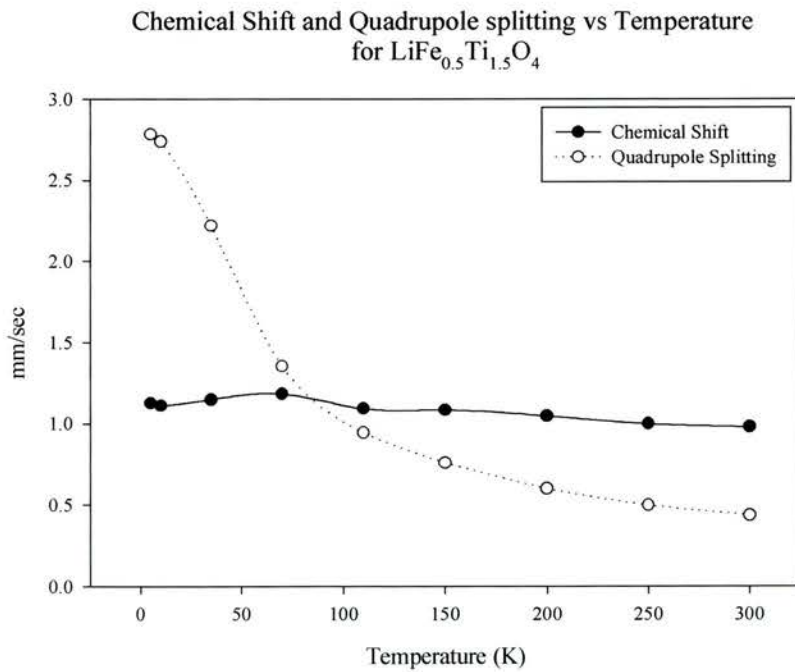


Figure 4-29: Chemical shift and Quadrupole splitting for $\text{LiFe}_{0.5}\text{Ti}_{1.5}\text{O}_4$ as a function of temperature

The Mössbauer data confirm the absence of magnetic ordering found from the susceptibility, exhibiting a single doublet of chemical shift ~ 1 mm/s, a value typical for tetrahedrally coordinated Fe^{2+} . With decreasing temperature it can be also seen that the quadrupole splitting of the sample increases in a dramatic and unusual fashion, suggesting that whilst the sample doesn't magnetically order, it does undergo some change which affects the environment of the tetrahedral Fe^{2+} .

It should be noted that the data were fitted with a small second doublet in order to describe a level of anisotropy in the larger one. This is actually an instrumental addition to the spectra arising from a "window" in the spectrometer, which contains a small amount of Fe. For the sake of consistency, this doublet was fully fitted for the 300K spectrum, and the obtained values of chemical shift and quadrupole splitting carried over to the subsequent refinements, in which only the peak area was allowed to vary.

4.3.2 Results for $\text{LiFe}_{0.75}\text{Ti}_{1.25}\text{O}_4$ and LiFeTiO_4

For the $x=0.75$ and $x=1$ samples we collected both susceptibility and neutron diffraction data, and for LiFeTiO_4 we also present Mössbauer data. Additionally, Curie temperatures of 450K and 330K were obtained for us by Karin Garcia for $\text{LiFe}_{0.75}\text{Ti}_{1.25}\text{O}_4$ and LiFeTiO_4 respectively.

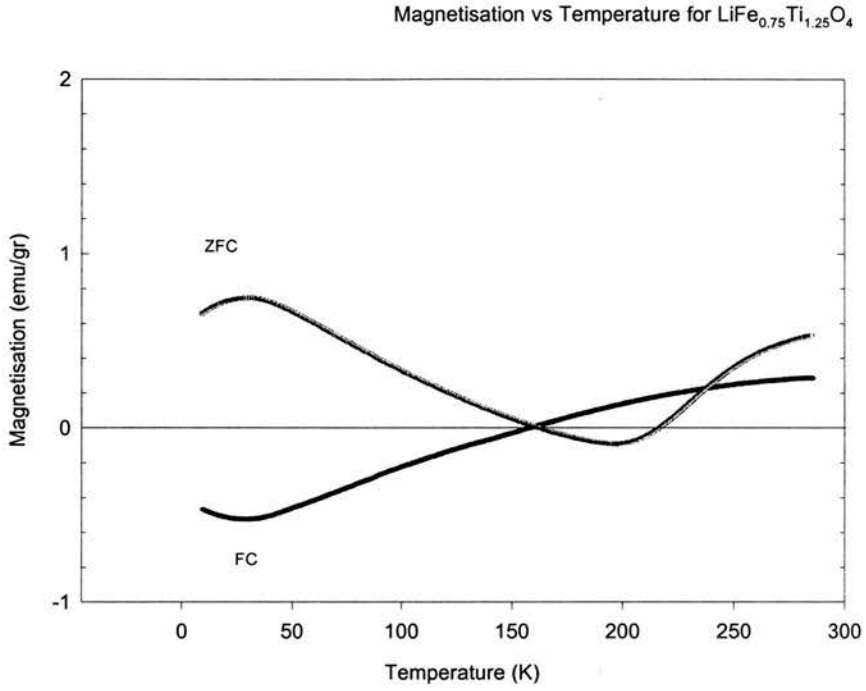


Figure 4-30: Magnetisation vs temperature for field cooled (FC) and zero field cooled (ZFC) $\text{LiFe}_{0.75}\text{Ti}_{1.25}\text{O}_4$

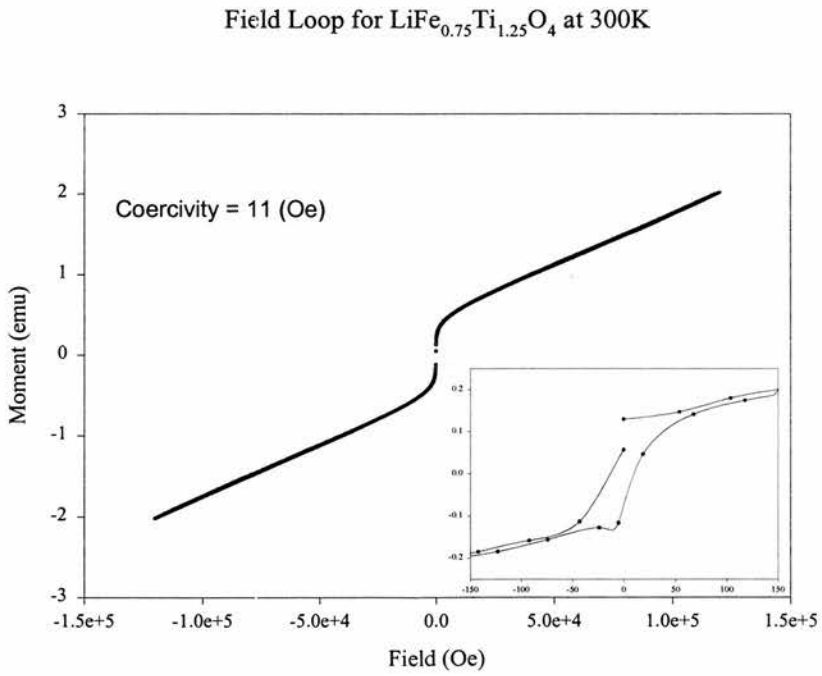


Figure 4-31: Field loop for $\text{LiFe}_{0.75}\text{Ti}_{1.25}\text{O}_4$ at 300K.

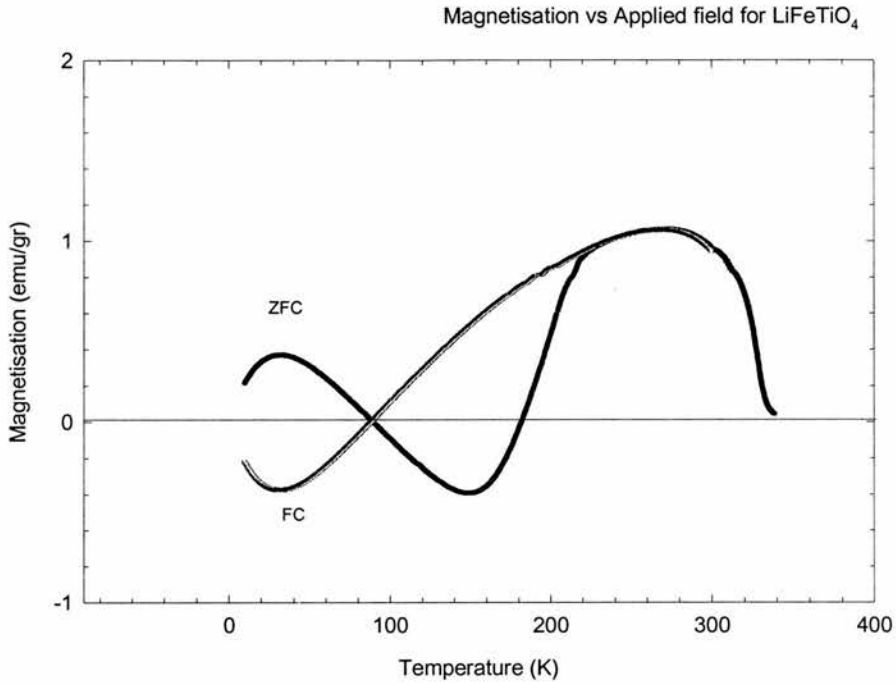


Figure 4-32: Magnetisation vs temperature for field cooled (FC) and zero field cooled (ZFC) LiFeTiO_4

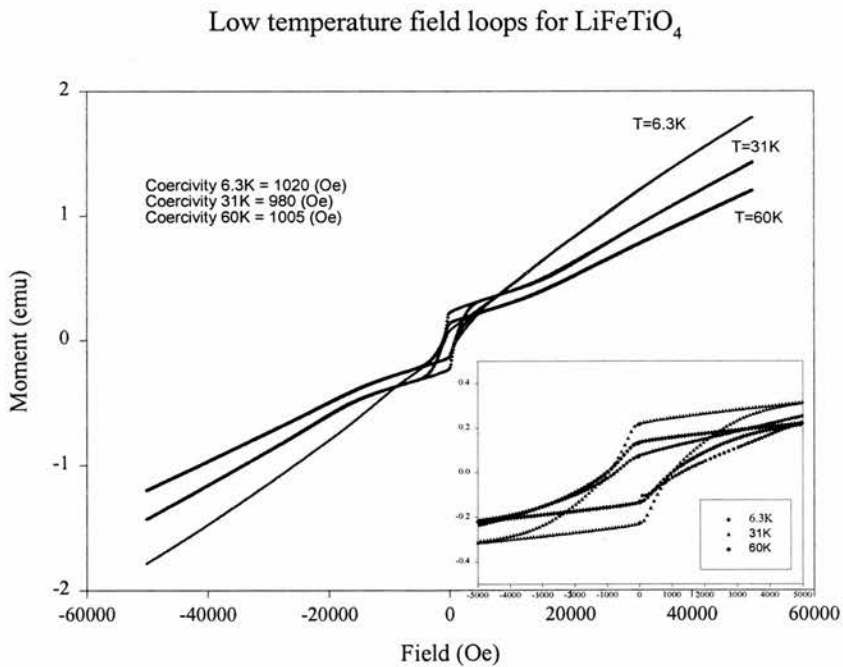


Figure 4-33: Field loops for LiFeTiO_4 taken at 6.3K, 31K and 60K.

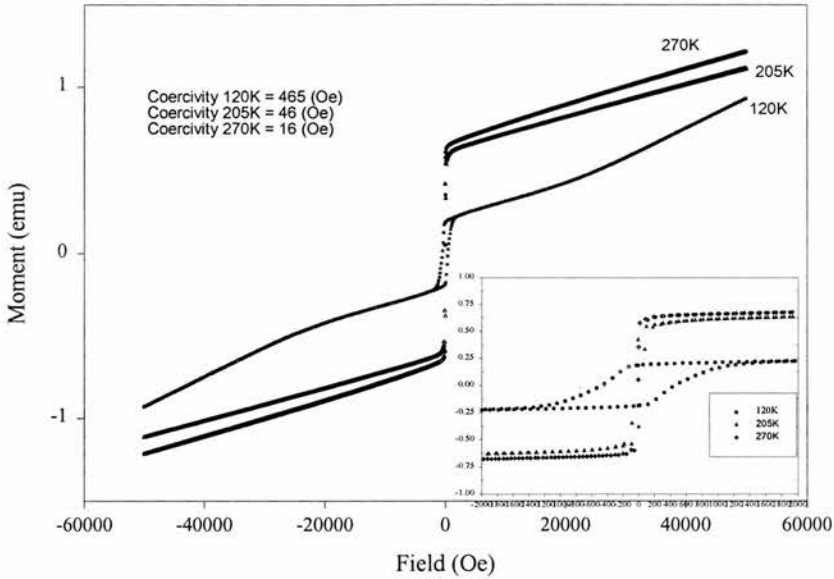
Low temperature field loops for LiFeTiO_4 

Figure 4-34: Field loops for LiFeTiO_4 taken at 120K, 205K and 270K.

The magnetisation data for the both $\text{LiFe}_{0.75}\text{Ti}_{1.25}\text{O}_4$ or LiFeTiO_4 are clearly unusual, particularly the two compensation points shown in the ZFC measurements, which indicate that the materials are not ordinary collinear Neel ferrimagnets. This is confirmed by the field loop data, which show an apparent linear dependence of magnetisation with applied field, and no sign of saturation even at the 12T limit of our magnet.

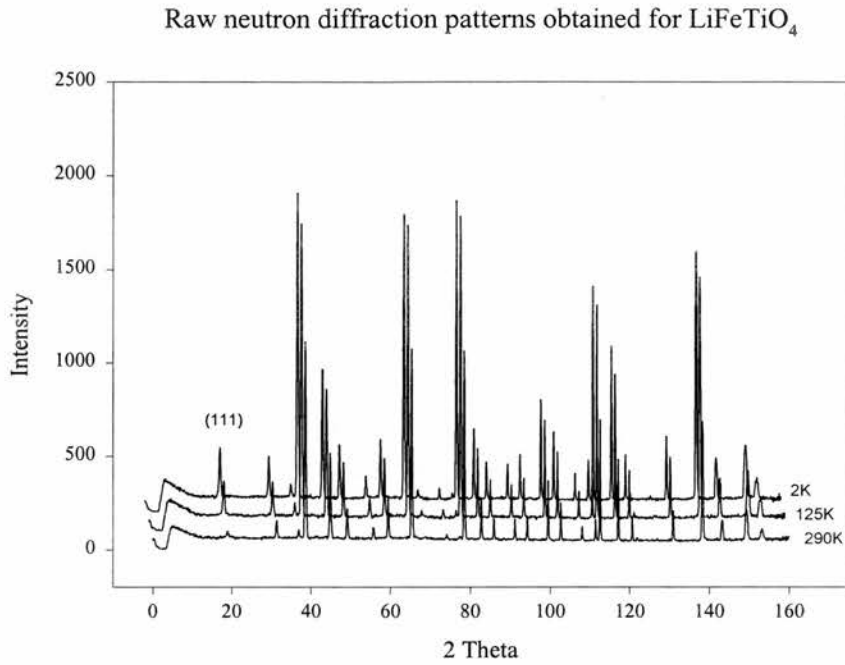


Figure 4-35: Raw neutron diffraction patterns for LiFeTiO_4 taken at 2K, 125K and 290K. Note the data are shifted in both intensity and 2θ for clarity.

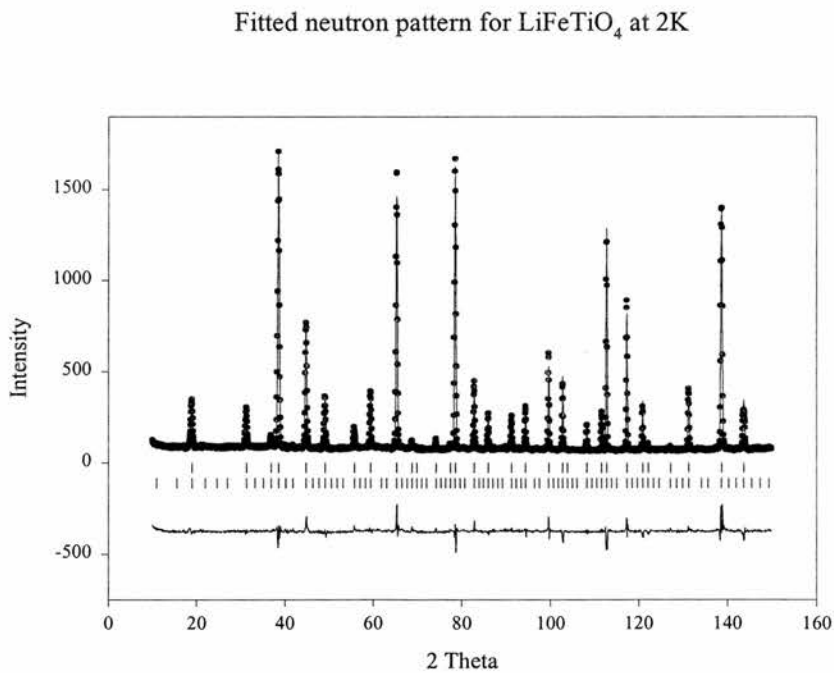
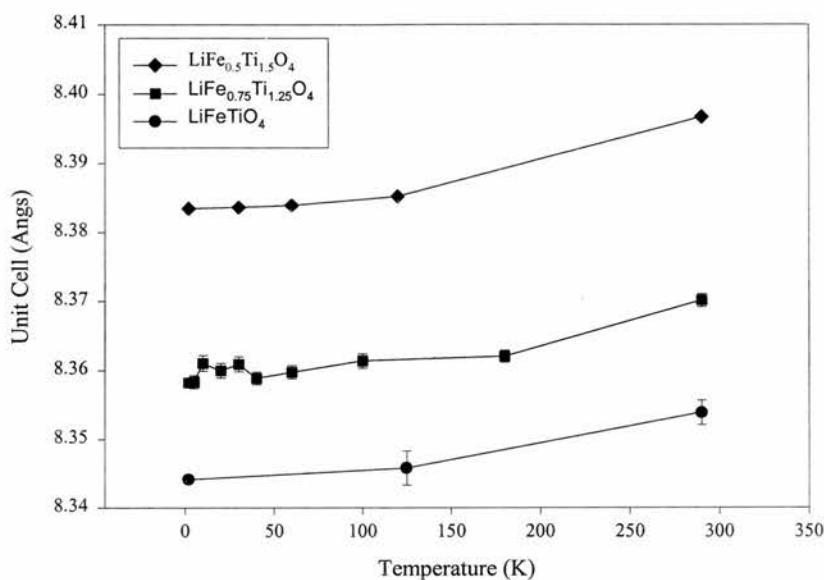


Figure 4-36: Fitted neutron diffraction pattern for LiFeTiO_4 at 2K

Temperature dependence of the unit cell edges for $\text{LiFe}_x\text{Ti}_{2-x}\text{O}_4$ Figure 4-37: The temperature dependence of the unit cell edges for $\text{LiFe}_x\text{Ti}_{2-x}\text{O}_4$

Cation	Wyckoff Position	Coordinates			Occ	B_{iso}^*
		x	y	z		
Li^+	8a	0.125	0.125	0.125	0.266	0.46097
Fe^{3+}	8a	0.125	0.125	0.125	0.234	0.46097
Li^+	16d	0.5	0.5	0.5	0.234	0.46097
Fe^{3+}	16d	0.5	0.5	0.5	0.266	0.46097
Ti^{4+}	16d	0.5	0.5	0.5	0.50	0.46097
O^{2-}	32e	0.25974	0.25974	0.25974	1	0.46097

Table 4-3: Refined atom positions and occupancies for LiFeTiO_4 at 2K. Structural phase R_{Bragg} for refinement was 6.71%, magnetic phase R_{Bragg} 8.62%. * indicates an overall B_{iso} was used.

As would be expected from the susceptibility data, initial fitting of the neutron diffraction data indicated the existence of magnetic ordering in the form of unreasonable thermal parameters and site occupancies. Close inspection of the diffraction patterns showed that the (111) peak in LiFeTiO_4 is particularly sensitive to the magnetic ordering (Figure 4-35 above), but no extra peaks corresponding to a magnetic supercell were found, suggesting that the magnetic and structural cells are the same.

Analysis of the 2K data for LiFeTiO_4 was carried out for us by Dr. Andrew Wills using Representational Analysis²¹ to suggest possible magnetically ordered structures and Fullprof²² to apply them to the data. Two ordered systems were suggested, a straight collinear ordering of the magnetic moments on A and B sites, and a system in which the moments on both sites are canted. It was found that there was a considerable improvement in the quality of the fit ($R_{\text{Bragg}} = 8.62\%$ vs 9.74%) for the canted model over the collinear. The calculated moments this model were $1.47\mu_{\text{B}}$ for the 16d site, $2.07\mu_{\text{B}}$ for the 8a. The as refined structure is shown in Figure 4-38 below. Refinements of the neutron data collected at other temperatures for this sample are presently underway.

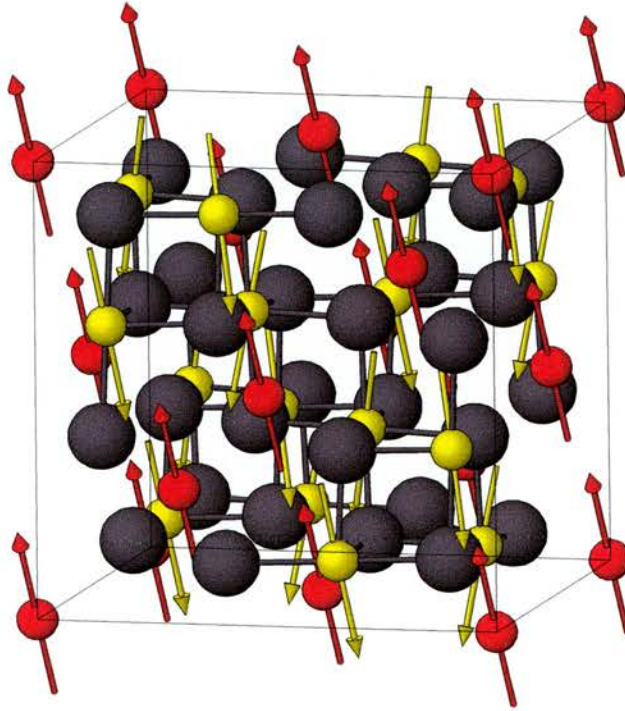


Figure 4-38: The canted arrangement of spins for LiFeTiO_4 at 2K

Cation	Equiv. Spinel position	x	y	z	Rx	Ry	Rz	Moment μ_B
Fe ³⁺	16d	0.5	0.5	0.5	1.438	-0.232	-0.232	1.47
Fe ³⁺	16d	0.5	0.0	0.0	1.438	-0.232	-0.232	1.47
Fe ³⁺	16d	0.0	0.5	0.0	1.438	-0.232	-0.232	1.47
Fe ³⁺	16d	0.0	0.0	0.5	1.438	-0.232	-0.232	1.47
Fe ³⁺	16d	0.25	0.75	0.0	1.438	-0.232	0.232	1.47
Fe ³⁺	16d	0.25	0.25	0.5	1.438	-0.232	0.232	1.47
Fe ³⁺	16d	0.75	0.75	0.5	1.438	-0.232	0.232	1.47
Fe ³⁺	16d	0.75	0.25	0.0	1.438	-0.232	0.232	1.47
Fe ³⁺	16d	0.75	0.0	0.25	1.438	0.232	-0.232	1.47
Fe ³⁺	16d	0.75	0.5	0.75	1.438	0.232	-0.232	1.47
Fe ³⁺	16d	0.25	0.0	0.75	1.438	0.232	-0.232	1.47
Fe ³⁺	16d	0.25	0.5	0.25	1.438	0.232	-0.232	1.47
Fe ³⁺	16d	0.0	0.25	0.75	1.438	0.232	0.232	1.47
Fe ³⁺	16d	0.0	0.75	0.25	1.438	0.232	0.232	1.47
Fe ³⁺	16d	0.5	0.25	0.25	1.438	0.232	0.232	1.47
Fe ³⁺	16d	0.5	0.75	0.75	1.438	0.232	0.232	1.47
Fe ³⁺	8a	0.125	0.125	0.125	-1.631	1.282	0.000	2.07
Fe ³⁺	8a	0.125	0.625	0.625	-1.631	1.282	0.000	2.07
Fe ³⁺	8a	0.625	0.125	0.625	-1.631	1.282	0.000	2.07
Fe ³⁺	8a	0.625	0.625	0.125	-1.631	1.282	0.000	2.07
Fe ³⁺	8a	0.875	0.375	0.375	-1.631	1.282	0.000	2.07
Fe ³⁺	8a	0.875	0.875	0.875	-1.631	1.282	0.000	2.07
Fe ³⁺	8a	0.375	0.375	0.875	-1.631	1.282	0.000	2.07
Fe ³⁺	8a	0.375	0.875	0.375	-1.631	1.282	0.000	2.07

Table 4-4: Refined magnetic moments for LiFeTiO₄ at 2K and their components along x, y and z axes.

Similar analysis of the reduced LiFe_{0.75}Ti_{1.25}O₄ sample was complicated by the semi-reduced nature of the sample, and without knowing the distribution of Fe²⁺ and Fe³⁺ across the three cation sites an accurate model is difficult to formulate. Unfortunately, the resolution of Mössbauer spectroscopy is too low to obtain this information for a complex system such as this (3 cation sites, 2 Fe oxidation states), and attempts using

Bond Valence sum theory have proven so far inconclusive. Work analysing these data is thus ongoing.

Raw Mossbauer data for LiFeTiO_4

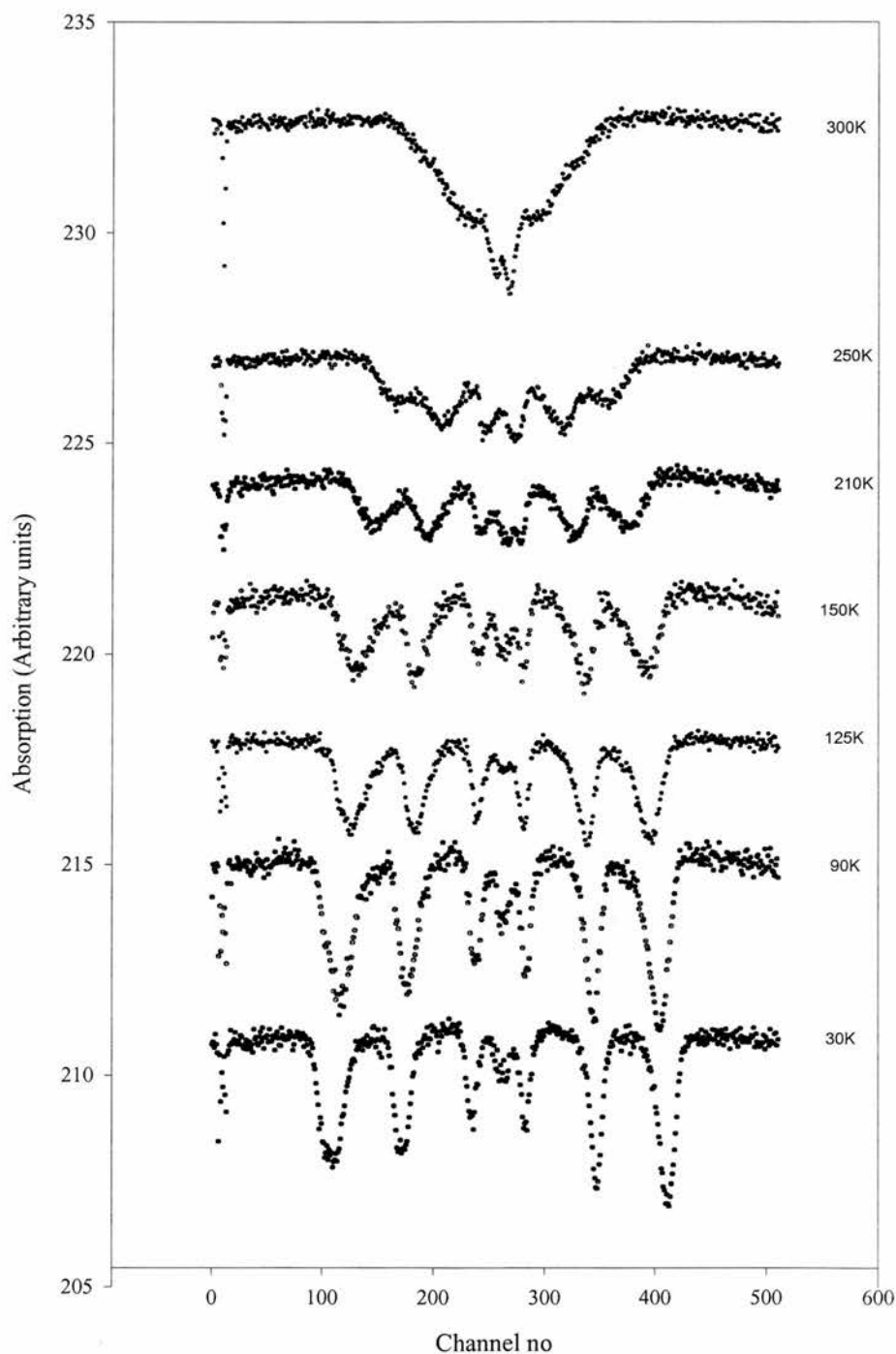


Figure 4-39: Raw Mössbauer data for LiFeTiO_4

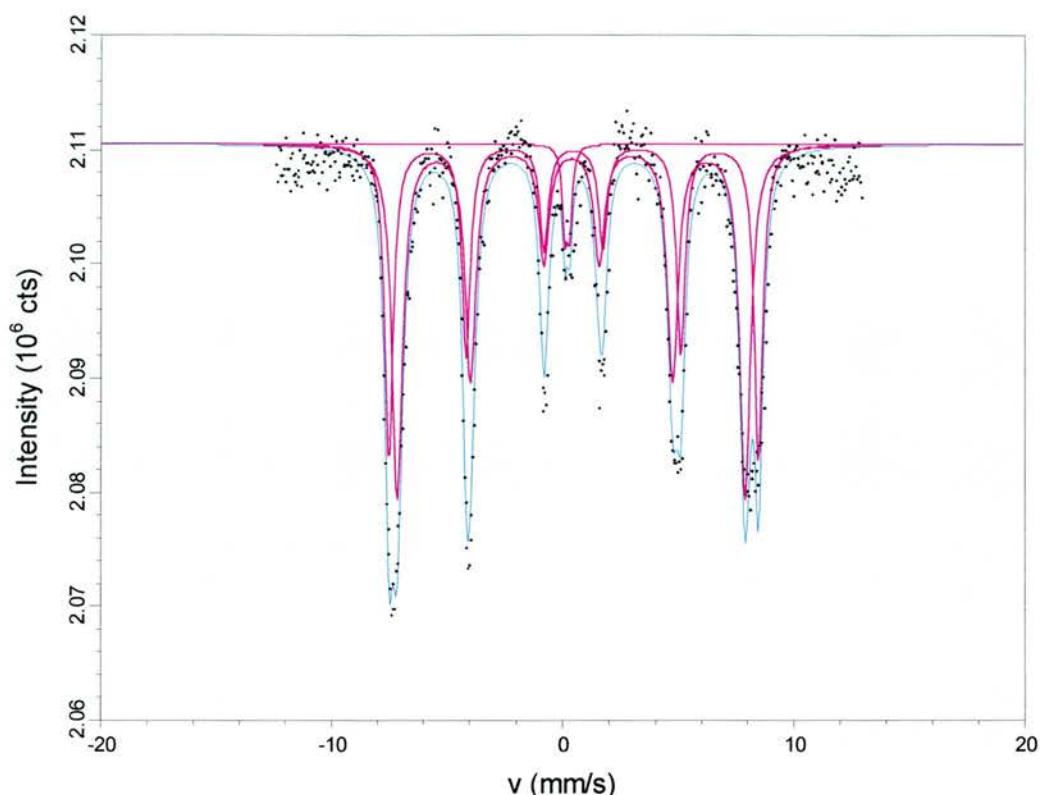


Figure 4-40: Fitted Mössbauer spectrum for LiFeTiO₄ at 32K

Mössbauer spectra of the LiFeTiO₄ sample shows at RT a quadrupole split doublet in addition to considerable relaxation of an ordered sextet or sextets. At low temperature the spectra becomes a magnetically split broad sextet. The 32K spectra was found to fit well to a pair of sextets and a small doublet. The presence of a small instrumental doublet in the LiFe_{0.5}Ti_{1.5}O₄ spectra has already been discussed, and it cannot be ruled out that this arises from the same origin. However, similar doublets have been reported for samples of this type thought to be arising from the existence of paramagnetic clusters in the sample²³. The hyperfine field values for the doublets (495.699±0.669kOe and 466.429±0.746kOe) were found to agree well with published values for this composition²⁴, and the area ratio of the doublets (57%/43%) agrees well with the cation distribution found earlier.

4.3.3 Discussion

The results for $\text{LiFe}_{0.5}\text{Ti}_{1.5}\text{O}_4$ are undoubtedly the most complete of the system, mainly by virtue of the fact that the sample was found to be paramagnetic, and thus the data interpretation was somewhat easier. Fitting the susceptibility data to Curie-Weiss behaviour ($\chi = C/(T-\theta)$), we calculated C to be 1.9985 emu.K/mol.g and θ to be -18K , indicating antiferromagnetic interactions within the sample. From the calculated value of C we were able to derive μ_{eff} for the sample with a value of 5.65 Bohr magnetons per Fe^{2+} being obtained. Whilst a little high compared to the spin only value of 4.89 for high spin Fe^{2+} , this does compare well with experimentally obtained value of 5.4 reported by Kittel²⁵.

The results from the neutron diffraction confirm well the model derived previously from the XRD and high temperature neutron studies, which placed Fe^{2+} almost entirely on the spinel A-site. This is an important result, because coupled with the susceptibility data it confirms the very weak nature of the A-A interactions in these spinels, and thus explains why this sample is paramagnetic whilst the more Fe rich members of the series are ferrimagnetic.

Despite showing no evidence of magnetic ordering, the sample still exhibits very interesting Mössbauer behaviour, with an unusual increase in the quadrupole splitting of the Fe^{2+} doublet with decreasing temperature. The Mössbauer technique effectively measures the perturbation of the nuclear energy levels by the s-electrons of the atom under investigation, and thus indirectly its magnetic and structural environment. From both the Mössbauer and susceptibility data we can see that the only evidence of possible magnetic ordering occurs at extremely low temperature ($<2\text{K}$) where the Fe^{2+} Mössbauer spectrum appears to relax somewhat. It seems reasonable to conclude that the phenomenon seen in the Mössbauer spectra arises from a structural effect.

Investigation of the literature reveals similar behaviour for FeCr_2O_4 and FeV_2O_4 ²⁶ at a Jahn Teller driven structural transition from cubic to tetragonal symmetry, and whilst close inspection of our neutron data shows no firm evidence of such distortion, the similar presence of tetrahedral Fe^{2+} makes it likely that behaviour seen in the Mössbauer plots could be related to a similar, if milder structural distortion.

Our results for the more oxidised members of the system are much more provisional, the most notable being the clear indication of canted magnetic ordering in the system. This is shown directly by the neutron diffraction, and indirectly by the behaviour of the field loops: The linear increase in magnetisation with field and inability to reach saturation magnetisation even at very high fields is indicative of a canted structure²⁷. The presence of canting also helps to explain the complexity of the magnetisation vs temperature data, in particular the presence of two compensation temperatures. This could not arise from a collinear two sublattice ferrimagnetic system, but the introduction of canting effectively increases the number of magnetic sublattices²⁸ and with each of these showing a different temperature dependence, much more complex magnetisation behaviour is possible.

4.4 Electrochemical studies of the $\text{LiFe}_x\text{Ti}_{2-x}\text{O}_4$ solid solution

4.4.1 Introduction

The spinel structure is in many ways ideal as an insertion host for lithium battery applications. Its 3D network of channels mean that it can easily uptake small cations such as Li and the cubic symmetry means that expansion and contraction effects are equivalent in all directions. Additionally, many cations are known to exist in spinel structured oxides and sulphides (see chapter 1), and they are generally easy to manufacture from common starting reagents. Not surprisingly, many promising lithium battery electrode materials are known to exhibit the spinel structure. Most work however, has been on the development of the lithium manganate systems, in particular the $\text{LiMn}_2\text{O}_4 - \text{Li}_4\text{Mn}_5\text{O}_{12}$ solid solution^{29,30,31,32,33}. A great deal of this has involved doping the materials to try and reduce degradation of the structure by the Jahn-Teller distortion resulting from the formation of Mn^{3+} on cycling^{34,35,36,37,38}, and the latest fruits of this work are the Co and Cu doped derivatives recently reported to show reversible lithium insertion in the 5V region^{7,8}. From a technological point of view these are extremely important as they offer very high energy densities.

Despite the focus on the manganate spinels, there is considerable published work on the vanadate³⁹, ferrite^{4,40} and titanate^{41,42} systems, with the latter of these being of most interest. $\text{Li}_4\text{Ti}_5\text{O}_{12}$ in particular is a very promising material, showing excellent cyclability, a first insertion capacity of the order of 150mAh/g and a very flat, reversible insertion plateau. Unfortunately, this insertion plateau occurs at 1.5V: Too low to be of use as a cathode, and a little too high to be used widely as an anode.

We present here some preliminary electrochemical studies performed on our system to evaluate how the high levels of Fe substitution affects the cycling properties.

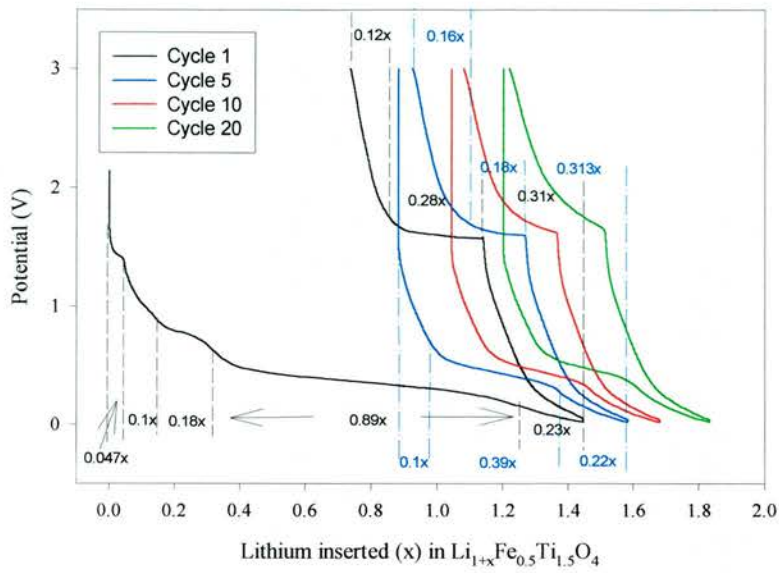
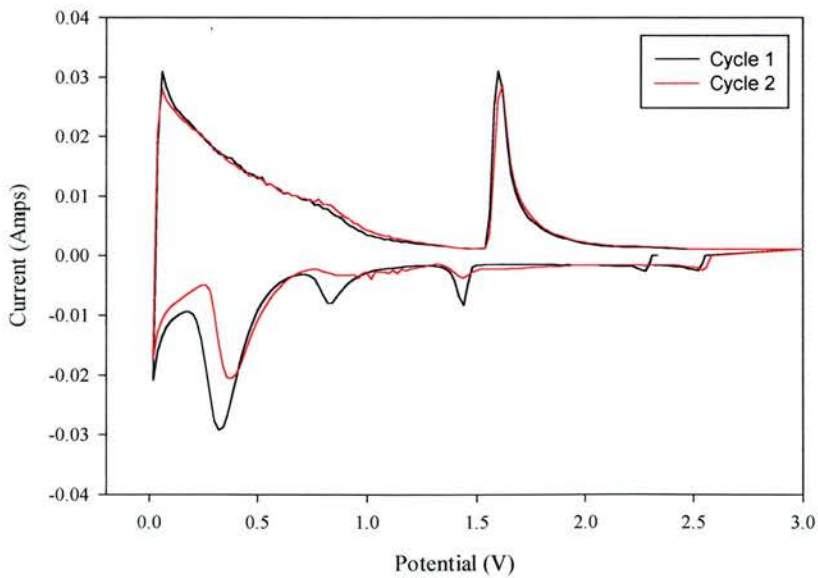
Cycling was carried out using the apparatus and techniques detailed in chapter 2:

Bellcore type electrodes were produced for each composition and cycled in model 2325 coin cells using Maccor™ and Macpile™ controllers to regulate voltage and current and to collect data. The cells were cycled galvanostatically, using a current of 0.05mA.

No optimisation of the materials was undertaken before evaluation. In situ XRD patterns were collected for one sample, $\text{LiFe}_{0.5}\text{Ti}_{1.5}\text{O}_4$. This sample was chosen by virtue of the fact that the diffraction peaks relating to the ordering were strongest for this composition and so it was felt that any changes in structure would be more easily observed.

4.4.2 Results

The results of our cycling on the $\text{LiFe}_x\text{Ti}_{2-x}\text{O}_4$ series are shown below. For each sample we present several selected cycles, along with a derivative plot (dx/dv) calculated from the galvanostatic cycling data. This is a similar representation to the cyclic voltammogram obtained from potentiostatic cycling, but rather than depicting current, instead depicts the rate of change of insertion. For comparison, the potentiostatic voltammogram for $\text{LiFe}_{0.5}\text{Ti}_{1.5}\text{O}_4$ is also shown. It should be noted that a dx/du plot is not an equilibrium measurement as the potentiostatic voltammogram is, but is nevertheless very useful in charting the change in the sample cycling characteristics. Also shown are comparisons of the first and fifth cycles for each sample along with the insertion capacities as a function of cycle number.

Selected cycles of $\text{LiFe}_{0.5}\text{Ti}_{1.5}\text{O}_4$ cycled between 0.02V/3V**Figure 4-41: Selected cycles of $\text{LiFe}_{0.5}\text{Ti}_{1.5}\text{O}_4$ taken between 0.02V and 3V.**Voltage vs Current plot for $\text{LiFe}_{0.5}\text{Ti}_{1.5}\text{O}_4$ **Figure 4-42: Potentiostatic Current/Voltage plot for $\text{LiFe}_{0.5}\text{Ti}_{1.5}\text{O}_4$**

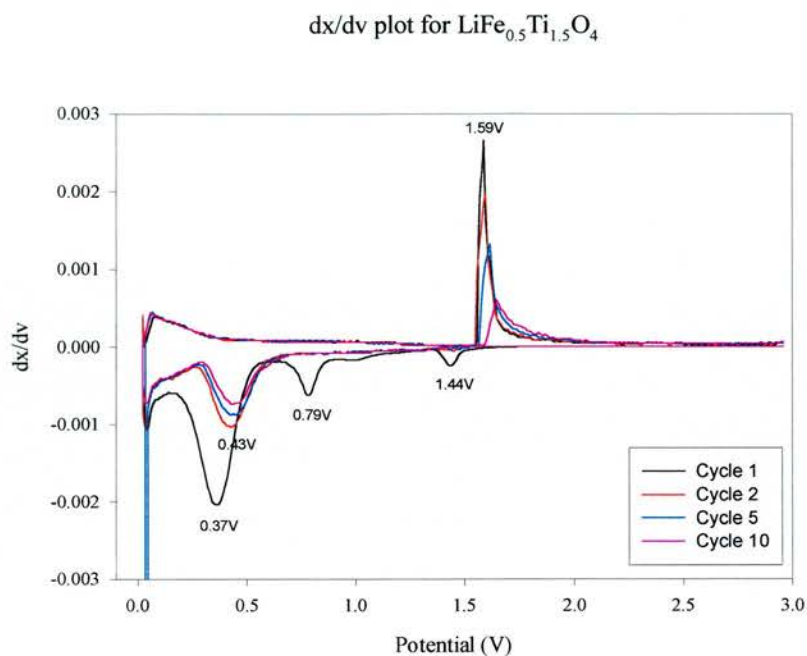


Figure 4-43: dx/dv plot for selected cycles of $\text{LiFe}_{0.5}\text{Ti}_{1.5}\text{O}_4$

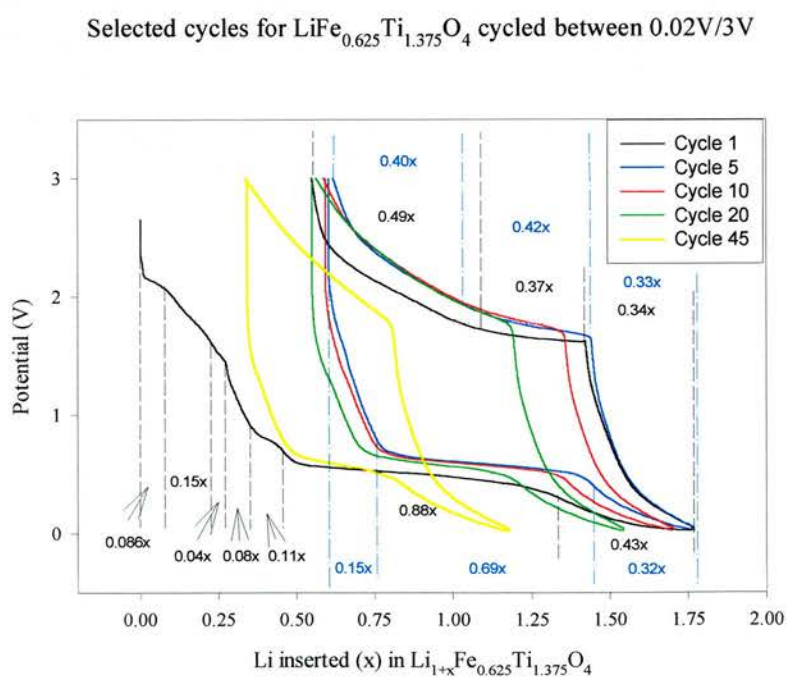


Figure 4-44: Selected cycles for $\text{LiFe}_{0.625}\text{Ti}_{1.375}\text{O}_4$ between 0.02V and 3V

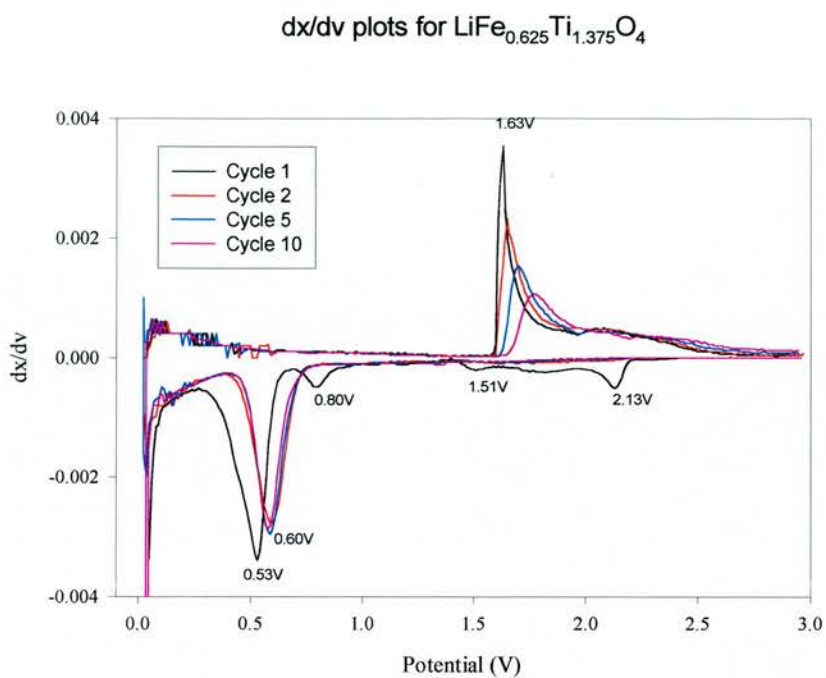


Figure 4-45: dx/dv Plot for $\text{LiFe}_{0.625}\text{Ti}_{1.375}\text{O}_4$

Selected cycles for $\text{LiFe}_{0.75}\text{Ti}_{1.25}\text{O}_4$ cycled between 0.02V/3V

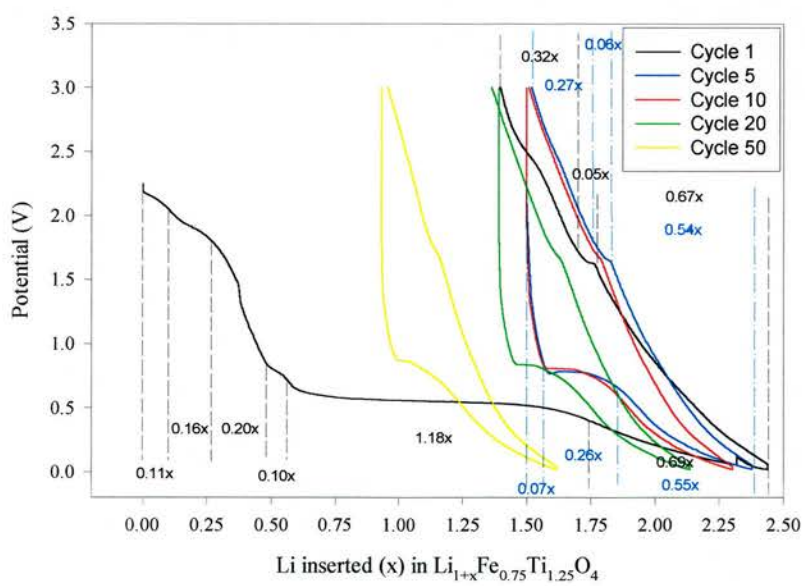


Figure 4-46: Selected cycles for $\text{LiFe}_{0.75}\text{Ti}_{1.25}\text{O}_4$.

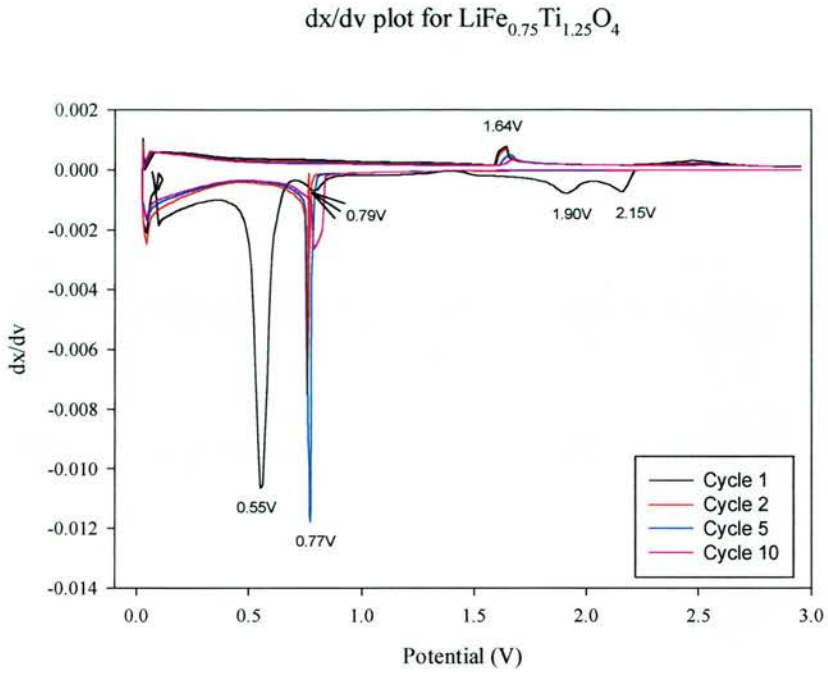


Figure 4-47: dx/dv plot for $\text{LiFe}_{0.75}\text{Ti}_{1.25}\text{O}_4$

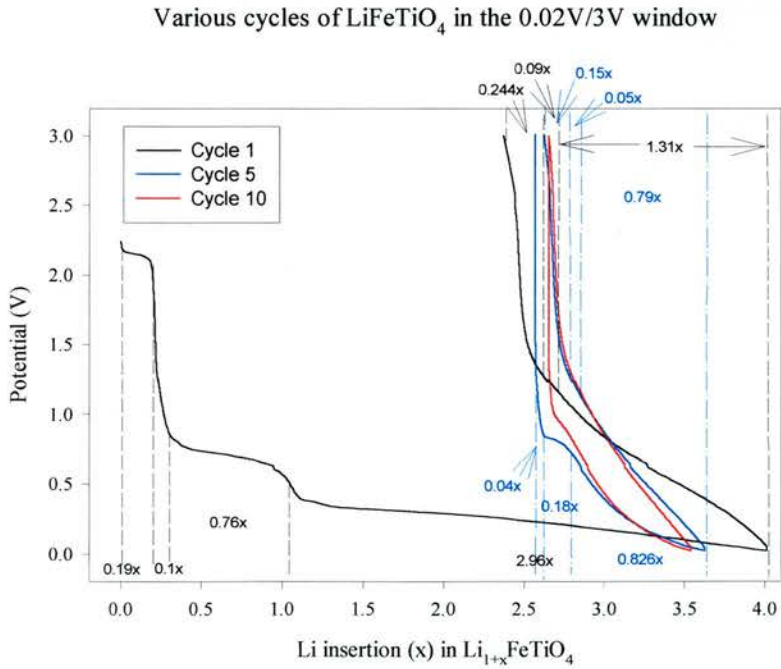


Figure 4-48: Selected cycles for LiFeTiO_4 .

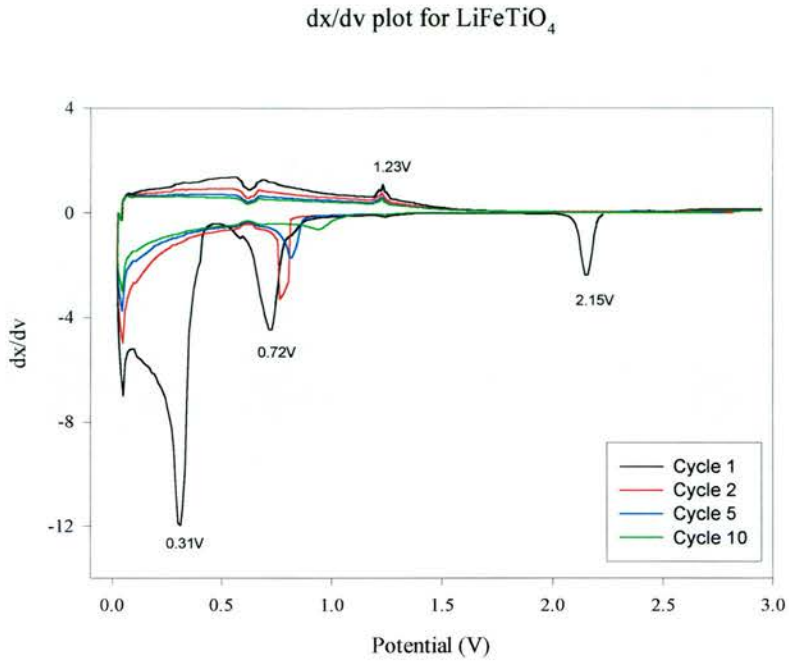


Figure 4-49: dx/du plot for LiFeTiO_4 .

First insertion profiles for the $\text{LiFe}_x\text{Ti}_{2-x}\text{O}_4$

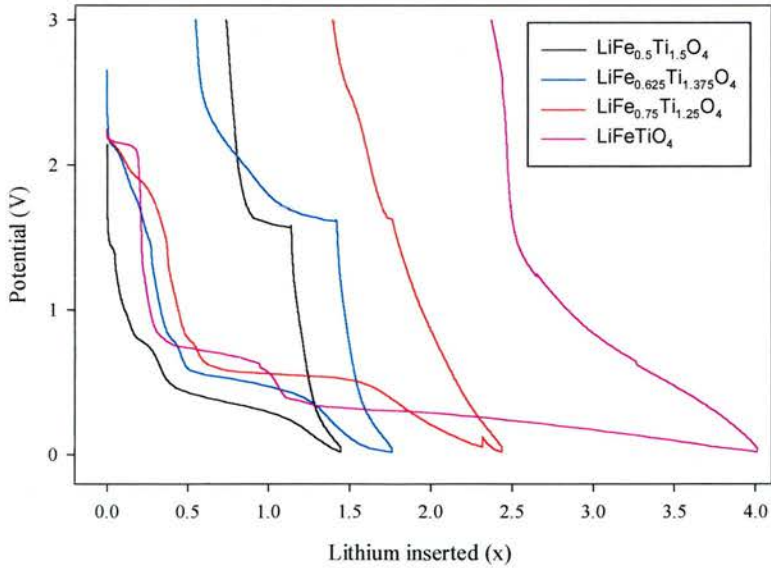
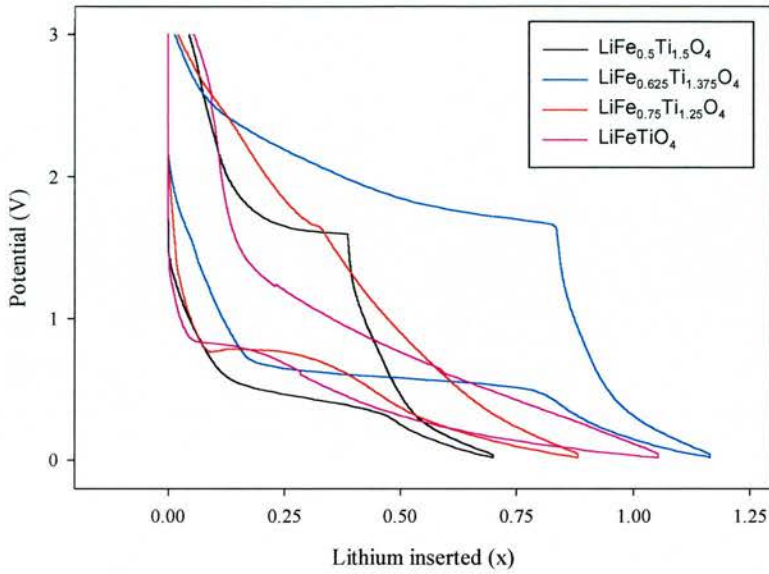


Figure 4-50: First insertion profiles for the $\text{LiFe}_x\text{Ti}_{2-x}\text{O}_4$ series

Fifth insertion cycles

Figure 4-51: Fifth insertion profiles for the $\text{LiFe}_x\text{Ti}_{2-x}\text{O}_4$ series

	$\text{LiFe}_{0.5}\text{Ti}_{1.5}\text{O}_4$		$\text{LiFe}_{0.625}\text{Ti}_{1.375}\text{O}_4$		$\text{LiFe}_{0.75}\text{Ti}_{1.25}\text{O}_4$		LiFeTiO_4	
	Insertion range	x	insertion range	x	insertion range	x	Insertion range	x
Range 1			2.6V-2.05V	0.09	2.2V-2.03V	0.11	2.20V-2.04V	0.19
Range 2			2.04V-1.59V	0.15	2.03V-1.8V	0.16	2.04V-0.9V	0.1
Range 3	1.80V-1.37V	0.05	1.59V-1.46V	0.04	1.8V-0.89V	0.2	↓	↓
Range 4	1.37V-0.90V	0.1	1.46V-0.95V	0.08	↓	↓	↓	↓
Range 5	0.90V-0.70V	0.18	0.95V-0.70V	0.11	0.89V-0.70V	0.1	0.9V-0.5V	0.76
Range 6	0.70V-0.18V	0.89	0.70V-0.30V	0.88	0.70V-0.40V	1.18	↓	↓
Range 7	0.18V-0.02V	0.23	0.30V-0.02V	0.43	0.40V-0.02V	0.69	0.5V-0.02V	2.96
Range 8	0.02V-1.55V	0.31	0.02V-1.57V	0.33	0.02V-1.58V	0.67	0.02V-1.18V	1.31
Range 9	1.55V-1.74V	0.18	1.57V-1.75V	0.42	1.58V-1.67V	0.05	1.18V-1.28V	0.09
Range 10	1.74V-3V	0.16	1.75V-3V	0.4	1.67V-3V	0.32	1.28V-3V	0.24

Table 4-5: Summary of the first cycle insertion ranges and lithium (x) inserted.

	$\text{LiFe}_{0.5}\text{Ti}_{1.5}\text{O}_4$		$\text{LiFe}_{0.625}\text{Ti}_{1.375}\text{O}_4$		$\text{LiFe}_{0.75}\text{Ti}_{1.25}\text{O}_4$		LiFeTiO_4	
	Insertion		insertion		insertion		Insertion	
	range	x	range	x	range	x	range	x
Range 1	3.00V-0.70V	0.1	3.00V-0.76V	0.17	3.00V-0.81V	0.09	3.00V-0.83V	0.05
Range 2	0.70V-0.30V	0.43	0.76V-0.40V	0.72	0.81V-0.65V	0.33	0.83V-0.70V	0.24
Range 3	0.30V-0.02V	0.24	0.40V-0.02V	0.36	0.65V-0.02V	0.6	0.70V-0.02V	1.11
Range 4	0.02V-1.55V	0.31	0.02V-1.60V	0.34	0.02V-1.59V	0.61	0.02V-1.19V	1
Range 5	1.55V-1.70V	0.25	1.60V-1.80V	0.39	1.59V-1.69V	0.06	1.19V-1.29V	0.06
Range 6	1.70V-3.00V	0.14	1.80V-3.00V	0.51	0.69V-3.00V	0.29	1.29V-3.00V	0.19

Table 4-6: Summary of the second cycle voltage ranges and capacities and lithium (x) inserted.

Summarising and comparing this data we observe the following:

- Initial insertion above 1V is quite complex, occurring via a series of insertion steps (two phase regions) separated by regions of steady voltage drop (single phase insertion). For $\text{LiFe}_{0.5}\text{Ti}_{1.5}\text{O}_4$ and LiFeTiO_4 the region is simplest, with the former showing just one plateau at 1.5V followed by steady insertion down to a short plateau at 0.8V. The latter shows instead a plateau at 2.15V. For $\text{LiFe}_{0.625}\text{Ti}_{1.375}\text{O}_4$ and $\text{LiFe}_{0.75}\text{Ti}_{1.25}\text{O}_4$ the profile is seemingly a complex mixture of the two end members, with the 2.15V plateau being seen to grow with increasing Fe content and the 1.5V plateau becoming less well defined. A region of insertion between 2V and 1.5V, absent in the two end members, is also seen to develop in these two samples.
- Insertion below 1V is much more consistent. For all samples a short plateau is seen at ~0.8V, followed by a larger one below this, then a region of single phase insertion over a steady voltage drop down to 0.02V. The second plateau is seen to shift from 0.37V in $\text{LiFe}_{0.5}\text{Ti}_{1.5}\text{O}_4$ to 0.72V in LiFeTiO_4 , partially obscuring in the latter the 0.8V insertion. Neither plateau is seen to follow any obvious trend, but the insertion range from this down to 0.02V is seen to increase dramatically with increasing Fe content, particularly for LiFeTiO_4 .
- Deinsertion occurs in 3 distinct stages: Two regions of steady deinsertion with increasing voltage separated by a plateau. For LiFeTiO_4 this plateau occurs at 1.23V, for the other members of the series it is slightly higher in

the 1.6V area. The magnitude of insertion at this stage also varies strangely. For the two compositions poorest in Fe it is quite significant, with deinsertion of 0.18x and 0.42x for $\text{LiFe}_{0.5}\text{Ti}_{1.5}\text{O}_4$ and $\text{LiFe}_{0.625}\text{Ti}_{1.375}\text{O}_4$ respectively. For the $\text{LiFe}_{0.75}\text{Ti}_{1.25}\text{O}_4$ and LiFeTiO_4 compositions the capacity at this point is negligible. Again, the only trend we see in the deinsertion profile is in the very lowest region, where capacity is seen to increase with Fe content.

- On second insertion, all samples are seen to behave in similar fashion. The complex region of insertion above 1V is lost and in its place is a region of insertion accompanied by steady reduction of the sample. The short plateau at 0.8V is also lost, but the one below this is retained, though shortened and shifted to higher potential in all samples. The steady reduction step down to 0.02V is also retained, again showing greater capacity with greater Fe content. For all regions, however, and consequently for the samples as a whole, there is considerable capacity drop between first and second insertions. The second deinsertion is seen to be very similar to the first, with capacities also similar.
- On extended cycling (see below), all samples show capacity levelling off after the first five cycles. Definition of the cycling profiles softens on long cycling also, indicating some degradation of the electrode material.
- Initial insertion capacities seem to follow a trend with increasing sample Fe content, LiFeTiO_4 showing the best initial insertion capacity at 615mAh/g. $\text{LiFe}_{0.625}\text{Ti}_{1.375}\text{O}_4$ though, shows the best cyclability, with capacity after 10 cycles of 173mAh/g. However, considering the disparity between the initial insertion capacities, the retained levels of lithium insertion for the series as a whole are surprisingly similar.

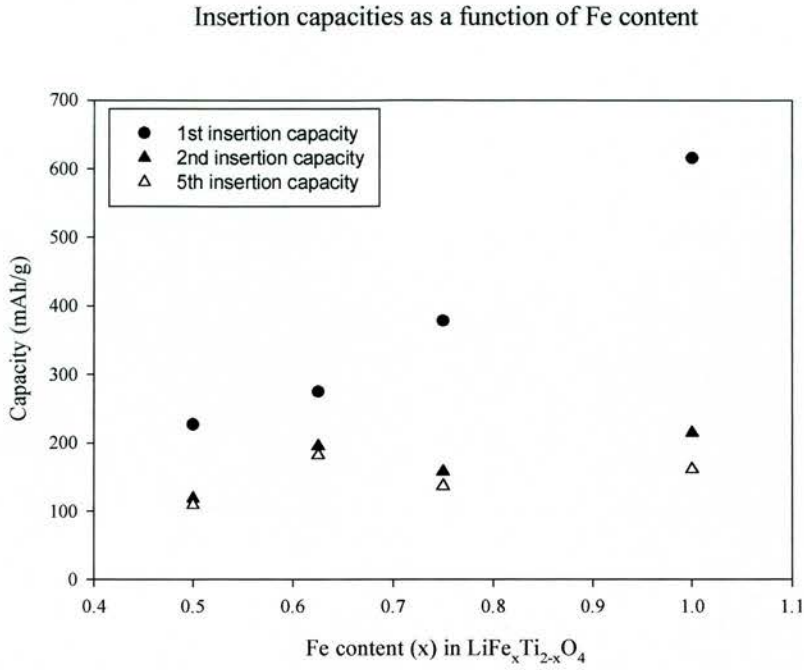


Figure 4-52: First insertion capacities for the $\text{LiFe}_x\text{Ti}_{2-x}\text{O}_4$ series

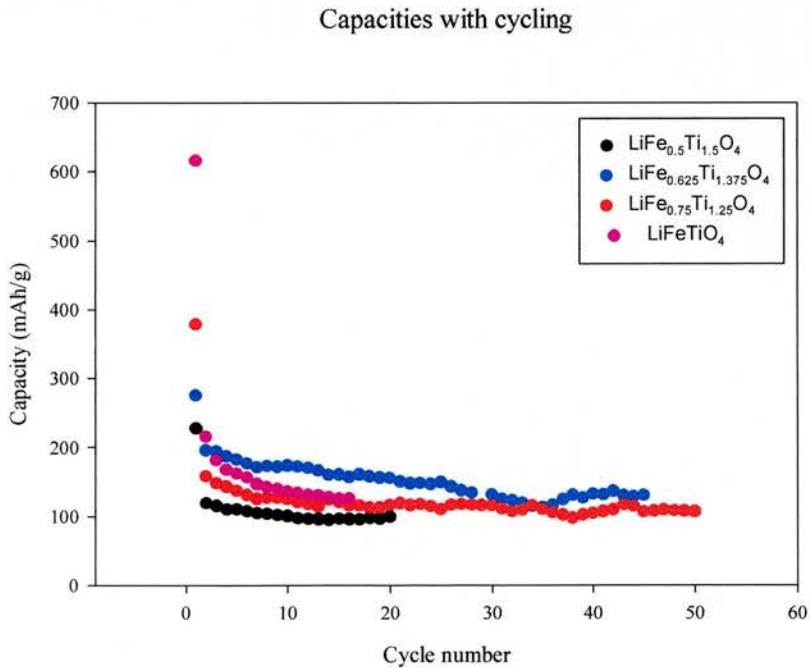


Figure 4-53: Cycling capacities for the $\text{LiFe}_x\text{Ti}_{2-x}\text{O}_4$ series

4.4.3 In-situ and ex-situ XRD studies

4.4.3.1 Introduction and experimental

As a complement to the cycling results reported above, we decided to perform a limited X-ray diffraction study on the electrochemically cycled materials. To do this we used a transmission mode in-situ XRD electrochemical cell, the design and limitations of which have already been discussed in earlier chapters. For the investigation, $\text{LiFe}_{0.5}\text{Ti}_{1.5}\text{O}_4$ was felt to be the best candidate material, as it displays the strongest ordering peaks and so any structural changes would be easiest seen for this sample. A similar potentiostatic cycling regime was employed as for the lithium titanate samples. Additionally, we collected XRD data on electrodes that had been cycled many times to assess the materials' stability over extended cycling.

4.4.3.2 Results

Presented below are the in-situ data collected for $\text{LiFe}_{0.5}\text{Ti}_{1.5}\text{O}_4$. Patterns were collected at 2.6V (pre cycling), 1.1V (Between the 1st and 2nd insertion plateaus), 0.6V (between 2nd and 3rd insertion plateau) and at 0.2V (after the 3rd insertion plateau). Further patterns were collected after oxidation back up to 1.5V and 2.2V.

In situ XRD plots for the $\text{LiFe}_{0.5}\text{Ti}_{1.5}\text{O}_4$ cell as made,
at 1.1V, and at 0.6V

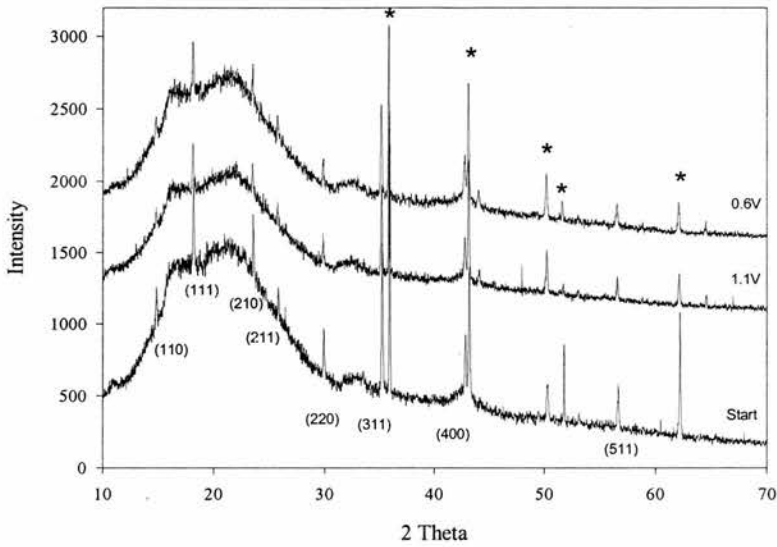


Figure 4-54: In situ XRD plots taken before cycling and at 1.1V and 0.6V after reduction. * indicates peaks associated with the in situ cell.

In situ XRD plots for $\text{LiFe}_{0.5}\text{Ti}_{1.5}\text{O}_4$ after cycling down to 0.2V
and back up to 1.5V and 2.2V

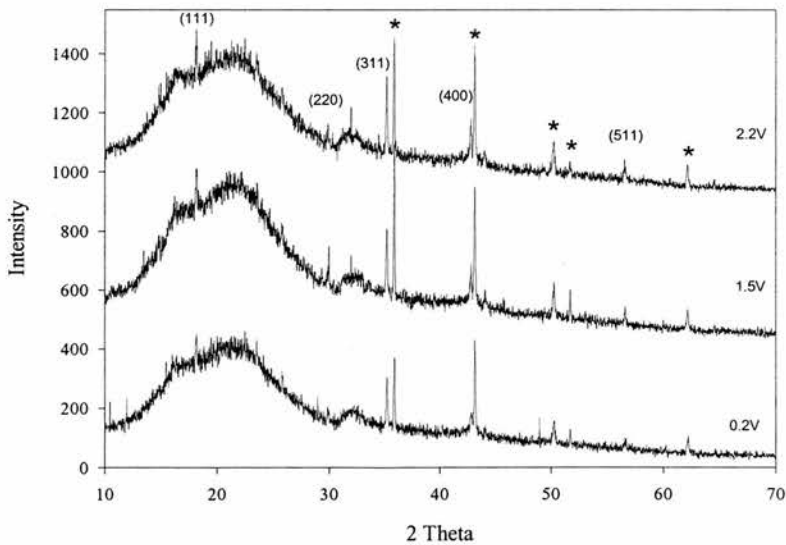
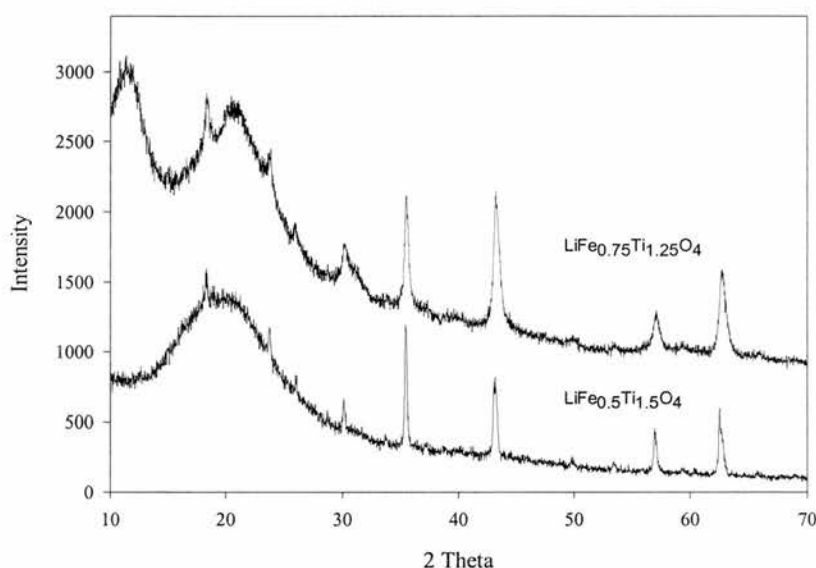


Figure 4-55: In situ XRD plots after reduction to 0.2V and then after oxidation to 1.5V and 2.2V. * indicates peaks associated with the in situ cell.

Voltage	Unit cell edge (Å)	Unit cell Volume (Å ³)
2.3V	8.435(2)	600.31(24)
1.1V	8.441(2)	601.5(3)
0.62V	8.446(2)	602.57(24)
0.20V	8.438(4)	600.7(5)
1.5V	8.442(9)	601.6(12)
2.2V	8.445(5)	602.3(6)

Table 4-7: Variation of unit cell with cycling.

Ex situ XRD patterns of $\text{LiFe}_{0.5}\text{Ti}_{1.5}\text{O}_4$ and $\text{LiFe}_{0.75}\text{Ti}_{1.25}\text{O}_4$ after cycling

Figure 4-56: XRD patterns of $\text{LiFe}_{0.5}\text{Ti}_{1.5}\text{O}_4$ and $\text{LiFe}_{0.75}\text{Ti}_{1.25}\text{O}_4$ electrodes after cycling.

On cycling, we see similar unit cell expansions for both the insertion between 2.3V and 1.1V and the insertion between 1.1V and 0.62V. Cumulatively they represent a $\sim 0.4\%$ change in cell volume on insertion (which compares with a 5.6% change in LiMn_2O_4 and a 1.8% change in LiV_2O_4). Below this voltage we see an anti-intuitive cell contraction over the last stage of insertion down to 0.2V.

Also interesting is the variation in intensity of the spinel phase diffraction pattern during cycling. It is clearly seen that on reduction below 0.6V the intensity of all spinel diffraction peaks is seriously diminished. Indeed, the (110), (210), (211) and (220) all but disappear. On re-oxidation though, the entire pattern becomes more intense and

these peaks are seen to grow back, the (111) and (220) in particular. None of the peaks are seen to grow back to the intensities seen before cycling, however, with the peaks relating to the ordering seeming to suffer more in comparison to the others. Any suggestion that the ordering is lost on cycling, though, is firmly disproved by the ex situ diffraction data collected for both $\text{LiFe}_{0.5}\text{Ti}_{1.5}\text{O}_4$ and $\text{LiFe}_{0.75}\text{Ti}_{1.25}\text{O}_4$. These show quite clearly that both the spinel framework and the cation ordering are retained on extended cycling, though broadening of the diffraction peaks, particularly in $\text{LiFe}_{0.75}\text{Ti}_{1.25}\text{O}_4$, may indicate some structural degradation.

4.4.4 Electrochemistry conclusions

Immediately evident from our results is the fact that the $\text{LiFe}_x\text{Ti}_{2-x}\text{O}_4$ system does not behave in a conventional fashion for an oxide spinel. The very high level of insertion into the materials, particularly into LiFeTiO_4 , far exceeds the capacity that would be expected to result from a normal insertion process. The cycling profiles also bear little resemblance to those of similar spinels: Ti^{4+} is known to cycle in the 1.5V region⁴², Fe^{3+} between this potential and 3V^{4,43}. The first insertion cycle is considerably more complex than those seen for either $\text{Li}_4\text{Ti}_5\text{O}_{12}$ ⁴² or LiFe_5O_8 ⁴, but has much in common with the behaviour of the Ti rich end of the $\text{Li}_4\text{Ti}_5\text{O}_{12}$ - LiFe_5O_8 system reported by Robertson *et al*⁴⁴ and Ma *et al*⁴⁵. Nevertheless, all materials display relatively good cyclability and capacity retention following the second lithium insertion, and insert in a very favourable voltage range for lithium battery applications.

Identifying and assigning the redox processes occurring here, particularly in the higher voltage region is impossible due to the possible presence of several redox couples involving at least Fe^{2+} , Fe^{3+} , Ti^{3+} and Ti^{4+} , along with the occupation of both tetrahedral and octahedral sites by transition metals. In many ways, though, such evaluation is unnecessary as on second insertion many of these processes are lost, being replaced by a more simple insertion profile. With this change in profile on second insertion we observe an enormous loss of capacity, the magnitude of which increases with the iron content of the sample. Noting that the first and second deinsertion profiles do not differ so greatly as the first and second insertion profiles, and correlating this with the observation that the major capacity loss occurs only on first insertion, we can suggest

that the samples undergo some irreversible and structure changing process on the initial cycle down to 0.02V.

It has been reported that for the structurally similar lithium ferrite spinel, high levels of insertion can lead to the formation of a two phase mixture of Li_2O and Fe. Our in situ and ex situ XRD studies show no evidence of this occurring for the $\text{LiFe}_x\text{Ti}_{2-x}\text{O}_4$ system, and instead confirm that the spinel framework is maintained on cycling. Robertson *et al* reported similar findings for the $\text{Li}_4\text{Ti}_5\text{O}_{12}$ - LiFe_5O_8 system, though noted that there may be some amorphisation occurring, and possibly some Fe extrusion from the sample. This would certainly fit well with our data, explaining in particular why the initial capacities are linked to the Fe content, whilst the long term cycling capacities are similar for all samples.

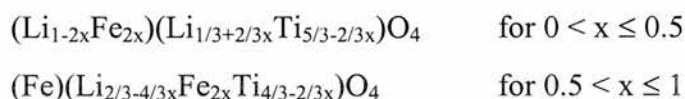
Also unusual is the hysteresis behaviour of the materials on cycling, with all samples displaying an apparent polarisation between insertion at 0.7V and 1.6V. Both Robertson *et al* and Ma *et al* observed similar hysteresis behaviour to that exhibited in our samples, with the latter attributing it to the “blocking” of the spinel channels by Fe on the 8a sites, a logical explanation if the insertion/deinsertion reactions were more conventional. Robertson *et al*, however, found that the apparent polarisation between the 0.7V insertion and 1.6V deinsertion was not dependent on the cycling rate, and concluded that the effect was thermodynamic rather than kinetic in origin. This suggests that there may be complex redox processes occurring, with insertion taking place over a long voltage decline reminiscent of the amorphous Tin oxide anodes, whilst deinsertion occurs at a voltage expected for $\text{Ti}^{4+}/\text{Ti}^{3+}$ redox.

4.5 Summary

In this work we have presented the results of our studies on a new system of ferrite spinels. A large region of the nominal “ Li_3O_4 ”-“ Ti_3O_4 ”- Fe_3O_4 phase diagram lying between the $\text{Li}_{4/3x}\text{Fe}_{2-2x}\text{Ti}_{1+2/3x}\text{O}_4$ (Fe^{2+}) and $\text{Li}_{0.5+0.5x}\text{Fe}_{2.5-1.5x}\text{Ti}_x\text{O}_4$ (Fe^{3+}) solid solutions has been synthesised, with a large region of 1:3 octahedral ordering being found towards the Fe-poor end of the system.

X-ray diffraction studies of the ordered region show that the ordering is not an on-off phenomena, but a gradual and consistent one, the degree of which can be characterised in terms of B site cation disorder and a changing length scale over which ordering occurs. Using neutron and x-ray diffraction in a complementary fashion, we have demonstrated that the stoichiometry $\text{LiFe}_{0.5}\text{Ti}_{1.5}\text{O}_4$ is probably the most ordered sample in the region, and that the 4b/12d cation disorder increases in a linear fashion between this composition and the disordered LiFeTiO_4 .

For the $\text{Li}_{4/3x}\text{Fe}_{2-2x}\text{Ti}_{1+2/3x}\text{O}_4$ solid solution joining $\text{Li}_{4/3}\text{Ti}_{5/3}\text{O}_4$ with Fe_2TiO_4 , it was found that Fe^{2+} rather surprisingly substitutes preferentially onto the tetrahedral A site, a result in contradiction to both crystal field theory and previous work on Fe_3O_4 . Based on our XRD studies we have been able to suggest a two stage substitution mechanism for the series.



Magnetic studies on the $\text{LiFe}_x\text{Ti}_{2-x}\text{O}_4$ solid solution have shown two distinct classes of magnetism. The composition $\text{LiFe}_{0.5}\text{Ti}_{1.5}\text{O}_4$ was found to be paramagnetic down to 5K, as would be expected considering the occupancy of only the A site by a magnetic cation. Fitting the data to Curie Weiss behaviour we found a negative value of θ , indicating the presence of antiferromagnetic interactions, and we were able to calculate the magnetic moment of the Fe^{2+} to be in good agreement with the literature at 5.65 Bohr magnetons. Unusual Mössbauer behaviour in the sample is thought to relate to a localised distortion of the A-site similar to that seen in FeCr_2O_4 and FeV_2O_4 , but not strong enough to cause the tetragonal distortion of the general structure seen in these samples.

The more oxidised $\text{LiFe}_{0.75}\text{Ti}_{1.25}\text{O}_4$ and LiFeTiO_4 samples were found to show very complex magnetisation behaviour not conducive with that of a normal ferrimagnet. Field loops of the samples at various temperatures showed a linear increase in magnetisation with applied field, with no sign of saturation even up to 12 Tesla. This is

indicative of a canted magnetic system. Neutron diffraction studies of LiFeTiO_4 confirms this to be the case.

Electrochemical investigations on the $\text{LiFe}_x\text{Ti}_{2-x}\text{O}_4$ solid solution also show unusual behaviour. Exceptionally high levels of insertion seen for the first cycle were lost on the second insertion, along with several features of the voltage profile. The magnitude of the initial insertion and the capacity loss were both found to be dependent on the Fe content of the starting material, suggesting that the irreversible capacity in the first insertion is related to an irreversible process involving this Fe, such as the extrusion of amorphous Fe from the sample. The formation of an amorphous type system akin to that of SnO_2 is shown to not be the case by XRD. An unusually large disparity between the insertion and deinsertion voltages was also seen, and is thought to indicate complex redox behaviour in the sample.

As previously mentioned, much of the work presented here is provisional, particularly the magnetic results. Attempts to discriminate Fe^{2+} and Fe^{3+} on the different crystallographic sites of the reduced samples in the series is still underway, and analysis of both neutron diffraction and Mössbauer data is expected to follow. More electrochemical testing of the samples, possibly combined with structural analysis, is also required in order to characterise the unusual insertion behaviour of the materials, in particular the large voltage difference between insertion and deinsertion.

References

- ¹ E. J. W. Verwey, *Nature (London)*. 144, (1939), 327.
- ² E. Schloemann, *J. Magn. Magn. Materials*. 209, (2000), 15.
- ³ M. Pardavi-Horvath, *J. Magn. Magn. Materials*. 215, (2000), 171.
- ⁴ L. A. de Picciotto, M.M. Thackeray. *Mater. Res. Bull.* 21, (1986), 583.
- ⁵ G. Blasse. *Philips Res. Rep. Suppl.* No.3. (1964).
- ⁶ J. Crangle. "Solid State Magnetism". Edward Arnold, London.
- ⁷ Y. Ein-Eli, W.F. Howard Jr. S. H. Lu, S. Mukerjee, J. McBreen, J.T. Vaughey, M.M. Thackeray. *J. Electrochem Soc.* 145, (1998), 1238.
- ⁸ H. Kawai, M. Nagata, H. Tukamoto, A.R. West. *J. Mater. Chem.* 8(4), (1998), 837
- ⁹ P.B. Braun. *Nature*. 170, (1952), 1123
- ¹⁰ H. Kawai, M. Tabuchi, M. Hagata, H. Tukamoto, A.R. West. *J. Mater. Chem.* 8(5), (1998), 1273.
- ¹¹ E. Wolska, K. Stempin, O. Krasnowska-Hobbs. *Solid State Ionics*, 101-103, (1997), 527.
- ¹² J. Åhman, G. Svensson, J. Albertsson. *Acta Chemica Scandinavica*. 50, (1996), 391.
- ¹³ S. Arakawa, S. Toinaga, S. Hayashi. *J. Mater Chem.* 8, (1998), 1589.
- ¹⁴ S. Scharner, W. Weppner, P. Schmid-Beurmann. *J. Solid State Chem.* 134, (1997), 170.
- ¹⁵ M.A. Arillo. M.L. López, E. Perez-Cappe, M.L. Veiga. *Solid State Ionics*. 107, (1998), 307
- ¹⁶ A. Tomas, P. Laruelle, J.L. Dormann, M. Nogues. *Acta Cryst.* C39, (1983), 1615.
- ¹⁷ S.J. Marin, M. O'Keeffe, D.E. Partin. *J. Solid State Chem.* 113, (1994), 413.
- ¹⁸ R. Famery, F. Queyroux, J.C. Gilles, P. Herpin. *J. Solid State Chem.* 30, (1979), 257.
- ¹⁹ M.J. Rossiter, P.T. Clarke. *Nature*. 207, (1965), 402.
- ²⁰ A. Maddock. *Mössbauer Spectroscopy Principles and Applications*. Horwood Publishing, Chichester.
- ²¹ A.S. Wills. *Physica B*, 276-278, (2000), 680.
- ²² J. Rodriguez-Carvajal. *15th C.Int. Un. Cryst.* (1990), 127.
- ²³ P. Kishan, C. Prakash, J. S. Baijal, K. K. Laroia. *Phys Stat Solidi (a)*. 84, (1984), 535.
- ²⁴ S.K. Kulshreshtha, *J. Magn. Magn. Materials*. 53, (1986), 345.
- ²⁵ C. Kittel. "Introduction to solid state physics", 7th ed. John Wiley and sons, New York, (1996).
- ²⁶ M. Tanaka, T. Tokoro, Y. Aiyama. *J. Phys. Soc. Japan*. 21(2), (1966), 262.
- ²⁷ J. B. Goodenough. *Magnetism and the Chemical Bond*. Interscience, (1963)
- ²⁸ Y. Yafet, C. Kittel. *Physical Review*. 87(2), (1952), 290.
- ²⁹ C. Masquelier, M. Tabuchi, K. Ado, R. Kanno, Y. Kobayashi, Y. Maki, O. Nakamura, J.B. Goodenough. *J. Solid State Chem.* 123, (1996), 255.
- ³⁰ Y. Xia, T. Sakai, C. Wang, T. Fujieda, K. Tatsumi, K. Takahashi, A. Mori, M. Yoshio. *J. Electrochem. Soc.* 148, (2001), A112.
- ³¹ F. Le Cras, D. Bloch, P. Strobel. *J. Power Sources*, 63, (1996), 71.
- ³² T. Takada, H. Enoki, H. Hayakawa, E. Akiba. *J. Solid State Chem.* 139, (1998), 290.
- ³³ M.M. Thackeray, M.F. Mansuetto, C.S. Johnson. *J. Solid State Chem.* 125, (1996), 274.
- ³⁴ C. Sigala, D. Guyomard, A. Verbaere, Y. Piffard, M. Tournoux. *Solid State Ionics*, 81, (1995), 167.

-
- ³⁵ Y-S. Hong, C-H. Han, K. Kim, C-W. Kwon, G. Campet, J-H. Choy. *Solid State Ionics*, 139, (2001), 75.
- ³⁶ C. Sigala, A. Verbaere, J.L. Mansot, D. Guyomard, Y. Piffard, M. Tournoux. *J. Solid State Chem.* 132, (1997), 372.
- ³⁷ M. Wakihara, L. Guohua, H. Ikuta, T. Uchida. *Solid State Ionics*, 86, (1996), 907.
- ³⁸ K. Amine, H. Tukamoto, H. Yasuda, Y. Fujita. *J. Electrochem. Soc.* 143(5), (1996), 1607.
- ³⁹ B. Zachau Christiansen, K. West, T. Jacobsen, S. Atlung. *Solid State Ionics*. 40, (1990), 580.
- ⁴⁰ C.J. Chen, M. Greenblatt, J.V. Waszczak. *J. Solid State Chem.* 64, (1986), 240.
- ⁴¹ E. Ferg, R.J. Gummow, A. de Kock, *J. Electrochem. Soc.* 141, (1994), L147.
- ⁴² S. Bach, J.P. Pereira-Ramos, N. Baffier. *J. Mater. Chem.* 8(1), (1998), 251.
- ⁴³ C.J. Chen, M. Greenblatt, J.V. Waszczak. *J. Solid State Chem.* 64, (1986), 240.
- ⁴⁴ A.D. Robertson, H. Tukamoto, J.T.S. Irvine. *J. Electrochem Soc.* 146, (1999), 3958.
- ⁴⁵ S. Ma, H. Noguchi. *J. Electrochem Soc.* 148, (2001), A589.

Appendix 1

Table 1: Unit cell data for LiTi₂O₄, Space Group Pbnm (62)

Temp (°C)	a (Å)	b (Å)	c (Å)	Unit Cell Vol (Å ³)
25	5.03138(9)	9.61844(18)	2.94685(5)	142.610(4)
75	5.03750(9)	9.61787(17)	2.95034(5)	142.944(4)
150	5.04374(9)	9.61843(17)	2.95380(5)	143.297(4)
300	5.05385(12)	9.62675(24)	2.95835(6)	143.930(6)

Table 2: Unit Cell Data for Li_{1.1}Ti_{1.8}O₄

Temp (°C)	a (Å)	b (Å)	c (Å)	Unit Cell Vol (Å ³)
25	5.01842(7)	9.57328(13)	2.94745(4)	141.6038(32)
75	5.02246(7)	9.57793(13)	2.94948(4)	141.8841(32)
150	5.02838(7)	9.58423(13)	2.95191(4)	142.2632(32)
300	5.03498(7)	5.59089(15)	2.95469(4)	142.682(4)

Table 3: Atom Position data for LiTi₂O₄. Occupancies for the Titanium and oxygen sites were held at 1 for stability purposes after preliminary refinements showed no obvious deficiency or excess. Li occupancy was refined once at 25°C, and the obtained value used for all temperatures.

		Temperature (°C)			
		25	75	150	300
Li	X	-0.0542(29)	-0.0538(28)	-0.0523(31)	-0.056(5)
	Y	0.4742(20)	0.4711(28)	0.4776(24)	0.467(6)
	SOF	0.4574(210)	0.4574	0.4574	0.4574
	Uiso (x100)	5.21(32)	5.8(4)	5.5(4)	8.2(7)
Ti	X	-0.0184(4)	-0.185(5)	-0.0180(5)	-0.0190(7)
	Y	0.14220(22)	0.14181(24)	0.14231(24)	0.14119(35)
	SOF	1	1	1	1
	Uiso (x100)	0.576(33)	0.596(35)	0.72(4)	0.84(5)
O1	X	0.69836(34)	0.69761(35)	0.69758(37)	0.6939(5)
	Y	0.27891(15)	0.27887(16)	0.27859(16)	0.27784(22)
	SOF	1	1	1	1
	Uiso (x100)	0.898(27)	0.903(29)	1.036(31)	1.08(4)
O2	X	0.20095(28)	0.20082(29)	0.20114(31)	0.2028(4)
	Y	-0.03511(14)	-0.03534(14)	-0.03538(15)	-0.03549(20)
	SOF	1	1	1	1
	Uiso (x100)	0.646(55)	0.629(26)	0.718(28)	0.77(4)

Table 4: Atom Position data for $\text{Li}_{1.1}\text{Ti}_{1.8}\text{O}_4$. Occupancies for the Li/Ti and oxygen sites were held at 1 for stability purposes after preliminary refinements showed no obvious deficiency or excess. Atomic position and Thermal parameters for the Li(2) and Ti sharing a site were constrained to refine together. Li(1) occupancy was refined once at 25°C, and the obtained value used for all temperatures.

	Temperature (°C)			
	25	75	150	300
Li(1) X	-0.0600(23)	-0.0584(25)	-0.0551(22)	-0.0608(30)
Y	0.47169(339)	0.47235(349)	0.4788(43)	0.45750(518)
SOF	0.4325(240)	0.4325	0.4325	0.4325
Uiso(x100)	8.31(42)	9.44(47)	10.67(54)	12.89(80)
Li(2) X	-0.0259(4)	-0.0255(4)	-0.0251(7)	-0.0261(4)
/Ti Y	0.14140(20)	0.14150(21)	0.1417(4)	0.14070(25)
SOF	0.1/0.9	0.1/0.9	0.1/0.9	0.1/0.9
Uiso (x100)	0.97(4)	1.13(5)	1.16(5)	1.47(6)
O1 X	0.68422(24)	0.68399(25)	0.68384(26)	0.68262(30)
Y	0.27627(12)	0.27615(13)	0.27606(13)	0.27602(15)
SOF	1	1	1	1
Uiso (x100)	1.111(38)	1.30(4)	1.44(4)	1.73(6)
O2 X	0.20259(21)	0.20273(21)	0.20276(21)	0.20338(24)
Y	-0.03401(10)	-0.03424(11)	-0.03413(11)	-0.03425(13)
SOF	1	1	1	1
Uiso (x100)	0.812(35)	1.02(4)	1.09(4)	1.42(5)

Table 5: Anisotropic Li Thermal Parameters (x100) for the channel site in LiTi_2O_4 and $\text{Li}_{1.1}\text{Ti}_{1.8}\text{O}_4$

Temp (°C)	LiTi_2O_4				$\text{Li}_{1.1}\text{Ti}_{1.8}\text{O}_4$			
	U11	U22	U33	U12	U11	U22	U33	U12
25	4.7(7)	11.4(14)	2.7(6)	5.5(8)	2.11(53)	32.13(326)	4.64(78)	3.33(101)
75	2.3(6)	18.5(22)	3.2(7)	4.6(10)	2.21(58)	30.89(339)	7.82(103)	5.09(109)
150	2.8(7)	11.0(15)	6.1(9)	2.8(8)	0.62(48)	41.25(441)	8.55(108)	3.09(108)
300	2.5(11)	30(6)	8.3(19)	3.6(20)	1.85(78)	42.79(601)	13.17(185)	6.52(166)

Table 6: Quality of Fit for LiTi_2O_4 and $\text{Li}_{1.1}\text{Ti}_{1.8}\text{O}_4$

Temp (°C)	LiTi_2O_4			$\text{Li}_{1.1}\text{Ti}_{1.8}\text{O}_4$		
	Rwp(%)	Rp(%)	Chi ²	Rwp(%)	Rp(%)	Chi ²
25	4.87	3.46	1.826	4.4	3.11	1.718
75	4.87	3.45	1.454	4.39	3.07	1.759
150	4.91	3.48	1.478	4.19	2.93	1.582
300	5.14	3.73	1.539	4.55	3.1	1.832

Table 7: Crystallographic data for delithiated and relithiated TiO₂R

		TiO ₂ R	LixTi ₂ O ₄ no Lithium	LixTi ₂ O ₄ one Lithium site	LixTi ₂ O ₄ two Lithium sites
	Unit cell a	4.83966(7)	5.00130(14)	5.00134(14)	5.00137(14)
	Unit cell b	9.43328(12)	9.57646(26)	9.57630(26)	9.57631(25)
	Unit cell c	2.96297(4)	2.95519(8)	2.95519(7)	2.95517(7)
	Vol	135.271(3)	141.538(7)	141.537(6)	141.537(6)
	Rwp	5.28	7.03	6.86	6.8
	Rp	3.27	4.35	4.17	4.13
	Chi2	4.916	11.25	10.73	10.54
Li(1)	X	N/A	N/A	-0.036(5)	-0.035(5)
	Y	N/A	N/A	0.4695(29)	0.4702(31)
	SOF	N/A	N/A	0.36	0.23
	Uiso(x100)	N/A	N/A	6.6(6)	2.4(5)
Li(2)	X	N/A	N/A	N/A	0.525(10)
	Y	N/A	N/A	N/A	0.0795(50)
	SOF	N/A	N/A	N/A	0.13
	Uiso(x100)	N/A	N/A	N/A	2.5(10)
Ti	X	-0.0707(4)	-0.0284(6)	-0.0277(6)	-0.0275(6)
	Y	0.13638(19)	0.1393(4)	0.1402(4)	0.1398(4)
	SOF	1	1	1	1
	Uiso(x100)	0.60(6)	1.25(6)	1.36(6)	1.41(6)
O1	X	0.62851(22)	0.6791(4)	0.6784(4)	0.6780(5)
	Y	0.26590(11)	0.27475(24)	0.27519(24)	0.27521(24)
	SOF	1	1	1	1
	Uiso(x100)	0.63(5)	1.62(4)	1.63(4)	1.68(4)
O2	X	0.20901(21)	0.2027(4)	0.2012(4)	0.2013(4)
	Y	-0.02624(11)	-0.03400(21)	-0.03349(20)	-0.03344(20)
	SOF	1	1	1	1
	Uiso(x100)	0.59(4)	1.34(4)	1.28(4)	2.5(10)

The End.